भौमिक एवं ग्रहीय पर्यावरण के उर्जा विज्ञान, गतिकी, एवं रसायन शास्त्र की वैज्ञानिक समझ, तथा समाज पर इनकी विवक्षा

वैज्ञानिक उपलब्धियाँ

Scientific understanding of the energetics, dynamics and chemistry of the terrestrial and planetary environments and implications to the society

SCIENTIFIC ACCOMPLISHMENTS

2019-2020

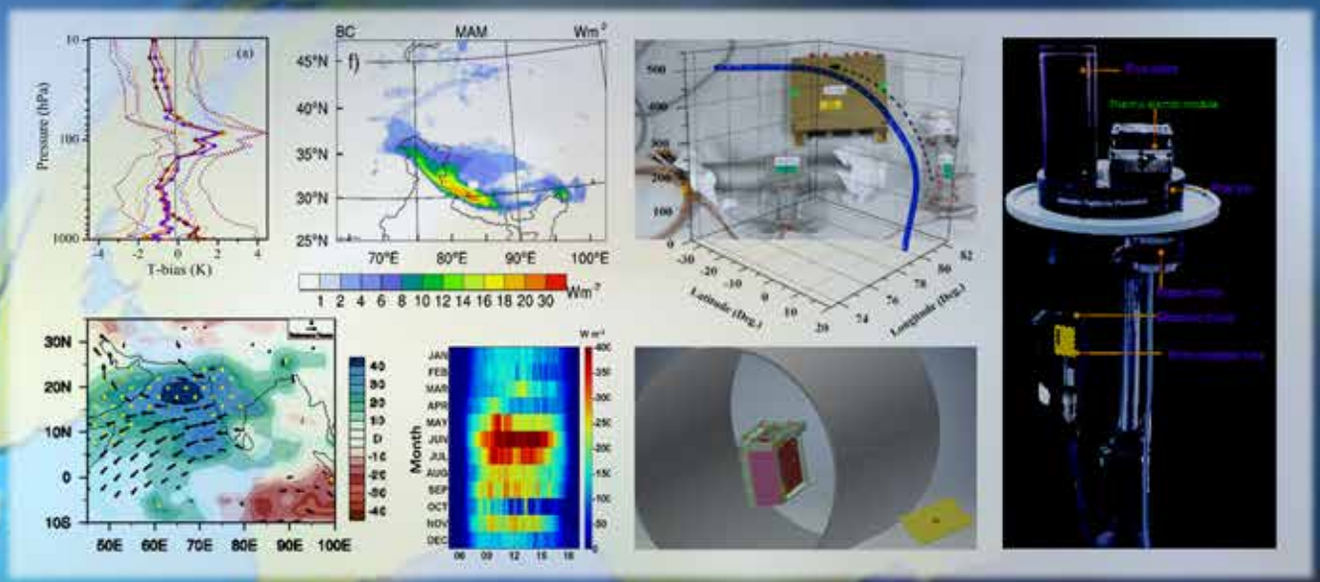

अंतरिक्ष भौतिकी प्रयोगशाला
विक्रम साराभाई अंतरिक्ष केंद्र
तिरुवनन्तपुरम

SPACE PHYSICS LABORATORY
Vikram Sarabhai Space Centre
Thiruvananthapuram

MBLP ATRF NAM ADB ITMP PSB ATD ADM

Scientific Advisory Committee of SPL: 2020 ...

Chairman

Dr. T. K. Alex, Hon. Distinguished Professor, ISRO HQ

Alternate Chairman

Dr. V. K. Dadhwal, Director, IIST

Members

Dr. D S Ramesh, Director, IIG
Dr. Jyotiranjan S. Ray, Director, NCESS, Trivandrum
Shri. Uma Maheswaran, Scientific Secretary, ISRO HQ
Director, SSPO, ISRO HQ
Dr. A K Patra, Director, NARL
Sri. Narayanan Namboodiripad, Deputy Director, AVN, VSSC
Dr. Raj Kumar, Deputy Director, SAC, Ahmedabad
Prof. S K Satheesh, Chairman, DCCC, IISc, Bangalore
Prof. K Mohan Kumar, Emeritus Professor, CUSAT
Prof. Animesh Maitra, Calcutta University
Prof. R Sridharan, Former Director, SPL
Prof. P Balarama Rao, Former Director, NARL
Dr. B V Krishna Murthy, Former Director, SPL
Dr. A Jayaraman, Former Director, NARL
Dr. S Seetha, Former Director, SSPO, ISRO HQ

Member Secretary

Dr. Radhika Ramachandran, Director, SPL

अंतरिक्ष भौतिकी प्रयोगशाला

SPL

Space Physics Laboratory

Scientific Accomplishments 2019-2020

Vikram Sarabhai Space Centre
Indian Space Research Organisation

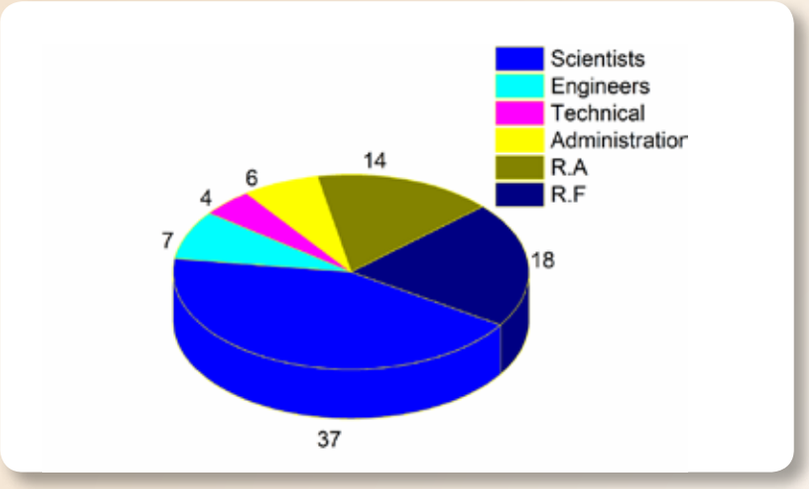

Human Resource

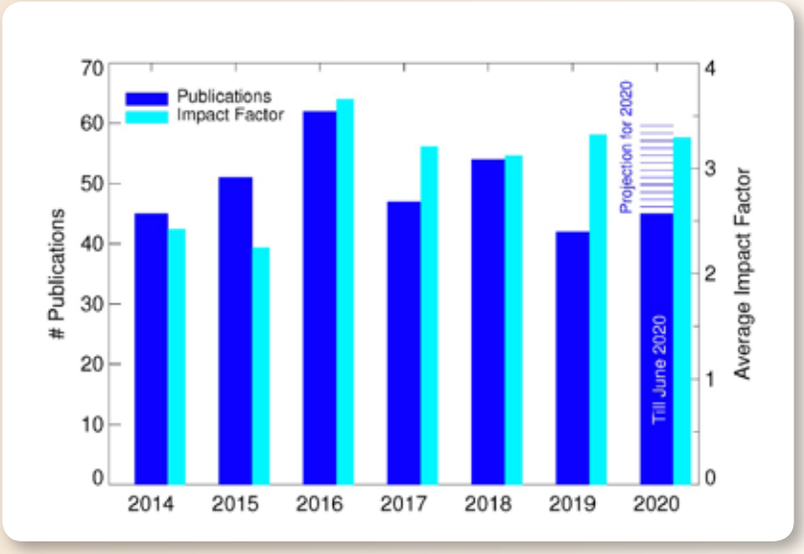

Publications

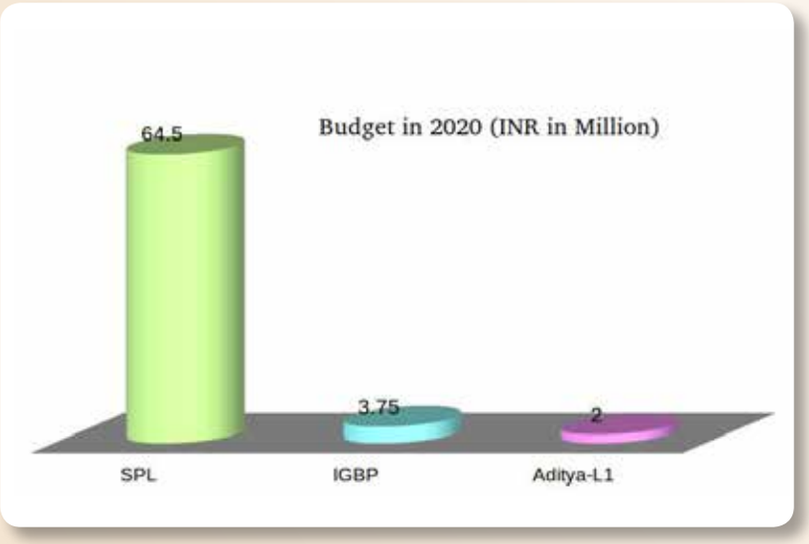

Budget
(₹ *in Millions*)

Looking Back…….

The unprecedented pandemic and the subsequent lockdown affected many of our pet projects, caused cancellation of meetings and scheduled visits. In phases we have arisen and are slowly coming to terms with the new reality.

On behalf of Team SPL, it is my privilege to present a brief report of our activities and accomplishments during the period July 2019-June 2020.

As in the past, this year also saw us investing heavily in the design, testing and development of scientific payloads for planetary missions of ISRO. CHACE-2 (Chandra's Atmospheric Composition Explorer-2), a quadrupole neutral mass spectrometer, on-board Chandrayaan-2 orbiter is currently orbiting around moon and has already completed more than 2000 hours of operation. CHACE-2 aims at observing the tenuous lunar exospheric composition from spacecraft altitude and it has covered both noon-midnight and dawn-dusk orbits. Currently, it is being operated twice a day, each lasting for 4 hrs duration. The analysis revealed conspicuous peaks of Argon-40 near dawn and dusk terminators over equatorial and mid-latitude regions of the Moon. Another significant highlight was the outcome of SPL's IDEA experiment on-board the fourth stage (PS4) of the PSLV C-38 mission, the first scientific experiment on PS-4 platform. The Langmuir probe observation of IDEA payload revealed for the first time, an enhancement in top side electron density concurrent with the operation of the PS4 stage of PSLV, demonstrating the plausible role of rocket burn and exhaust gases in modulating the ionosphere in the vicinity. The realisation of the engineering model of the PAPA payload on-board Aditya-L1 mission is a major milestone, with which the schedules for the QM and FM are being worked out currently. Though we lost the Chandra's Surface Thermo-Physical Experiment (ChaSTE) payload and the Langmuir Probe in the Chandranyaan-2 lander mishap on Sept 6, 2019, extensive tests and validations help us to develop these payloads easily for the Chandrayaan-3 launch slated for 2021. Payloads for the PS4 experiments, DISHA twin satellite mission, Venus mission etc are also in the pipeline. The second phase of the SOUREX experiment on board RH-560 is being planned during February-March 2021 period from SHAR.

Coming to the highlights of the research areas, from the microwave and boundary layer physics area, the first direct estimations of the effect of clouds on the diurnal variation of atmospheric boundary layer height (BLH) over the tropical coastal region under onshore and offshore flow conditions were made using collocated multi-year microwave radiometer profiler and meteorological observations. Radiative-transfer simulations were performed to identify the millimetre (mm) and sub-mm wave spectral bands most suitable for estimating the concentration of species like CO, CO_2, SO_2, water vapour, HDO and HCl, present in the Venusian mesosphere which in turn will be useful in instrument design, frequency and bandwidth selection as well as pointing accuracy determination for future Venus missions. The Ka-band beacon signal (20.2 and 30.5 GHz) received from GSAT-14 satellite beacon at Thumba and the precipitation measured using a collocated laser precipitation monitor were used for quantifying the Ka-band attenuation as a function of precipitation intensity during the summer monsoon season and the convective rain dominated pre-monsoon period. An empirical model for the rain attenuation of Ka-band signal over the tropical coastal station was also developed.

In the area of aerosols trace gases and radiative forcing, the observational and modelling studies on aerosols over Himalayas have brought out the importance of aerosol-induced snow albedo feedback on the regional radiation balance and atmospheric thermodynamics. The first long term observations of microphysical properties of black carbon aerosols from Indian region revealed the dominance of thickly coated BC particles in the IGP outflow, coated with sulfates and organics, leading to enhanced atmospheric absorption having implications on regional climate. Based on the extensive aircraft observations on the altitude variation of cloud condensation nuclei (CCN) characteristics and aerosol number size distributions, the role of natural dust and BC on the CCN efficiency of aerosols at different altitudes over IGP was delineated, which is an important input for the assessment of indirect effect of aerosols. Role of long-range transport and water vapor on the dynamical nature of tropospheric ozone over the tropical coastal region was established based on long term ozone profiling using high altitude balloons. The unique ICARB–2018 field experiments brought forth several pioneering results, which include, frequent occurrence of new particle formation over equatorial Indian Ocean and its role in CCN activation efficiency, delineation of anthropogenic fraction of south Asian outflow using aerosol chemical analysis and role of inter-continental transport on the upper tropospheric carbon monoxide concentration over Indian Ocean.

In the area of Atmospheric Modelling, as in the past, weather prediction support was extended to all the launch campaigns conducted from SDSC-SHAR through the COSMO model. A revised Indian atmospheric model has been developed from surface to 1000 km using 44 years of radiosonde, 21 years of M-100 rocket, 17 years of SABER satellite and 44 years of MSIS data for use in the design and analysis of missions from Indian tropical region, particularly SDSC. A sensitivity experiment with the aid of ERA-Interim Reanalysis and satellite observations was conducted to explore the mechanism behind 'mini break' kind of conditions during the years with early onset of monsoon over the Indian peninsula. A study on the Upper Tropospheric Humidity (UTH) measurements from Kalpana-1, MT-SAPHIR and MLS, shows that the upper troposphere remains dry during the active phase, whereas it becomes wet during the break phases of the Indian summer monsoon.

In the realms of atmospheric dynamics, the pathways through which low-and high-latitude coupling takes place during the sudden stratospheric warming (SSW) events were investigated using a network of meteor radars. For the first time, observational evidence for westward acceleration of zonal winds at stratopause level during SSW events was brought out using RH-200 observations from Thumba. Using three-dimensional wind simulations in the mesosphere lower thermosphere, an algorithm for retrieving the gravity wave momentum fluxes using meteor radar is evaluated. Another major outcome is the validation of INSAT-3D measurements of temperature and humidity using radiosonde observations over land, ocean and coastal regions. The zonally resolved relationship between cold point tropopause and the lower stratospheric water vapor was also investigated using space-based observations. Further, using two decades of MST radar observations over Gadanki, stratosphere-troposphere exchange processes were investigated, comprehensively. Also, the altitudinal structure of turbulence in the troposphere and its contrasting features over the Indian peninsula were delineated using radiosonde observations carried out at six stations.

The Ionosphere Thermosphere Magnetosphere Physics branch focussed the research in investigating the terrestrial upper atmosphere in context of its energetics and dynamics. A delayed response of E region to solar eclipse forcing was brought out and explained on the basis of varying downward diffusion of atomic oxygen. In a study based on the Coherent Radio Beacon (CRABEX) measured TECs, it was shown that the anomaly trough undergoes significant transitions across the dip-equator. For the first time, it was demonstrated experimentally that the process of reverse fountain leads to an enhancement in the post midnight plasma density over the equatorial region. Using the Radio Occultation measurements from Akatsuki satellite, it was demonstrated for the first time, how the wave dynamics lead to isothermal regions in the Venus high-latitude. Another study concerning the Equatorial Spread-F (ESF) phenomenon stresses on the need of thermospheric neutral wind measurements, by analyzing the critical role of the time of F-region zonal plasma drift/wind reversal in modifying the onset time of ESF. In a simulation

study, it was shown that the warm thick-target model involving X-class solar flare plasma is a more consistent model compared to cold thick-target model. Continuing with the space weather aspects, the nightside Martian ionosphere was shown to be primarily controlled by the precipitating Solar Energetic Particles and pickup ions transported across the Martian terminator.

In the planetary sciences area, a photochemical model for the dayside ionosphere of Mars has been brought out for calculating the density profiles of ions and electrons under steady state photochemical equilibrium condition using the in-situ measurements from instruments onboard MAVEN as input. Further, an energy deposition model is employed for calculating the attenuated photon and photoelectron fluxes at different altitudes in the Martian ionosphere, which could reproduce the observed structure of the major ion profiles (O^{2+}, CO^{2+}), and electron density reasonably well. Such a comparison for the deep dip periods is reported for the first time, which showcases the level of the current understanding of the ion chemistry in the Martian ionosphere. In another study, the ionization efficiency is calculated for the dayside Martian ionosphere using MAVEN observations.

The Atmosphere Technology Division focussed on the technological aspects of experimental systems designed for atmospheric, space and planetary science areas, including the development and testing of ground based, balloon, rocket and space-borne payloads from the proof of concept to their realization. It has made significant contributions to the scientific and technical activities of SPL during the reporting period. They include major contributions to the technology development programs for Solar Occultation Experiment and Atomic Oxygen sensor, testing of the modules of PAPA payload onboard Aditya-L1, development of a 2.5 kW power amplifier module for radar systems and augmentation of the night-time photometer. ATD also carried out the operation and maintenance of HF Radar, Digi sonde, and Clean Room as well as the mechanical fabrication activities for scientific instruments.

The year also witnessed certain unique scientific campaigns carried out for probing various domains of the atmosphere. An innovative experiment was carried out to study the horizontal structure of atmospheric gravity waves in the stratosphere by drifting the radiosonde at a constant altitude (~31 km) using the TIFR balloon facility at Hyderabad. A national level experimental campaign “Suryagrahan-2019” was conducted by SPL, VSSC in collaboration with several national institutes by simultaneously launching series of radiosonde and ozone sonde and also placing magnetometers and GPS receivers at different locations to study the response of different atmosphere regions to the annular solar eclipse of 26 December 2019. A portable Carbo sensor was flown on an Unmanned Aerial Vehicle for investigating the variability of CO_2 within the atmospheric boundary layer.

Several of our scientists have received national and international awards and recognitions this year. Active international collaborations with eight foreign agencies (from Australia, Germany, Italy, Japan and USA), and collaborations with several national laboratories continue to strengthen our efforts.

We have been able to continue our outreach activities, though in a restricted manner due to the protocols being imposed. During the period of this report, there were fifty-seven peer-reviewed publications with a cumulative Impact Factor of 184.3 and an average Impact Factor of 3.3. We have an all-time record of ten Ph.D. awarded during the period of this report.

I would like to conclude acknowledging the efforts put in by all members of SPL in the realisation of our objectives. There were several challenges and lessons learnt in this journey which made us emerge stronger and helped us gain valuable insights…… the saga will continue!!

राधिका रामचन्द्रन

राधिका रामचन्द्रन
Radhika Ramachandran

16 October 2020

Awards, Honours & Recognitions

RADHIKA RAMACHANDRAN

- Member, Science Organizing Committee, Committee on Space Research (COSPAR), 2020.
- Co-Editor, Acta Astronautica (Elsevier).
- Member, Commission-I and Publication & Communication Committee, International Academy of Astronautics (IAA).

SNEHA YADAV

- INSA Young Scientist Medal from Indian National Science Academy, 2019.

DHANYA M. B.

- BUTI Foundation Award in the field of Plasma Science and Technology, 2019.

KANDULA V SUBRAHMANYAM

- Young Associate of Indian Academy of Science, 2019-2022.
- Associate Fellow of Andhra Pradesh Academy of Science, 2019.

LAKSHMI N. B.

- Young Scientist Award from the URSI General Assembly and Scientific Symposium, 2020.

VRINDA MUKUNDAN

- INSPIRE Faculty Fellowship from DST, Govt. of India, 2020.

KOUSHIK N.

- SCOSTEP Visiting Scholarship, 2020.

GIRACH IMRAN A.

- Certificate of Excellence in Reviewing, Journal of Earth System Science, 2019 & 2020.

Academic Excellence

KANDULA V SUBRAHMANYAM

- P Krishna Rao Award on “Application of Satellite data and Remote Sensing in Meteorology” by Indian Meteorological Society-2019 for the year 2019 during TROPMET -2019 held at Andhra University, Visakhapatnam on 11 December 2019.

SIDDARTHA SHANKAR DAS

- Young Scientist Award for Best paper published on “Tropical Meteorology for the year 2018” from Indian Meteorological Society (IMS) during TROPMET-2019 held at Andhra University, Visakhapatnam on 11 December 2019.

ARUN B.S.

- Young Polar Scientist Award, National conference on Polar Sciences (NCPS), NCPOR, Goa, 20-22 August, 2019.

SATHEESH CHANDRAN

- Best paper Award, “Dynamic Influence of ASMA on Variability of Ozone in the Upper Troposphere Region Revealed From In Situ Ozone sonde Observations” ASMA International Conference, Chennai, 10-11 February 2020 [Co-authors: S. V. Sunil Kumar]

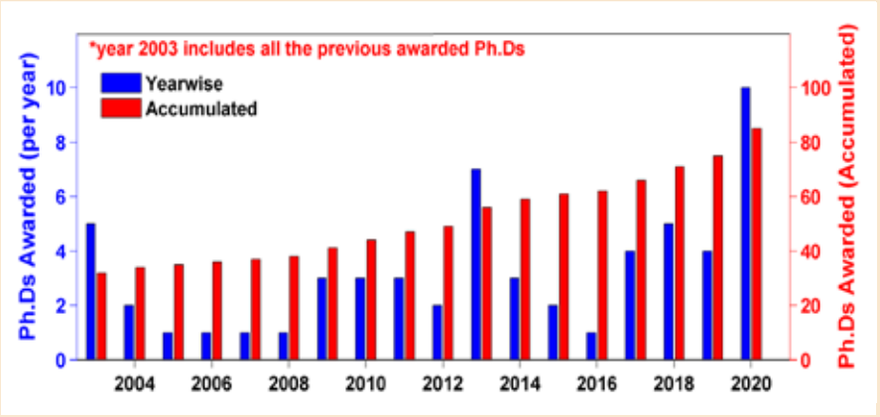

Ph.D. Awarded

ANEESH S.

- Studies on the Indian summer monsoon variabilities and its relation to regional meteorological processes, University of Kerala, Thiruvananthapuram, December, 2019 [Supervisor: Dr. Sijikumar S.].

ASWATHY R. P.

- Investigations on the dynamics of the equatorial and low-latitude ionosphere-thermosphere system and its association with equatorial Spread F, University of Kerala, December, 2019 [Supervisor: Dr. Manju G.]

AJESH A.

- Investigation of the thermosphere ionosphere system over the low and equatorial latitudes, University of Kerala, Thiruvananthapuram, December 2019 [Supervisor: Dr. Tarun Kumar Pant]

SNEHA SUSAN MATHEW

- Poleward Expansion of the Hadley Circulation and Associated Dynamics, Cochin University of Science and Technology, Kochi, July, 2019 [Supervisor: Dr. K. Kishore Kumar]

SUNEETH K. V.

- Studies on the Variability of Tropical Tropopause and its Implication in Stratosphere-Troposphere Exchange, Cochin University of Science and Technology, Kochi, December, 2019 [Supervisor: Dr. Siddarth Shankar Das]

MARIA EMMANUEL

- Spatio-temporal Variability of Water Vapour in the Troposphere and Lower Stratosphere over the Indian Monsoon Region, University of Kerala, Thiruvananthapuram, May, 2020 [Supervisor: Dr. Sunilkumar S. V.]

GIRACH IMRAN ASATAR

- Investigations on the distribution of tropospheric carbon monoxide over India and surrounding oceanic region, Cochin University of Science and Technology (CUSAT), Kochi, November, 2019 [Supervisor: Dr. Prabha R. Nair]

MANOJ M. R.

- Regional Synthesis of Aerosol Properties and its Radiative Impacts over India, Andhra University, Vishakhapatnam, November, 2019 [Supervisor: Dr. S. Suresh Babu].

LAKSHMI N. B.

- Investigations of elevated aerosols over the Indian region and their radiative impacts, Cochin University of Science and Technology (CUSAT), Kochi, January 2020 [Supervisor: Dr. S. Suresh Babu].

JAYACHANDRAN V.

- Characteristics of Cloud Condensation Nuclei over distinct environments in India, Cochin University of Science and Technology (CUSAT), Kochi, January, 2020 [Supervisor : Dr. S. Suresh Babu]

IN-HOUSE INSTRUMENTATION

Plasma Analyser Package for Aditya (PAPA) onboard Aditya-L1 Mission

Engineering Model (EM) of Plasma Analyser Package for Aditya (PAPA) payload onboard Aditya-L1 mission has been developed and tested in-house successfully. PAPA is meant for exploring the solar wind emanating from the Sun and to understand its dynamics from the first Lagrangian point (L1). The payload has been developed indigenously at VSSC and is of first of its kind in India. The integrated EM was successfully tested and validated in the laboratory under high vacuum conditions using Helium ions.

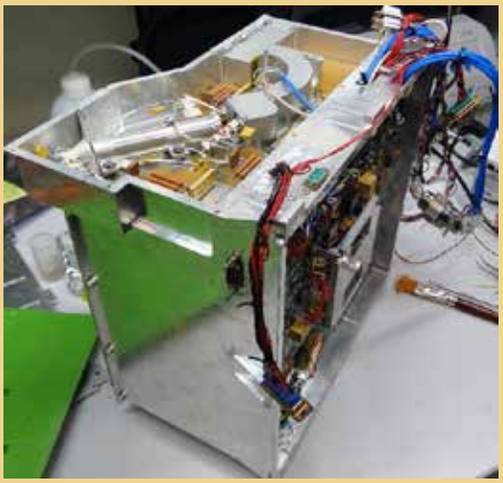

Contents

SCIENTIFIC DISCIPLINES AND ACTIVITIES

Microwave and Boundary Layer Physics

NETWORK OF OBSERVATORIES FOR BOUNDARY LAYER EXPERIMENTS (NOBLE) PROJECT

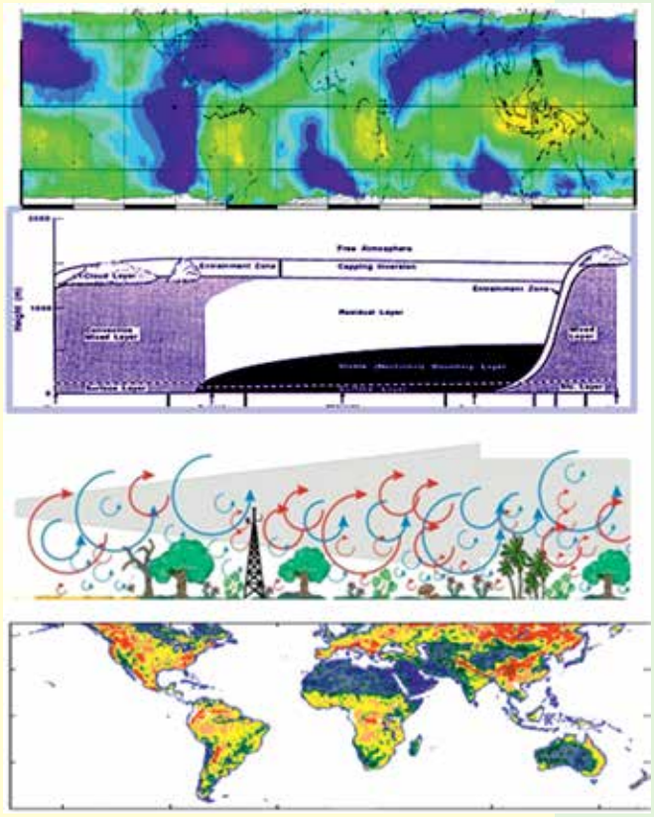

The MBLP branch focuses on the surface characteristics, structure and dynamics of atmospheric boundary layer (ABL) and its coupling with free-troposphere, clouds, convection, precipitation, and microwave remote sensing of the Earth and other planetary bodies. Main objectives are: (i) to improve the understanding of the ABL processes including surface-air interaction processes, diurnal evolution of ABL, and the role of ABL processes in pollutant dispersal, cloud development and hydrological processes, (ii) improve the understanding on clouds, precipitation and energetics of the Earth-atmosphere system, and (iii) spaceborne and ground-based microwave remote sensing of Earth's surface and atmosphere for deriving the surface properties, atmospheric water vapour, cloud characteristics and precipitation, including their potential impact on microwave propagation through the atmosphere. The ChaSTE payload onboard Chandrayaan-3 lander aims at understanding the thermal characteristics of lunar regolith. The NOBLE project of ISRO-GBP is aimed at characterising the ABL on a national canvas covering distinct climate and geographical zones.

Science Team

K. Rajeev
C. Suresh Raju
N. V. P. Kiran Kumar
Manoj Kumar Mishra
Nizy Mathew
M. Santosh
R. Renju

Technical Team

P. T. Lali
P. S. Ajeesh Kumar
P. P. Pramod
Dinakar Prasad Vajja

Research Associates

Sivakumar Reddy
S. Lavanya

Research Fellows

Edwin V. Davis
Sisma Samuel
R.S. Aswathy

Boundary Layer Physics

Effect of Clouds on the Diurnal Evolution of Atmospheric Boundary Layer Height over a Tropical Coastal Station

Growth of daytime convective atmospheric boundary layer (CABL), which plays a pivotal role in the vertical mixing and dispersal of water vapour and pollutants, is modulated by cloud radiative effects. Direct observations on the daytime development of ABL height over coastal regions under contrasting conditions of cloudiness as well as their differences when the background wind is onshore and offshore, are non-existent over tropical coastal regions. The atmospheric temperature and humidity profiles derived from the multi-year (2010–2016) Microwave Radiometer Profiler (MRP) observations (with a time resolution of 3 minutes), along with collocated measurements of infrared brightness temperature (IRT_b) using an up-looking IR radiometer, over the tropical coastal location Thumba (8.5°N, 77°E), provide a unique opportunity for determining the occurrence of clouds and investigation of the diurnal evolution of BLH under clear and cloudy conditions. These observations, together with the background meteorological parameters (near-surface atmospheric temperature, humidity, downwelling shortwave radiative flux, precipitation rate, soil temperature and soil moisture) are used to carry out comprehensive investigations on (i) daytime development of CABL and its seasonal variation during onshore and offshore flows and under contrasting cloud conditions, (ii) shortwave cloud radiative forcing at surface and its impact of soil skin temperature, (iii) driving factor for the rapid growth rate of forenoon CABL through the evolving lower tropospheric thermal structure under cloudy and clear sky periods and (iv) physical mechanisms responsible for the effect of clouds on CABL development. These observations provide essential constraints for evaluating model simulations of ABL under contrasting conditions of clouds and background circulation. As part of this study, a technique based on temporal coherence has been developed for the identification of cloud-free sky and broken and overcast clouds using the up-looking IR radiometer.

Diurnal evolution of ABL height under clear sky and cloudy periods

Finer altitude variations in temperature and humidity may not be well represented in MRP observations since the uncertainty of temperature can be up to 1.5 K at higher altitudes. Hence, this study employs "parcel method" for deriving the CABL height from MRP derived vertical profiles of virtual potential temperature. Parcel method is generally followed for BLH estimates using MRP observations and is found to be in reasonable agreement (within an uncertainty of 150 m) with the BLH estimated using vertical gradients of virtual potential temperature and humidity. The BLH thus calculated are separated into clear sky and cloudy periods by applying temporal coherence method to the collocated IRT_b observations. As the cloud radiative effect on BLH may not be instantaneous, the analysis has been carried out for different duration of clouds (clouds present for >80% of the time during 4 hours and 24 hours prior to the local time of observation).

Figure 1 shows the multi-year (2011–2016) seasonal mean diurnal variations of BLH (following an 'equivalent day' analysis) when clear sky and cloudy conditions prevailed for 24 hours winter (December–February), pre-monsoon (March–May), summer monsoon (June–September) and post-monsoon seasons (October–November). This represents the average effect without discriminating into onshore and offshore winds. During clear sky periods, the

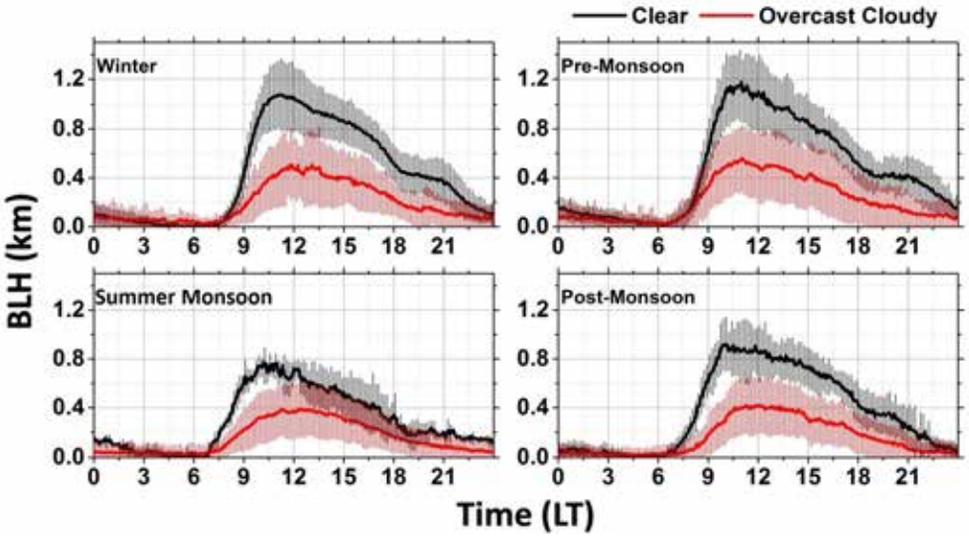

Figure 1: Multi-year (2010-2016) seasonal mean diurnal variations of BLH under clear-sky and cloudy conditions when such scenarios prevailed for >80% of the 24 hour period prior to the local time of observation. The vertical bars show standard deviations of BLH. [Davis et al., 2019].

monthly mean BLH shows a rapid increase from 08 LT (BLH <150 m) to attain a day time peak value (750–1100 m) around noon, with the highest noon-time BLH in pre-monsoon season (1100 m) and the least in summer monsoon season (750 m). In general, BLH shows a weak decrease (by <200 m) from the noontime peak value till about 16 LT, which is followed by a rapid decrease till about 18–19 LT and a relatively slow decrease throughout the night. In general, trend in the seasonal mean diurnal variation of BLH during overcast cloudy period (clouds present for 24 hours) is similar to that during the clear sky period, with an increase in BLH after about 08 LT to attain a peak value around noon (11–12 LT). Remarkably, the average daytime value of BLH during overcast cloudy period is always less than that during clear sky periods in all seasons. The largest reduction of the noontime peak BLH during cloudy periods compared to the clear sky values occur in winter and pre-monsoon seasons (ΔBLH of 400 to 600 m). The corresponding values of ΔBLH during summer monsoon and post-monsoon seasons are in the range of 400–450 m. The magnitudes of ΔBLH are well above the standard errors (<25 m) of the respective BLH values and are mostly outside the respective standard deviations. While the noontime peak BLH values show significant seasonal variations during clear sky periods (peak BLH of 750–1100 m), its values during overcast cloudy periods have substantially smaller seasonal variation (peak BLH of 400–500 m).

Daytime evolution of BLH during onshore and offshore winds and effect of clouds

Figure 2 shows the seasonal mean diurnal variations of BLH during onshore and offshore wind conditions for clear sky and cloudy conditions prevailing for 4 and 24 hours. The standard deviations of BLH for cloudiness of 4 hours are similar to those for 24 hours and are not shown in Fig. 2. When onshore winds prevailed in the winter and pre-monsoon seasons, the seasonal mean noontime peak BLH values are in the range of 1000 to 1100 m during clear sky periods and about 600 m during cloudy periods, indicating a decrease of 400 to 500 m in BLH (ΔBLH) due to clouds. The corresponding values of noontime peak BLH when onshore winds prevailed in the summer monsoon and post-monsoon seasons are 700–800 m during clear sky periods and 500 m during cloudy periods, yielding a ΔBLH of 200–300 m due to clouds during these seasons. In contrast, when offshore flows prevailed in winter and pre-monsoon seasons, the noontime peak BLH values during clear sky periods (1300–1500 m) are substantially higher than those during cloudy periods (450 m), indicating that the effect of clouds during offshore winds is to reduce the BLH (ΔBLH) by 850–1050 m. Thus, the effect of clouds on BLH during offshore winds is almost a factor of 2 larger than that during onshore winds. This difference primarily stems from the significantly higher noontime BLH values during clear sky offshore wind periods (1300 –1500 m), which represents the CABL development over continents. In contrast, during cloudy periods in these seasons, the noontime peak BLH values are higher by 150 m when onshore winds prevail (600 m) compared to offshore winds (450 m). During cloudy periods, the BLH is lower due to reduced solar flux and land surface temperature.

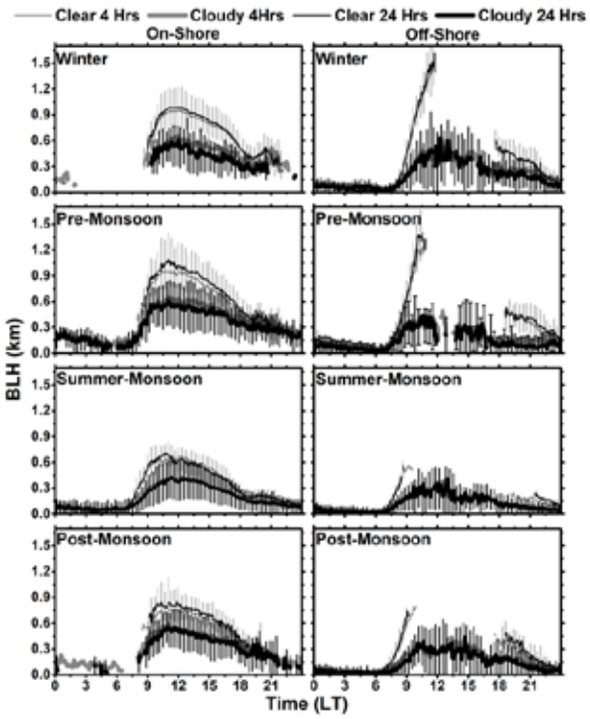

Figure 2: Multi-year seasonal mean diurnal variations of BLH during offshore and onshore winds under clear and overcast cloudy conditions when such scenarios prevailed for at least 80% of the period during 4 and 24 hours prior to the observation. The average for a given local time is shown only when at least 5 days of observations are available in the respective case. [Davis et al., 2019].

Driving mechanism for the rapid growth of BLH during the forenoon period

Growth rate of ABL is a crucial factor in the entrainment of airmass from the residual layer during the development phase of CABL and from the free troposphere during the later period. The BLH growth rate (during 08-11 LT) for clear sky period is about 380 m hr^{-1} in winter and pre-monsoon seasons, which is significantly more than the corresponding values in summer monsoon and post-monsoon seasons (250–280 m hr^{-1}). During cloudy conditions, the forenoon BLH growth rate is comparable during all seasons (140–170 m hr^{-1}) and is distinctly smaller than those for clear sky periods. Figure 3 shows the multi-year monthly mean diurnal time-height cross sections of temperature anomalies during clear sky and cloudy periods in the winter months of December, January, and February, derived from MRP observations. The temperature anomalies are obtained by subtracting the diurnal mean (monthly average) altitude profile of temperature during

all days (without discriminating cloudy or clear sky) from the respective individual temperature profiles during clear sky or cloudy periods. Figure 3 shows that, during clear sky days, the atmosphere below about 300 m altitude gets heated up faster during 09–11 LT, which is followed by a slow increase in temperature. The atmospheric warming above 300 m altitude is significant only after 11–12 LT, with largest temperature anomaly obtained during 13–17 LT, which is notable up to the altitude of about 1500 m. The increase in near-surface atmospheric temperature during the forenoon period is larger (seasonal mean anomaly of >1.5 K). These features cause the following: (1) Thermals generated near the surface during the forenoon period (during 09–11 LT) rise rapidly due to larger vertical temperature gradient arising from the rapid heating of the near surface and rather slow heating of the atmosphere above 300 m during daytime. This leads to rapid growth of BLH during 09–11 LT. (2) The maximum ascending altitude of thermals from the surface layer gets reduced after 12 LT because the atmosphere above 300 m also warms significantly after this time, causing an increase in virtual potential temperature in the altitude band of 300–1500 m, which reduce the altitude up to which the thermals generated near the surface can raise in the atmosphere. (3) Though the near-surface temperature also increases till 14 LT, the increase in atmospheric temperature above 300 m does not favour the rapid growth of BLH in accordance with the near-surface warming. On the contrary, positive temperature anomaly above 500 m between 13–17 LT causes a small reduction in BLH in the afternoon. (4) The slow reduction in BLH till 16 LT and the rapid reduction between 16–18 LT, which are followed by a slow reduction throughout the night are also in accordance with the time-height variations of temperature anomaly. The time-altitude variations of temperature anomaly during cloudy periods are somewhat similar to those during clear sky periods, except for the following: (1) The atmospheric warming below about 300 m is smaller during cloudy periods compared to clear sky periods, and (2) The atmospheric warming above about 800 m is enhanced during cloudy periods after about 11 LT. This might be due to the latent heat released during cloud formation at the altitudes above 800 m. Due to these reasons; the daytime thermals from the surface do not penetrate to higher altitudes during cloudy days compared to clear sky days. This inhibits the BLH and its growth rate during cloudy periods. Effect of the cloud radiative forcing is given below.

Diurnal variation of cloud radiative forcing at surface

Shortwave cloud radiative forcing at surface at any given local time, SWCRF(LT) is given by:

$$SWCRF(LT) = SWF_{obs}(LT) - SWF_{clear}(LT)$$

$SWF_{obs}(LT)$ is the observed downwelling shortwave radiative flux reaching the surface at the given local time and SWF_{clear} is the corresponding downwelling shortwave radiative flux reaching the surface during clear

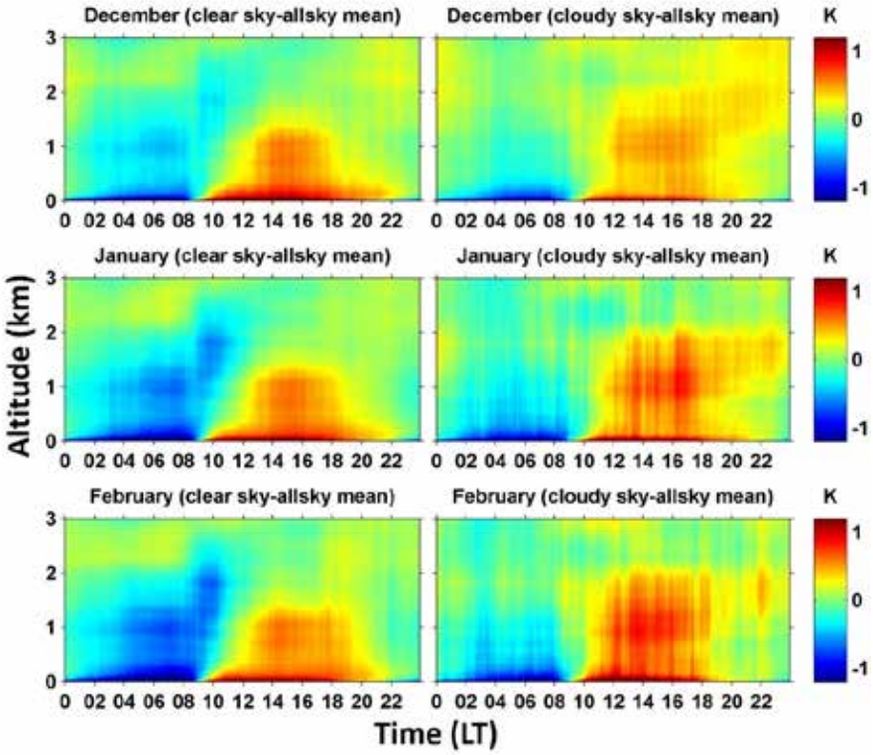

Figure 3: Multi-year monthly mean diurnal time-height cross sections of temperature anomalies during clear sky and cloudy periods in December, January, and February [Davis et al., 2019].

sky conditions. Here the SWF_{clear}(LT) for each month is estimated here using Santa Barbara DISORT Atmospheric Radiative Transfer Model (SBDART) by providing observed inputs, including aerosol optical depth (AOD), Angstrom exponent, and integrated water vapour content. Maximum uncertainty in the estimated SWF_{clear} at any local time is <20 W m^{-2}. The SWCRF (LT) estimated for individual days for the same local time are averaged to obtain the monthly mean diurnal variation of SWCRF.

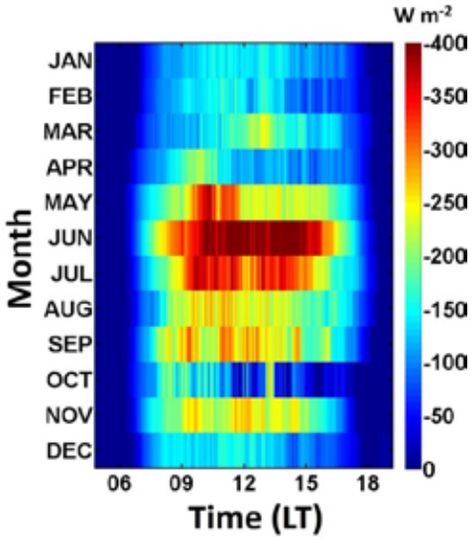

Figure 4: Monthly mean diurnal variation of shortwave cloud radiative forcing at surface (SWCRF) during 2013, estimated from pyranometer observations of downwelling shortwave fluxes at surface [Davis et al., 2019].

Figure 4 shows the monthly mean diurnal variation of SWCRF during 2013, which quantifies the effect of clouds in reducing the surface-reaching solar radiative flux as a function of local time. The magnitude of the SWCRF (surface cooling by clouds) increases systematically from morning till around noon. Magnitude of the SWCRF is least in winter (when the region mostly witnesses only low level clouds) and is largest during summer monsoon season (especially June–July) when the region is manifested by widespread occurrence of clouds associated with the Asian summer monsoon. The SWCRF during November (with significant mesoscale convective activity) is comparable to that during the latter part of pre-monsoon season. Systematic increase in SWCRF since morning till 11 LT can cause a corresponding decrease in surface temperature and inhibition of BLH under cloudy conditions. It may be noted that, though the development of convective clouds and isolated precipitation occur generally in the afternoon during the pre-monsoon and post-monsoon seasons, occurrence of low level clouds is very frequent in the forenoon period. During winter and pre-monsoon seasons, the present study shows a slope of 260 to 400 m per 100 W m^{-2} in the variation of BLH with SWCRF. During summer monsoon and post-monsoon seasons (period with largest rainfall, wet soil, moderate to high surface winds and almost omnipresent upper tropospheric cirrus) this is in the range of 130 to 230 m per 100 W m^{-2}. The observed seasonal variation in this slope is because the BLH and soil temperature will also depend on several other parameters including soil moisture, atmospheric circulation, sensible and latent heat fluxes, and background meteorological conditions.

Temporal coherence technique for cloud detection using IR brightness temperature

The IR brightness temperatures (IRT_b) observed at 3 minutes intervals using an IR Radiometer (spectral band: 9.6–11.5 μm) can be used to identify cloud occurrence. Conventionally, periods with IRT_b above a threshold value (e.g., >270 K) are treated as cloudy. However, as seen in Fig.5, considerable short-term variations of IRT_b occur even at IRT_b <270 K due to passage of broken clouds,

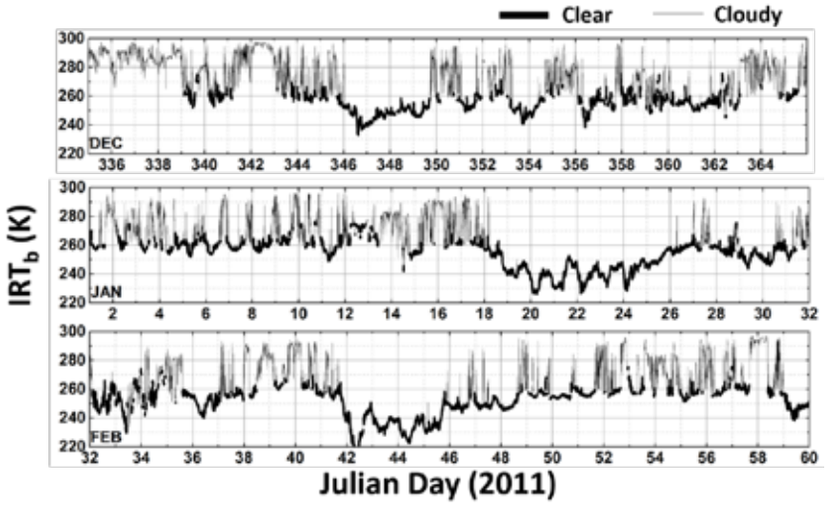

Figure 5: Time series of IRT_b during December 2010-February 2011 and the discriminated clear and cloudy periods by applying temporal coherence technique [Davis et al., 2019].

indicating the inadequacy of a simple threshold method for identifying clouds. Application of the threshold method to IRT_b can lead to an underestimation (for high threshold value of IRT_b) or overestimation (for low threshold value of IRT_b) of clouds. Fixing an adequate threshold value of IRT_b to identify the clouds is further complicated by the effect of greenhouse gases in varying the IR atmospheric transmittance and hence the observed IRT_b. In Fig.5, the time variability of IRT_b over short periods (about 30 mins) is considerably smaller when the values of IRT_b are low (<265 K). Such slow and small variations of IRT_b are associated with the variations in greenhouse gases, predominantly water vapour. Large time variations of IRT_b seen in this figure (within about 30 minutes having variations of >5 K) are associated with the passage of clouds. These time variations are used to detect the clouds in the temporal coherence technique (whose principle is similar to the spatial coherence technique applied to satellite data for cloud detection). Higher values of IRT_b correspond to lower cloud base altitude while low values of IRT_b occur when clouds are absent. However, the upper tropospheric cirrus clouds may not be detectable by the ground-based IR radiometer (observed values of IRT_b below 220 K are rare).

The Fig. 6 shows the plot of standard deviations of IRT_b (σ_{IRTb}) within a period of 33 mins (11 values of IRT_b) against the mean IRT_b values in the window, in different seasons. Values with small σ_{IRTb} (typically <3 K) correspond to nearly homogeneous conditions (either clear sky or overcast clouds), while those with higher σ_{IRTb} values are due to passage of clouds having small spatial extent. In the latter case, occurrence of clouds leads to high values of IRT_b while the clear sky points between passing of successive cloud patches cause low values of IRT_b, thereby producing larger variability in IRT_b and high values of

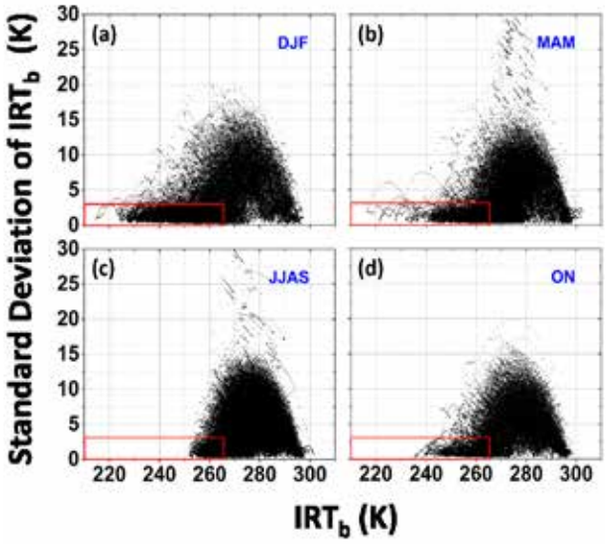

Figure 6: Plot of the mean infrared brightness temperatures (IRT_b) against the corresponding standard deviations (σ_{IRTb}) for a 33 minute moving window [Davis et al., 2019].

σ_{IRTb} over the 33 minutes time interval. Occurrence of long-duration (>33 mins) clear sky periods will have persistently low values of IRT_b (typically IRT_b <265 K) and σ_{IRTb} (<3 K) (points located within the small boxes marked in the subplots in Fig. 6). In contrast, clouds persisting for more than 33 minutes (including overcast clouds) will be manifested by high values of IRT_b (typically IRT_b >290 K) and low values of σ_{IRTb} (<3 K). All values with σ_{IRTb} >3 K can be treated as clouds and most of them have IRT_b values ranging between 265 K and 290 K. The above conditions together are used here to discriminate cloudy and clear sky periods. Time variations of IRT_b with cloudy and clear sky periods identified based on the application of temporal coherence test described above are depicted in Fig.5, which show that the identified clear sky periods indeed correspond to homogeneous occurrence of low IRT_b values only, while all the cloudy points are associated with high variability of IRT_b. This demonstrates the potential of the temporal coherence method for effective discrimination of cloudy periods.

Network of Observatories for Boundary Layer Experiments (NOBLE) Project

Atmospheric boundary layer characteristics at distinct geographical and climate zones (Fig.7), on a national canvas, are being investigated under the ISRO-GBP-NOBLE project, led by SPL. The experimental investigations of ABL parameters are carried out through observations using tower-based fast-response micrometeorological sensors mounted at multiple levels. The NOBLE project aims to establish long-term monthly mean variations of ABL parameters and energy fluxes and investigate the role of ABL in regional meteorology and associated feedback processes at different geographical locations representing typical geographic and climate conditions prevailing in the Indian region. Meteorological data obtained from the 32 m meteorological tower from Challekere were also used for studying the near-surface atmospheric conditions as part of the Reusable Launch Vehicle project.

Support for the RLV – LEX project

Provided scientific support for ascertaining the near-surface wind features (including gusts) for the RLV-LEX project, conducted at the Aeronautical Test Range (ATR), Chitradurga. Tower-based surface winds observed at 2 m, 4 m and 16 m levels on 32 m at Chellekere (NOBLE project at IISc) were used for understanding the near-surface background winds and their diurnal variations (including gusts) in this region during different seasons.

Microwave Remote Sensing

Millimeter-Wave Radiometric Information Content Analysis for Venus Atmospheric Constituents

Various gaseous constituents present in the Venus atmosphere have been detected and measured using in-situ and

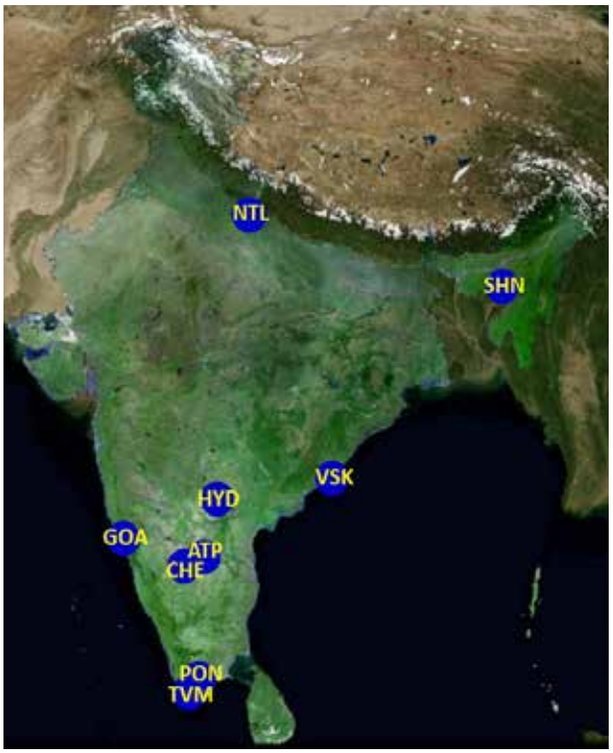

Figure 7: Locations of the network of NOBLE observations.

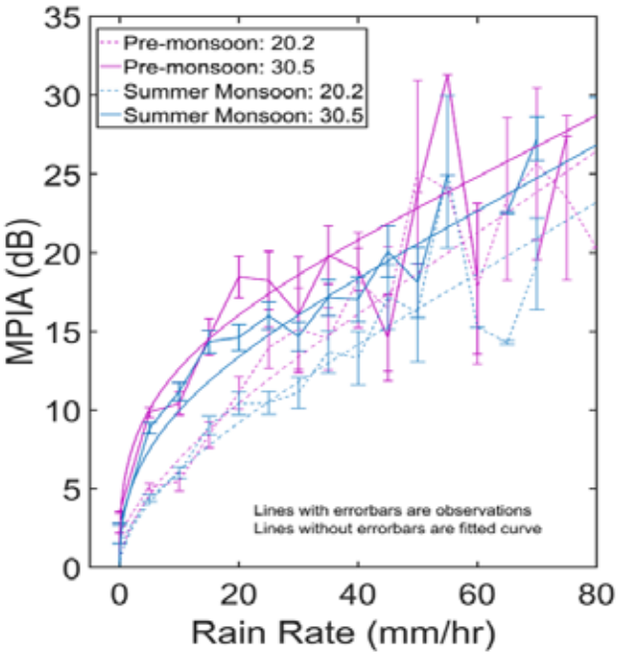

Figure 9: Mean Path Integrated Attenuation (MPIA) at 20.2 GHZ and 30.5 GHz with rain rate observed during pre-monsoon and summer monsoon season over Thumba [Manoj et al., Radio Science, 2020].

remote sensing instruments. However, measurements of mesospheric constituents above the cloud level are still sparse and inadequate owing to their very low abundance and large variability at high altitude. The millimeter and sub-millimeter (mm and sub-mm) spectral regime are found to be useful for Venus mesosphere studies, because several minor species in the mesosphere have strong rotational transition emission/absorption bands at these wavelengths. Radiative-transfer simulations (Fig. 8) were performed to identify the mm and sub-mm wave spectral frequency bands most suitable for estimating concentration of species like CO, CO_2, SO_2, water vapour, HDO and HCl, present in the Venusian mesosphere using atmospheric radiative transfer simulator (ARTS). The most suitable set of frequency bands that are identified to detect the mesospheric constituents for Venusian daytime and nighttime include (a) 183, 380, 448, and 556 GHz for water vapour measurements, (b) 115, 230, and 345 GHz for CO measurements, and (c) 600, 621, and 690 GHz for HCl detection. This study will be useful in instrument

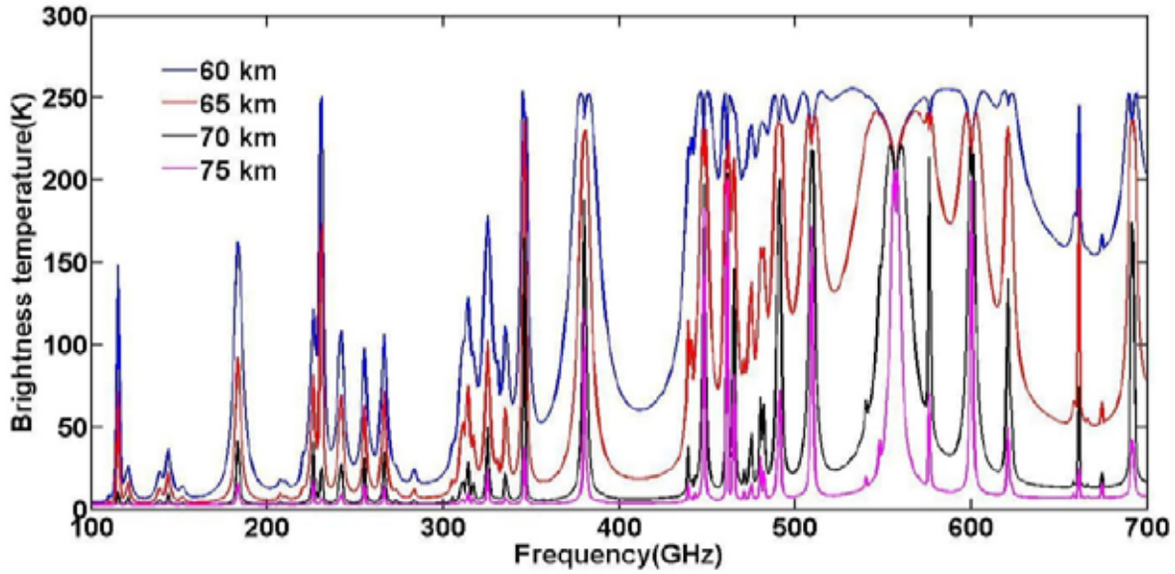

Figure 8: Brightness temperatures simulated for CO, H_2O, HCl, SO_2 and HDO for 100-700 GHz [Mathew et al., Radio Science, 2020].

design, frequency and bandwidth selection as well as pointing accuracy determination for future Venus missions to detect and estimate the concentration of various gaseous constituents present above the cloud level.

Characterization of GSAT - 14 satellite Ka-band microwave signal attenuation due to precipitation over Thumba

The Ka-band beacon signal (20.2 and 30.5 GHz) received from GSAT-14 satellite beacon at Thumba, Thiruvananthapuram (8.5°N, 77°E) and the precipitation measured using a collocated laser precipitation monitor (LPM) were used for quantifying the Ka-band attenuation as a function of precipitation intensity during the summer monsoon season and the convective rain dominated pre-monsoon period. The observed attenuation is compared with the rain attenuation model (ITU model) recommended for predicting the rain attenuation over tropical region (Fig. 9). The ITU model estimations are in agreement with the mean values of the observed variation in the attenuation with rain intensity. However, the ITU model is general in nature and does not predict the localised variation in attenuation due to different types of rain and drop size distributions. Based on this study, an empirical model for the rain attenuation of Ka-band signal has been derived for the Thumba station and validated.

Final Preparations and On-board Operations of ChaSTE payload– Chandrayaan-2

Chandra's Surface Thermo-physical Experiment (ChaSTE) is a payload on board the lander - Vikram - of Chandrayaan-2 mission with the objectives of in-situ measurement of temperature and thermal conductivity of the outermost 100 mm layer of the lunar surface regolith by using a thermal probe embedded with PRT sensors and heater. The flight model of ChaSTE was integrated with the lander craft and space qualification tests were conducted at URSC and SDSC. The ChaSTE is stowed to the + Y panel of lander (Fig.10) and upon landing, it will be released from the stowed configuration and deployed normal to lander bottom deck. Then the thermal probe will be inserted 140 mm into the regolith. A Shape Memory Alloy (SMA) actuator and Frangi-bolt based hold & release system are configured. The deployment system is designed using a BLDC motor-gear head actuator and the penetration mechanism is designed using a BLDC motor-gear head actuator and ball screw. All these mechanical operations are controlled and executed through the control electronics module which resides inside the lander. All the operation commands will be sent sequentially from the earth station. This is the most crucial and important post-landing operation for the ChaSTE payload. The procedure to be followed for the operation of the payload during the mission, and contingency operational plan were developed for various scenarios, as given below.

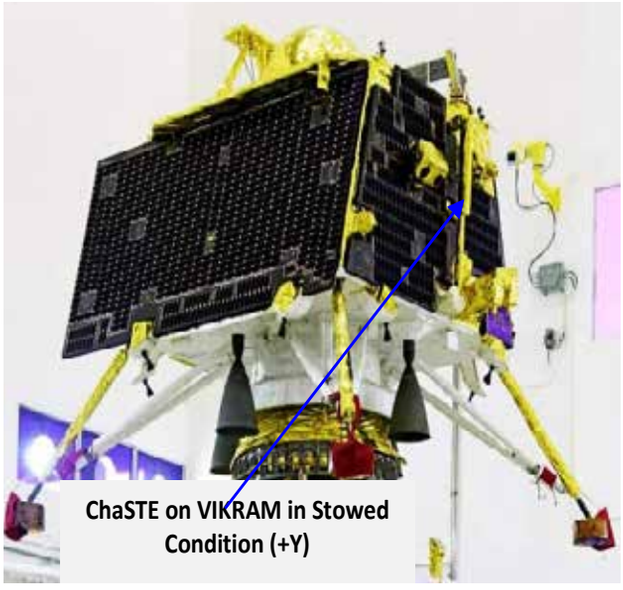

Figure 10: ChaSTE payload in stowed condition on the + Y panel of lander VIKRAM

1. Responsibility for payload operations of ChaSTE is identified with Mission Operations Director. He shall consult PI ChaSTE and Chandrayaan-2 project in case of contingency situations to decide further course of action.
2. Assessing the post-touchdown state of the lander
3. Touchdown sensing of the probe: Detailed operation scheme has been developed and tested in the laboratory by creating different surface temperature scenarios.
4. Detailed contingency plans of operation have been developed and tested.
5. The payload operation, switch on and acquisition of PRT thermal data, were conducted twice: the first operation was in the transit orbit for 30 minutes and the second operation was in the lunar orbit for 30 minutes. The data was streamed to Earth station at ISSDC/ISDA, where the data was decoded, calibrated and transformed to ASCII format, quick look display was made and the data was archived in PDS format using the in-house developed software. The chain of payload operations, including the data receiving system, software for archival, quick look display (QLD), evaluation of the PRT sensors, health check parameters and telemetry/telecommand, were tested.

On-going Activities and New Initiatives

Dependence of the Daytime Evolution of Atmospheric Boundary Layer Height on Meteorological variables

Dependence of the daytime development of ABL height on sea breeze onset time and the coupled variations of

near-surface air temperature (AT), soil temperature (ST), soil moisture content (SMC), atmospheric instability and shortwave radiative flux (SWF) over the coastal station Thumba was quantified based on multi-year observations. The ABL height is found to be dominantly controlled by the near-surface air temperature during all wind conditions. While the variations of SWF, ST and AT are coupled and increase rapidly in tandem with ABL height in the morning, advection of cold marine airmass after sea breeze strengthening retards further increase in AT, resulting in maximum AT during 1100–1400 local time (LT) and the highest ABL height during 1100–1200 LT. (Revised manuscript submitted).

Atmospheric boundary layer characteristics over Chellekere: A semi-arid, inland location

Characterization of ABL over the semi-arid inland station Chellekkare (IGBP-NOBLE) has been carried out based on observations from multi-level sensors mounted on a 32-m meteorological tower. Measurements made using slow and fast response sensors were used to study the seasonality of the background flow and the turbulent fluxes prevalent in the hitherto unexplored region. Both the sensible heat flux and turbulent kinetic energy showed well-defined diurnal variations with peaks occurring in the afternoon period. Seasonally, both these parameters were highest in pre-monsoon & summer monsoon season followed by the dry winter season. (Manuscript under review)

Direct observations of the multi-year seasonal mean diurnal variations of TOA cloud radiative forcing over tropics using Megha-Tropiques-ScaRaB/3

Direct observations of the seasonal mean longwave and shortwave cloud radiative forcing over the entire tropics have been carried out using multi-year (2012-2016) broadband radiation measurements made by ScaRaB/3 onboard the low-inclination Megha-Tropiques satellite. Diurnal variations of 15 to 25 Wm^{-2} in LWCRF (20 to 35% of the mean) are observed with peak values occurring at 18 - 21 local time (LT) over continents and 00 - 06 LT over oceans. Certain specific features including the CRF associated with the double inter-tropical convergence zone, day-night changes in net CRF, and the effect of El Niño on CRF are also delineated. (Revised manuscript submitted).

Attenuation characteristics of Ka-band signals over the tropical coastal station:

Ka-band radiowave attenuation due to precipitation has been studied using collocated observations from Ka-band receivers operating at 20.2 GHz and 30.5 GHz, ground based microwave radiometer profiler and micro rain radar. A manuscript titled "Attenuation characteristics of Ka-band signals over the tropical coastal region" has been submitted.

Future Projections

- Development of UHF wind profiler
- Studies on lunar regolith thermal characteristics using ChaSTE/Chandrayaan-3 data.
- Characterization of surface layer parameters over NOBLE stations.
- Effect of tropical circulation cells on the global distribution of cirrus clouds and their radiative impact.
- Three-dimensional distribution of clouds and precipitation over the tropics and their impact on atmospheric energetics

Publications in Peer-Reviewed Journals

1. Davis, E. V., K. Rajeev, Manoj Kumar Mishra, "Effect of clouds on the diurnal evolution of atmospheric boundary layer height over a tropical coastal station", *Boundary-Layer Meteorology,* https://doi.org/10.1007/s10546-019-00497-6, (2020).
2. Mathew, N., S. Sahoo, R. Renju, and C. Suresh Raju, "Millimeter wave radiometric information content analysis for Venus atmospheric constituents", *Radio Science*, *55*, *e2019RS006913, https://doi.org/10.1029/2019RS006913* (2020).
3. Manoj Kumar Mishra, R. Renju, N. Mathew, C. Suresh Raju, M. R. Sujimol, K. Shahana, "Characterization of GSAT-14 satellite Ka-band microwave signal attenuation due to precipitation over a tropical coastal station in the southern peninsular region of the Indian subcontinent", *Radio Science,* 55, *e2019RS006910.-https://doi.org/10.1029/2019RS006910*, (2020).

Presentation in Symposia/Workshop:

1. M.Santosh "Atmospheric Boundary Layer over a tiny island (Mahe, Seychelles) in the Equatorial Indian Ocean", TROPMET-2019, 11-14 December Andhra University, Vishakapatnam.
2. R. Renju, Nizy Mathew, C. Suresh Raju C. and S. Sahoo, "Millimeter-Wave Radiometry for studying Venus Atmospheric Constituents", Indian Planetary Science Conference-2020, Feb. 19-21, PRL, Ahmedabad.

Invited Lectures

K. Rajeev

1. Atmospheric Dynamics & Clouds – in the light of Guwahati ST Radar applications, NEAR2019 (Organized by SAMEER, Mumbai), IIT Guwahati, 09 Aug. 2019.

Suresh Raju C

1. "Atmospheric Water Vapor Studies using Microwave Remote Sensing", URSI Regional Conference on Radio Science (URSI-RCRS 2020), February 12-14, IIT BHU) Varanasi, India.

Training Attended

Nizy Mathew

1. Training program on "Climate Change: Challenges and Response", Centre for Disaster Management, Lal Bahadur Shastri National Academy of Administration, Mussoorie, 10-14 February, 2020.

Aerosols Trace gases and Radiative Forcing

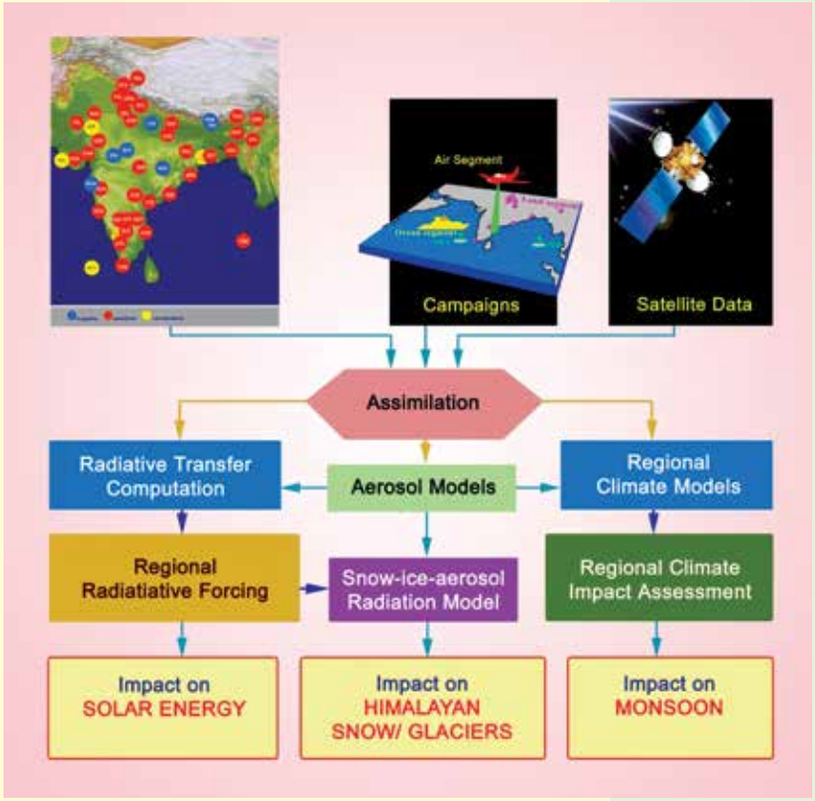

Aerosols Trace gases and Radiative Forcing (ATRF) Branch of SPL aim at the scientific understanding of the physical/chemical properties of aerosols and trace gases, processes that control their three-dimensional atmospheric distribution and interaction with radiation leading to climate changes.

The primary objectives are (i) development of spatially and temporally resolved aerosol and trace gas database over the Indian subcontinent, adjoining Oceans as well as the Himalayan and Polar environments by combining the space borne and ground-based observations, (ii) conducting thematic multi-platform (ship, aircraft, and high altitude balloon) field experiments addressing specific problems pertinent to the climate impact of aerosols and trace gases, (iii) assimilation of the aerosol and trace gas data with regional climate models for the assessment of potential climate impact

Science Team

Suresh Babu S.
Vijayakumar S Nair
Prashant Hegde
Mukunda Gogoi
Sobhan Kumar Kompalli
Girach Imran Asatar
Revathy S Ajayakumar

Technical Team

Ajeeshkumar P. S.
Santosh KR Pandey

Research Associates

Suresh Kumar Reddy B.
Lakshmi N. B.
Subin Jose
Remya C. B.

Research Fellows

Usha K. H.
Arun B. S.
Ajith T. C.
Reshma R. A.

Over the Himalayas

Implications of aerosol induced snow albedo feedback

The deposition of the absorbing aerosols (black carbon (BC) and dust) on the highly reflecting surfaces like snow and ice significantly reduces its surface albedo (snow darkening effect), resulting in positive radiative forcing (warming) at the surface. Several model simulations suggest that warming due to BC induced snow albedo forcing is two or three times more than the warming caused by the same amount of forcing by CO_2. This enhanced warming is the result of the complex positive feedback mechanism involving the thermodynamics and microphysical properties of the snowpack. Himalayan regions are vulnerable to the absorbing aerosols because of its proximity to the highly industrialized and populated Indo-Gangetic Plain and the desert regions like Thar and Taklimakan. The health of Himalayan glaciers has become a major concern due to its conspicuous role in regional hydroclimate. In the present study, a regional climate model coupled with aerosol and snow albedo model (RegCM-Chem-SNICAR) is used to simulate the deposition and concentration of aerosols over the Himalayas and Tibetan Plateau and estimate the direct radiative effect of total aerosols and snow albedo effect of BC, dust and total aerosols.

The spatial distribution of the snow albedo changes due to aerosols, dust, and black carbon (BC), respectively, over the Himalayan–Tibetan region during spring (March-May) are shown in Fig. 1. The snow albedo reduces by 0.2–0.3 due to the deposition of BC and dust. The dust contributes significantly to the albedo reduction over the western and northern Tibetan regions, whereas the southern slopes are affected mainly by BC. Being close to the major anthropogenic (Indo Gangetic Plain) and dust (West Asian and Thar deserts) sources, Himalayan glaciers/snow experiences high aerosol loading leading to the significant reduction in snow albedo. The amount of incoming solar energy that gets trapped in the snowpack

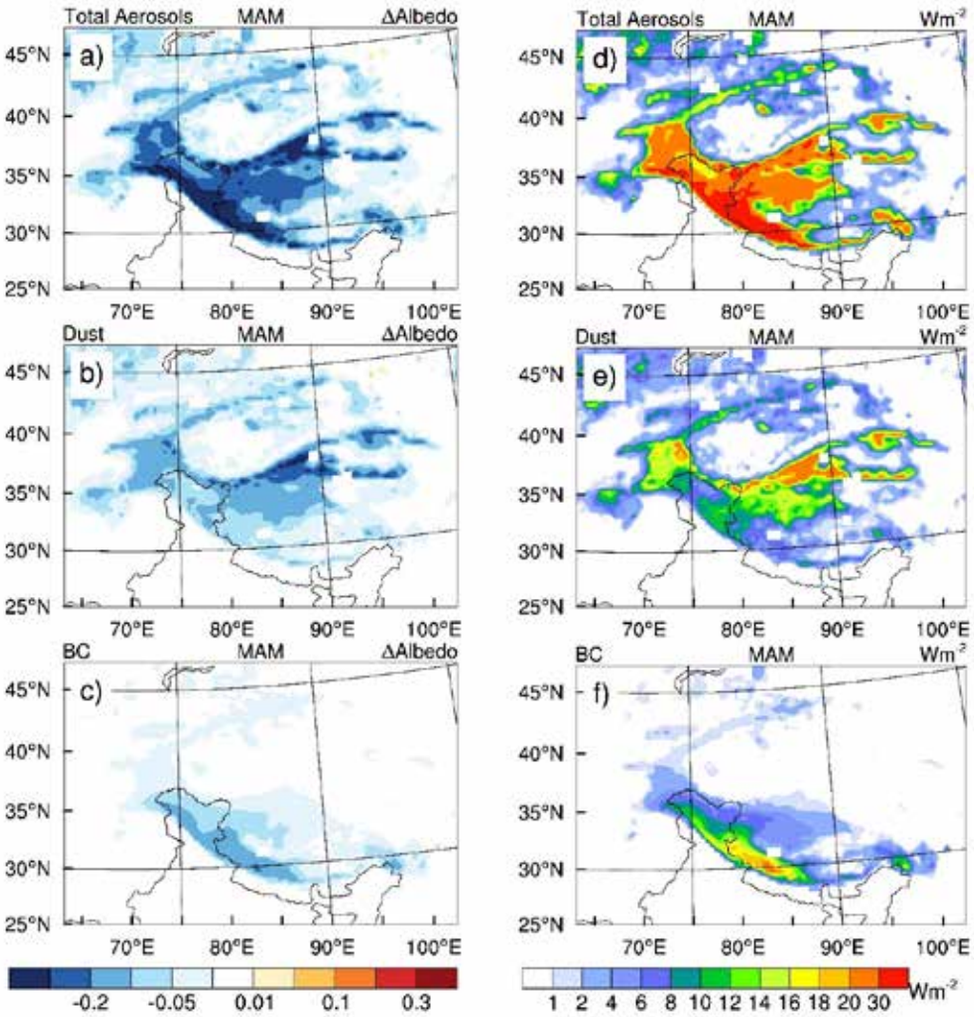

Figure 1: Change in the snow albedo due to deposition of (a) all aerosols with respect to pure snow, (b) dust only with respect to all aerosols, (c) BC only with respect all aerosols. The surface radiative effect due to snow darkening from (d) all aerosols with respect to pure snow, (e) dust only with respect to all aerosols and (f) BC only with respect to all aerosols [Usha et al., Climate Dynamics, 2020].

due to the aerosol-induced snow darkening is estimated using the SNICAR module as the difference between the absorbed radiation with all aerosols and pure snow in each radiative transfer time step. Also, the radiative effect due to the deposition of BC and dust on snow is estimated as the difference between absorbed radiation with all aerosols and all aerosols except the aerosol type in a question (radiative effect of BC or dust = total aerosols − total aerosols without BC or dust). The Western Himalayas and Northern Tibetan Plateau show a radiative effect exceeding 20 W m^{-2}. The large radiative effect over this region is mostly attributed to the high concentration of impurities in the snow and also due to the high solar insolation because of high elevation and less atmospheric extinction. The contribution of dust to the total radiative effect is about 6.7 ± 7.8 W m^{-2} and exceeds more than 12 W m^{-2} over the Northern Tibetan Plateau, which coincides with the region of maximum dust deposition. The snow radiative effect due to BC is about 3.6 ± 4.4 W m^{-2}, which reaches as high as 16 W m^{-2} over some parts of western and middle Himalayas. Thus, it is clear that the deposition of absorbing aerosols on snow results in a reduction of snow albedo by 0.2–0.3, i.e., about 20–30 % more incident solar flux gets trapped in the land-atmosphere system over this region. This large change in albedo is the result of multiple positive feedbacks within the snowpack. The contribution of dust on the albedo reduction is comparable with BC and, therefore, cannot be overlooked.

Physico-chemical and optical properties of aerosols at a background site (~ 4 km a.s.l.) in the western Himalayas

The Himalayan environment and climate, which is under the influence of distinct anthropogenic impacts of south and East Asia, is a serious climatic concern. The transport of light-absorbing aerosols and their gradual build-up in the Himalayan atmosphere and subsequent deposition on snow surfaces can lead to a large reduction in snow albedo and retreat of snow/ice, triggering large radiation perturbation in the free-tropospheric environment. Thus, in view of the paramount requirement of the quantification/characterization of the spatio-temporal heterogeneities of aerosols over the Himalayan region, a first of its kind, simultaneous observations of the physico-chemical and optical properties were carried out from the Lahaul and Spiti valley, located close to major glaciers in the western part of Himalayas. The observational site is located at Sutri Dhaka, Chandra Basin, where the aerosol measurements were carried out from 'Himansh' observatory from 22 August 2017 to 11 October 2017 (represents summer and parts of autumn). Located far from any human influence (very low population density of 2.3 per square kilometer), Himansh is India's first high-altitude glacier research facility (Fig. 2) under the Ministry of Earth Sciences (MoES), Govt. of India.

During the entire study period, columnar aerosol optical depth (AOD) was found to be extremely low (mean AOD equal to 0.07 ± 0.03), while the lower values of Angstrom exponent (α, varied between 0.1 and 0.9) indicated the dominance of coarse mode aerosols to the observed columnar loading. The values of composite (M_T), coarse (M_C), and accumulation (M_A) mode aerosol mass concentrations remained nearly steady during the period of observation, where the contribution of coarse mode mass to total aerosol mass was significant in most of the days, depicting a mean value of ~ 0.56. The concurrent measurements of BC concentrations depicted that the share of BC to total aerosol mass is ~4%.

The total suspended particulate (TSP) matter showed

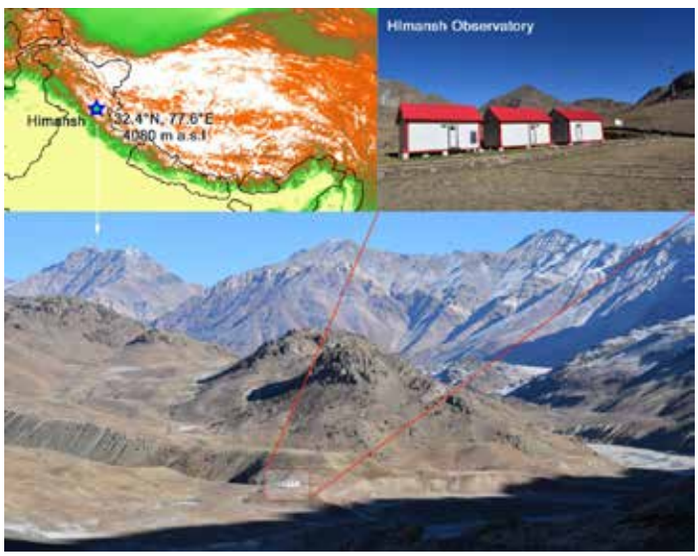

Figure 2: Geographical position of Himansh observatory (32.4° N, 77.6° E, 4080 m a.s.l.) in the topographical map of Lahaul and Spiti valley in the western Himalayas, along with a close-up view of the experimental huts. [Arun et al., Atmos. Environ. 2019].

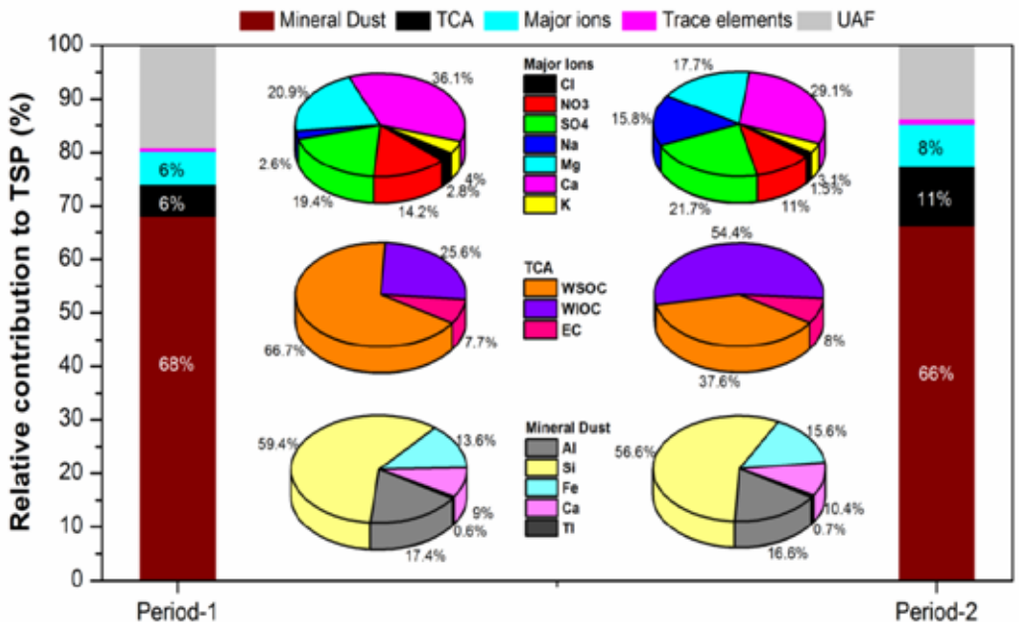

Figure 3: Relative contribution of mineral dust, total carbonaceous aerosols (TCA), water-soluble ions, trace elements and unanalysed fractions (UAF) in total mass loading during period 1 and 2; the relative variation of each aerosol constituent in each of the categories among the analysed components are shown by the pie diagram [Arun et al., Atmos. Environ. 2019].

significant variations between 5 μg m^{-3} to 40 μg m^{-3}, having dominance of mineral dust components (~ 61%) followed by total carbonaceous aerosols (~ 13.8%). The ratio of organic carbon (OC) to elemental carbon (EC) varied over a wide range from 7.8 to 18.9, with a mean value of 12.5 ± 2.95. The higher fraction of water-soluble OC in the total OC component indicated the aged nature of the carbonaceous species. While fossil fuel combustion and biomass burning are the major sources of OC and EC respectively, carbonaceous aerosols emitted from biomass burning (BB) emission are reported to be enriched in OC compared to EC, thus, providing relatively higher OC/EC ratio. As the present study location is situated in a near-pristine environment and is unaffected by the major anthropogenic activities, higher contribution from the OC could be transported from the biomass burning emissions at north Indian locations to this pristine Himalayan site. However, higher OC/EC can also be attributed to the secondary production mechanisms. Being a high-altitude site, the probability of secondary production is high over the observational site. With a view to identifying this, day to day variations of water-soluble and insoluble fractions of OC (WSOC and WIOC) were examined. Several earlier investigators have reported that the dominant contribution of WIOC includes primary emissions (biomass and fossil fuel combustion), while WSOC can be originated from secondary formation sources and aging processes in addition to primary (e.g., biomass combustion) emissions. In line with this, the examination of the WSOC fraction in OC (i.e., WSOC/OC) revealed an average value of 0.56 ± 0.20, which (relatively higher ratio) indicates the prevalence of aged aerosols. This might be due to long-range transport because a significant amount of OC can be oxidized to WSOC during transport. Interestingly, WSOC remained more or less consistent throughout the period of observation, its contribution to OC was significant (> 70%) during August-September, while the dominance of WIOC to OC took over (> 60%) during October. Thus, to delineate possible source processes, the association between different carbonaceous species are examined separately for the two periods (considered as Period-1: 22-Aug to 29-Sep and Period-2: 30-Sep to 11-Oct), as the larger value of the correlation between two species is indicative of the possibility of the same/ similar sources of the species.

It is observed that while total carbonaceous aerosols (TCA) and major ions displayed an enhancement during the second period, mineral dust fraction remained nearly consistent (Fig. 3). The contribution of TCA to TSP increased from 6% during Period-1 to 11% during period-2, while the contribution of mineral dust to TSP remained nearly consistent (68% during period-1 and 66% during period-2). The share, though negligible, of trace elements increased slightly to 0.96% during period-2 from 0.63% in period-1, along with the slight increase in the percentage contribution of major ions from 6% in period-1 to 8% in period-2. Dominant ionic contributors were $Ca^{2+} > Mg^{2+} >>> K^{+} > Na^{+} > Cl^{-}$ during period-1 and $Ca^{2+} >> Mg^{2+} > Na^{+} > K^{+} > Cl^{-}$ during period-2.

The above observations thus indicate that even though the contribution of carbonaceous aerosol species varied significantly (~ nearly double in period-2 compared to that in period-1), the other chemical species of aerosols did not show significant temporal variation during the experimental period. This is indicative of the consistent background features of aerosol chemical properties over the observational site prevailing throughout summer and

autumn, while the biomass burning activities modulate the magnitude of background aerosols properties during the beginning of autumn. Even though K^+ is an ideal tracer for identifying the influence of biomass emission sources, the contribution of K^+ from crustal sources dominates over this region due to the observed predominance of mineral dust in aerosol mass loading. This was also reflected in the higher correlation of K^+ with Al and Fe (R~ 0.7). However, the correlation of K^+ with carbonaceous species showed significant variation between the two periods. It exhibited a better correlation with OC, EC, WSOC, and WIOC during Period-2 as compared to Period-1, indicating the possibility of biomass activities modulating the background properties during the beginning of autumn.

An enrichment factor estimated from the concentrations of trace elements also revealed the influence of anthropogenic source contribution. The regions located west and northwest of the measurement site, which includes the regional hot-spots of Indo-Gangetic Plains, west Asia, and the Middle East, are possible source regions to modulate the aerosols over the observational site through long-range transport. These observations have far-reaching implications in view of the role of aerosols on regional radiative balance and impact on snow/ glacier coverage.

Over the Subcontinent

Mixing state of aerosol black carbon in the Indo-Gangetic Plain outflow

Over the Indian region, aerosol absorption is considered to have a potential impact on regional climate, monsoon, and hydrological cycle. The absorption potential of BC is determined mainly by its microphysical properties, including its concentration, size, and mixing state with other aerosol components. As BC has a longer atmospheric lifetime, it undergoes significant changes in its mixing state during its '*aging*'. Any coating of scattering material over BC leads to its absorption enhancement and increased hygroscopicity. The Indo-Gangetic Plains (IGP) is one of the regional aerosol hot spots with diverse sources, both natural and anthropogenic, but still the information on the mixing state of the IGP aerosols, especially BC, is limited. In this context, the first-ever year-long intensive measurements of refractory BC (rBC) microphysical properties were carried out over Bhubaneswar. It is an urban site on the eastern coast of India and experiences contrasting air masses (the IGP outflow or coastal/marine air masses) in different seasons. The observations were carried out as part of "South West Asian Aerosol Monsoon Interactions (SWAAMI)" experiment during July 2016-

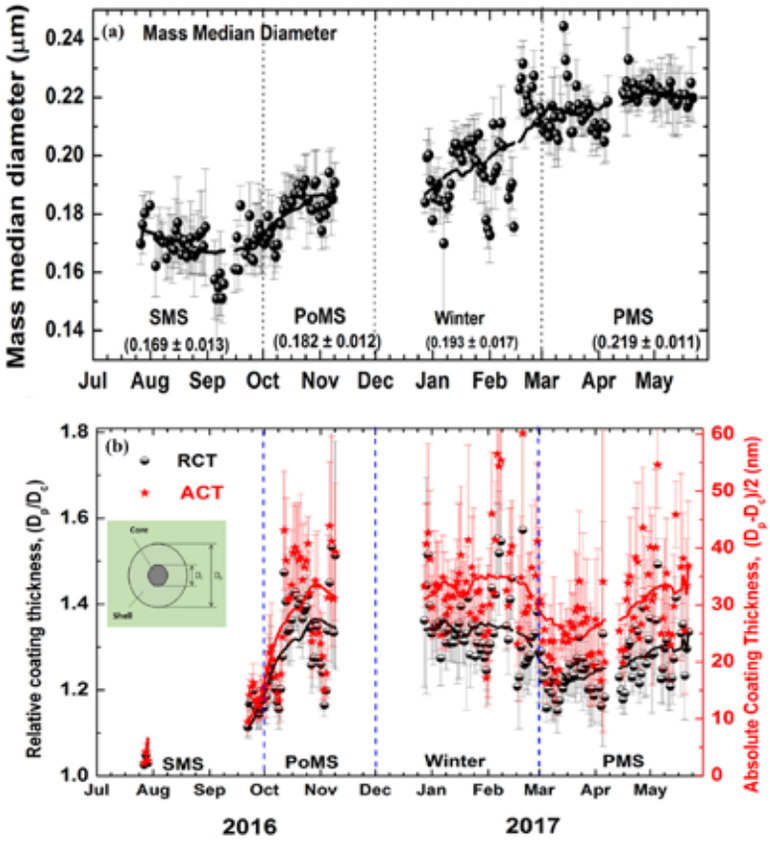

Figure 4: Temporal variation of the daily mean (a) mass median diameter, (b) relative coating thickness (hall filled circle), and absolute coating thickness (star). The symbols present the mean value for the day, and the vertical line passing through them is the standard deviation. The solid continuous line shows the 30-day smoothed variation. Dotted vertical lines highlight different seasons [Kompalli et al., ACP, 2020].

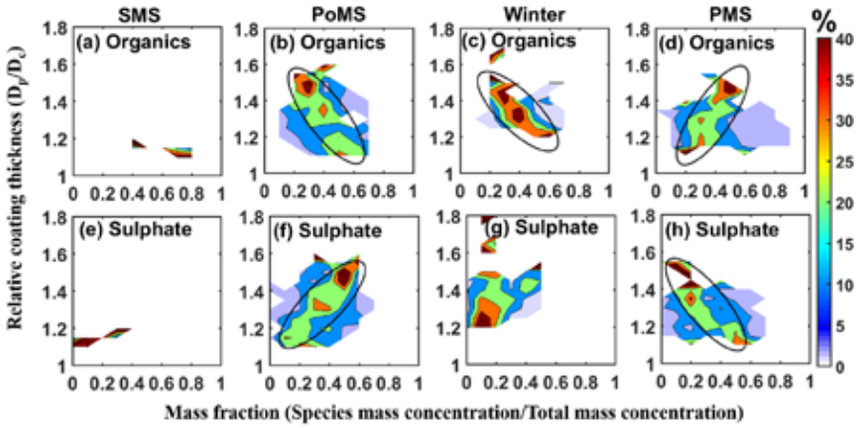

Figure 5: Association between mass-fraction of organics (top panels; a-d) and sulphate (bottom panels e-h) with relative coating thickness during different seasons. The colour bar indicates the percentage of occurrence of RCT for corresponding mass fraction values of the species[Kompalli et al., ACP, 2020].

May 2017, using a single particle soot photometer (SP2) that uses a laser-induced incandescence (LII) technique to measure the mass and mixing state of individual BC particles and an aerosol chemical speciation monitor (ACSM) to infer possible coating material.

By representing the rBC mass size distributions using mono-modal log-normal fit, the mass median diameters (MMD) are determined, which reflect the nature of BC sources. Further, in the LII technique, while the amplitude of the scattering signal provides the information about the optical size (D_p) of the particle, the amplitude of the incandescence signal is proportional to the mass of the rBC. From this, the mass equivalent diameter, or BC core diameter (D_c), defined as the diameter of a sphere containing the same mass of rBC as measured in the particle is obtained using a density, ρ ~1.8 g cm^{-3} for atmospheric BC. Two parameters are defined to quantify the mixing state of BC; relative coating thickness (RCT), and absolute coating thickness (ACT), given by D_p/D_c and $(D_p–D_c)/2$, respectively. In Fig. 4, the temporal variation of the MMD, mixing state parameters, RCT, and ACT are shown. The lowest seasonal mean MMD of ~ 0.169 ± 0.013 µm, occurring during the summer monsoon season (SMS), highlighted the possible dominance of fresh emissions containing smaller sized particles (and/or externally mixed particles) when washout also is quite significant. As the season advances, MMD increased, due to aging processes (including the coagulation of the agglomerates), as the removal mechanism is weakened (significantly low precipitation) during these seasons. The model values during the post-monsoon season (PoMS) and winter seasons (MMD ~ 0.182 ± 0.012; ~ 0.193 ± 0.017 µm respectively) are comparable with those reported from the continental outflow regions suggesting mixed sources and/or aged BC. By the pre-monsoon season (PMS), the MMD reached beyond 0.20 µm and continued to remain so throughout the PMS, highlighting the dominance of larger core BC particles (likely solid fuel, e.g., coal/biomass burning emissions).

The figure highlighted a strong seasonality even in the coating on BC, which is due to several controlling factors. Both RCT and ACT are very low during the SMS (mean RCT ~1.16 ± 0.04; ACT ~12.12 ± 4.98 nm); but when the IGP air masses prevail over the region, the values of mixing state parameters gradually increased towards winter (RCT ~1.34 ± 0.12; ACT ~ 33.51 ± 11.76 nm) through the PoMS (RCT~1.32 ± 0.14 and ACT ~28.74 ± 12.31 nm). Thus, the IGP outflow contains thickly coated BC aerosols. As the season changes to the PMS, the RCT decreased (mean RCT~1.26 ± 0.10) because of the larger BC cores while the absolute coating thickness remained high (mean ~27.41 ± 10.72 nm). Such variations in mixing state parameters reflected the aging and the concentrations of condensable gas-phase precursors that act as potential coating materials. The seasonal association between the coating on BC and the mass fraction of organics/sulphate is shown in Fig. 5. It revealed a negative association of RCT with the mass concentration of sulphate during the pre-monsoon season and with organics during the post-monsoon season, suggesting varying dominant coating species. This first ever-experimental data on the mixing state of BC from a long time series over the Indian region helps in improving the understanding of regional BC microphysical characteristics and their climate implications.

Carbonaceous aerosols over a semi-arid location in North-West India

Knowledge of the chemical composition of composite aerosols is crucial in model simulations for inferring their climatic and environmental effects. Realising the contrasting roles of carbonaceous aerosols in atmospheric radiative forcing (in terms of absorption and scattering), adverse effects on our environment and the sparse information available, detailed investigations were carried out on the various carbon-containing aerosols over a semi-arid region, Udaipur (24.5°N; 73.6°E), in north western India, based on the analysis of PM_{10} (particulate matter ≤ 10 µm in aerodynamic diameter) samples (N=128)

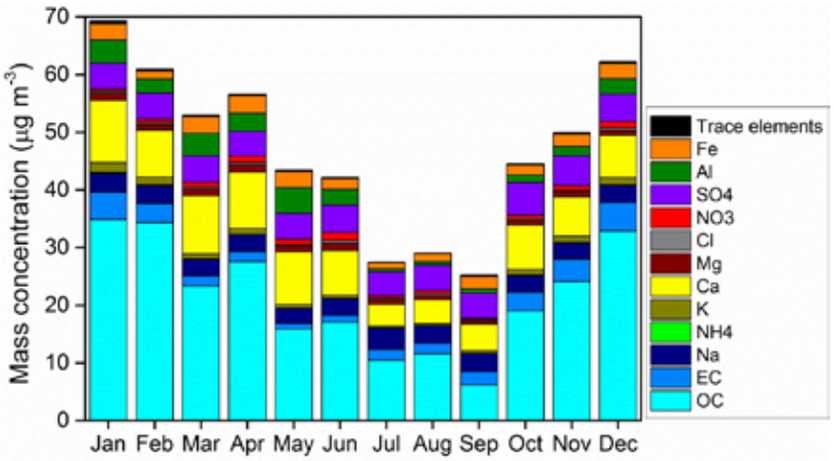

Figure 6: Monthly average mass concentration of measured chemical species during 2010-14 [Hegde et al., J. Arid Environ. 2020].

collected during 2010-14. The study presents the seasonal features of major carbonaceous components, their source characteristics, and the role of meteorology in influencing the chemical characteristics. The samples were analysed for OC, EC, CC (carbonate carbon), WSOC, WSTN (water-soluble total nitrogen) and water-soluble inorganic ions. Primary and secondary OC (POC and SOC), WIOC, and water-soluble organic nitrogen (WSON) were also estimated.

The annual average mass (PM_{10}) loading observed over Udaipur is estimated as 112 ± 56 µg m^{-3}, which is much higher than the prescribed air-quality standards. The period from June-September, effective removal of aerosols from the atmosphere through wet scavenging takes place. The period from October till May witnesses high aerosol mass loading due to the dry atmospheric conditions combined with seasonal effects of sources and favourable continental transport.The annual average concentration of OC during the study period was 23±14 µg m^{-3} while that of EC was 2.6±2.1 µg m^{-3}. The EC contribution to mass loading ranged from 0.9 to 3.5%, with the lowest recording in May and highest in December. The total carbon (TC=OC+EC) fraction in PM_{10} aerosols was highest in winter (25-27%), followed by post-monsoon (21-24%), pre-monsoon (14-20%) and lowest in monsoon (13-18%).

Among the different components of OC, its water-insoluble and secondary components were found to dominate over the region with a significant correlation between them. This implies the presence of water-insoluble SOC, formed from the less hydrophilic anthropogenic volatile organic carbon (VOC) or aged semi-volatile POCs aided by the prevailing low ambient relative humidity conditions.The enhancement of WSOC during the post-monsoon period, and its significant relationship with nss-K^+, shows the influence of biomass emissions over the region and the conspicuous presence of light-absorbing OC, brown carbon present in the carbonaceous content of aerosols. Among the different measured chemical species, OC was found to be the major component, followed by Ca^{2+}, SO_4^{2-} and HCO^{3-}. Most of the anthropogenic species and PM_{10} mass loading were found to show peak concentrations during the winter period, while natural aerosols such as crustal and sea-salt species showed high values during pre-monsoon and monsoon, respectively.

Combining the concentrations of various chemical species, the percentage contribution of major aerosol components was estimated and shown in Fig.6. As seen, the highest contribution of carbonaceous aerosols over the study region is obtained during the months of December-February. The contribution of water-soluble ions is found to peak during June–September when the site is influenced by aerosols of marine origin. Mineral dust is the major contributor to aerosol mass over the region, with the highest contribution (36-54%) during March-June. The monthly variation of major aerosol components along with the airmass cluster analysis revealsthe influence of mineral dust transported by westerlies from Middle East peaking during March-June, sea-salt species transported by south-westerlies from the Arabian Sea during July-September and anthropogenic species (including carbonaceous) transported by northerlies and north-easterlies from IGP during October-February. This study is the first detailed chemical analysis of dust aerosols from the Indian desert region and delineation of carbonaceous species over the North-Western arid region.

Airborne in-situ measurements of aerosol size distributions and BC across the IGP during SWAAMI –RAWEX

In recent years, several campaign-mode airborne measurements have been made over the IGP to estimate the altitude-resolved properties of aerosols that are important in aerosol-radiation interactions. However, the altitude-resolved measurements of aerosol size distribution are extremely sparse, or non-existent, despite its importance in improving the accuracy of aerosol radiative forcing estimation. During the SWAAMI - RAWEX (Regional Aerosol Warming Experiment), collocated airborne

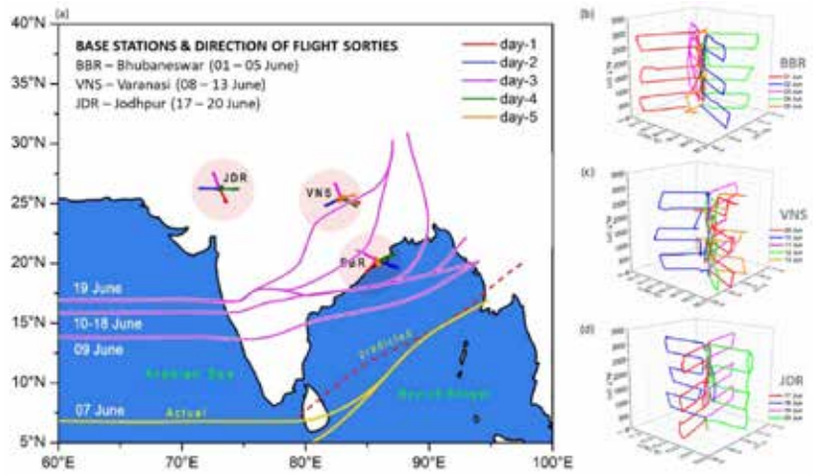

Figure 7: (a) The onset (actual) of SW-Monsoon at different parts of India shown by the yellow and pink (solid) lines. Horizontal and vertical flight paths during each of the sorties at (b) Bhubaneswar (BBR), (c) Varanasi (VNS), and (d) Jodhpur (JDR) are shown in the right panel [Gogoi et al., Atmos. Chem. Phys., 2020].

measurements of aerosol number-size distributions in size (diameter) regime 0.5 to 20 µm and BC mass concentrations were made across the IGP from three distinct locations, during 01 to 20 June 2016, just prior to the advent of Indian Summer Monsoon (Fig.7). These measurements provided an east-west transect of region-specific properties of aerosols as the environment transformed from mostly-arid conditions of western IGP (represented by Jodhpur, JDR; 26.25°N, 73.04°E) having dominance of natural aerosols to the Central IGP (represented by Varanasi, VNS; 25.44°N, 82.85°E) having very high anthropogenic emissions, to the eastern IGP (represented by the coastal station Bhubaneswar, BBR; 20.25°N, 85.81°E) characterized by a mixture of the IGP outflow and marine aerosols. Despite these, aerosol size distribution depicted significant altitudinal variation in the coarse mode regime at western IGP, having the highest coarse mode mass fraction (72%) near the surface.

The altitude distribution of volume size distribution of aerosols (Fig. 8) clearly shows (i) near-uniform distributions

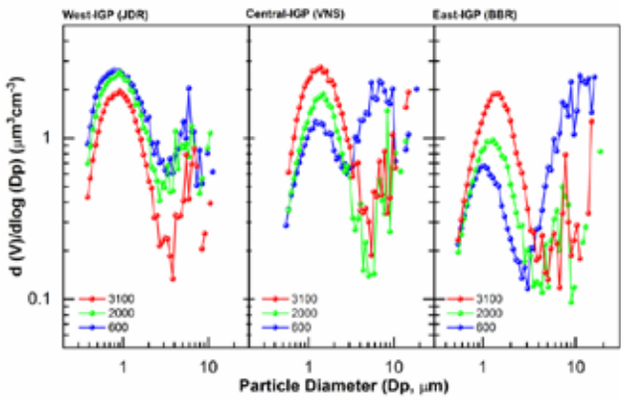

Figure 8: Aerosol volume size distributions (mean profiles averaged for all the days) at three distinct altitudes (600 m, 2000 m, and 3000 m) of the atmosphere (shown by a different color) over JDR, VNS and BBR [Gogoi et al., Atmos. Chem. Phys., 2020].

in the entire column at JDR, (ii) significant enhancement in coarse mode aerosols in the upper levels (at 2 and 3 km altitudes) of the atmosphere at VNS and BBR.

Consequently, coarse mode aerosol mass concentrations and mass fractions (F_{MC}), along with geometric mean radii of the size distributions showed an increase with altitude. The high values of coarse mode mass fraction and an increasing trend with altitude is indicative of the role of upper-level transport of dust from the western desert regions, in addition to those contributed locally due to thermal convective processes. As compared to the other two stations, the highest value of F_{MC} (~ 70%) near the surface was seen at JDR, indicating the role of the arid nature of the region. This study explains the abundance of coarse mode dust decreasing from west to east; along with an increase in the contribution of anthropogenic fine/ accumulation mode aerosols. This was further corroborated by data from Cloud Aerosol Transportation System (CATS) onboard International Space Station (ISS), which also revealed that the vertical extent of dust aerosols reached as high as 5 km during this period.

The fractional contribution of BC (F_{BC}) to the total composite aerosol mass (estimated from the volume size distribution, considering a uniform density of 2 gcm^{-3}, especially in view of the abundance of dust) remained lowest (~6%) in the western IGP, with very little altitude variation. In the central IGP, F_{BC} is quite high (~15 % to 20%) within the boundary layer and values decreased above 2 km (10%). Interestingly, F_{BC} at BBR showed higher values at higher altitudes, where the near-surface values are much lower and comparable to those at JDR. Following this, the altitudinal profiles of the heating rate due to BC alone are distinctly different over the regions, BBR showing an increase with altitude (~ 0.35 K day^{-1} at 3 km altitude), while VNS shows the opposite pattern with maximum heating within the boundary layer (~ 0.81 K day^{-1}).

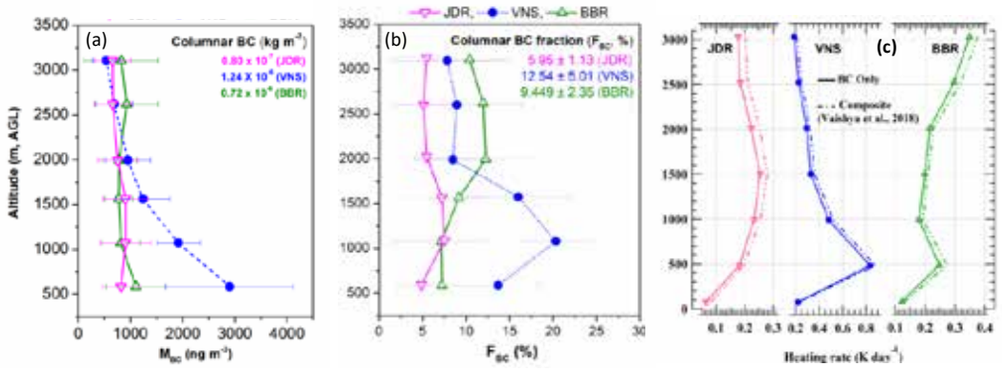

Figure 9: Vertical profiles of (a) mean values of BC mass concentrations (M_{BC}); (b) BC mass fractions (F_{BC}) at JDR, VNS, and BBR and (c) atmospheric heating rate due to BC (solid lines) and composite (dashed lines) aerosols for the regions of the IGP [Gogoi et al., Atmos. Chem. Phys., 2020].

Enhanced heating at 500-2000 m altitude is seen over JDR. These results indicate the dominant role of absorbing aerosols near the surface at VNS, while the atmospheric heating due to BC is significant at higher altitude at BBR.

Altitude profiles of CCN characteristics across the Indo-Gangetic Plain prior to the onset of the Indian summer monsoon

The information on the vertical distribution of the cloud condensation nuclei (CCN) number concentration, CCN efficiency, and its variation with supersaturation (ss) are necessary to understand the complex aerosol-cloud interactions (ACI). To understand the ACI and its linkage to the Indian Summer Monsoon, concurrent and collocated airborne measurements of the vertical structure of the physical, optical, and CCN characteristics of aerosols were made across the IGP, just prior to the onset of the monsoon under the SWAAMI - RAWEX campaign. Aircraft measurements were carried out from three base stations, each representing distinct regions of IGP viz. (i) Bhubaneswar (BBR, 20.24º N, 85.81º E, 42 m a.m.s.l.) – a semi-urban coastal location at the eastern end of the IGP, (ii) Varanasi (VNS, 25.45º N, 82.85º E, 81 m a.m.s.l.) representing aerosol-laden (polluted) Central IGP, and (iii) Jodhpur (JDR, 26.25º N, 73.04º E, 219 m a.m.s.l.), representing a semi-arid location on the western IGP.

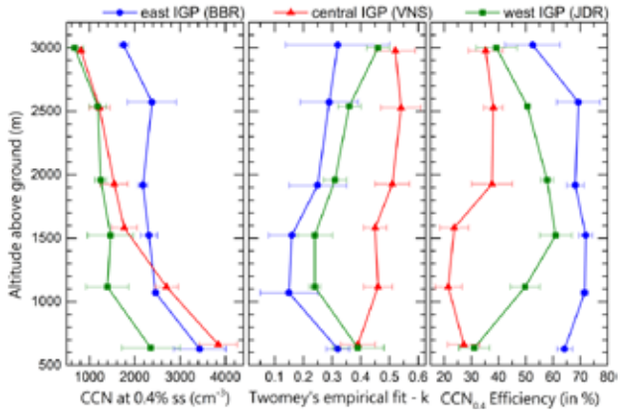

Figure10: Vertical distribution of CCN at 0.4 % supersaturation (left panel), Twomey's empirical fit (middle panel) and CCN activation efficiency at 0.4% supersaturation (right panel), over east - BBR (blue circle), central - VNS (red triangle), and west - JDR (green square) IGP regions. Error bars represent standard error of the mean [Jayachandran et al., Atmos. Chem. Phys., 2020].

In general, the CCN concentration has been highest in the Central IGP, decreasing spatially from east to west above the planetary boundary layer (PBL), which is ~1.5 km for the IGP during pre-monsoon. Despite this, the CCN activation efficiency at 0.4% supersaturation has been, interestingly, the highest over the eastern IGP (~72%), followed by that in the west (~61%), and has been the least over the central IGP (~24%) within the PBL. In general, higher activation efficiency is noticed above the PBL than within it. The Central IGP showed remarkably low CCN activation efficiency at all altitudes, which appears to be associated with high BC mass concentration there, indicating the role of anthropogenic sources in suppressing the CCN efficiency. First-ever CCN measurements over the western IGP, encompassing 'The Great Indian desert', also known as 'The Thar Desert', showed high CCN efficiency, ~61% at 0.4% supersaturation, indicating hygroscopic nature of the dust. The vertical structure of CCN properties is found to be airmass-dependent; with higher activation efficiency even over the central IGP during the prevalence of marine airmass. Wet scavenging associated with precipitation episodes seems to have reduced the CCN activation efficiency below cloud level. An empirical relation has emerged between the CCN concentration and the scattering aerosol index (AI), which would facilitate the prediction of CCN from aerosol optical properties.

Over the Oceans

Continental outflow of anthropogenic aerosols over the northern Indian Ocean during winter: ICARB-2018 campaign

Chemical characterisation of atmospheric aerosols over the Arabian Sea (AS) and Indian Ocean (IO) has been carried out onboard a research vessel during the winter period (January to February 2018) as part of the Integrated Campaign for

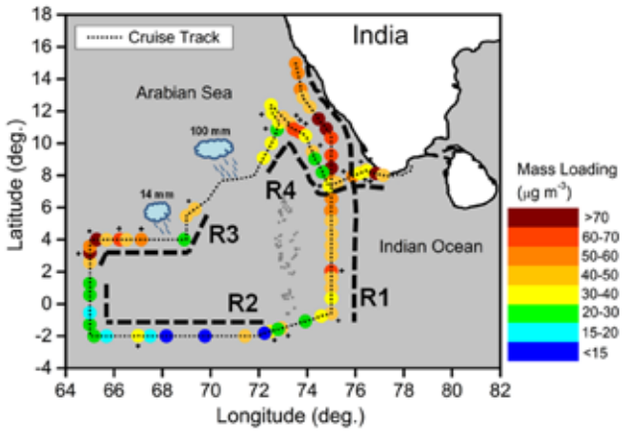

Figure 11: Cruise track during the ICARB campaign (dotted line) along with aerosol mass loading (PM_{10} and TSP) shown at the mean position of the ship when the samples were collected. TSP samples are indicated as black star marks next to the circles [Aswini et al., Sci. Total Environ., 2020].

Aerosols, gases, and Radiation Budget (ICARB-2018) to understand the sources and formation pathways of carbonaceous aerosols and impact of continental outflow to the adjacent oceanic regions. A complete chemical characterisation of near-surface aerosol samples from the marine boundary layer of AS and IO, including OC, EC, water-soluble and insoluble OC, primary and secondary OC, inorganic ions and trace metals have been carried out with a view to evolve a complete picture of the chemical nature of aerosols in the marine environment and to identify and quantify the major anthropogenic pollutants affecting the oceanic environments. Aerosol mass loadings showed large spatial heterogeneity during the cruise period, varying from 13 to 84 μg m^{-3} (Fig. 11). High mass loadings were observed over region R1 (the southeast Arabian Sea near to Indian coast) and R3 (Equatorial North IO along 4°N) while lowest over region R2 (Equatorial South IO along 2°S).

The pie charts shown in Fig.12 depict the chemical composition of aerosols in each of the four distinct regions, in terms of the percentage contribution of respective chemical species in PM_{10} as well as TSP samples. The corresponding airmass back trajectories are also shown along with. Region R4 is split into two, with trajectories from the Gujarat coast (R4 (a)) and trajectories from Bay of Bengal (R4 (b)). Sea-salt include Na, Cl, ss-Ca, ss-Mg, ss-K, ss-SO4; others constitute methanesulfonate, oxalate, nss-Mg, trace metals. Mineral dust is calculated using the relation, 2.2×Al+2.49×Si+1.63×Ca+2.42×Fe+1.94×Ti. The aerosol chemical characterisation revealed strong anthropogenic influence (accounting for 73% of PM_{10} mass) over region R1. The dominant constituent was nss-SO_4^{2-} (38%), followed by carbonaceous aerosols (21% Organic matter (=OC*2.6), 3.2% EC) and NH_4^+(9.7%). During the cruise (winter), airmasses with strong continental influence (north-easterlies) originating mostly from IGP and its outflow regions of Bay of Bengal, after passing through southern peninsular India, imparted strong

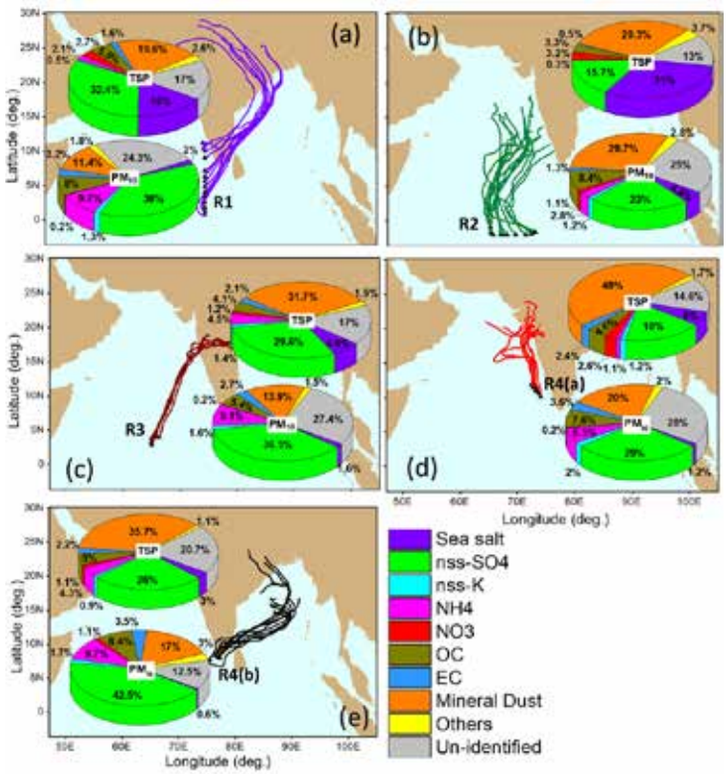

Figure 12: Chemical composition of TSP and PM_{10} aerosols shown as pie-charts along with the influencing airmass over different regions [Aswini et al., Sci. Total Environ. 2020].

anthropogenic signatures over the south-eastern Arabian Sea. Anthropogenic nss-SO_4^{2-} existing mainly as $(NH_4)_2SO_4$ was found to be the dominant aerosol throughout the cruise period.

The contribution of organic aerosols in the pollution plume transported to the oceanic region was found to be comparatively less as compared to that observed from anthropogenic source regions over continents. This reduction in OC mass fraction can be due to the net loss in carbon atoms through oxidation and volatilization during long-range transport. A higher OC to organic matter (OM) conversion needs to be used for aerosols that have undergone long-range transport and aging. The OM to OC conversion factor estimated using the mass closure approach was obtained as 2.6±0.85. A comparison of nss-SO_4^{2-} obtained from the present study with that of previous cruise observations revealed a strong increasing trend in its concentration over the continental outflow region over the Arabian Sea. This study provided important evidence of change in emission patterns periodically over oceanic regions, the transport pathways of anthropogenic pollutants to the pristine environment.

CCN properties of South Asian outflow: ICARB 2018 campaign

The fundamental parameter relevant for understanding the aerosol-cloud interaction is the CCN concentration, which are those aerosols that become activated at supersaturations pertinent to atmospheric conditions. Hence, the large uncertainty in the estimates of aerosol-cloud interaction points to the necessity of dedicated field campaigns and modelling efforts to improve the level of scientific understanding on CCN activation and to accurately quantify the change in microphysical properties of clouds due to anthropogenic aerosols. The South Asian region, especially northern India, experiences high aerosol loading during the winter season. Due to the favourable prevailing wind system, these continental aerosols are being transported over the northern Indian Ocean (Arabian Sea and Bay of Bengal). The dedicated ship borne measurements onboard the oceanographic research vessel Sagar Kanya was carried out as part of the ICARB experiment during winter 2018 (ICARB-2018) with a broad objective to characterize the South Asian outflow. The measurements were carried out within the continental outflow and remote oceanic regions far away from South Asia. The present study focuses on the CCN concentrations at different supersaturations, along with simultaneous measurements of the aerosol properties when the entire northern Indian Ocean was under the influence of continental outflow from South Asia.

The scatter plot between the total aerosol number concentration (condensation nuclei, CN) and CCN over the northern and equatorial Indian Ocean is shown in Fig. 13a, and the colour scale indicates a geometric mean diameter (GMD) corresponding to the composite aerosol number size distribution. CCN being a specific subset of CN, the

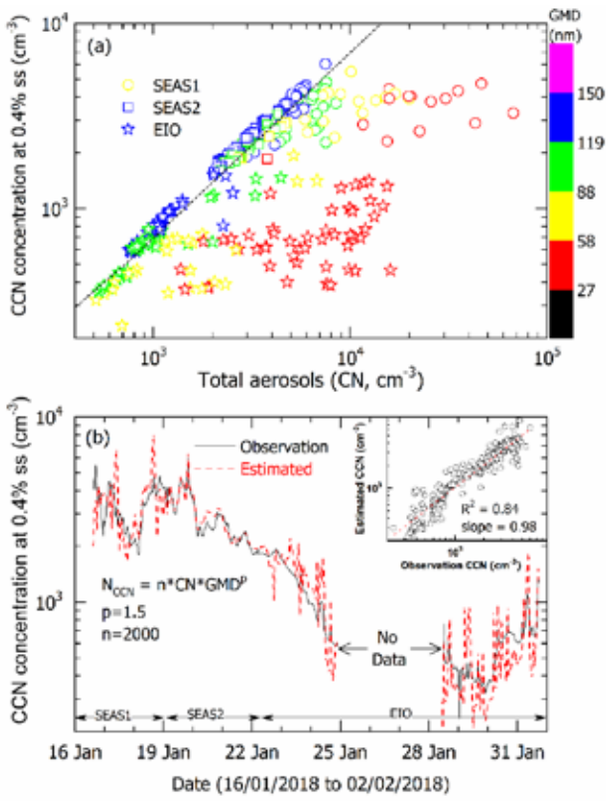

Figure 13: (a) Scatter plot between total aerosol (CN) and CCN at 0.4% supersaturation over SEAS1, SEAS2 and EIO. The colour shows the geometric mean diameter (GMD) of the aerosol size distribution. Regression fit for a GMD greater than100nm is shown as a black dotted line. (b)Temporal variation in CCN concentration at 0.4% supersaturation (SS) measured using a CCN counter and estimated using the empirical relationship between total aerosol number concentration and geometric mean diameter. The "p" and "n" are empirical constants estimated using the regression technique. The scatter plot of measured and estimated CCN concentration is shown inset [Nair et al., Atmos. Chem. Phys., 2020].

CCN concentrations increased with increasing total aerosol concentrations during most of the observations. Regression analysis of CN and CCN at 0.4% (slope ~0.2 and R^2~0.45) and 1.0% (slope ~0.29 and R^2~0.44) supersaturations has a poor association during the entire campaign period. When the CN concentration was very high, and ultrafine-mode aerosols contributed significantly to the CN concentrations, as evident from the lower values of the GMD of the aerosol size distribution (Fig. 13a, colour scale), a weak association between CCN and CN was observed. For GMD values greater than 100nm, CCN and CN followed an excellent relationship with R^2~0.99 and mean activation efficiency of 69±10% over all the regions. This highlighted that most of the particles in this size range become activated as CCN, irrespective of the regional heterogeneities in the aerosol composition. As aerosol system having a GMD of less than 60nm (when ultrafine particles dominate the aerosol size distribution) has deviated significantly from the regression line. This implies that the abundance of ultrafine particles has a direct impact on activation efficiency, since most

of these particles may not become activated at 0.4% and 1.0% supersaturation levels. The influence of the GMD on the CN–CCN association is further investigated using the regression analysis between the observed CCN at 0.4% supersaturation with the CCN concentration estimated from the CN and GMD empirically (Fig. 13b). The coefficient of determination (R^2) had improved from 0.44 to 0.84 when CN is multiplied with the GMD. The regression coefficient between measured and estimated CCN increased to 0.94 for a power law, where constants are estimated iteratively for the highest value of R^2. The temporal variation and scatter plot of measured and estimated CCN concentrations at 0.4% supersaturation are shown in Fig.13b. By accounting for the effect of the GMD on CCN concentration, this analysis demonstrated the primary role of aerosol number size distribution on CCN activation.

Tropospheric carbon monoxide over the northern Indian Ocean during winter: Influence of inter-continental transport

As part of the ICARB campaign, shipborne measurements of surface carbon monoxide (CO) were carried out during the winter season (16 January to 14 February 2018) over the northern Indian Ocean (IO) characterising the outflow from South Asia. As shown in Fig. 14a, surface CO varied from ~50 to 365 ppbv (179±67 ppbv) with higher levels over the coastal region of the southeast Arabian Sea (R1 region) and lower levels over the equatorial IO (R3 region). The northwesterly winds over the region transport CO (as well as other trace gases) over the northern IO from South Asia. The observation of CO conducted about 2 decades ago during the Indian Ocean Experiment (INDOEX)-1999 is compared with the measurements made during ICARB-2018. Aircraft-based CO measurements very close to the surface (below 970 hPa, i.e., ~350 m) during INDOEX-1999 are shown in Fig. 14b. Over a region bordered by dashed lines in Fig. 14b, the average CO during the INDOEX-1999 was 229 ± 40 ppbv as compared to 200 ± 43 ppbv during ICARB-2018. Though the standard deviation of the mean observed during both the campaigns is comparable (~40 ppbv), the mean CO value during ICARB-2018 shows a reduction of ~30 ppbv, which is indicative of the possible decline in CO (0.7 % $year^{-1}$) over the period of ~2 decades. Surface CO anomalies (ΔCO), obtained by removing mean seasonal variations, based on MOPITT (Measurements of Pollution in the Troposphere) and CAMS (Copernicus Atmosphere Monitoring Service) estimations show statistically significant ($p<0.05$) decreasing trend of -0.35 and -0.5% $year^{-1}$, respectively. This is consistent with in situ observations as well as our previous study. Prior to the trend analysis, satellite (MOPITT) and model (CAMS) results were compared with in situ observations and found to be in a good agreement (r^2=0.60–0.65).

While the South Asian outflow influences the lower tropospheric CO over northern IO during winter, the transport from Southeast Asia enhances the upper tropospheric CO. The MOPITT retrieved upper-tropospheric CO (300 hPa) shows relatively higher CO mixing ratios (95–100 ppbv; higher or comparable to that at the surface) over the equatorial IO (R3 region) during January 2018 (Fig. 15a). However, a significant enhancement of CO mixing ratios (100–125 ppbv) over the equatorial IO is noticed in February 2018 with a reversal of winds from easterly to westerly or south-westerly. Magenta rectangle (Fig. 15a & b) depicts the region of maximum increase of CO (20–30%) during February-2018 as compared with the climatological mean CO over 10 years (2009–2019, excluding 2018) of February month.

A rising branch of the Walker circulation, located over Southeast Asia around Indonesia, outflows in the upper-troposphere resulting in easterlies in the upper-troposphere

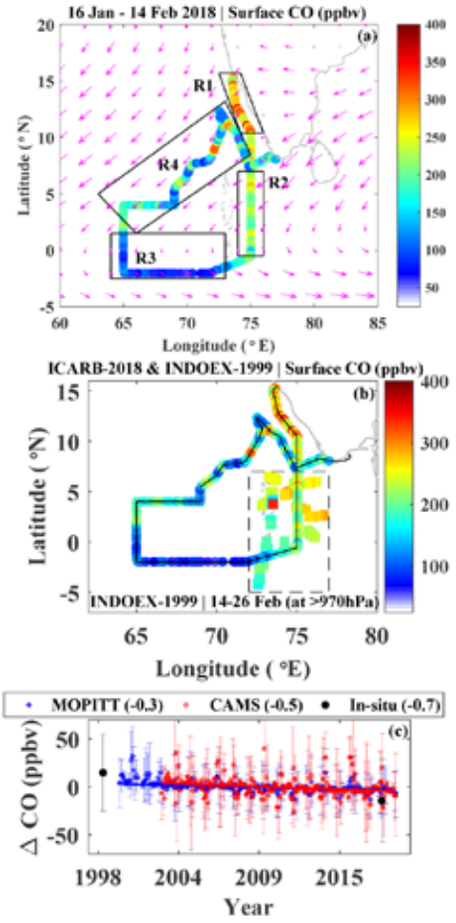

Figure 14: (a) Distribution of surface CO along with synoptic winds (magenta arrows) over the northern IO during ICARB-2018 (January-February 2018). The boxes show four regions (R1–R4) based on distinct airmasses. (b) Distribution of surface CO over during ICARB-2018 and INDOEX-1999 campaigns. (c) Surface CO anomaly (ΔCO) averaged over dashed region marked in (b) from MOPITT, CAMS, and in-situ observations. Numbers shown in the legend represent the trend of CO in % $year^{-1}$ [Girach et al., Climate Dynamics, 2020].

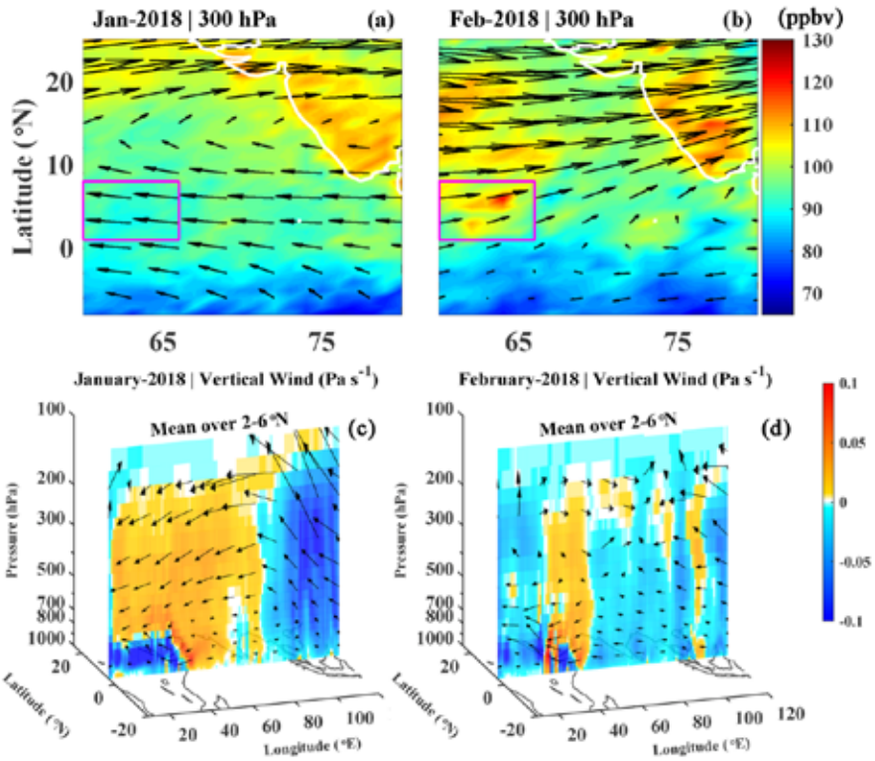

Figure 15: (a-b) Mean distributions of CO and synoptic wind at 300 hPa over northern IO during January and February 2018. Longitudinal cross-section (at 2–6° N latitude) of mean vertical winds (c–d) during January and February 2018. The magenta rectangles in figure (a-b) highlight the region of CO enhancement and wind reversal during February 2018 [Girach et al., Climate Dynamics, 2020].

(300–200 hPa). The updrafts over the Indonesian region can uplift CO-rich air infused with anthropogenic and biomass burning emissions in the Southeast Asian region to the upper troposphere over the equatorial IO (Fig. 15c). This leads to the enhancement in the upper-tropospheric CO over the region. Interestingly, this Walker circulation cell (Indonesia-IO cell) is disturbed, and the easterly winds change to westerly in the upper troposphere during February 2018 (Fig. 15b and d). The descending branch of the Walker cell disappeared; instead, an updraft is seen over most of the IO, as shown in Fig. 15c. Strong fire activities over Africa (not shown here) enhanced the lower tropospheric CO, which is uplifted by the rising branch of Africa-IO cell to the upper troposphere, which is redistributed over the larger region as far as the equatorial IO. Generally, meandering of the sub-tropical jet (around 30° N) penetrates towards equator up to ~10° N, however, it penetrated up to the equator, and westerlies/south-westerlies are seen over the equatorial IO during February 2018. The advection of convectively uplifted CO from African biomass burning emissions contributed to significantly enhanced upper tropospheric CO over the equatorial IO during February 2018. Thus, the combined effect of disturbed Walker cell over the equatorial IO and deeper penetration of sub-tropical jet transported the airmasses influenced by forest fires from the African region. Further analysis showed that such westerlies were not observed over equatorial IO over a decade. In a nutshell, while the lower-troposphere over northern IO is influenced by the South Asian outflow during winter, upper-troposphere is influenced by long-range transport from Southeast Asia. Anomalously, the influence of African biomass burning was observed in the upper-troposphere during February-2018.

O_3 and CO in the South Asian outflow over the Bay of Bengal during monsoon

To characterise the South Asian outflow over the Bay of Bengal (BoB) during monsoon season, the measurements of O_3 and CO were carried out as part of the second International Indian Ocean Expedition (IIOE-2) during 06 July–06 August 2018. Surface O_3 and CO varied in the range of 14–45ppbv (mean of 27.4±6.3ppbv) and 50–164ppbv (mean of 87±24ppbv), respectively over the BoB during the summer monsoon, with higher levels over the coastal region (Fig. 16 a & b). A patch of high-O_3 downwind of the Chennai region referred to as the Chennai-plume, is seen deeper over the BoB, having a spatial extent of ~5° with enhanced levels of O_3 (42–45 ppbv) and CO (100–140 ppbv). The O_3 production rate was observed to be 2.5 ppbv h^{-1} in the plume. Relatively cleaner airmasses from the Arabian Sea get exposed to regional anthropogenic influences over southern India and Sri Lanka.

CAMS simulated O_3 along the airmass trajectories are shown in Fig. 17a, and O_3 production is evident during

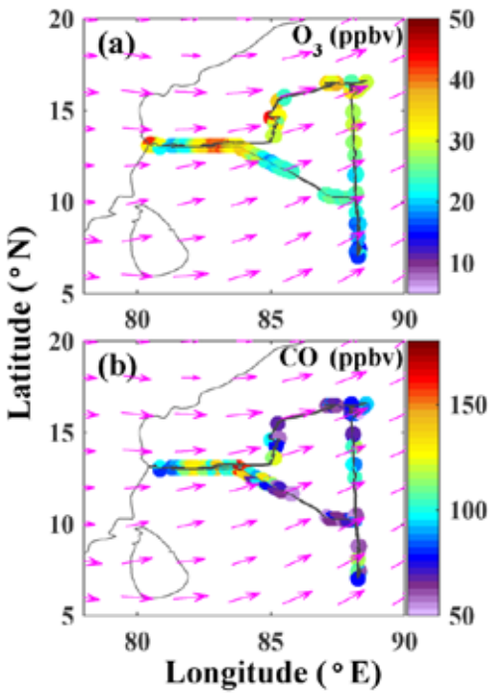

Figure 16: Spatial distributions of surface O_3 (a) and CO (b) along with synoptic winds (magenta arrows) during the IIEO-2 campaign (July-2018)[Girach et al., Atmos. Environ., 2020].

daytime (white colour marks on the trajectories represent sunlight hours) in the outflowing airmasses over the BoB. The mean ratios of formaldehyde to nitrogen dioxide ($HCHO/NO_2$) during the morning (8:30 IST), noon (11:30 IST), and afternoon (14:30 IST) using the CAMS results are shown in Fig. 17c-e. The $HCHO/NO_2$ ratios > 2 ppbv/ppbv indicate NOx-limited chemistry, ratios < 1 ppbv/ppbv indicate VOC-limited chemistry, and the ratios of 1–2 ppbv/ppbv represent a transition regime where O_3 production is sensitive to the levels of both NO_x and VOCs. $HCHO/NO_2$ ratios show VOC-limited O_3 production in the morning over a major portion of the Chennai-plume (as well as over east coast) followed by transition and then NO_x-limited regime over the BoB in the afternoon.

Shipping emissions around 6° N causes higher values NO_2-an ozone precursor, as seen in the Tropospheric Monitoring Instrument (TROPOMI) observations (Fig. 17b). The cleaner airmass from the equatorial Indian Ocean gets enriched with shipping emissions, and in the downwind of the shipping lane, O_3 production is seen over southern BoB (the dashed region in Fig. 17a). The influence of shipping emissions causes higher values of CO (80±19 ppbv) and O_3 production rate (1.1–1.3 ppbv h^{-1}) over the southern BoB (the dashed region in Fig. 17a). The O_3 production is in the transition regime during the morning and in the NO_x-limited regime during the rest of the day (Fig. 17c-e). In contrast, away from the continental influences (where precursor concentration is minimal; see Fig. 17b), the daytime photochemical O_3 destruction (0.7–1.0 ppbv h^{-1}) is evident over central BoB.

Dynamical nature of tropospheric ozone over a tropical location in Peninsular India: Role of transport and water vapour

The temporal changes in the altitude distribution of tropospheric ozone (O_3) based on the balloon-borne O_3-sonde measurements (121 profiles) during 2011 to 2014,

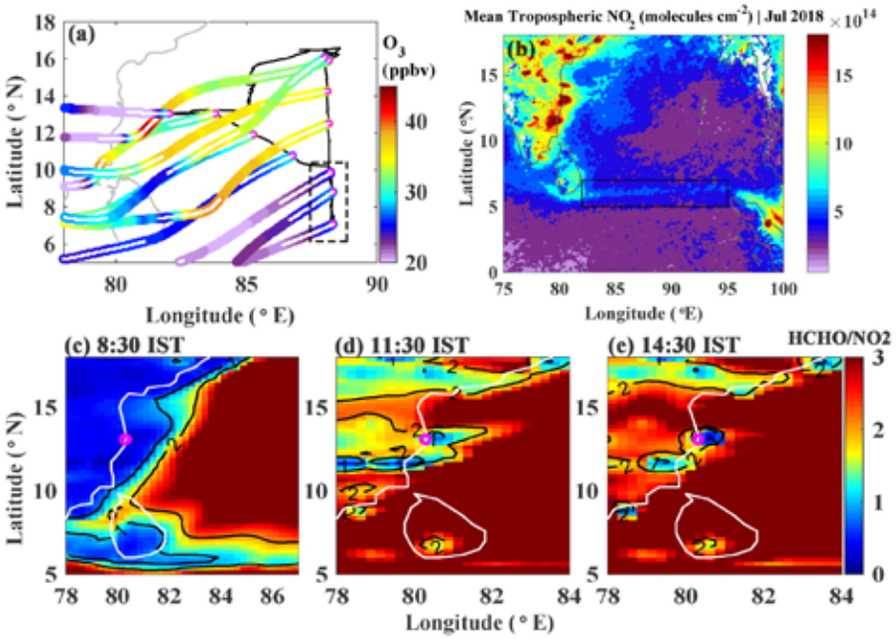

Figure 17: (a) Airmass back-trajectories ending at the measurement locations (small magenta circles) color-coded with model O_3. (b) Mean tropospheric NO_2 during July 2018 from TROPOMI. (c-e) Mean $HCHO/NO_2$ ratio (ppbv/ppbv) during 8:30, 11:30, and 14:30 IST (Indian Standard Time) during July 2018 [Girach et al., Atmos. Environ., 2020].

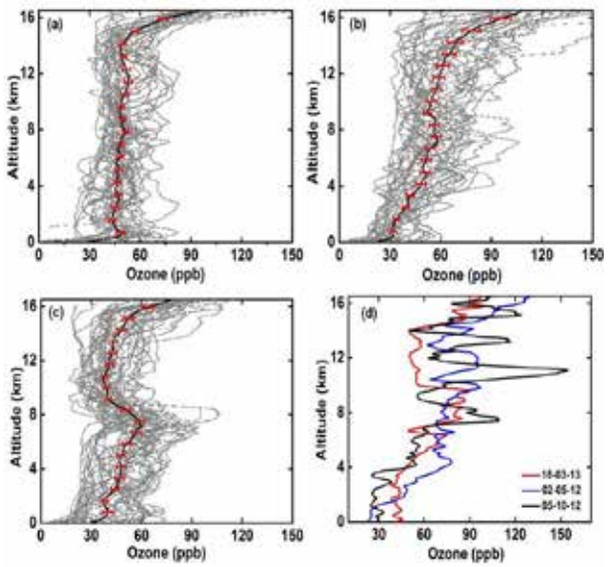

Figure 18: Four different types of troposphere O_3 profiles with (a) steady troposphere O_3 mixing ratio (b) increasing O_3 (c) mid-troposphere enhancement (d) multiple layers. The solid line in (a), (b) and (c) represent the mean profile. [Ajayakumar et al., Atmos. Environ., 2019]

conducted at the tropical, coastal site Thiruvananthapuram on the south-west coast of India have been studied. This is the first analysis from this region that shows the highly dynamic nature of tropospheric O_3 profiles exhibiting noticeable stratification, with single or multiple peaks.

Based on the structure and the broad features of the tropospheric O_3 profiles, they were grouped into four major categories (Fig. 18) namely, profiles with (i) more or less steady O_3 mixing ratios (ii) increasing O_3 mixing ratios with altitude, (iii) with mid-tropospheric enhancement, and (iv) those with laminar/layered structures depicting peaks in the altitude profiles. The observed differences in the tropospheric O_3 distribution are attributed to meteorological conditions in particular the synoptic-scale circulations, long-range transport, intrusion from the stratosphere, and photochemistry including the important role of water vapour. Water vapour and O_3 showed complex dependence with a positive and negative association. The steady tropospheric O_3profiles are observed in all seasons except in monsoon season. The O_3 mixing ratio remains more or less steady up to about 14 km or throughout the troposphere, with variability within 15-25 ppb and the absence of significant peaks/ stratification (Fig. 18). This group of profiles appear to be little affected by any strong source of O_3 and its precursors and represents a fairly well-mixed condition (i.e., constant O_3). The second category of O_3 profiles shows a clear increase in O_3 mixing ratio with altitude. Presence of multiple peaks at variable altitudes is also observed in many of these profiles. Most of the monsoon profiles and a few from pre-monsoon/ post-monsoon seasons fall under this category and are occurring mainly due to (1) the strong convective activities during this period (pre-monsoon and monsoon) which carries surface level O_3precursors to higher altitudes controlled by monsoon dynamics (2) intrusion of O_3 from the stratosphere (3) strong solar irradiance at upper levels favouring in-situ photochemical production. The third group, profiles with mid-tropospheric O_3 enhancement have a single well defined, broad mid-tropospheric peak maximising around 6–9 km, where values often reach as high as 80-110 ppbv. Above this maximum relatively lower O_3occurs, where the values gradually decrease. Most of these types of profiles occur during winter (DJF) season with higher near-surface values. This enhanced O_3 at this altitude region is primarily due to various reasons like (1) weakening of OH induced O_3 depletion due to unavailability of water vapour (2) transport of O_3 and /or its precursors to this region and subsequent enhanced photochemical production under low water vapour/OH levels etc. Finally, the fourth group, profiles with multiple layers exhibit sharp peaks of varying amplitudes at different altitudes, mostly above 6kmand have no seasonal dependence. Weakening of tropopause structure, stratosphere-troposphere exchange processes and presence of wave activities are the main controlling factors for this type of O_3 structure.

Figure 19 shows the seasonal variation in tropospheric O_3 profile. In the lower troposphere (within 2km), the O_3 mixing ratio attains a maximum in winter-time (DJF) followed by post-monsoon (ON), pre-monsoon (MAM) and monsoon (JJAS). The highest O_3 mixing ratio is seen in the pre-monsoon season above 2 km (boundary/mixing height).On the other hand, at higher altitudes, O_3 mixing ratio maximises in monsoon/pre-monsoon period. The average tropospheric column O_3 is 35±5.7 DU with a maximum in March, (43.25 DU; 27% of total columnar O_3) and minimum in October, (25.66 DU; 9%).The increase in solar radiation during summer results in more intense photochemistry involving precursors of O_3 leading to the greater O_3 production.

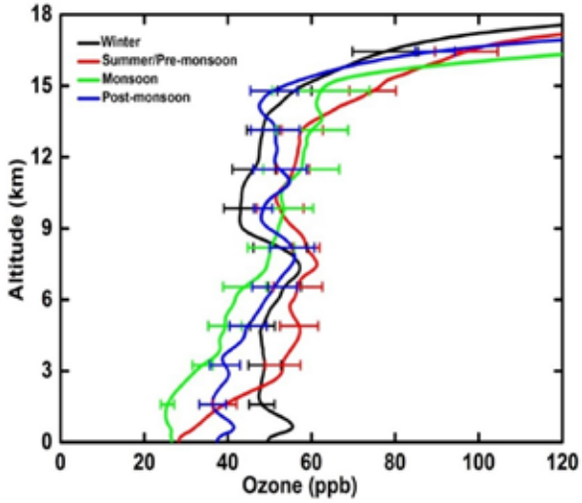

Figure 19: Seasonal mean of tropospheric ozone profiles over Thiruvananthapuram [Ajayakumar et al., Atmos. Environ.,2019].

Beyond Boundaries

Impact of ice-free oases on the chemical composition of particulate matter over the East Antarctic

To better understand the impact of ice-free regions on the particulate matter over East Antarctic, PM_{10} samples were collected at an Indian Antarctic research station, Bharati (Fig. 20). Aerosol sampling was conducted as part of the 36th ISEA (Indian Scientific Expedition to Antarctica) during the austral summer (17th December 2016 to 2nd February 2017) and analyzed for carbonaceous(OC, EC, and WSOC), water-soluble species (MSA^- Cl^-, nss-SO_4^{2-}, PO_4^{3-}, Na^+, NH_4^+, nss-Ca^{2+}, and Mg^{2+}) and trace metals(Al, Fe, Sr, Cr, Cu, Mo, Zn, Ni, Li, Co, Ti, V, Pb etc.).

Figure 20: The geographical location of the sampling site, Bharati, and its surrounding ice-free regions over the East Antarctic [Boreddy et al., Polar Sci. 2020].

Results show that chemical composition at Bharati characterized by a high abundance of organic matter followed by mineral dust particles. A key finding is that significant differences in the mass concentrations of all measured species in PM_{10} aerosols were associated with air masses originated from high altitude tropospheric air masses (HTAs; 17 December to 8 January) clearly distinguishable those from low altitude tropospheric air masses (LTAs; 9 January to 02 February 2017) as inferred from the Hysplit backward trajectory analysis as well as temporal variations observed in PM_{10} mass and meteorological parameters during the study period. The temporal trend of air temperature showed significant ($p<0.05$) higher values in HTAs than those of LTAs. PM_{10} mass is couple of times higher in LTAs than those of HTAs. Most of the chemical and trace metal species showed higher concentrations in LTAs than those of HTAs. Significant ($p<0.05$)positive correlations ($R^2=0.78$ in (Fig. 21) HTAs and $R^2=0.33$ in LTAs) between methanesulfonate (MSA^-) and nss-SO_4^{2-} suggest that they have common source associated with Dimethylsulfate (DMS) oxidation, particularly in HTAs. Aerosol liquid water content (ALWC) is a proxy for the aqueous-phase formation of atmospheric aerosols. To further examine the formation of PM_{10} aerosols at Bharati, we estimated ALWC using the ISORROPIA II model. ALWC showed a significant ($p<0.05$) correlation ($R^2=0.67$) with PM_{10} mass in HTAs while there is no such correlation was observed in LTAs. Moreover, WSOC/OC (a proxy for the atmospheric chemical processes) and WSOM/WIOM (provide information about the primary versus secondary organic matter) mass ratios (0.05-0.89 and 0.06-7.98 in HTAs 0.01-0.19 and 0.01-0.24 in LTAs) suggest that photochemical oxidations of secondary organic aerosols and primary emission are major sources in HTAs and LTAs, respectively.

PM_{10} aerosols collected at Bharati showed alkaline nature owing to erosion of soil/dust particles from the ice-free regions from the vicinity of the sampling site. The trace metal analysis revealed that high abundance of trace elements like Fe, Ti, Pb, Ba, and V in LTAs than those of HTAs further suggesting that soil-derived (crustal) emissions and local anthropogenic sources (so-called in-situ emissions) are possible sources of PM_{10} aerosols, especially when LTAs arrived at the sampling site. This point further supported by a significant ($p<0.05$) correlation of PM_{10} with Ti and Pb in LTAs ($R^2=0.58$; $R^2=0.30$) as well as the enrichment factor analysis.

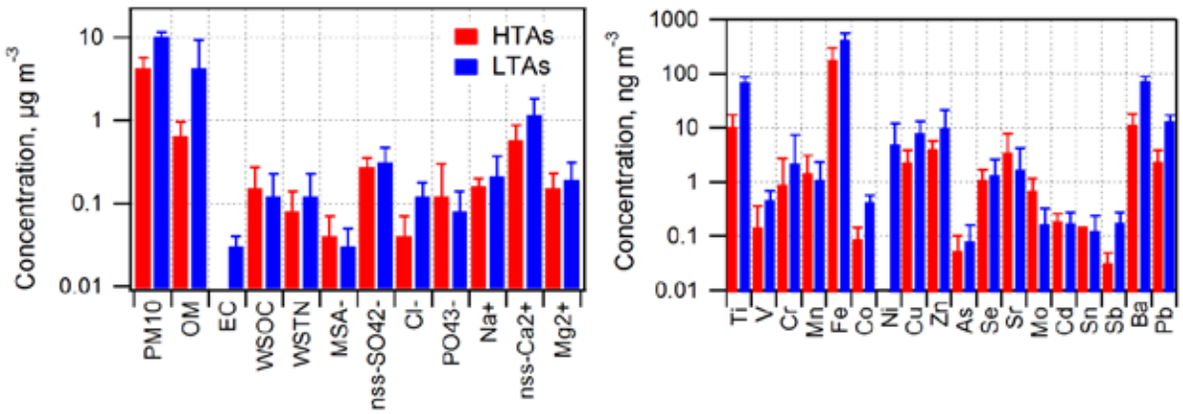

Figure 21: Differences in chemical composition (left panel) and trace metal composition (right panel) between HTAs and LTAs periods [Boreddy et al., Polar Sci. 2020].

In conclusion, the aqueous-phase formation of secondary aerosols followed by atmospheric processing has possible sources in HTAs. In contrast, primary emissions associated with soil/dust from ice-free regions and *in-situ* sources are major sources in LTAs at Bharati during Austral summer of 2016-2017. The present study demonstrated that ice-free regions in East Antarctic might be able to act as significant sources of aerosols by providing mineral dust as well as so-called *in-situ* emissions, which may play a major role in Antarctic climate by increasing the aerosol loading in the atmosphere.

Recent trend in the global distribution of aerosol direct radiative forcing from satellite measurements

Assessing the global distribution of aerosol direct radiative forcing (DRF) and their long-term trends are important for the quantification of aerosol climate forcing as well as the effectiveness of emission control policies. In the present study, the global distribution of DRFs and trends are studied using Clouds and Earth's Radiant Energy System (CERES) Synoptic (SYN) climate quality daily data sets. The synoptic data used in the present study is highly accurate and leads to improved estimation of DRF over both regional and global scale. This estimation of DRF trends in the global scale gave insight into the identification of the regional impact of aerosols on the Earth's energy budget, associating distinct regional changes (increase/decrease).

During 2001-2017, a statistically significant change of global DRFs is revealed (Fig. 22) with a general decreasing trend (i.e., a reduced cooling effect) at the top of the atmosphere (DRF_{TOA} ~ 0.017 Wm^{-2} yr^{-1}) and the surface (DRF_{SFC} ~ 0.033 Wm^{-2} yr^{-1}) with rapid change over the land compared to the global ocean. South Asia and Africa/Middle East regions depict a significant increasing trend of atmospheric warming by 0.025 and 0.002 Wm^{-2} yr^{-1} whereas, the rest of the regions show a decline. These regional variations significantly modulate the overall global mean DRF (-5.36 ± 0.04 Wm^{-2} at the TOA and -9.64 ± 0.07 Wm^{-2} at the surface). This indicates that there has been a profound change in aerosol burden and its radiative impact across the globe in recent decades. We find potential enhancement of atmospheric warming (>0.04 $Wm^{-2}yr^{-1}$) over central, eastern IGP and southern India, southern and central parts of Africa and Middle East countries, and their adjacent water bodies. The rest of the globe is experiencing the opposite trend. The observed DRF trends are found to coincide with the change in the aerosol optical depth (AOD), Ångström exponent (α), and columnar burden of SO_2. We see that there have been significant positive trends of AOD over the continental regions, such as central and eastern parts of the IGP (R5), Middle East countries and the central part of Africa (R4), along with their adjacent water bodies such as the Arabian Sea, the northern Bay-of-Bengal and the east coast of Africa. Whereas, continental regions such as eastern parts of the United States, South America, European countries, eastern China, and their adjacent water bodies show negative trends in AOD. In line with this, the values

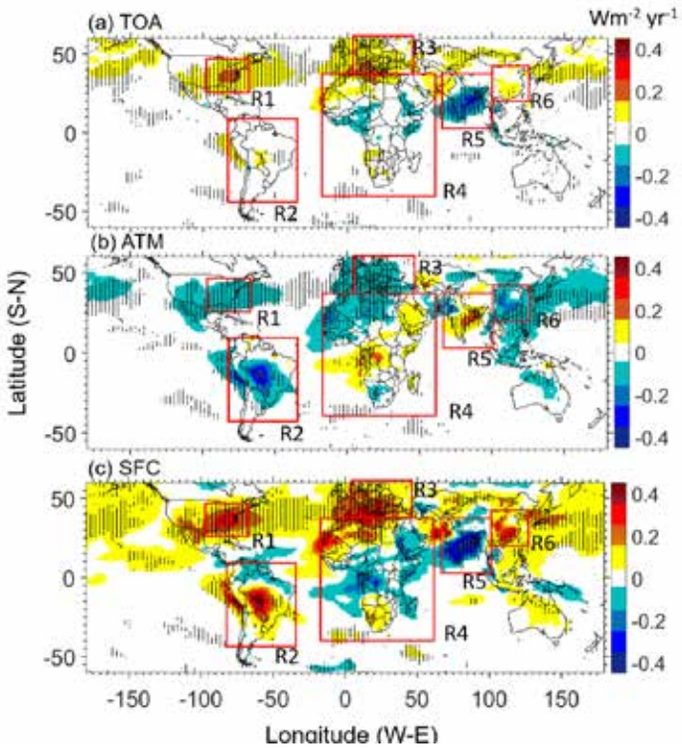

Figure 22: The global distributions of the trend in clear-sky shortwave aerosol direct radiative forcing (a) at the top of the atmosphere (TOA), (b) in the atmosphere (ATM), and (c) at the surface (SFC). The red boxes represent distinct geographic regions denoted by R1-R6. Dotted areas are regions having a significant trend above the 95% confidence level [Subba et al., Atmos. Sci. Letts., 2020].

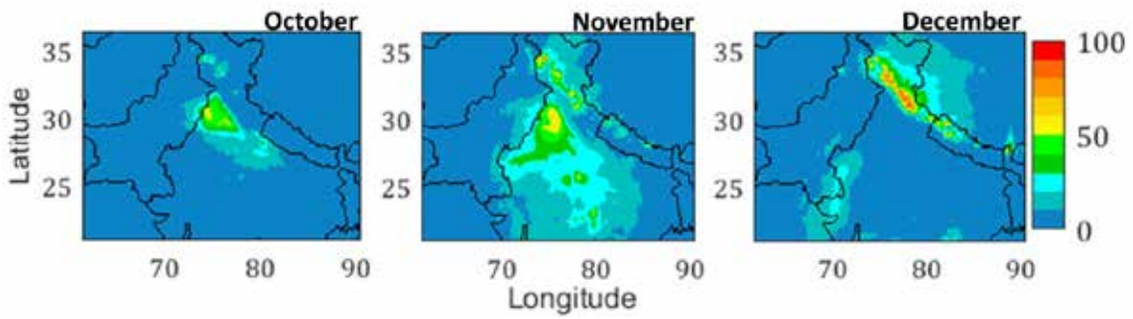

Figure 23: Biomass burning contribution (%) to PM2.5 over Indo Gangetic Plain during October-December 2016 [Ojha et al., Scientific Reports, 2020].

of Angstrom exponent (α) also exhibit significant changes over the period 2003 to 2017; over eastern China, India, Europe, the Middle East countries, and Africa. This reveals that not only the amount of global aerosol loading has changed; simultaneously, the physicochemical properties of aerosols have also changed. However, change in total columnar AOD is not just caused evenly by the change in the amounts of all types of aerosols, but is rather driven by the predominant contributors of the composite aerosols. This can be observed in terms of the changes of α, which increase over the Indian subcontinent and central China. This is attributed to increasing anthropogenic activities in response to the growing population and urbanization, which results in higher emission of small-sized particles. It is also noticed that the increase in α coincides with the increase in SO_2 loadings over the outflow region of the IGP in the Indian subcontinent (region R5). However, the positive trend of SO_2 over the boundary of Peru and Chile (region R2) and central Africa (Republic of Congo; region R4) is not consistent with the collocated positive trend of α. The above-mentioned discrepancies may be attributed to the influence of the aerosol loading which is driven by other sources such as dust and biomass burning.

On the widespread enhancement in fine particulate matter across the Indo-Gangetic Plain towards winter

Based on the Weather Research and Forecasting model coupled with Chemistry (WRF-Chem) simulations, large scale biomass burning (mainly agricultural residue burning) contributes ~ 50–60% of fine particulate matter ($PM_{2.5}$) over northwest IGP including Delhi region during October as well as November. The influence of biomass burning over central and eastern IGP is minimal (less than 30%), especially during November. The widespread enhancement in $PM_{2.5}$ concentration during December (shown in Fig. 23) is mainly due to anthropogenic emissions and meteorological conditions. The contribution of biomass burning is less than 10% across the IGP. The decline in air temperature; significantly shallower atmospheric boundary layer; and weaker winds lead to stagnant conditions (ventilation coefficient lower by a factor of ~4), besides the topographical features around the IGP, confines the anthropogenic influences closer to the surface. This causes widespread enhancement in $PM_{2.5}$ towards winter; however, the contributions from small-scale biomass burning and aerosol feedback mechanisms to make boundary layer shallower cannot be neglected over the IGP.

Technical Developments

As part of the ARFI Project ISRO GBP, technical development and maintenance activities are regularly being carried out which includes the fabrication and installation of Multi-Wavelength Radiometers for different stations in ARFINET, developed sub-systems for the smooth operation of aerosol and trace gas monitoring instruments and technical support to regular data collection and campaign mode observations.

- Development of Data Processing Software for Multi Wavelength Radiometer (MWR-DPS)

A state-of-the-art data processing software is designed and developed in Visual Basic platform for quick analysis of MWR data at the ARFINET observatories to retrieve aerosol optical depth (Fig.24). A cloud screen algorithm is implemented in the software to screen the clear sky data which considerably reduces the analysis time. The interactive GUI is the speciality of this software and it works in all present versions of Windows computers.

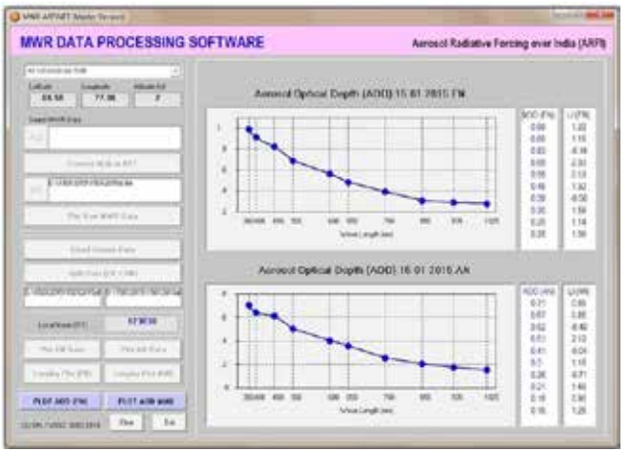

Figure 24: MWR Data Processing Software

Future Projections

Role of microphysical properties on the life cycle and climate impact of Aerosols over India

Aerosol life cycle is one of the intensely investigated topics in recent years due to its importance in aerosol direct and indirect radiative effects and climatic implications. To understand their life cycle aspects, information on aerosol microphysical properties (number, size, mixing state, hygroscopicity etc.) is essential. This requires focussed studies on aerosol formation, transformation, ageing and removal processes that are highly heterogeneous in nature. However, the information on aerosol microphysical properties over Indian region is rather scarce. Especially, processes governing secondary aerosol formation (through gas to particle conversion), aerosol mixing state and hygroscopicity of highly heterogeneous aerosol system are the least explored over the Indian region.

Modelling of Aerosol – Climate Interactions

The understanding on the various factors contributes to the present day regional hydro-climate is rather limited and several uncertainties persist. State of the art climate models (both regional (RegCM and WRF-Chem) and global (CAM)) will be used to investigate the scientific problems associated with the masking effects of aerosols on regional surface temperature and the trend in monsoon rainfall. Regional/global models having coupled atmospheric chemistry will be used in this study.

Publications in Peer-Reviewed Journals

1. Jayachandran, V., Babu, S. S., Vaishya, A., Gogoi, M. M., Nair, V. S., Satheesh, S. K., Moorthy, K. K., "Altitude profiles of CCN characteristics across the Indo-Gangetic Plain prior to the onset of the Indian summer monsoon", Atmospheric Chemistry and Physics, 20, 561-576, DOI: 10.5194/acp-20-561-2020, (2020).
2. Kompalli, S. K., Babu, S.S., Satheesh, S. K., Moorthy, K.K., Das, T., Boopathy, R., Liu, D., Darbyshire, E., Allan, J.D., Brooks, J., Flynn, M.J., and Coe, H., "Seasonal contrast in size distributions and mixing state of black carbon and its association with PM1.0 chemical composition from the eastern coast of India", Atmospheric Chemistry and Physics, 20, 3135–3149, DOI: 10.5194/acp-20-3135-2020, (2020).
3. Usha, K. H., Nair, V. S., Babu, S. S., "Modeling of aerosol induced snow albedo feedbacks over the Himalayas and its implications on regional climate", Climate Dynamics, 54, 4191–4210, DOI: 10.1007/s00382-020-05222-5, (2020).
4. Nair, V. S., Jayachandran, V. N., Kompalli, S. K., Gogoi, M. M., and Babu, S. S., "Cloud condensation nuclei properties of South Asian outflow over the northern Indian Ocean during winter", Atmospheric Chemistry and Physics, 20, 3135–3149, DOI: 10.5194/acp-20-3135-2020, (2020).
5. Boreddy, S. K. R., Hegde, P., Aswini, A. R., Girach, I. A, Koushik, N., and Nalini K., "Impact of ice-free oases on particulate matter over the East Antarctic: inferences from the carbonaceous, water-soluble species and trace metals", Polar Science,24, 100520, DOI: 10.1016/j.polar.2020.100520, (2020).
6. Aswini, A. R., Hegde, P., Aryasree, S., Girach I. A., and Nair, P. R., "Continental outflow of anthropogenic aerosols over Arabian Sea and Indian Ocean during wintertime: ICARB-2018 campaign", Science of the Total Environment, 712, 135214, DOI: 10.1016/j.scitotenv.2019, (2020).
7. Hegde, P., Vyas, B. M., Aswini, A. R., Aryasree, S., and Nair, P. R., "Carbonaceous aerosols over a semi-arid location in North West India: seasonal variations and source characteristics", Journal of Arid Environments, 172, 104018, DOI: 10.1016/j.jaridenv.2019.104018, (2020).
8. Girach, I. A., Tripathi, N., Nair, P. R., Sahu, L. K., and Ojha, N., "O_3 and CO in the South Asian outflow over the Bay of Bengal: Impact of monsoonal dynamics and chemistry", Atmospheric Environment, 233, 117610, DOI: 10.1016/j.atmosenv.2020.117610, (2020).
9. Girach, I. A., Nair, P. R., Ojha, N., and Sahu, L. K., "Tropospheric carbon monoxide over the northern Indian Ocean during winter: influence of inter-continental transport", Climate Dynamics, 54, 5049-5064, DOI: 10.1007/s00382-020-05269-4, (2020).
10. Gogoi, Mukunda M., V. Jayachandran, A. Vaishya, S. S. Babu, S.K. Satheesh and K.K. Moorthy, "Airborne in-situ measurements of aerosol size distributions and BC across the IGP during SWAAMI–RAWEX", Atmospheric Chemistry and Physics, 20, 8593–8610,DOI: 10.5194/acp-2020-144, (2020).
11. Subba, T., M.M. Gogoi, B. Pathak, P. K. Bhuyan and S. S. Babu, "Recent trend in the global distribution of aerosol direct radiative forcing from satellite measurements: regional impacts", Atmospheric Science Letters, e975, DOI:10.1002/asl.975, (2020).

12. Ojha, N, Sharma, A, Kumar, M, Girach, I., Ansari, T. U., Sharma, S. K., Singh, N., Pozzer, A. and Gunthe, S. S., "On the widespread enhancement in fine particulate matter across the Indo-Gangetic Plain towards winter", Scientific Reports, 10:5862, DOI: 10.1038/s41598-020-62710-8, (2020).

13. Joshi, H., L.M. David, T. Gupta, M.M. Gogoi, S.S. Babu and M. Naja, "Absorption characteristics of aerosols over the central Himalayas and its adjacent foothills", Atmospheric Research, 233, 104718, DOI: 10.1016/j.atmosres.2019.104718, (2020).

14. Singh, P., Vaishya, A., Rastogi, S., and Babu, S.S., "Seasonal heterogeneity in aerosol optical properties over the subtropical humid region of northern India", Journal of Atmospheric and Solar–Terrestrial Physics, 201, 105246, DOI: 10.1016/j.jastp.2020.105246, (2020).

15. Kant, Y., Shaik, D.S., Mitra,D., Chandola, H.C., Babu, S.S., Chauhan, P., "Black carbon aerosol quantification over north-west Himalayas: Seasonal heterogeneity, source apportionment and radiative forcing", Environmental Pollution, 257, 113446, DOI: 10.1016/j.envpol.2019.113446, (2020).

16. Rastogi,N., Agnihotri, R, Sawlani,R., Patel, A., Babu,S.S., Satish, R., "Chemical and isotopic characteristics of PM10 over the Bay of Bengal: Effects of continental outflow on a marine environment", Science of the Total Environment, 726, 138438,DOI: 10.1016/j.scitotenv.2020.138438, (2020).

17. Arun, B. S., Aswini, A. R., Gogoi, M.M., Hegde, P., Kompalli, S. K., Sharma, P. and Babu, S.S., "Physico-chemical and optical properties of aerosols at a background site (~4 km a.s.l.) in the western Himalayas", Atmospheric Environment, 218, 117017, DOI: 10.1016/j.atmosenv.2019.117017, (2019).

18. Ajayakumar, R. S., Nair, P. R., Girach, I. A., Sunilkumar, S. V., Muhsin, M., Chandran, P. S., "Dynamical nature of tropospheric ozone over a tropical location in Peninsular India: Role of transport and water vapour", Atmospheric Environment, 218, 117018,DOI: 10.1016/j.atmosenv.2019.117018,(2019).

19. Brooks, J., Liu, D., Allan, J. D., Williams, P. I., Haywood, J., Highwood, E. J., Kompalli, S. K., Babu, S. S., Satheesh, S. K., Turner, A. G., and Coe, H., "Black carbon physical and optical properties across northern India during pre-monsoon and monsoon seasons", Atmospheric Chemistry and Physics, 19, 13079–13096, DOI: 10.5194/acp-19-13079-2019, (2019).

20. Pathak, H. S. P., Satheesh, S.K., Nanjundiah, R.S., Moorthy, K.K., Lakshmivarahan, S., and Babu, S.S., "Assessment of regional aerosol radiative effects under the SWAAMI campaign – Part 1: Quality-enhanced estimation of columnar aerosol extinction and absorption over the Indian subcontinent", Atmospheric Chemistry and Physics, 19, 11865–11886, DOI: 10.5194/acp-19-11865-2019, (2019).

Scientific/Technical Reports

1. Kompalli, S.K. and Ajeeshkumar P.S., "Design of Mechanical Layout of the Aerosol Humidograph Instrument (AHI)", Space Physics Laboratory, Vikram Sarabhai Space Centre, ISRO-VSSC-TR-0130-0-20, April, 2020.

2. Kompalli, S.K. and Ajeeshkumar P.S., "Development of the isokinetic inlet system for ambient aerosol sampling", Space Physics Laboratory, Vikram Sarabhai Space Centre, ISRO-VSSC-TR-0129-0-20, April, 2020.

3. Mukunda M. Gogoi, Ashok Bandyopadhyay, Rathidevi Satishkumar, Rakesh K, Praveen K S, Ajeeshkumar P S, ARFINET Data Archival and Dissemination System; Part-1: Procedures for data uploading and classified archival, ISRO-VSSC-TR-0060-0-20, 2020.

4. Mukunda M. Gogoi, Intercomparison and performance evaluation of aethalometers in the ARFINET, ISRO-VSSC-TR-0059-0-20, 2020.

5. Mukunda M. Gogoi, S.L.N. Desikan and Ajeeshkumar P S, Isokinetic flow evaluation of shrouded diffuser air-inlet in Open Jet Facility, VSSC, ISRO-VSSC-TR-0035-0-20, 2020.

6. Ajeeshkumar P. S. and Mukunda M. Gogoi, Development of a Data Processing Software for Multi-Wavelength Radiometer, ISRO-VSSC-TR-0605-0-1, 2019.

Presentation in Symposium/Conferences/Workshops

International

1. Kompalli, S. K., Babu, S.S., Satheesh, S. K., Moorthy, K.K., Das, T., Boopathy, R., Liu, D., Darbyshire, E., Allan, J.D., Brooks, J., Flynn, M.J., and Coe, H. "Microphysical properties and mixing state of refractory black carbon aerosol in the Indo Gangetic Plain (IGP) outflow", Water Future International Conference, Session: Aerosols, Clouds, Precipitation, and Hydrological Cycle, Indian Institute of Science, Bengaluru, 23-25 September, 2019.

2. B.S. Arun, M. M Gogoi, A. Borgohain, S. S. Kundu, S.K. Kompalli, S. Suresh Babu, "Regional synthesis of Black Carbon Aerosols over the Himalayas: Impact of synoptic source processes and long-term trends", International Water Future Conference, Session: Aerosols, Clouds, Precipitation, and Hydrological Cycle, Indian Institute of Science, Bengaluru, 23-25 September,2019.

3. Subin Jose, Vijayakumar S Nair and S. Suresh Babu "Aerosol interactions on marine warm clouds over northern Indian Ocean": Water Future International Conference, Session: Aerosol, Clouds, Precipitation and Hydrological Cycle, Indian Institute of Science, Bengaluru, 23-25, September, 2019.

4. Gogoi, Mukunda M., Aerosol Radiative Forcing from the simultaneous measurements of aerosol properties and radiation over India, Special session on aerosols, clouds, precipitation and hydrological cycles, Water Future Conference, Bangalore, September 24-27, 2019.

National

1. Girach, I. A., Ojha, N., and Nair, P. R., Validation of Satellite retrieved Tropospheric CO and CH_4, URSI (International Radio Science Union) Regional Conference on Radio Science (URSI-RCRS) -2020, Varanasi, 12 - 14 February 2020.

2. Ojha, N., Girach, I. A., and Sahu, L. K., Tropospheric Chemistry over the Indian Subcontinent: Space-based Observations and Modeling, URSI (International Radio Science Union) Regional Conference on Radio Science (URSI-RCRS) - 2020, Varanasi, 12 - 14 February 2020.

3. Chutia, L., Ojha, N., Girach, I. A., Pathak, B., Sahu, L. K., and Bhuyan, P. K., Long term changes in sulfur dioxide (SO_2) over South Asia during 2005-2017 period, URSI (International Radio Science Union) Regional Conference on Radio Science (URSI-RCRS) - 2020, Varanasi, 12 - 14 February 2020. (3^{rd} Prize in student paper competition)

4. Ojha, N., Girach, I., Soni, M., Singh, N., and Gunthe, S. S., Modelling the atmospheric chemistry and dynamics over India, National conference on Recent Trends in Environmental Pollution and Disaster Risk Reduction (RTEPDRR-2020), FICCI, New Delhi, 6–7 February 2020.

5. Chutia, L., Ojha, N., Girach, I., Sahu, L. K., Sarangi, C., Pathak, B., Bhuyan, P. K., Distribution of Trace Gases over South Asia: Model Simulation versus Observations, 4th ISSE National conference (INAC-4), Space Applications Centre, Ahmedabad, 26-27 September, 2019.

6. Ajayakumar, R. S.,P. R Nair, Girach I. A.,"Dynamical nature of tropospheric ozone over a tropical location in Peninsular India: Role of transport and water vapour", International Conference on the Asian Summer Monsoon Anticyclone: Gateway of Surface Pollutants to the stratosphere, SRM Institute of Science and Technology, Chennai.09-10 February, 2020.

7. Boreddy, S. K. R., Aswini, A. R., Hegde, P.,"Determination of carbonaceous, water-soluble species and trace metals in aerosols collected at Bharati station over the East Antarctic: role of ice-free oases and local meteorology", Proceedings of the National Conference on Polar Sciences, NCPS-2019, Page 234, 22 August, 2019.

8. Hegde, P., Aswini, A.R., "Continental outflow of different aerosol chemical constituents over Arabian Sea and Indian Ocean" Proceedings of national conference on "Recent advances in analytical separation techniques", ISAS-2019, Trivandrum, Page 64, 19-20 September, 2019.

9. Hegde, P., Participated in the National Conference on "Manufacturing trends in Electrochemical Energy Systems" MEES - 2019, organised by Indian Institute of Chemical Engineers, Trivandrum Regional Centre, 21 September, 2019.

10. Boreddy, S. K. R., "Publishing Scientific Content",Springer Author work shop organised by VSSC Library in connection with NLW-19, VRC, 15 November, 2019.

11. Kompalli, S. K., Babu, S.S., Satheesh, S. K., Moorthy, K.K., Das, T., Boopathy, R., Liu, D., Darbyshire, E., Allan, J.D., Brooks, J., Flynn, M.J., and Coe, H. "On the mixing state of black carbon in the Indo Gangetic Plain (IGP) outflow", TROPMET-2019, National Symposium on Land, Ocean and Atmosphere Interactive Processes in the Context of Weather and Climate, Andhra University, Visakhapatnam, 11-14 December, 2019.

12. Arun, B.S., M.M Gogoi, P. Hegde, A.R. Aswini, A. Borgohain, S. S. Kundu and S. Suresh Babu, "Characterization of the zonal asymmetry in aerosols types over the "Third pole": Radiative implications", National Conference on Polar Sciences (NCPS), NCPOR, Goa, 20-22 August,2019.

Session Chairman/Convener in Conference/Symposium/Workshops

Vijayakumar S. Nair

Co-Chair, International Conference on Regional Climate (ICRC-CORDEX), Beijing, China, 14-18 October, 2019.

Invited Talks

S. Suresh Babu

1. "Aerosol Radiative Forcing over India", International Global Atmospheric Chemistry (IGAC) – Monsoon Asian and Oceania Networking Group meeting and workshop, ARIES, Nainital, 28 – 30 November 2019.

Giarch Imran Asatar

1. "Climate Change" at Graphic Era Deemed to be University, Dehradun on 19 September 2019.

Training Programme

Hegde, P.

1. One day Training Programme on "ISRO e-Procurement for Indenters (Batch II)", HRDD, VSSC, Thiruvananthapuram, 27 January, 2020.

Vijayakumar S. Nair

1. One day Training Programme on "ISRO e-Procurement for Indenters (Batch II)", HRDD, VSSC, Thiruvananthapuram, 28 January, 2020.

Girach Imran Asatar

1. One day Training Programme on "ISRO e-Procurement for Indenters (Batch II)", HRDD, VSSC, Thiruvananthapuram, 28 January 2020.
2. Attended the phase-1 and phase-2 of the Artificial Intelligence (AI) training programme organized by Directorate of Technology Development and Innovation (DTDI), ISRO Head Quarters, Bangalore, 4–9 November 2019 and 3–7 February 2020.

Kompalli, S. K.

1. One day Training Programme on "ISRO e-Procurement for Indenters (Batch II)", HRDD, VSSC, Thiruvananthapuram, 28 January, 2020.

Numerical Atmosphere Modelling

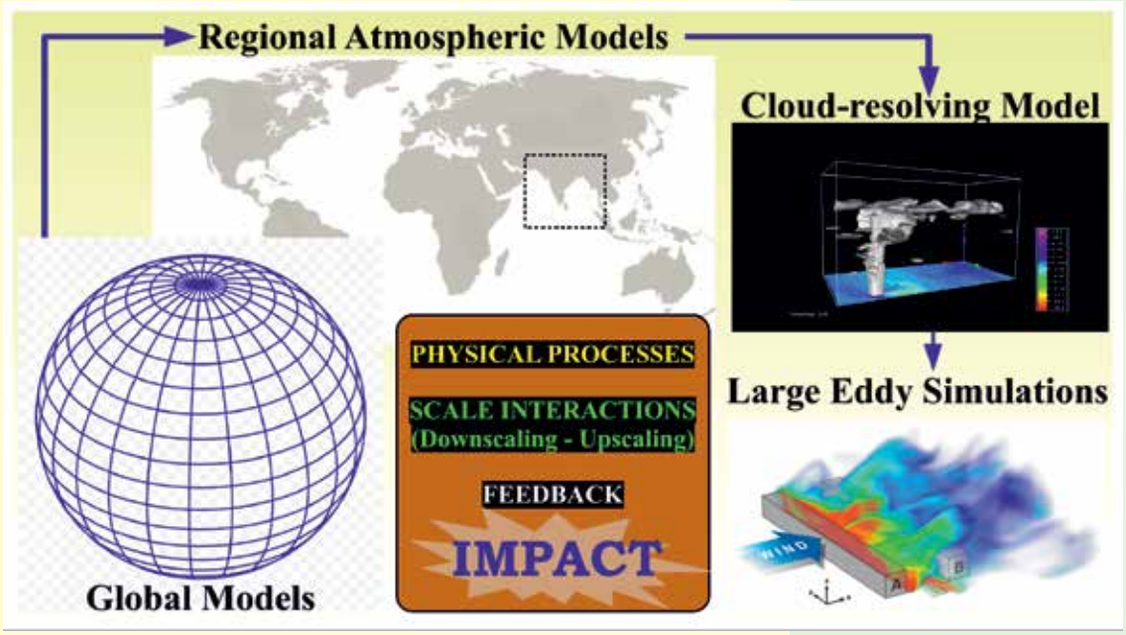

The Numerical Atmosphere Modelling (NAM) branch focuses on the "Prediction and Analysis of the Weather and Climate System of planet Earth" through various numerical weather prediction and regional atmospheric transport models, such as COSMO, WRF, RegCM, FLEXPART and NIES, to name a few. This branch is also responsible for providing short-range weather predictions through COSMO model for SHAR region in support of ISRO's PSLV and GSLV missions undertaken from Sriharikota. During the review period, this branch has taken up detailed investigations on various aspects of: (i) Theoretical study on the design of surface CO_2 monitoring network stations over the Indian region; (ii) Existence of 'mini-break' like conditions during early Indian monsoon onset years; (iii) Role of Intra-seasonal variability in the Indian summer monsoon on hydration and dehydration of the upper troposphere; and (iv) the tropical cyclones over the Bay of Bengal and the Arabian Sea through COSMO model.

NEW INITIATIVES: Besides the ongoing activities, the branch has also undertaken a first and unique experiment on Unmanned Aerial Vehicle (UAV) for studying the variability of CO_2 in the atmospheric boundary layer. Large Eddy Simulations with the help of PALM model are also progressing well.

Science Team

Radhika Ramachandran
D. Bala Subrahamanyam
S. Sijikumar
K. N. Uma

Research Fellows

K. Nalini
Freddy P. Paul
S. Roshny
Anjumol Raju
Bukya Sama

Atmospheric Transport Modelling

Designing surface CO_2 monitoring network to constrain the Indian land fluxes

An optimal network design, for ground-based monitoring of atmospheric mole fractions of carbon dioxide (CO_2) over India is proposed using a Lagrangian Particle Dispersion Model FLEXPART and Bayesian inversion methods to constrain the Indian terrestrial surface fluxes. Potential emission sensitivity from FLEXPART, prior flux uncertainties from CASA-GFED biosphere fluxes, CDIAC fossil fuel fluxes, and assumed uniform observational uncertainty of 2 ppm were used to calculate prior and posterior cost functions. A total of 73 grid cells were identified over the Indian region in 2º x 2º latitude by longitude resolution assuming each cell as a potential site, '*a-priori' (Fig. 1)*. Further, the effectiveness of CO_2 observations from these locations to reduce the Indian terrestrial flux uncertainty was quantified using an incremental optimization method. Based on the above objectives, we have (a) ranked the existing nine stations; (b) devised a methodology to design an extended network by adding a few more potential stations to the existing stations; and (c) identified a completely new set of optimal stations for measuring atmospheric CO_2 over India.

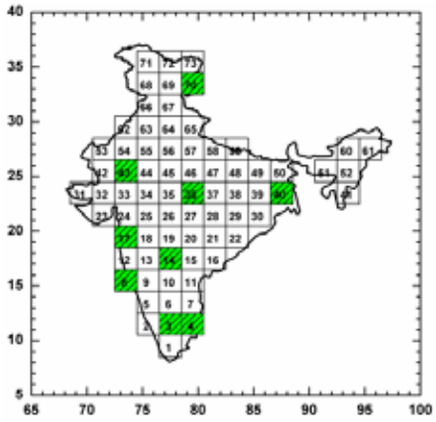

Figure 1: A map of India indicating the 2º x 2º grids, identified as potential site for CO_2 observation. Grid cells already containing existing stations are shaded and hatched (Nalini et al., Atmos. Env., 2019).

The study showed that the base network of existing stations scattered over India could reduce the uncertainty of Indian terrestrial surface flux estimation in an inversion framework, at this resolution, by more than 30% during post-monsoon and winter season, and by more than 15% during other parts of the year (Table 1). Addition of five new stations to the base network could reduce the uncertainty by an additional 15% for all the seasons reaching up to 45%. In the 'new network', twelve stations were able to achieve an equivalent flux uncertainty reduction of fourteen stations achieved by the 'extended network' during each season. Locations of stations are more important than the magnitude of reduction since it depends on the values of the prior and observational uncertainties. The most important and essential 'new' stations in the extended network are over the northeastern region and Indo-Gangetic plain, during most of the year (Fig. 2). Only during the post-monsoon season, additional stations are required in the western peninsular region. Finally, a consolidated set for all seasons comprising seventeen members was proposed (Fig. 3). The study highlights a major zone of CO_2 'observational void' that exists in potential locations near east and northeast parts of India. Immediate requirement of CO_2 monitoring initiative in these areas is highly recommended.

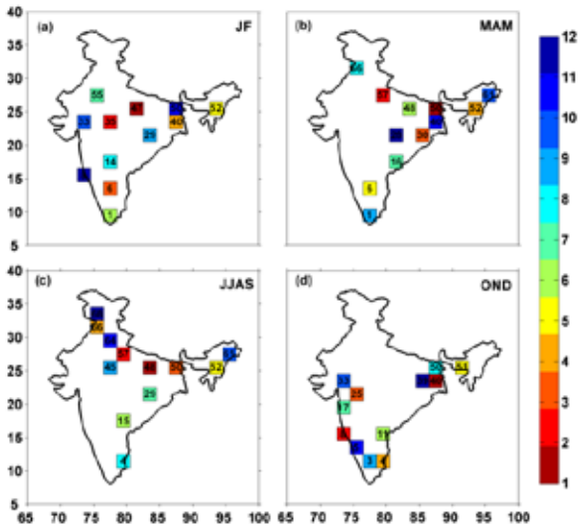

Figure 2: Location of optimized stations in the 'new network' for different seasons (a) winter (JF) (b) pre-monsoon (MAM) (c) monsoon (JJAS) and (d) post-monsoon (OND) (Nalini et al., Atmos. Env., 2019).

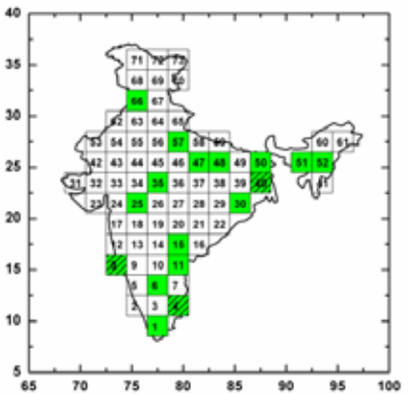

Figure 3: The optimal network developed for CO_2 measurements over India, proposed by this study. The hatched grids contain existing stations (Nalini et al., Atmos. Env., 2019).

Investigation on different aspects of the Indian Summer Monsoon

Existence of 'mini-break' like condition during early Indian monsoon onset years

A tendency of advancement of Indian summer monsoon onset over the Arabian Sea and Bay of Bengal (BoB)

Table 1: Uncertainty reduction (UR) and ranking for the existing stations in the 'base network' in terms of their ability to reduce the uncertainty of CO_2 flux for different seasons.

Rank	JF		MAM		JJAS		OND	
	Station	UR (%)	Station	UR (%)	Station	UR (%)	Station	UR (%)
1	Kharagpur	8.84	Kharagpur	6.29	Kharagpur	10.08	Kharagpur	12.72
2	Sagar	14.66	Kodaikanal	9.48	Sagar	15.2	Shadnagar	18.07
3	Kodaikanal	18.82	Sagar	11.98	Pondicherry	17.55	Pondicherry	22.48
4	Shadnagar	22.52	Shadnagar	14.13	Mount Abu	19.59	Sagar	25.94
5	Mount Abu	24.96	Pondicherry	15.29	Shadnagar	21.48	Mount Abu	28.88
6	Cape Rama	27.18	Cape Rama	16.57	Hanle	23.17	Cape Rama	31.61
7	Pondicherry	28.99	Sinhagad	17.19	Sinhagad	23.89	Sinhagad	33.75
8	Sinhagad	30.3	Mount Abu	17.79	Kodaikanal	24.5	Kodaikanal	35.75
9	Hanle	30.34	Hanle	17.94	Cape Rama	24.88	Hanle	35.98

Table 2: Uncertainty reduction (UR) and ranking for the "new network" in terms of their ability to reduce the uncertainty in CO_2 flux estimation for different seasons.

Rank	JF		MAM		JJAS		OND	
	Station	UR (%)	Station	UR (%)	Station	UR (%)	Station	UR (%)
1	STN_47	8.8	STN_50	7.4	STN_48	12.1	Kharagpur	9.92
2	STN_35	14.6	STN_57	11.9	STN_57	18.4	Cape Rama	19.24
3	STN_6	19.3	STN_30	16	STN_50	23.2	STN_25	24.8
4	Kharagpur	24	STN_52	19.9	STN_66	26.9	Pondicherry	29.95
5	STN_52	28.2	STN_6	23.7	STN_52	30.4	STN_51	33.96
6	STN_1	32.1	STN_48	26.2	STN_15	33.7	STN_11	37.45
7	STN_55	35.3	STN_16	28.7	STN_29	36.5	Sinhagad	40.46
8	Shadnagar	38.4	STN_66	31.1	Pondicherry	39.1	STN_50	43.36
9	STN_29	40.6	STN_1	33.4	STN_45	41.2	Kodaikanal	46.21
10	STN_33	42.8	STN_61	35.7	STN_61	43.1	STN_33	48.52
11	STN_50	44.9	Kharagpur	37.8	STN_64	45	STN_5	50.62
12	Cape Rama	46.9	STN_28	39.9	STN_68	46.7	STN_39	52.5

during recent period was revealed by observational and modelling studies. In this context, detailed examinations of early monsoon onset features were carried out. Data used for the study include daily wind and mean sea level pressure from ERA-Interim Reanalysis, daily precipitation data from Global Precipitation Climatology Project (GPCP) and TRMM Multisatellite Precipitation Analysis (TMPA), interpolated outgoing longwave radiation (OLR) data by the NOAA/ESRL and optimum interpolation daily sea surface temperature (SST) from NOAA. Details of normal and early monsoon onset years are given in Table 3. Comparison of precipitation between early and normal onset years showed an anomalous increase in precipitation over the BoB and west coast of peninsular India during the onset pentad (±2 days from the onset day) of early years (Fig. 4). It was also noticed that the monsoon low level jet (LLJ) became stronger, particularly over the southern peninsular India, during the onset period of early years. Even though the onset features such as precipitation and LLJ are more vigorous during early years, a considerable decrease in precipitation is observed after a week from the onset day (Fig.5). The LLJ show substantial reduction over the Indian region and convection over the eastern Arabian Sea and western India suppressed during this period which in turn inhibits the systematic northward propagation of monsoon convection. This induced a 'mini break' like condition immediately after a week from the onset day during early years. It was observed that SST over the north eastern Arabian Sea had a lower value during early years compared to normal years (Fig. 6). The reduced SST suppresses further enhancement of convection which results in precipitation decrease over the west coast of peninsular India.

The observed reduction in precipitation and weakening

Table 3: Early and normal onset years during the 1982-2016 period. Onset date for each year is represented in the bracket.

Normal Onset years	Early Onset Years
1982 (1 June), 1984 (31 May), 1985 (28 May), 1987 (2 June), 1989 (3 June), 1991 (2 June), 1993 (28 May), 1994 (28 May), 1996 (3 June), 1998 (2 June), 2000 (1 June), 2002 (29 May), 2007 (28 May), 2008 (31 May), 2010 (31 May), 2011 (29 May), 2013 (1 June)	1988 (26 May), 1990 (19 May), 1999 (25 May), 2001 (23 May), 2004 (18 May), 2006 (26 May), 2009 (23 May)

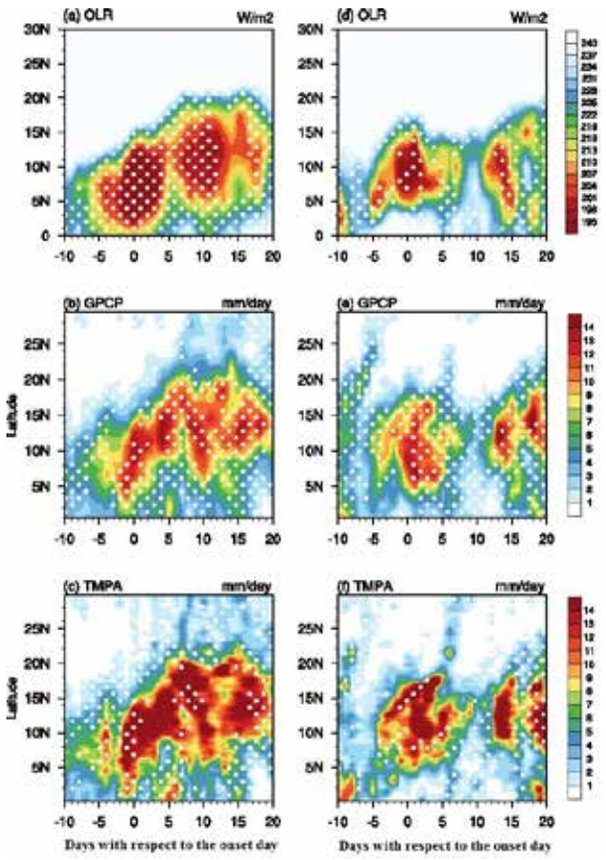

Figure 4: Latitude-time diagram of composites of OLR and precipitation averaged over the longitude band 65°-80°E during 10 days before and 20 days after the onset date of normal years (first column) and early years (second column). '0' in the x-axis represents the mean onset day. (a) and (d) from OLR, (b) and (e) from GPCP, and (c) and (f) TMPA. Dots represent the statistical significance. The unit of OLR is watts m^{-2} and precipitation is in mm day^{-1} (Aneesh and Sijikumar, Clim. Dyn. 2020).

of LLJ after a week from the onset day and the role of SST over the Arabian Sea was examined using numerical experiments with WRF model. Simulations were conducted for five normal years (2007, 2008, 2010, 2011 and 2013) and five early years (1999, 2001, 2004, 2006 and 2009). Three different sets of simulations were carried out to support the hypothesis. The first set consists of the control simulations with initial and lateral boundary conditions from the ERA-interim reanalysis data for all the normal and early years (CTRL). In the second set of simulations, SST over the north eastern Arabian Sea reduced up to 1.5°C, 4 days after the onset day during normal years and all other conditions were same as that of control simulations (COLD). The third set of simulations was for early years in which SST over the north eastern Arabian Sea enhanced up to 1.5°C, 4 days after the onset day of each year (WARM). Broad features of monsoon onset were well captured by control simulations. The sensitivity experiments with lower SST value during normal years could reduce precipitation over the eastern Arabian Sea and west coast of peninsular India after a week from the onset day. The LLJ also became weaker over the Arabian Sea and peninsular India in those simulations compared to that of control simulations (Fig. 7a). Whereas in the third set of simulations, when the SST enhanced over the north eastern Arabian Sea during early years, the precipitation over the west coast of peninsular India enhanced, the LLJ become stronger and the 'mini break' like situation disappears (Fig. 7b). This supports the hypothesis that the reduction of SST over the north eastern Arabian Sea has a prominent role in the precipitation reduction and weakening of LLJ after a week from the onset day.

Role of Intra-Seasonal Variability in the Indian Summer Monsoon on Hydration and Dehydration of the Upper Troposphere

Seven years of high resolution measurements of upper tropospheric humidity (UTH) from the Indian Geostationary satellite, Kalpana-1, MT- SAPHIR and water vapour mixing ratio MLS data are utilized to understand the hydration and dehydration process during the active and break phases of the Indian Summer Monsoon (ISM). Fig. 8a shows the seasonal (JJAS) mean UTH during 2010-2016. UTH is high (80-90 %) over the BoB, Indian Ocean and the west coast of the Indian region. Figs. 8b and 8c shows UTH anomaly during the active and break phases of the ISM respectively. Fig. 8b shows dryness over the northern part, east BoB and wetness over the southern parts and Western Ghats of the Indian region during the active phase. During the break (Fig. 8c), usually wetness is observed over the complete Indian region. UTH is also observed to be high over the South China Sea and also the western North Pacific, Southern BoB during both the phases of ISM. We have divided the Indian region into two sections (R1 (18°-28°N, 65°E-88°E) and R2 (8°-15°N, 65°E-88°E) based on the distribution of UTH. During the active

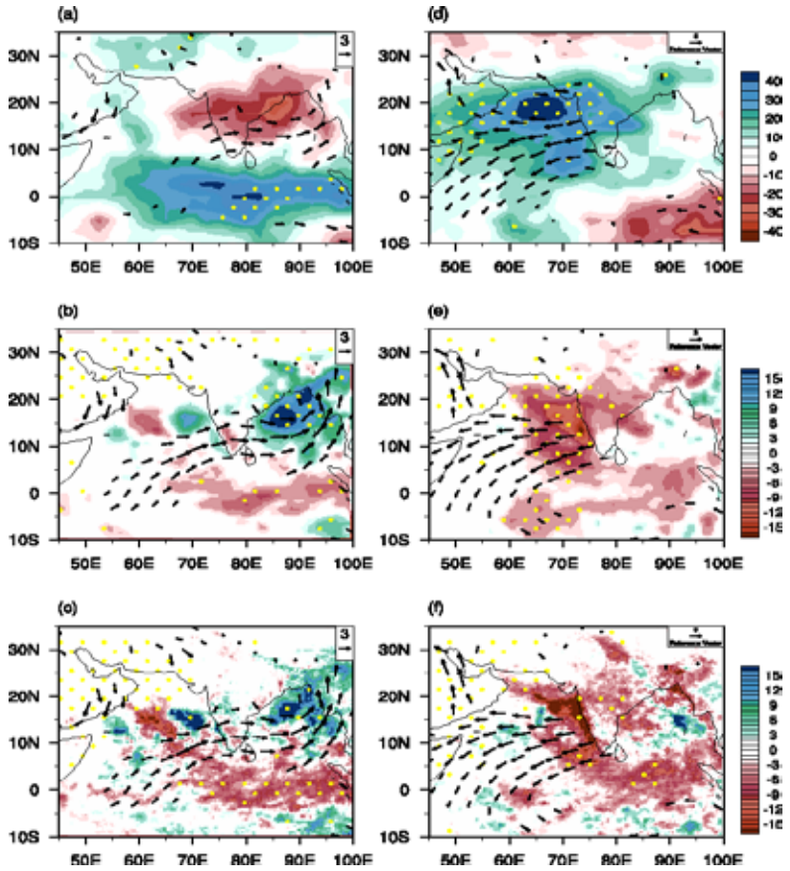

Figure 5: (a) shading shows the difference in composite mean OLR averaged during the onset pentad consists of ±2 days from onset date between early years and normal years. Arrows represent corresponding difference in the wind at 850 hPa level (only statistically significant winds are shown). (b) same as (a) but for the pentad consists of 8 to 12 days after onset date. (b) and (e) are same as (a) and (b) but from GPCP data. (c) and (f) are same as (a) and (b) but from TMPA data. Doted area represent the statistical significance of the difference in precipitation (above 90%). The unit of precipitation is mm day^{-1}, OLR is watt m^{-2} and wind is ms^{-1} (Aneesh and Sijikumar, Clim. Dyn. 2020).

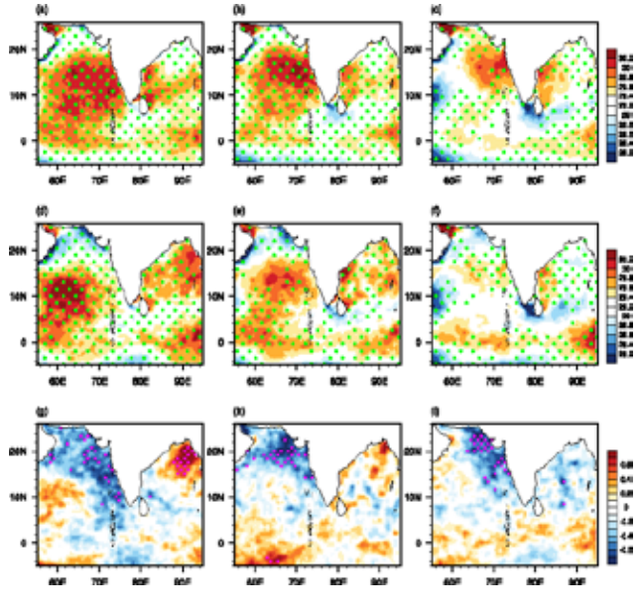

Figure 6: (a) Composite mean of SST averaged during the pentad corresponding to 4-8 days before the onset in normal years. (b) composite mean of SST averaged during the onset pentad (±2 days from onset) of normal years (c) composite mean of SST averaged during the pentad corresponding to 4-8 days after the onset. (d), (e) and (f) and same as (a), (b) and (c) but for corresponding pentads of early onset years. (g), (h) and (i) are the difference between the composite mean SST in early and normal onset year averaged during the pentad 4 to 8 days before the onset, ±2 days from onset and 4 to 8 days after the onset. Dots represent statistically significant regions. The unit is in °C (Aneesh and Sijikumar, Clim. Dyn. 2020).

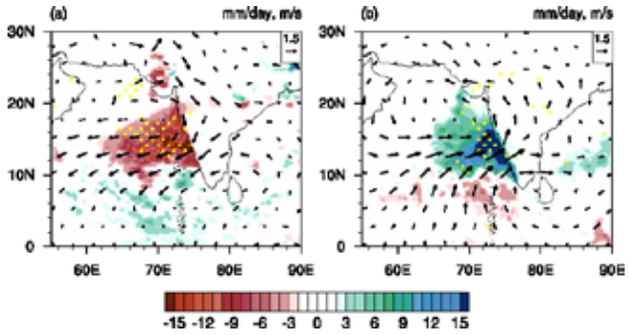

Figure 7: Difference between composite mean of sensitivity and control simulation precipitation (shading) and wind at 850 hPa level (arrows) averaged during 8 to 12 days after the onset day. (a) between COLD and CTRL simulations (b) between WARM and CTRL simulations. Doted areas represent where precipitation difference is statistically significant. The unit of precipitation is mm day^{-1} and wind is ms^{-1} (Aneesh and Sijikumar, Clim. Dyn. 2020).

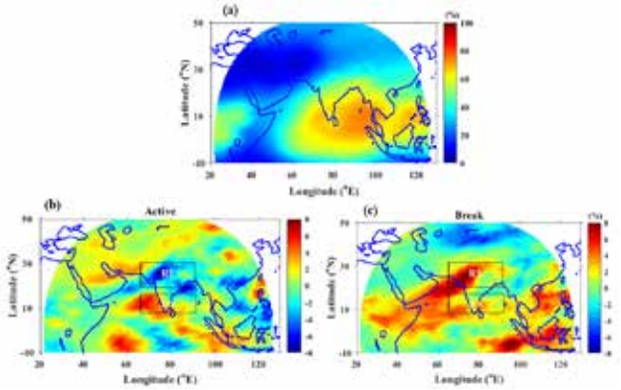

Figure 8: (a) Seasonal mean of the UTH from June to September (ISM) obtained from Kalpana. (b) Anomaly of the UTH during the active phase of ISM (c) same as b but during the break phase of ISM (Uma et al., Theoretical and Applied Climatology (2020)

phase, the R1 region is dry, and R2 is wet. During the break phase, large positive UTH anomalies are seen over the Indian region and surrounding oceanic regions (Fig. 8c). Regions R1 and R2 show the wet troposphere during the break phase. From Figs. 8b and 8c, it appears that during the active phase, ISM contributes to dryness and during the break phase to wetness. We have analyzed the humidity from MT-SAPHIR for the period 2012-2016 during JJAS. For the present study we have used 400-250 and 250-100 hPa. It shows that during the active phase (Figs. 9a-9b), the UTH is dry and during the break phase (Figs. 9c-9d) it is wet at all the layers over the core monsoon region R1 supporting Kalpana-1 observations. The water vapour mixing ratio (WMR) from Aura-MLS measurements is used. Fig. 10a-10c shows the WMR anomaly at 215, 177, and 147 hPa respectively for the active phase and 10d-10f shows the WMR anomaly for the break phase of monsoon.

The region R1 shows low WMR during the active phase and high during the break phase at all the pressure levels considered in this work. The region R2 shows high WMR during the break phase of ISM.

A well-defined area of upper-level divergence (Fig. 11a) of the order of $3 \times 10^{-5}\,s^{-1}$ over the region R1, BoB, and central Indian regions during the active and on contrary, the intense convergence at 200 hPa over both the regions R1 and R2 is observed. The active phase (Fig. 11c) is dominated by strong updrafts in the troposphere over the region R1 and the head BoB and downdrafts in the region R2. The break phase is dominated by downdrafts in both the regions R1 and R2. The temperature anomaly shows warm condition during the active (Fig. 11e) and cold during the break phase of ISM over R1 and vice versa over the equatorial Indian Ocean. The presence of warm anomalies at around 300 hPa level in R1 is a signature of the presence of deep convection

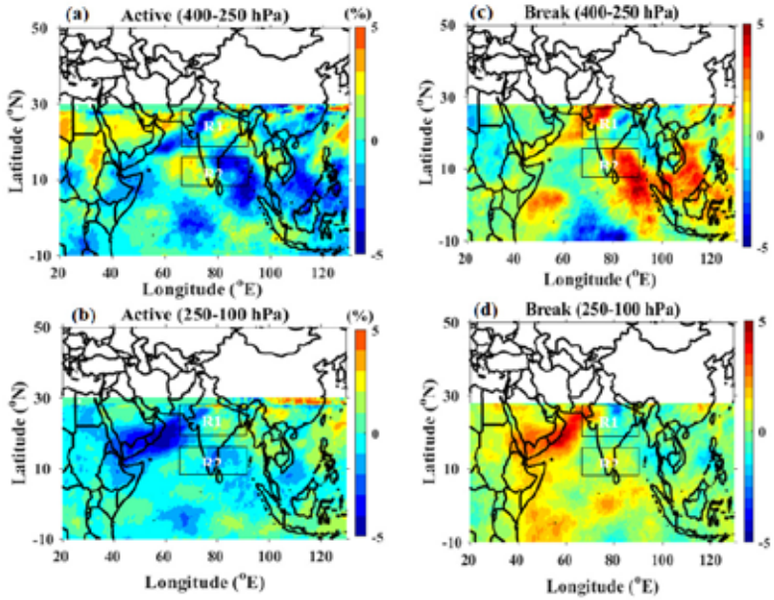

Figure 9: Relative humidity obtained from MT-SAPHIR at (a) 400–250 hPa and (b) 250–100 hPa for active phase. (c) and (d) are similar to (a) and (b) but during the break phase (Uma et al., Theoretical and Applied Climatology (2020)

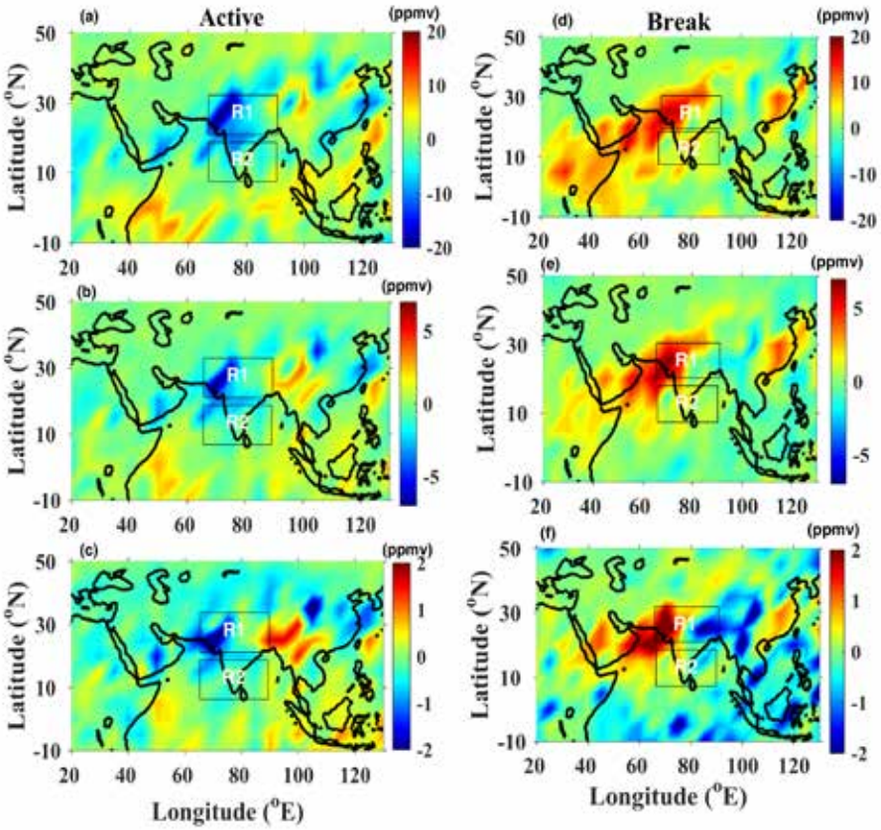

Figure 10: MLS water vapour mixing ratio (a-c) during Active (Left Panel) and (d-f) Break (Right Panel) at 215, 171 and 147 hPa respectively (Uma et al., Theoretical and Applied Climatology (2020)

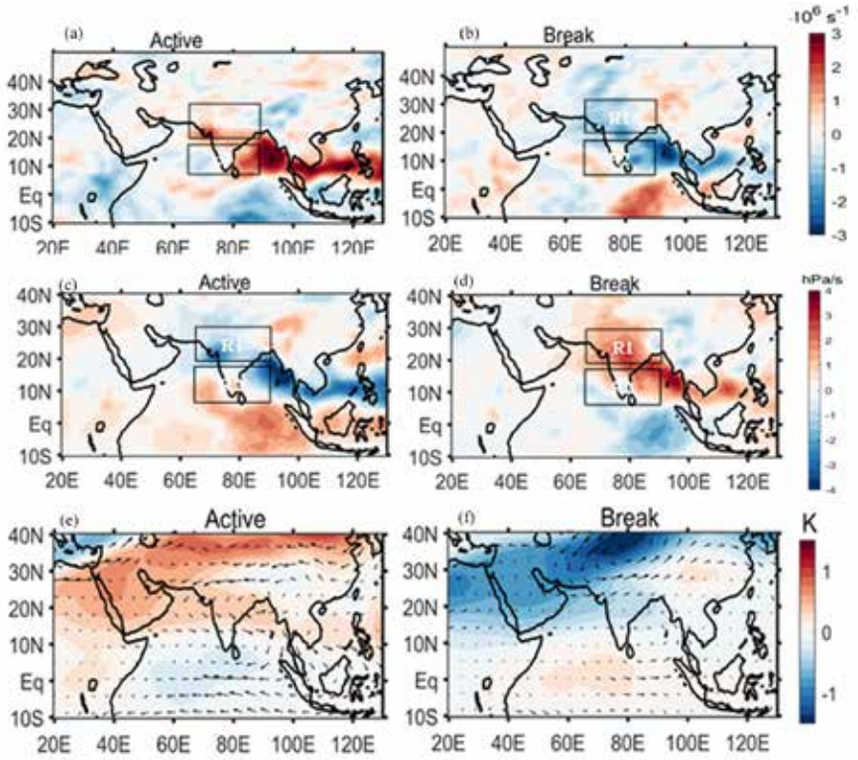

Figure 11: Spatial composites of divergence (in s^{-1}) components during active (a) at 200 hPa, (b) during break, (c) and (d) are for omega at 300 hPa and (e) and (f) are for temperature along with winds at 300 hPa (Uma et al., Theoretical and Applied Climatology (2020)

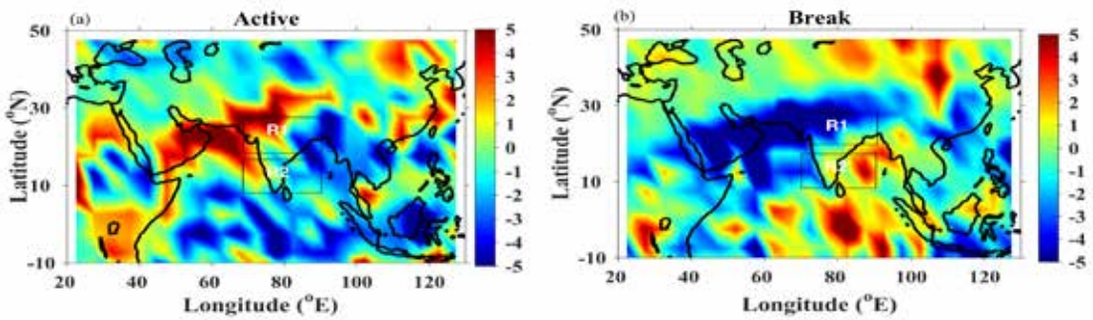

Figure 12: (a) Anomaly of cirrus between 8 and 12 km during active and (b) during break.

due to latent heat release which corroborates the finding of dryness in the upper troposphere in the region R1 that is observed during the active phase.

Figure 12a-b shows the anomalies of cirrus during active (left panel) and break (right panel), respectively During the active phase, the cirrus is observed to be high over the region R1 compared to the break phase over the active monsoon region of India. The occurrence is comparatively high over the region R2 during active and high during the break. This clearly shows that cirrus is high over the core monsoon region R1 during the active compared to that of the break phase. This cirrus can play a major role in the dehydration of the troposphere during the active phase.

Atmospheric Modelling Support to the Launch Vehicle Activities

Development of the Revised Indian Atmospheric Model

The atmospheric model at any location is an altitude variation of temperature, pressure and density. In our operational and developmental programmes atmosphere parameters are required for various launch vehicle applications. On the other hand, with respect to the scientific aspect, the long-term characteristics of temperature, density and winds are required to understand the atmospheric wave characteristics and its propagation. Even though a few models exist for the above applications over the Indian region, a need is felt to revamp and regenerate the model to accommodate the appropriate temporal variability and dispersions of these parameters over a course of time. The focus of the present revised model is to look into the variability on monthly as well as on an annual scale using significantly large number of observations. Therefore, the revised model utilizes data from different platforms in order to provide a robust mean and bounds for the temperature, pressure and density for launch vehicle applications. The model utilizes radiosonde observations from 1975 to 2018 (25602 profiles from Chennai), M-100 data from 1971-1991 (836 profiles from Thumba), Satellite data from 2002-2018 (1468 profiles over SHAR) and MSIS (66480 profiles over SHAR) from 1975-2018 to construct the mean profile and 3-sigma bounds of temperature, pressure and density from surface to 1000 km. Using the above profiles, the model also provides a methodology to sequentially generate any required number atmospheric profiles through a Monte Carlo process, preserving their associated statistical correlations properties. The model also discusses the impact of the dispersions in the trajectory design process, dynamic pressure, heat flux and heat load for PSLV, GSLV and GSLV-MK III.

Figure 13 shows the difference between the revised and previous models up to an altitude of 25 km. The temperature deviation is observed to be higher in the present analysis compared to Sasi and Sengupta (1986) and ERA-interim reanalysis. The dispersion calculated in the figure is 3σ for present analysis and ERA-interim reanalysis. The corresponding pressure and density deviation is also observed to be more in the radiosonde compared to the other two. In-fact the deviation is two times higher than that reported by Sasi and Sengupta (1986) and ERA-interim reanalysis. For the altitude region between 25 and 110 km, we used M-100 and SABER satellite data. The comparison between the two (Fig. 14) agrees well and shows that we

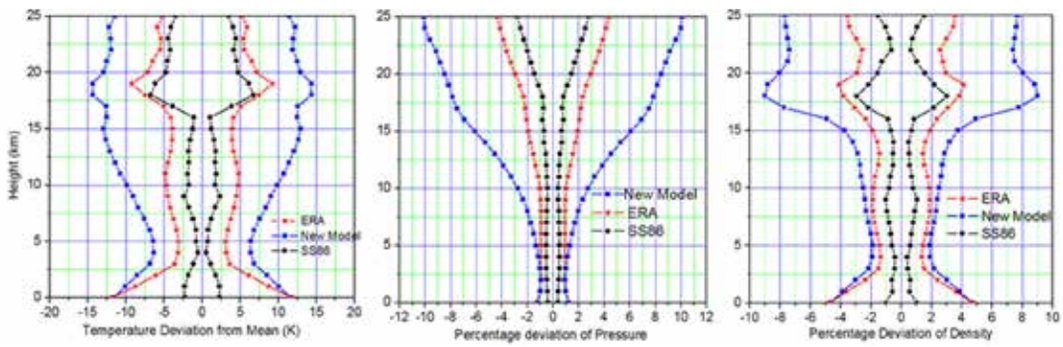

Figure 13: Percentage deviation in Temperature Pressure and Density between present analysis over New model, SS86 and ERA-interim Reanalysis.

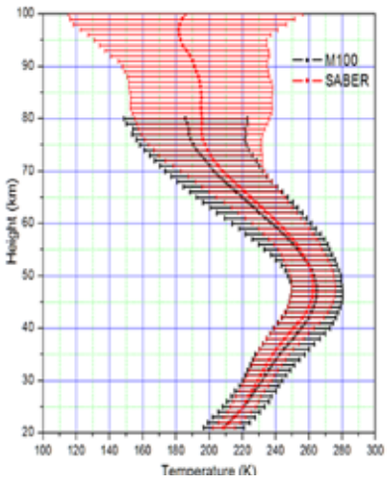

Figure 14: Comparison of temperature between M-100 and SABER

can utilize SABER over SHAR. The combined monthly mean of temperature, pressure and density is obtained by combining both M-100 and SABER. The temperature obtained from surface to 110 km is merged with MSIS up to 1000 km (Fig. 15).

Weather Prediction support to the PSLV and GSLV Launch Vehicle campaigns

The NAM branch of SPL is one of the team-members is the Inter-Centre Weather Forecast Expert Team of ISRO constituted by Satish Dhawan Space Centre, Sriharikota. As part of the operational activities with the aid of COSMO (**Consortium for Small-scale Modelling**) regional NWP model, short-range weather predictions are carried out for a domain centered around the SHAR region during the launch campaigns. The onus of these operational predictions is to provide a precise weather outlook and its trends over Sriharikota during the PSLV / GSLV launch campaigns. Since Chandrayaan-1 mission, SPL is actively participating in all launch campaigns by providing the short-range weather predictions through COSMO. During the review period, weather prediction support was extended to all the PSLV and GSLV missions undertaken from Sriharikota.

New Initiative

First and unique experiment on Unmanned Aerial Vehicle (UAV) for studying the variability of CO_2 in the boundary layer

In order to understand the variability of CO_2, GMP343 CO_2 sensor was procured and installed at SPL in July 2019. GMP343 carbo sensor (flow through type) is silicon based non-dispersive infrared sensor. It can measure in the range of 0- 1000 ppm with an accuracy of ±3 ppm+1% of reading. The sensor was validated with surface CO_2 analyzer. The sensor worked and compared well with the surface CO_2 analyzer and the difference is found to lie within ±2 ppmv. UAV developed by National Aerospace Laboratories (NAL) located at Bengaluru has been utilized to conduct the experiments of GMP343 carbo sensor. UAV can fly up to an altitude of 5 km and the payload weight it can carry is about 1 kg. In order to fit into the requirements of the UAV, the payload was integrated along with temperature, pressure and humidity sensor, GPS and WiFi sensor. The data recorded are time, date, latitude, longitude, pressure, temperature, humidity and CO_2. Test flight was conducted in October and UAV was flown at 100, 200, 300, 400 and 500 m.

Proposal on three dimensional structure of MCS

To investigate the three dimensional structure, intra and inter-seasonal variability of Mesoscale convective Systems during pre-monsoon, South-West and North East monsoon" a proposal submitted has been accepted at National Atmospheric Research Laboratory, Gadanki. The proposed investigation is expected to bring out the intra-seasonal and inter-seasonal variability of MCS, three dimensional structures and the background thermodynamics that control the formation and dissipation of storms using the new active phased array MST Radar.

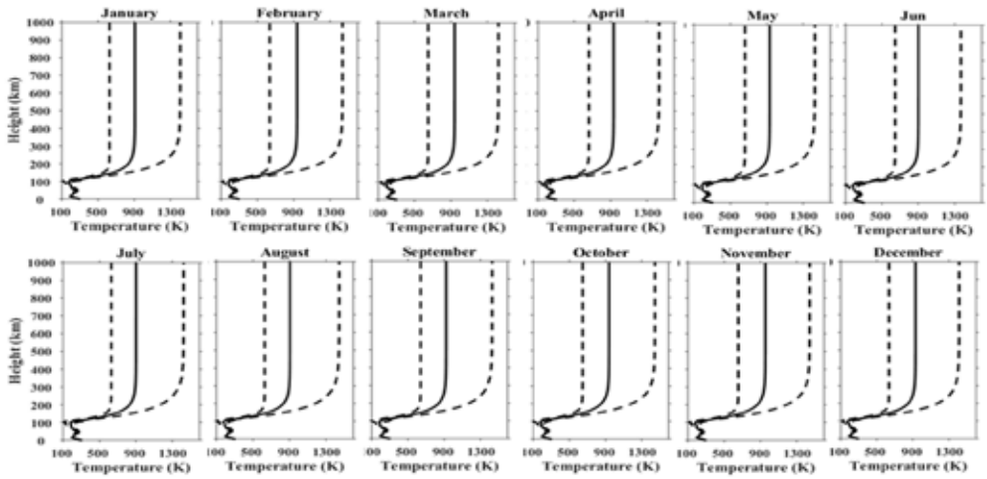

Figure 15: Temperature profile with 3 sigma dispersion from surface to 1000 km

Future Projections

- Impact of OCKHI Cyclonic Storm on the Vertical Structure of Marine Atmospheric Boundary Layer and Coastal Sea-Breeze Circulation
- Sensitivity of the COSMO model's grid resolution to the convection parametrization scheme
- Assessment of the PALM model simulations for understanding the treatment of convection in LES models
- The evolution, dynamics and microphysics of mesoscale convective systems using Active phased MST radar, Doppler weather radar and modeling.

Publications in Peer-Reviewed Journals

1. Aneesh, S., S. Sijikumar, "Existence of 'mini-break' like condition during early Indian monsoon onset years" Climate Dynamics, 54, 2403 – 2418, *DOI: 10.1007/s00382-020-05121-9, (2020).*
2. Das, S. S., K. V. Suneeth, M. V. Ratnam, K. N. Uma, M. Durga Rao and A. Narendra Babu, "Long-term observations of stratosphere-troposphere exchange using MST Radar and Aura MLS measurements over a tropical station Gadanki", Radio Science, *DOI: 10.1029/2019RS006969, (2020).*
3. Nalini, K., S. Sijikumar, Vinu Valsala, Yogesh K. Tiwari, Radhika Ramachandran, "Designing surface CO2 monitoring network to constrain the Indian land fluxes", Atmospheric Environment, 218, 117003, *DOI: 10.1016/j.atmosenv.2019.117003, (2019).*
4. Uma, K. N., T. S. Mohan, and S. K. Das, "Role of Intra-Seasonal Variability in the Indian Summer Monsoon on the Hydration and Dehydration of the Upper Troposphere". Theoretical and Applied Climatology, 141, 747 – 761, *DOI: 10.1007/s00704-020-03243-y, (2020).*

Scientific Reports

1. K. N. Uma, V. Adimurthy and Radhika Ramachandran, (2020), Review on the existing models and the need for the development of new model, ISRO-VSSC-TR-0020-0-20
2. K. N. Uma, and Radhika Ramachandran, (2020), Revised Atmospheric Model from surface to 25 km, ISRO-VSSC-TR-0020-0-20.
3. K. N. Uma, and Radhika Ramachandran, (2020), Revised Atmospheric Model from 25 to 110 km using In-situ and Satellite measurements, ISRO-VSSC-TR-0024-0-20.
4. T. K. Pant, K. N. Uma, and Radhika Ramachandran, (2020), Revised Model from 110 to 1000 km- MSIS Perspective, ISRO-VSSC-TR-0025-0-20.
5. K. N. Uma, T. K. Pant, and Radhika Ramachandran, (2020), Combined Temperature model from Surface to 1000 km, ISRO-VSSC-TR-0032-0-20.
6. K. N. Uma, and Radhika Ramachandran, (2020), A New Empirical model from Surface to 110 km using in-situ and space based observations taking into account the tropical oscillations, ISRO-VSSC-TR-0033-0-20.
7. Report of the Committee for Generation of Revised Indian Atmospheric Model, 2020, ISRO-VSSC-SP-0089-0-20.

Presentation in Symposia/Conference/Workshops

1. Bala Subrahamanyam D., "From Reynolds Averaged Navier-Stokes (RANS) Models to the Large Eddy Simulation (LES): An Assessment of the importance of Urban Climate Elements", National Workshop on Urban Climate Network, ICWaR, IISc, Benguluru, August 02 – 03, 2019.
2. Uma, K. N., R. Ramachandran, M. V. Ratnam and S. B. Thampi, "Evolution, structure and dynamics of tropical cyclone using Doppler weather radar and MST radar", TROPMET-2019, Andhra University, Vishakhapatinam, December 10-14, 2019. [Lead Talk]
3. Uma, K. N., R. Ramachandran, M. V. Ratnam and S. B. Thampi, "Dynamics of Thane and Nilam using Doppler weather radar", IRAD-2020, IIT, Chennai, February 05-08, 2020.

Invited/Plenary Talks

Radhika Ramachandran

1. "Climate and Environmental Sciences Activities at SPL", NICES Meeting organized by NRSC, DOS Branch Secretariat, New Delhi, August 2019.
2. "Estimation of the atmospheric carbon dioxide emission over the Indian region for Scientists and Policy makers", Planetary Talk, URSI Regional Conference on Radio Science, (URSI-RCRS 2020), IIT BHU, Varanasi, February 12-14, 2020.

Atmospheric Dynamics Branch

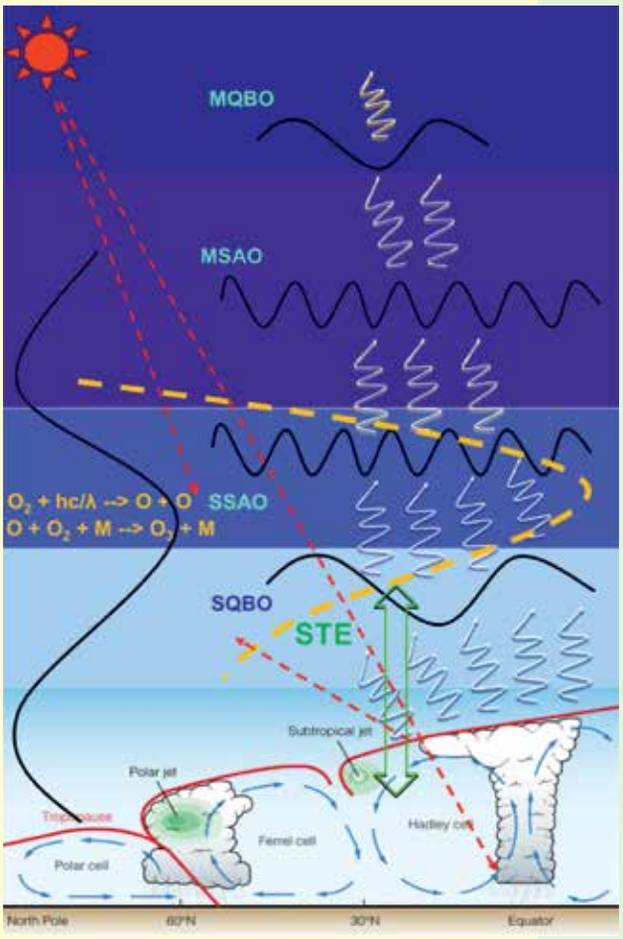

Atmospheric Dynamics Branch is carrying out front line research on atmospheric processes responsible for altering the motion of the Earth's atmosphere, right from the ground to mesosphere-lower thermosphere. With this broad objective, the research activities are aimed at quantifying the atmospheric motion spectra from gravity waves (few minutes) to solar cycle (11 years) using ground and space based observations and to quantify the various aspects of atmospheric waves such as source mechanism, propagation characteristics, role in atmosphere coupling, short and long-term variability and their representation or parameterization in global models. Apart from the studies on waves and oscillations, the branch focuses on the tropical tropopause dynamics and associated stratosphere-troposphere exchange processes making use of simultaneous measurement of wind, temperature, ozone and water vapour. As a part of SPL's Polar research program, the branch has initiated experimental campaigns at Bharati station in Antarctica, focusing on high latitude–low latitude coupling processes. Recently, the horizon is expanded by initiating the studies under the realms of cloud and climate dynamics, which is getting strengthened year after year.

Science Team

Geetha Ramkumar*
Kishore Kumar K.
Siddarth Shankar Das
Sunilkumar S.V.
Venkata Subrahmanyam K.
Jayadev Pradeep

Technical Team

Manikantan Nair
Mohammad Nazeer M.

Research Associates

Suneeth K.V.
Vishnu R.
Pramitha M.&
Maria Emmanuel#
Kousik N.#

Research Fellows

Satheesh Chandran P.R.
Anjana U.&
Venus V.&

* Retired in February 2020
\# Joined in June 2020
& Joined in December 2019

Middle Atmospheric Dynamics

Meteor Radar Estimations of Gravity Wave Momentum Fluxes in the Mesosphere- Lower Thermosphere: Evaluation Using Simulations and Observations

Meteor radars provide hourly zonal and meridional wind observations round the clock in 80-100 km height domain known as mesosphere- lower thermosphere (MLT) region. These wind observations can be employed to estimate gravity wave (GW) momentum fluxes. The present study evaluated the meteor radar observations of GW momentum fluxes over Thumba [8.5°N, 77°E (2006-2015)], Kototabang [0.2°S, 100.3°E (2002-2017)] and Tirupati [13.63°N, 79.4°E (2013-2018)] using three-dimensional wind field simulations, which include specified tidal, planetary and GW fields. Meteor radar measurements of zenith and azimuth angles of detected meteor trails are used to sample the simulated wind field. Six test cases are formulated to verify the algorithm by changing the vertical as well as spatio-temporal structure of mean winds, tides and GWs. The retrieved wind, tidal and GW fields are compared with those used for the simulations.

The results for a test case with mean winds [zonal (U_M):10 $ms^{-1}$and meridional (V_M) 5 ms^{-1}], diurnal tides [zonal (U_D): 40 ms^{-1} and meridional (V_D): 40 ms^{-1} with vertical wavelength of 25 km], semi diurnal tides [zonal (U_{SD}): 10 ms^{-1} and meridional (V_{SD}): 10 ms^{-1} with vertical wavelength of 50 km] and gravity waves [u'w': -75 m^2s^{-2} and v'w': 30 m^2s^{-2} with four sets of gravity waves having periods 20 min, 30 min, 2.5 hr and 3 hrs and various combinations of vertical and horizontal wavelengths] are shown in Fig.1. From this Fig., it is clear that simulated and retrieved winds and tides are agreeing very well over Thumba and Tirupati whereas over Kototabang some deviations are observed between the two, which can be attributed to less number of meteors detections by this radar. GW momentum fluxes in zonal and meridional directions show a variation of 1% and 3%, respectively at maximum echo height (~90 km) over Tirupati, 2% and 3% over Thumba and 10% and 6% over Kototabang. Over all heights, variation is within 12% over Thumba and Tirupati, where relatively good agreement is found between simulated and retrieved GW momentum fluxes.

It is noted that the algorithm successfully retrieved all the specified wind fields, which confirms the applicability of meteor radar observations in estimating the GW momentum fluxes. These are the first such simulations carried out over the Indian region to evaluate the efficacy of meteor radars in estimating GW momentum fluxes. Further, mean annual cycle of GW momentum fluxes is constructed over the three radar locations as shown in Fig. 2. The height-month sections of GW momentum fluxes in zonal and meridional directions exhibited semi-annual oscillations below 90 km and annual oscillations above this altitude with varying vertical structures. There are a few discrepancies in the annual cycle of zonal momentum fluxes especially in the vertical structure over Tirupati and Thumba. The observed vertical structure as well as annul cycle of meridional GW momentum fluxes over the three radar sites do not show

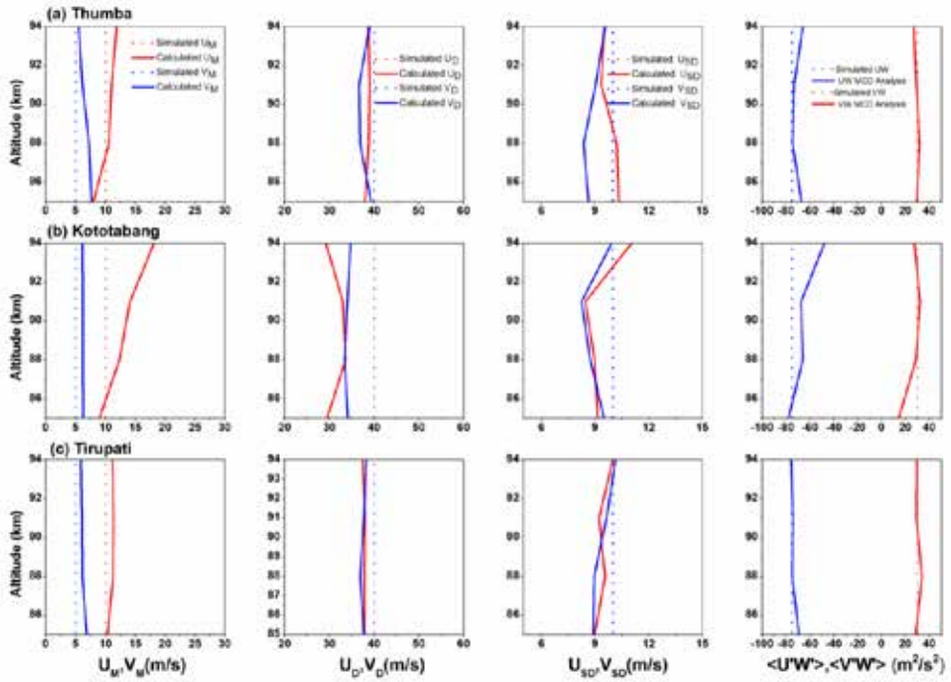

Figure 1. Monthly mean profiles of simulated (dashed) and retrieved (solid) mean winds (first column), diurnal tide (second column), semi-diurnal tide (third column) and GW momentum fluxes (fourth column) over (a) Thumba, (b) Kototabang and (c) Tirupati. In all the plots blue colour represents zonal and red colour represents meridional components [Pramitha et al., Journal of Geophysical Research: Space Physics, 2019]

much similarities. It is to be noted that the duration of observations used to construct the mean annual cycle varies from one location to another. It is envisaged that the meteor radar estimations of GW momentum fluxes can be used to verify the gravity wave ray tracing algorithms.

Planetary Waves in the Mesosphere Lower Thermosphere during Stratospheric Sudden Warming: Observations using a network of meteor radars from high to equatorial latitudes

The characteristics of mean winds and planetary waves in the mesosphere lower thermosphere (MLT) region during sudden stratospheric warming (SSW) events using observations from four meteor wind radars located at high, middle, low and equatorial latitudes are investigated. The response of the respective MLT regions to three SSW events that occurred during 2008-09, 2009-10 and 2011-12 winters are studied in detail. Fig. 3 shows the climatology of zonal winds over the four observational sites in terms of height – month sections. Black contours represent zero wind lines. It can be seen that over Andenes, the mean zonal wind is characterized by a weak eastward flow during winter at all heights. During summer months (June-August) the zonal flow is strongly westward below

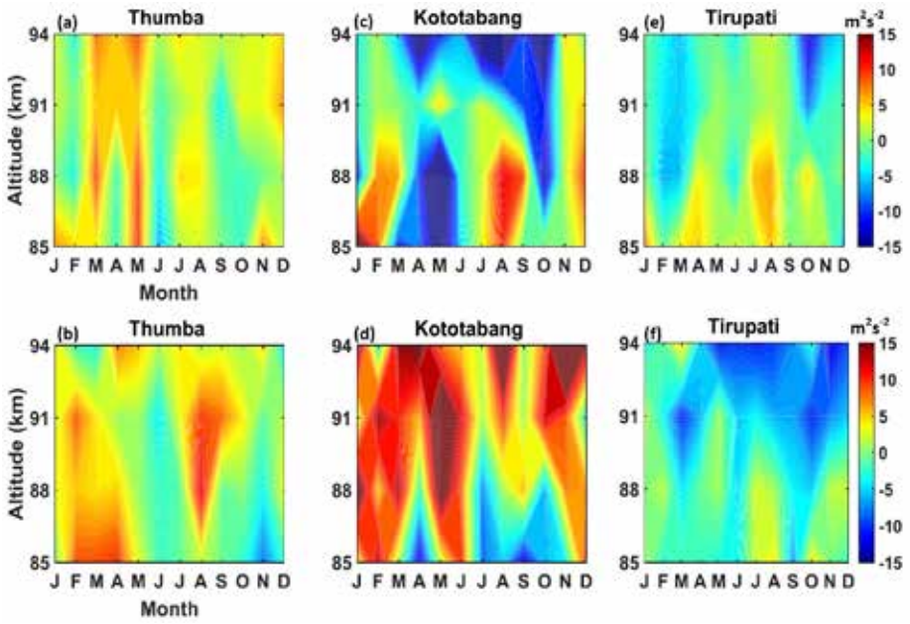

Figure 2: Height-month section of mean zonal (top panel) and meridional (bottom panel) GW momentum fluxes over (a, b) Thumba, (c, d) Kototabang and (e, f) Tirupati [Pramitha et al., Journal of Geophysical Research: Space Physics, 2019]

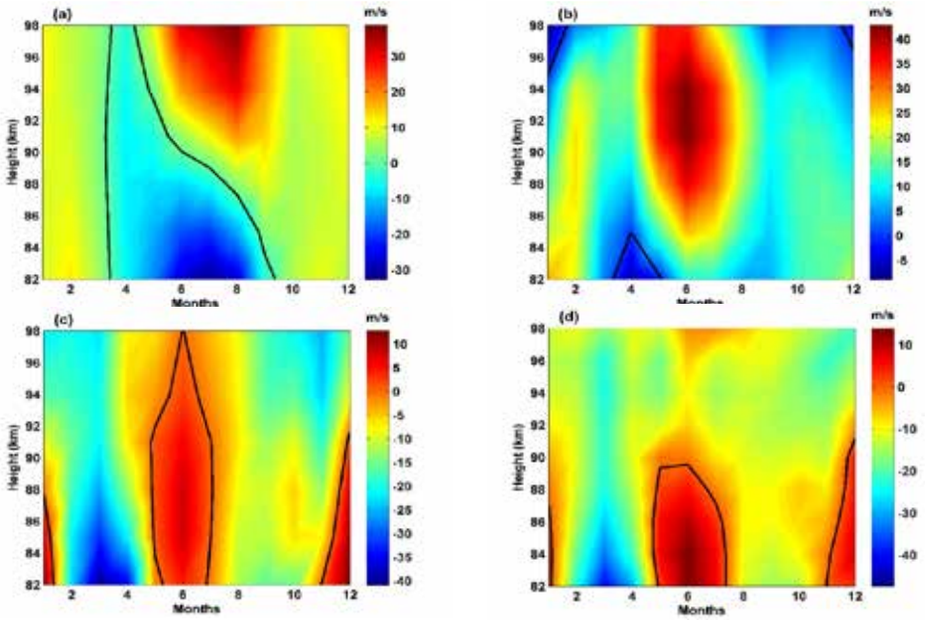

Figure 3. Monthly mean zonal winds in the MLT region over (a) Andenes, (b) Socorro, (c) Thumba and (d) Kototabang [Koushik et al., Climate Dynamics, 2020]

90 km. It can be noted that there is a strong eastward jet near the mesopause region (>90 km) during the summer months. Zonal winds over the midlatitude location Socorro also show a strong eastward flow in the 86-98 km height region during summer months. Weak westward winds prevail below 86 km from March to May and above 94 km during December-January months. Over the low latitude and equatorial stations Thumba and Kototabang zonal winds show a strong semiannual oscillation primarily below 90 km and an annual cycle in the 90-100 km height region.

Apart from mean winds, planetary wave activity in the MLT region over the observational sites are also examined, which show a systematic progression of planetary waves from high to equatorial latitudes during major as well as minor SSW events. To elucidate the origin of the observed planetary waves in the MLT region, the stratospheric winds are analyzed. Fig. 4 (e-h) depicts the zonal winds in the 100-1 hPa pressure levels over the nearest geographical locations of four observational sites obtained from ERA-Interim Reanalysis Dataset during the 2008-09 winter. Bottom panel gives the wavelet spectrum of zonal winds at 1hPa. From Fig. 4a it can be seen that there are enhancements of wavelet amplitudes near 4-6 day periodicities close to day 10 and 6-8 day periodicities close to day 50 over the high latitude location Andenes. A ~20 day period wave also can be noted from this figure before the central day. At the same time at 1hPa, ~20 day and ~6-8 day periodicities enhance near the central day. From Fig. 4b, it is evident that there are two distinct peaks in wavelet amplitudes at 88 km over Socorro, one with 4-6 day periodicity almost coinciding with the wind reversal and another one with ~10 day periodicity peaking around day 65, approximately 10 days after the central day. On closer examination, it can be identified that the 4-6 day periodicity appears to propagate from the stratopause region whereas the ~10 day periodicity is not present in the stratosphere. Over low and equatorial latitude stations Thumba and Kototabang, 6-10 day periodicities enhance after the central day. It should be noted that there is a marked time delay in the occurrence of the peaks over these two locations compared to that over Socorro. It follows from these features that the enhancements observed over Thumba and Kototabang are not propagating from below. Results thus suggest that the observed planetary waves have originated in the high-middle latitude mesosphere/MLT regions. The present study provides observational evidence for secondary planetary wave generation in the high-middle latitude mesosphere/MLT regions and their equatorial propagation as predicted by previous numerical modelling studies. Significance of the present study lies in employing a network of meteor radar observations to investigate the SSW signatures in the MLT region over high, middle, low and equatorial latitudes, simultaneously.

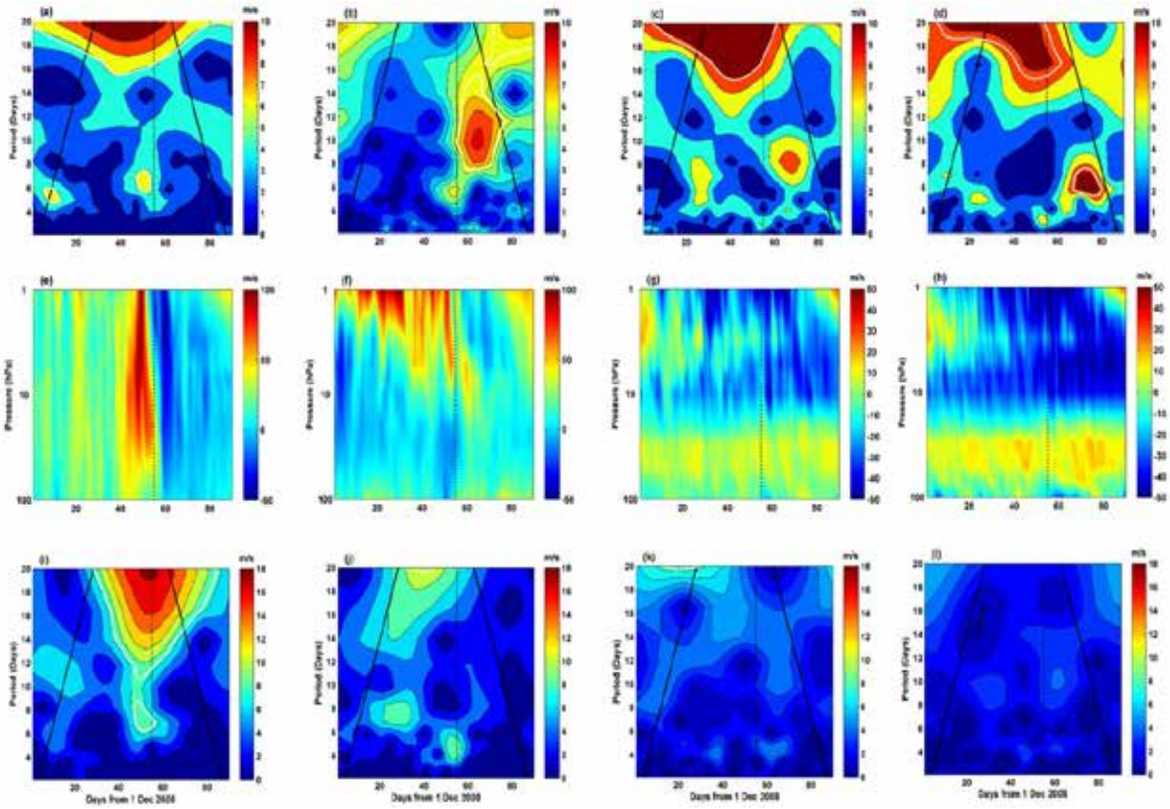

Figure 4. Wavelet spectra of zonal winds at 88 km over (a) Andenes, (b) Socorro, (c) Thumba and (d) Kototabang, the corresponding stratospheric winds over (e) Andenes, (f) Socorro, (g) Thumba and (h) Kototabang, and wavelet spectra of zonal winds at 1hPa over (i) Andenes, (j) Socorro, (k) Thumba and (l) Kototabang for 2008-09 winter [Koushik et al., Climate Dynamics, 2020].

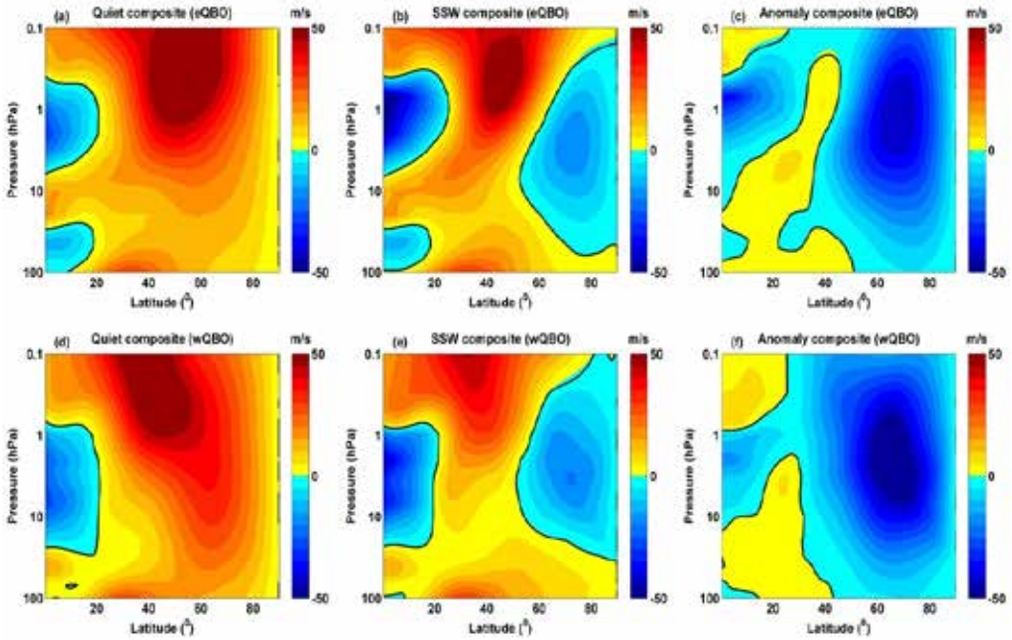

Figure 5. Latitude-pressure composites of zonal mean zonal winds derived from MERRA reanlysis datasets for SSW events during (top) Eastward QBO and (bottom) Westward QBO: (left) Quiet composite, (middle) SSW composite and (right) Anomaly composite during the years 2001-2019 [Koushik et al., Geophysical Research Letters, 2020].

Westward Acceleration of Tropical Stratopause Zonal Winds during Major Sudden Stratospheric Warming Events

SSW events are observed to affect mesospheric winds, tides and several ionospheric parameters over low and equatorial latitudes. Even though there are evidences focusing on low latitude stratospheric signatures of SSW events, very few of them have addressed the dynamical changes in this region by employing model simulations and reanalysis datasets. In this regard, using reanalysis datasets, rocketsonde observations and 'specified dynamics- whole atmosphere community climate model' (SD-WACCM) simulations, the present study reports in-situ observational evidence for westward acceleration of tropical stratopause zonal winds during major SSW events for the first time.

Latitude-pressure sections of composites of zonal mean zonal winds from MERRA-2 during boreal winters (December-February) for the (top) eastward and (bottom) westward phases of the Quasi Biennial Oscillation (QBO) are depicted in Fig. 5. Composites shown in this Fig. 5 are constructed from five and three SSW events, respectively for eastward and westward phases of the QBO. Bold lines in left and middle panel indicate zero wind line whereas those in right panels demarcate the regions with positive

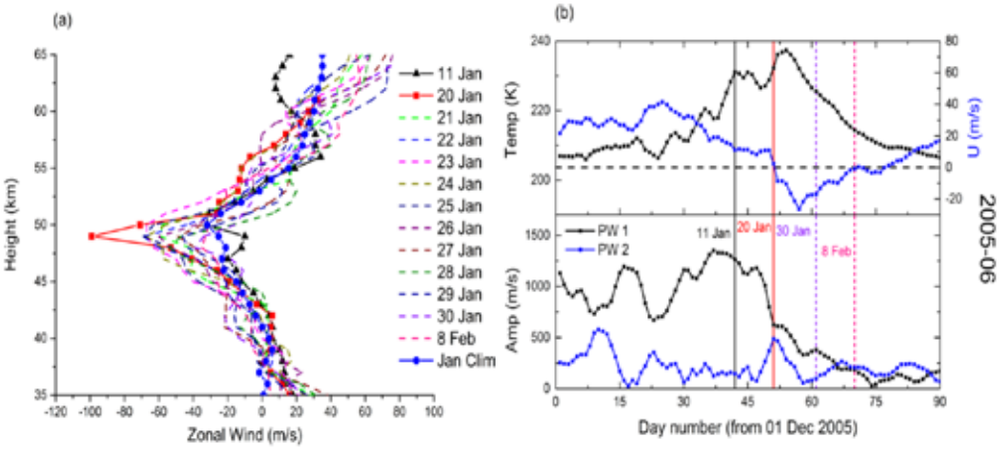

Figure 6. (a) Vertical profiles of zonal winds derived using rocketsonde measurements over Thumba from 11 Jan to 8 Feb 2006. Blue solid line with circles represents the climatological mean profile. (b) Polar stratospheric parameters derived from MERRA reanalysis datasets during 2005-06: (top) Zonal mean temperature in the polar cap at 10hPa (black) and zonal mean zonal wind (blue) at 60°N, 10hPa. (bottom) Amplitude of wavenumber 1 planetary wave (black) and wavenumber 2 planetary wave (blue). Vertical lines indicate the days corresponding to the rocket profiles[Koushik et al., Geophysical Research Letters, 2020].

and negative anomalies. The strong negative anomalies poleward of 50°N seen in the anomaly composites are associated with the well-known wind reversals due to SSW. The most interesting feature in the anomaly composites is the westward anomaly seen at the tropical upper stratosphere –lower mesosphere (10hPa- 0.1hPa). This feature is seen irrespective of the phase of the QBO. Apart from the westward anomaly around the stratopause, a minor eastward anomaly can also be noted around the 0.1hPa level in both the cases.

To seek further insights into the enhanced westward winds in the tropical upper stratosphere, rocket observations from Thumba during the 2005-06 SSW events are employed. During this event, a series of rockets with one day interval were launched to measure the winds in the 20-65 km altitude. The vertical profiles of zonal wind over Thumba during this event and the climatological profile obtained from 5 years of rocket observations in January (blue solid line) are depicted in Fig. 6a. Top panel of Fig. 6b depicts the mean polar cap temperature at 10hPa (black line) and zonal mean zonal wind at 60°N, 10hPa (blue line). The bottom panel in Fig. 6b shows the amplitudes of wave number 1 (black) and 2 (blue) planetary waves at 60°N, 10 hPa respectively. Vertical lines in Fig. 6b are used to examine the state of the polar stratosphere on days corresponding to the rocket launches. The campaign period spanned from 20 January to 30 January with daily launches. The profiles corresponding to 11 January and 08 February are part of regular fortnightly observations from the station. It can be seen that during the SSW period, zonal winds in the upper stratosphere over Thumba are significantly westward, both compared to the climatological profile as well as the non-warming day profile (11 January). Maximum westward winds (-99 m/s) were observed on 20 January, one day before the reversal of zonal winds at 60°N, 10 hPa. As time progresses, a clear progression of zonal winds towards lesser westward magnitudes can be visibly seen around 50 km. Zonal wind profiles further reveal eastward acceleration above 60 km with enhanced eastward winds during the SSW period, which also happen to be higher than the corresponding climatological values. This eastward acceleration was also present above 1hPa in the composites given in Fig. 5. Thus the present study clearly brought out the westward acceleration of zonal winds near the tropical stratopause level, which is the first observational evidence for this phenomenon.

Stratosphere-Troposphere Exchange

Assessment of INDAT-3D retrieved temperature and water vapour over Indian region

The performance of the INSAT-3D sounder data (temperature and water vapour) is evaluated by comparing with the collocated radiosonde observations at different stations over the Indian region for almost one year. The assessment is carried out in terms of bias in the INSAT-3D measurements by assuming the radiosonde observations as a standard measurement technique. The study is carried out over different surface types (land, coast and ocean) and different latitude zones in different seasons. The systematic mean bias in the temperature and water vapour measurements of INSAT-3D sounder is computed at each pressure level.

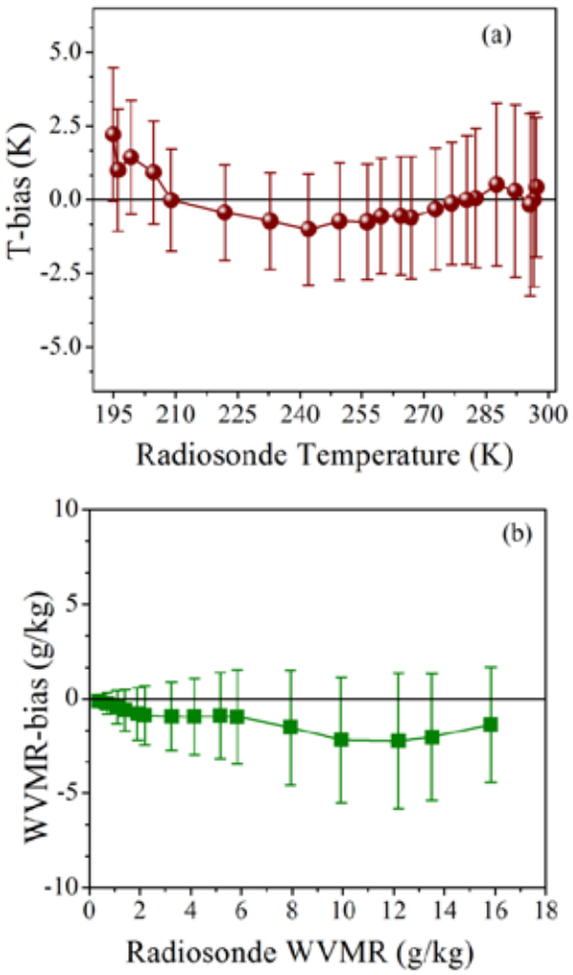

Figure 7. (a) Mean difference between INSAT-3D and radiosonde obtained temperature (INSAT-3D-Radiosonde) against the radiosonde measured temperature in the troposphere irrespective of pressure levels during the period January-December 2017. (b) Same as (a), but for water vapour mixing ratio (WVMR). The vertical bars represent standard deviation [Kumar and Sunilkumar, IEEE Trans. Geosci. Rem. Sens.,2020].

The difference of temperature and water vapour mixing ratio between INSAT-3D and radiosonde are estimated for all the collocated profiles over 30 stations during the year 2017. Fig. 7 shows the mean and standard deviation of temperature difference (T-bias) and water vapour mixing ratio difference (WVMR-bias) between INSAT-3D and radiosonde measurements against the absolute value of radiosonde measured temperature and water vapour irrespective of pressure levels. This figure shows that WVMR-bias is mostly negative (dry bias) for all the ranges of WVMR in the troposphere derived from

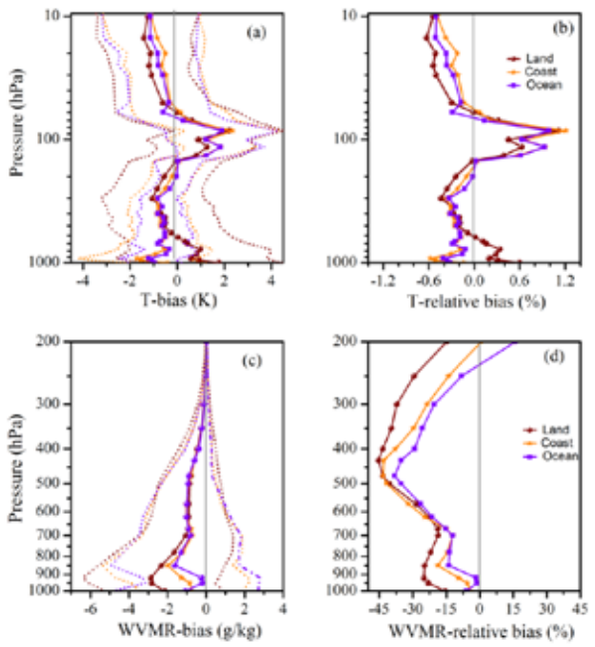

Figure 8. Mean temperature difference (T-bias) and water vapour mixing ratio difference (WVMR-bias) between INSAT-3D and Radiosonde measurements al different pressure levels during the year 2017 over different surface types (land, coast and ocean) along with relative bias in temperature and WVMR with respect to the radiosonde measurements.[Kumar and Sunilkumar, IEEE Trans. Geosci. Rem. Sens., 2020]

radiosonde. In general, the mean of the T-bias is positive when the radiosonde measures the colder (195-205 K) and warmer (285-300 K) ranges of temperatures and the mean bias is negative when the radiosonde measures the intermediate range of temperatures (220-270 K). Large standard deviation in the temperature difference is noticed particularly when radiosonde measure warm temperatures. This suggests the requirement to evaluate the satellite derived data products on different surface types.

Figure 8 shows the mean temperature difference (T-bias) and water vapour mixing ratio difference (WVMR-bias) between INSAT-3D and radiosonde measurements at different pressure levels along with their relative biases with respect to radiosonde measurement. In general, INSAT-3D retrieved water vapour shows a dry bias in the lower troposphere and mid troposphere. Relatively large dry bias (~15%) is observed near surface over land compared to ocean and coastal stations. The relative dry bias of 10-15% observed in the lower troposphere gradually increases to 25-45% in the mid troposphere over all the surface types. This study shows large bias in INSAT-3D derived temperature and water vapour profiles over land compared to coastal and oceanic stations, which may be attributed to the large contrasting surface emissivities over land. Generally, near the surface, INSAT-3D derived temperature shows a warm bias (~2K) over the land and a cold bias (~1K) over the coastal and oceanic stations. The large contrasting differences in surface temperatures and surface emissivities over the land could be the reason for the large biases in temperature and high standard deviation over land near the surface. Cold bias of ~1K (land) and ~0.5K (coastal and oceanic) are observed in the middle troposphere. However, the variability of the temperature bias is relatively large over land particularly during winter and pre-monsoon. The variability of temperature bias is large in 25-35°N

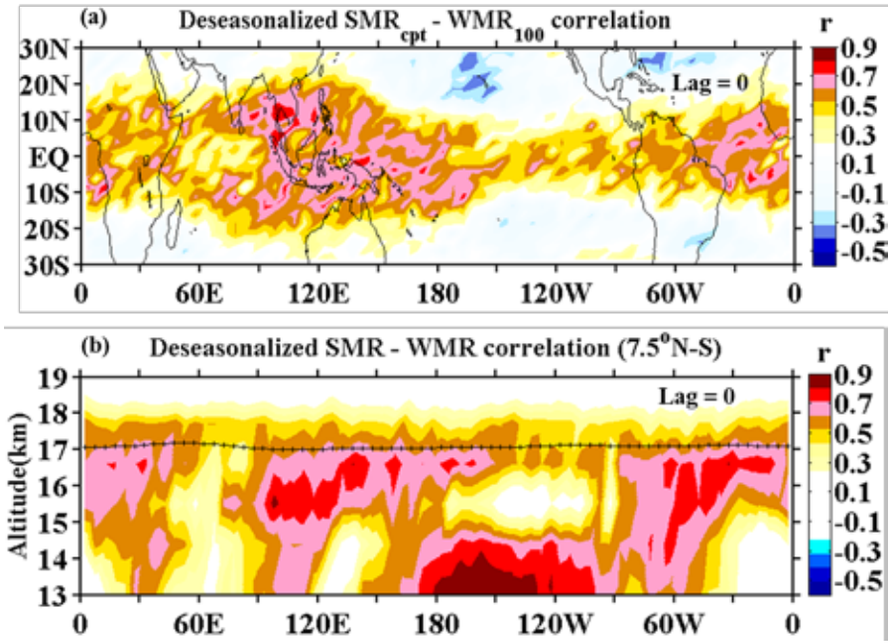

Figure 9. (a) Latitude-longitude structure of correlation coefficients between interannual anomalies of saturation mixing ratio (SMR) at CPT and water vapour mixing ratio at 100 hPa (WMR_{100}). (b) Longitude-altitude structure (7.5°N-S) of correlation coefficients between interannual SMR anomalies at tropical tropopause layer (TTL) temperature and corresponding WMR anomalies at each MLS pressure levels [Suneeth and Das, Clim. Dyn., 2020].

latitudinal zone mainly in winter followed by pre-monsoon and post-monsoon and least during monsoon. A consistent warm bias of 2-3K is observed in the upper troposphere particularly around 100 hPa on all the surface types in all seasons over all latitude zones. Thus, the bias correction is advised in using this data for upper tropospheric and lower stratospheric (UTLS) dynamics studies.

Zonally resolved water vapour coupling with tropical tropopause temperature: seasonal and interannual variability

Global stratospheric water vapour is strongly coupled to the tropical tropopause temperatures. Owing to the strong coupling, their relationship have been studied at various temporal and spatial scales in the past and reported in the literature. In most of the previous studies, the relationship between cold-point tropopause (CPT) temperature and stratospheric water vapour are discussed mainly focusing on the zonal mean values. The present study quantified the coupling between temperature and water vapour in the tropical tropopause region on seasonal and interannual time scale using 10 years of satellite (Aura MLS and COSMIC-1) based observations, focusing on the zonal asymmetries arising from the Walker circulation. Results suggested near perfect correlation values in the tropical tropopause layer (TTL) (between ~15.5 km to cold-point level) at ascending branches of Walker circulation, indicating a strong coupling between annual cycles of cold-point and water vapour variability. Descending branches of Walker circulation are characterized by weak temperature-water vapour coupling and local lapse-rate minima at about 1-1.5 km below CPT level.

The interannual anomalies of the saturation mixing ratio (SMR) estimated from TTL temperature were correlated with observed water vapour mixing ratio (WMR) and the correlation coefficients are depicted in Fig. 9a. The correlation pattern shows a strong zonal asymmetry, with peak correlation values over the following regions: a) Maritime Continents including western Pacific Ocean, and b) Atlantic Ocean. These higher correlation values indicate a strong coupling between interannual variabilities of CPT-T and water vapour over these regions. Further, the vertical structure of SMR-WMR correlation pattern was explored, to get a more detailed picture of the correlation pattern in the TTL. This was carried out by correlating near-equatorial (7.5°N-7.5°S) anomalies of SMR and WMR as a function of pressure level and longitude and is shown in Fig. 9b. The regions with highest correlations are consistent with the observed horizontal picture in Fig. 9a. In the TTL, highest correlation coefficients for interannual anomalies were noticed between 15 km and CPT-A. It is interesting to note the westward tilt of peak correlation values at the Atlantic region. In the upper troposphere, below ~14 km strong correlations over Niño region are due to the connection between El Niño related tropospheric warming and enhanced convention that leads to more water vapour in the upper troposphere.

The El-Niño Southern Oscillation (ENSO) and Quasi-biennial Oscillation (QBO) are the key modes of interannual temperature variability in the UTLS region. To estimate the influence of QBO and ENSO on the CPT-T variability, a linear regression analysis is performed individually between interannual anomalies of CPT-T and indices of QBO or ENSO. Fig. 10(a-b) represents the QBO and ENSO regression coefficient of CPT-T. The QBO regression map shows an equatorial maximum that reduces with increase in latitude and extends up to 10°N-10°S. The QBO related amplitude in CPT-T is not zonally symmetric even though QBO itself is zonally symmetric. In the equatorial region, the QBO amplitude in CPT-T is found to be maximum (~0.6) over the Maritime Continent and the Atlantic Ocean near the east Africa and minimum (~0.2) over the Niño region in the central Pacific. The observed zonal asymmetry in QBO related amplitude in CPT-T could be due to QBO-convection coupling, in which QBO influence CPT-T through its interaction with deep convection.

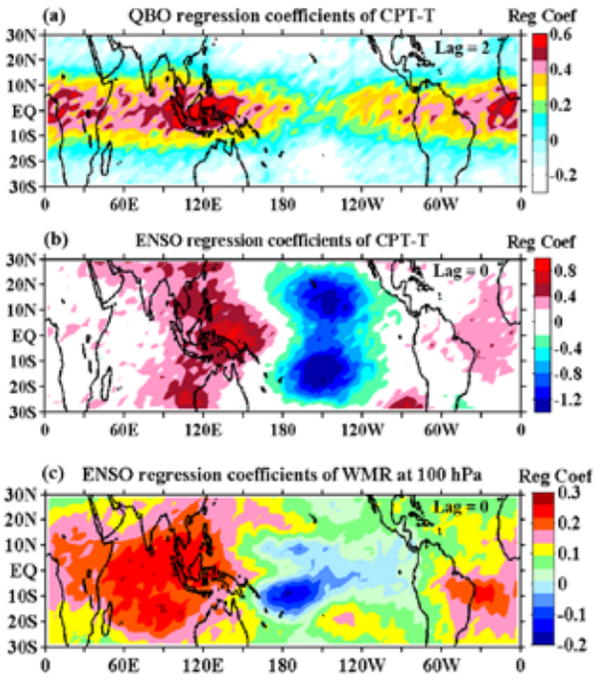

Figure 10. Univariate linear regression coefficients of CPT-T with (a) QBO and (b) ENSO indices. (c) Univariate linear regression coefficients of WMR_{100} with ENSO indices. The QBO and ENSO indices are 50 hPa Singapore zonal wind and Sea Surface Temperature anomalies at Niño 3.4 region, respectively [Suneeth and Das, Climate. Dynamics,2020].

Similarly, the ENSO influence on the CPT-T is represented by the ENSO regression coefficients of CPT-T in Fig. 10b. The regression map indicates that, during El-Nino conditions, CPT-T over the western Pacific and Maritime Continent is largely influenced with warm anomaly, while off-equatorial region in the central Pacific with cold anomaly. Unlike QBO component, the ENSO related component in the Pacific Ocean produce a zonally

asymmetric changes in the CPT-T. To examine how these zonally asymmetric changes in the CPT-T reflect in 100 hPa water vapour, a linear regression analysis between WMR_{100} anomaly and ENSO index was carried out and is shown in Fig. 10c. The result indicated a large enhancement in WMR_{100} and ENSO correlation over the Indian Ocean between 20°N-20°S and relatively small enhancement over the western side of Atlantic Ocean near ~10°S, during El-Nino conditions.

Seasonal and interannual variations of water vapour in the UTLS over the Asian Summer Monsoon region

The Asian summer monsoon (ASM) region is of paramount interest in water vapour transport studies. The unique features, such as the topography of Tibetan Plateau, presence of large upper-level anticyclone and the deep convection associated with the south Asian monsoon has a profound role in lifting and transporting the energy and moisture during the Northern Hemisphere summer. In this context, seasonal and interannual water vapour distributions in the upper troposphere and lower stratosphere (UTLS) over the domains of ASM anticyclone were explored using thirteen years (2005-2017) of Aura-Microwave Limb Sounder observations. Also, the role of CPT-T in regulating the stratospheric water vapour is studied.

Figure 11 shows the latitude-longitude distributions of OLR during boreal winter and summer over the ASM region. During boreal summer, the main region of deep convection is over the North Bay of Bengal and the south-east Asia. On the basis of distribution of tropopause altitude, OLR and water vapour distribution, the ASM region is classified into three domains: viz. Region-1 (R1), Region-2 (R2), and Region-3 (R3). R1 covers mostly the central part of ASM anticyclone, R2 covers the central India which is active monsoon region and R3 covers the equatorial Indian Ocean.

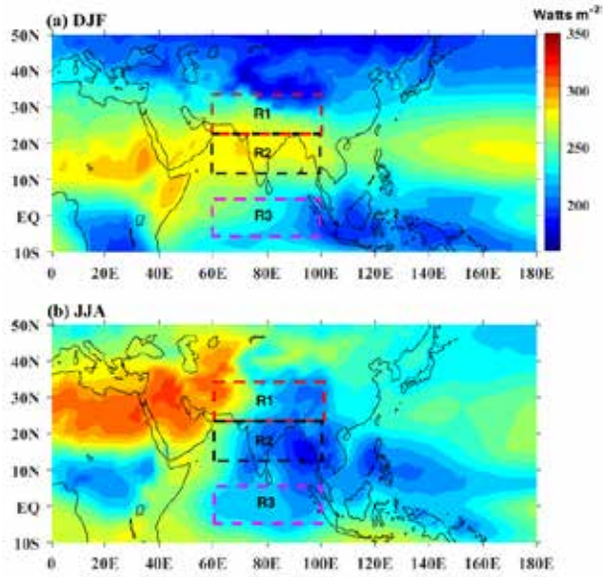

Figure 11. Latitude-longitude distributions of OLR during boreal (a) winter and (b) summer over the ASM region [Das and Suneeth, J. Atmos. Sol.-Terr. Phys., 2020]

Figure 12(a) shows the deseasonalized interannual anomalies of water vapour at 82 hPa (left) and CPT-T (right) averaged for all the three regions. Interestingly, all the three regions show a similar interannual variability of water vapour (residue) between ±1 ppmv. Since the interannual anomalies of water vapour at 82 hPa and CPT-T are also influenced by QBO, ENSO and Brewer-Dobson

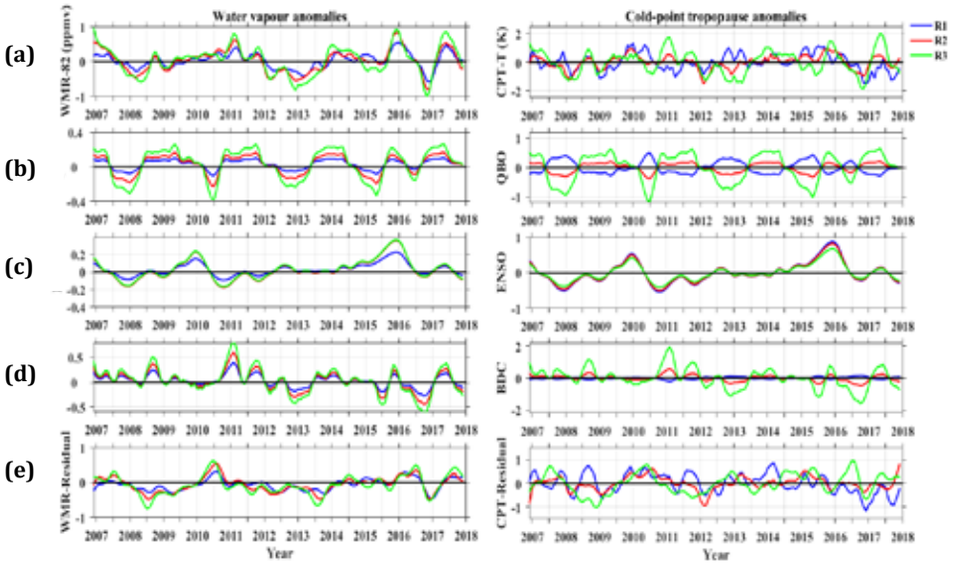

Figure 12. Time series of (a) de-seasonalized monthly variability of water vapour at 82 hPa (left), and CPT-T (right) and its corresponding regression fits components to (b) the QBO, (c) ENSO, and (d) BDC variability over the regions R1, R2, and R3. (e) Residual time series of (a) de-seasonalized interannual variability of water vapour at 82 hPa (left), and CPT-T (right). The data were averaged for three months running mean [Das and Suneeth, J. Atmos. Sol.-Terr. Phys., 2020].

circulation (BDC) modes of variability, thus such effects are removed from the analysis by multi-correlation regression fitting using respective indices as shown in the Fig. 12(b-d): (b) QBO fit, (c) ENSO fit, (d) BDC fit. The residues after removing QBO, ENO and BDC fits are depicted in Fig. 12(e). These residues are used to investigate co-variability of water vapour anomaly and CPT-T anomalies over the study regions R1, R2 and R3. Results reveal that the tropopause temperature is not significantly controlling the stratospheric water vapour over the R1 as that of R2 and R3 regions in sub-seasonal scale and suggests that water vapour accumulated inside the central part of ASM anticyclone is primarily transported from the low-latitude oceanic region by horizontal advection and relatively less from the local process.

Long-term observations of stratosphere-troposphere exchange using MST Radar over a tropical station Gadanki

The tropical upper troposphere and lower stratosphere (UTLS) is a complex region of the Earth's atmosphere, where the mixing of ozone rich stratospheric air and humid tropospheric air takes place across the tropical tropopause. This mixing process plays an important role in injecting water vapour from the troposphere into the lower stratosphere and intrusion of stratospheric ozone into the troposphere and the phenomena is known as Stratosphere-troposphere exchange (STE). In this context, the climatology of stratospheric intrusion into the troposphere during (1995-2015) Indian Summer Monsoon (ISM) season was explored using mesosphere-stratosphere-troposphere (MST) radar located at Gadanki (13.5^{o}N, 79.2^{o}E).

Figure 13 shows the climatology of (a) Signal-to-Noise Ratio (SNR) and its (b) annual mean removed SNR in the zenith direction obtained from MST radar. In the vicinity of the tropopause, absolute SNR is found to be as high as -2 to 2 dB. This is due to the strong temperature gradient arising at CPT. The strength of annual mean removed SNR in the vicinity of tropopause is found to be 2 dB higher during ISM periods as compared to other months. There may be two possible reasons for this strong refractive index gradient in the UTLS region: (1) atmosphere is highly turbulent, and/or (2) inhomogeneous mixing between two constituents (probably water vapour or ozone/dry air) which give rise to increase in atmospheric refractive index gradient. Due to the inhomogeneous mixing of these two constituents, i.e. dry air (ozone/stratosphere) and moist air (water vapour/troposphere), the gradient in the refractive index will be increased. The increase in refractive index gradient gives rise to the enhanced radar backscattered signal and thus indicates the possibility of exchange of ozone or water vapour or both across the UTLS region during ISM months.

The prime candidate for mixing of air masses of two different origins can be either due to tropopause weakening/break associated with deep convection or due to presence of

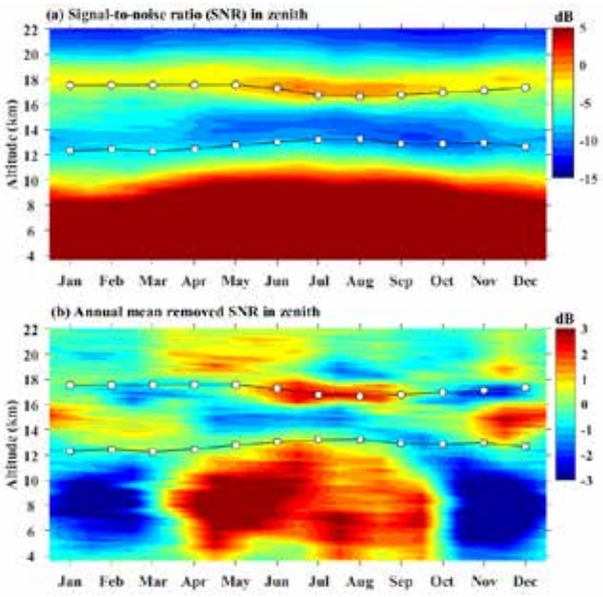

Figure 13. Altitude-month intensity plot of (a) signal-to-noise ratio (SNR) and (b) it annual mean removed in zenith direction obtained from Gadanki MST radar. Circles and squares indicate the cold-point (CPT) and convective tropopause (COT) altitude, respectively, derived from radiosonde temperature measurement [Das et al., Radio Sci., 2020].

small scale turbulence associated with the wind shear. Fig. 14 shows the climatology of (a) zonal 'u', (b) meridional 'v', (c) vertical 'w' winds and (d) spectral width derived from MST Radar. The zonal wind shows strong easterly (u>|-30| ms-1), known as Tropical easterly Jet (TEJ) between 14-18 km during ISM period. Low meridional wind is observed during ISM period. The vertical wind shows the presence of strong updrafts in the vicinity of CPT during ISM. Downdrafts in the UTLS regions expected to enhance the episode of stratospheric intrusion, whereas, updrafts increase penetration of water vapour to the lower stratosphere. We do not observe any strong downdrafts in the TTL region during ISM, thus direct intrusion of stratospheric air into the troposphere can be ruled out over Gadanki.

MST radar measures spectral width, which is a direct indicator of turbulence. Enhanced spectral width is observed during ISM period indicating the presence of turbulence as show in in Fig. 14(d). The maximum spectral width is observed in the vicinity of tropopause from June to July. The shear generated turbulence can contribute to the direct vertical mixing of two different air masses, from the stratosphere (dry) to the troposphere (humid) across the tropopause or horizontal mixing of two different air masses in addition to the tropopause altitude modulation. The occurrence of vertical mixing at UTLS region and horizontal advection during ISM can increase the ozone concentration in the upper troposphere and water vapour in the lower stratosphere. This may enhance the refractive index gradient in the vicinity of tropopause which causes the strong SNR during ISM. The present study shows the

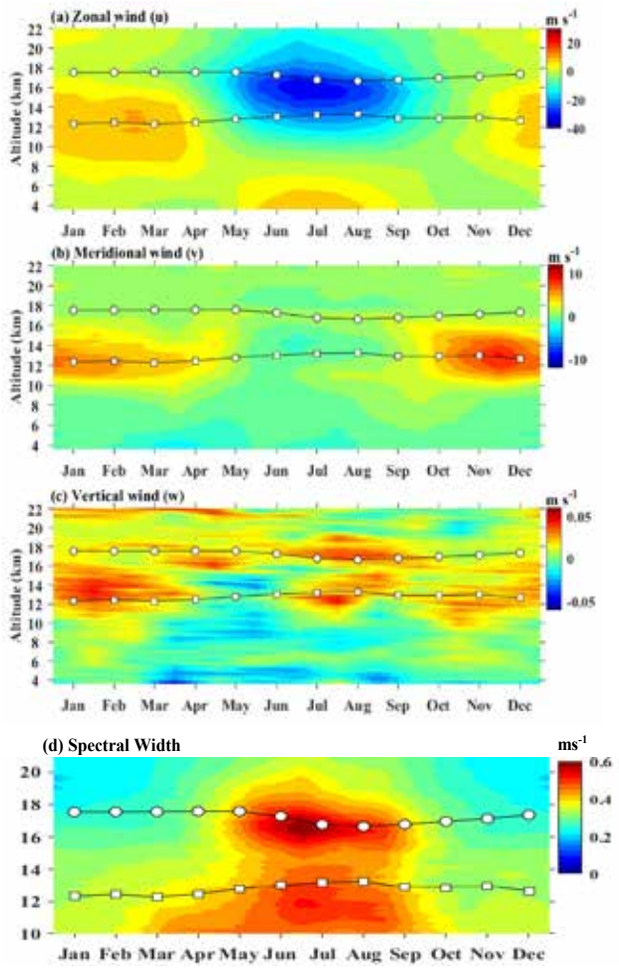

Figure 14. Climatology of (a) zonal, (b) meridional,(c) vertical velocity and (d)spectral width obtained from Gadanki MST Radar. Vertical velocity is directly derived from zenith Doppler of Gadanki MST radar. Circles and squares indicate the cold-point (CPT) and convective tropopause (COT) altitude, respectively, derived from radiosonde temperature measurement [Das et al., Radio Sci., 2020].

role of the Indian summer monsoon in exchange of minor constituents between the UTLS and how the MST radar can be effectively utilized to understand these phenomena.

Contrasting features of tropospheric turbulence over the Indian peninsula

Altitude structure of turbulence in the troposphere and its contrasting features over the Indian peninsula are delineated using radiosonde observations carried out at six stations during the period August 2013 to December 2017. The radiosonde flights conducted at Trivandrum (8.5° N,76.9° E), Cochin (10.0° N,76.3°E), Coimbatore (10.9° N,76.9°E), Gadanki (13.5°N, 79.2°E), Goa (15.5° N,73.8° E) and Hyderabad (17.5° N,78.6°E), as part of the Tropical Tropopause Dynamics (TTD) Campaign under the GPS Aided Radiosonde Network Experiment for Troposphere–stratosphere Studies (GARNETS) program are used in this study.

Thorpe analysis applied to the potential temperature profiles, taking into account the impact of atmospheric moisture and instrumental noise, are used to estimate the turbulence and stability parameters. This study shows that the occurrence of turbulence is relatively high in the lower (0-2 km) and upper (10-15 km) troposphere and the altitude region 3-8 km is relatively devoid of turbulence over all the six stations. Over Cochin, the occurrence of turbulence in the upper troposphere is relatively less compared to other stations. In general, the eddy length scale (usually referred as Thorpe scale and represented by L_T) decreases with altitude. In the troposphere ~60% values of Thorpe scale is less than 250m in all stations, except Cochin. In the 0-3km altitude region, the Thorpe scale is relatively large at Hyderabad and small at Coimbatore (*Fig. 15*). Around 75% of turbulence length scale are below 700 m, 600 m, 500 m, 600 m, 600 m and 1100 m over Trivandrum, Cochin, Coimbatore, Gadanki, Goa and Hyderabad respectively. In the 3-8 km and 8-15 km altitude regions, Cochin shows

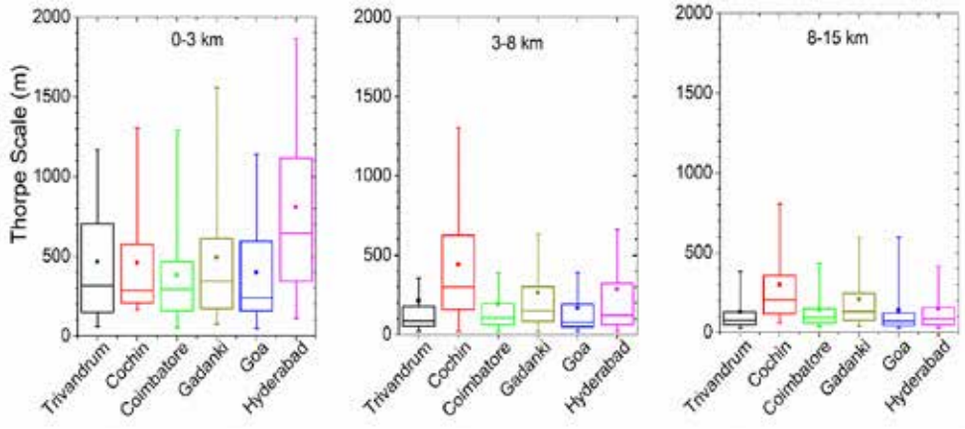

Figure 15. Box chart delineating the distribution of the Thorpe scale for the altitude regions 0-3km, 3-8km and 8-15km. Each box represents a particular station such as Trivandrum, Cochin, Coimbatore, Gadanki, Goa and Hyderabad respectively. The solid square inside the box indicates the mean value. The lower boundary of the box is 25th percentile (1st quartile), the middle line is the 50th percentile and the upper boundary of the box is the 75th percentile (3rdquartile). The lower and upper bars represent the minimum and maximum values, respectively [Muhsin et al., J. Atmos. and Sola. Terres. Phys., 2020].

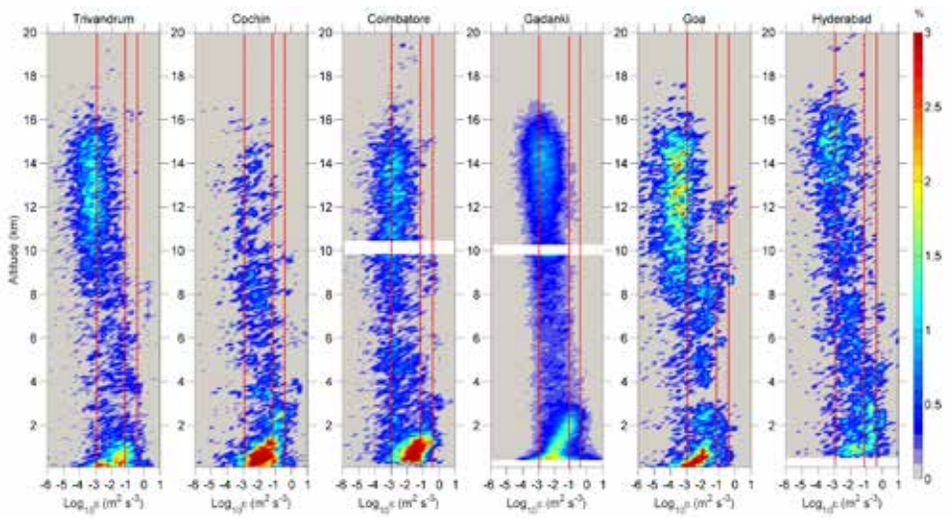

Figure 16. Contour Frequency Altitude Diagram depicting the percentage of occurrence of $Log_{10}\varepsilon$ (with a width interval of 0.25) over Trivandrum, Cochin, Coimbatore, Gadanki, Goa and Hyderabad. These are estimated using the entire dataset during the entire study period. Vertical lines at $log_{10}\varepsilon$ values 3, -1.2 and -0.465 corresponds to the EDR ($\varepsilon^{1/3}$) values of 0.1 $m^{2/3}s^{-1}$, 0.4 $m^{2/3}s^{-1}$and 0.7 $m^{2/3}s^{-1}$, respectively [Muhsin et al., J. Atmos. and Sola. Terres. Phys., 2020].

relatively large Thorpe scales with values of 600 m and 400 m respectively at the75th percentiles. In the altitude region of 8-15 km, 75% of Thorpe scale observations falls below 250 m at all the stations except Cochin, indicating the dominance of smaller scale turbulence in the upper troposphere over these stations. A strong turbulent layer is observed around 2 km at all the stations and weaker layers at higher altitudes. In the lower troposphere the turbulent kinetic energy dissipation rate (ε) varies from 10^{-3} to 1 m^2 s^{-3} and in the upper troposphere it is in the range of 10^{-6} to 10^{-1} m^2 s^{-3} (Fig. 16).

The eddy dissipation rate (EDR), defined as $\varepsilon^{1/3}$, showed moderate (EDR between 0.4 and 0.7). Severe turbulence (EDR > 0.7) does exist in the altitude region below 4 km at all the stations. In the free troposphere, EDR is mostly less than 0.4 (~ 20-60% for no turbulence and ~30-65% for light turbulence) with a few encounters of moderate (~4-15%) and severe turbulence (~1-2%) over these stations. The occurrence of moderate and severe turbulence is the highest over Cochin. Though the altitudinal structure of turbulence shows large variability from station-to-station, it does not show any systematic latitudinal pattern. An interesting result obtained in this analysis is that whenever the dynamic instability is significant, the turbulence detected by Thorpe method is less compared to that estimated using the critical value of Richardson number. This can be explained based on the fact that the Thorpe method is more sensitive towards turbulence generated from convective instability.

This study showed that in the lower troposphere, turbulence is induced by both convective and dynamic instabilities over all the stations. In the 10-15 km altitude region, turbulence is generated mainly due to convective instability over Coimbatore and Goa, dynamic instability over Cochin, and both convective and dynamic instabilities over Trivandrum and Hyderabad. Convective instability exists in the upper troposphere even under clear air conditions; their generation mechanism could be wave breaking. The reduction in static stability causing convective instability in the 10-15 km region under in-cloud conditions could be due to saturation layers and/or sublimation of ice crystals beneath cirrus layers.

Cloud Dynamics

Multi-layered cloud distribution over Thumba using Radiosonde humidity observations and CloudSat measurements

A method is formulated for extracting the number of cloud layers using radiosonde measured relative humidity (RH) profiles over Thumba. The radiosonde observations with 100 m vertical resolution during 2000-2009 are used for the study. A total number of 5090 profiles were used for deriving the cloud vertical structure information. A minimum and maximum RH threshold of 84% and 87%, respectively are used for identifying the cloud layers. RH is computed with respect to liquid at all altitudes. The RH profiles are examined to identify cloud layers by following steps: (1) The base of the lowest moist layer is determined as the level that satisfy any of these two conditions (a) minimum RH at least 85% and (b) RH increases at least 3% from the adjacent lower level; (2) RH is at least 84% above the base of the moist layer; (3) the top of the moist layer is identified when RH decreases by more than 3% and is lower than 84%; (4) the moist layer is classified as a cloud layer if the maximum RH within this layer is more than 87%; and (5) minimum cloud height is set to 500 m above ground level. This method is able to detect a maximum of five cloud layers over Thumba. However, there are a few limitations in the present method. As the RH profile is used to indicate cloud top and cloud base

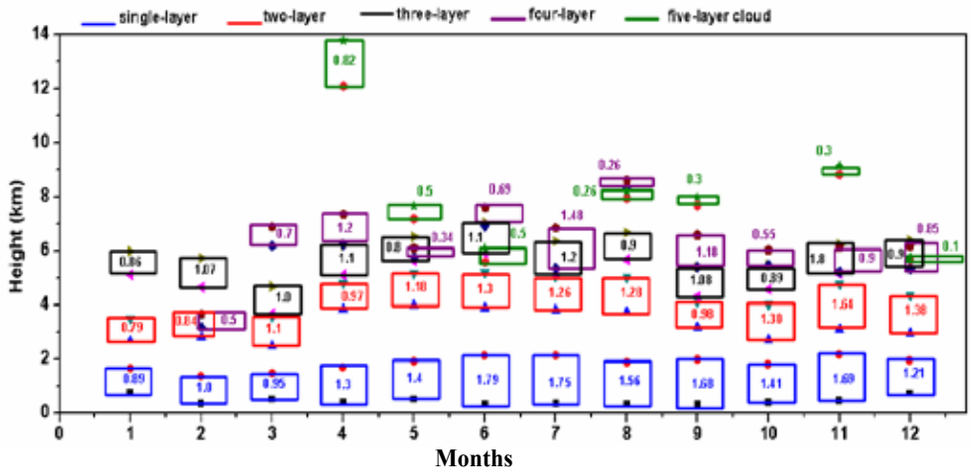

Figure 17. Monthly mean altitude and thicknesses of single-, two-, three-, four- and five-layered clouds over Thumba [Subrahmanyam and Kumar, Environment and Natural Resources Research, 2019]

locations, more attention must be paid to biases in RH due to instrument errors and finite vertical resolution. A cloud is characterized by RH ~ 100%; however 100% RH is rarely observed by radiosonde within the clouds because of 1) systematic biases of radiosonde measurements; 2) RH cut off mentioned in the analysis 3) the fact that the RH is always calculated with respect to water at all temperature, which is smaller with respect to ice at temperatures below 0^0C. All these factors imply the underestimation of RH using radiosonde observations. Accordingly, a cloud can exist at a measured RH less than 100%. Keeping these limitations in view, we have estimated the occurrence of multi-layer clouds over Thumba.

Ten years of monthly mean occurrence of single-, two-, three-, four- and five-layered clouds derived from radiosonde observations are shown in Fig. 17. The magnitudes given inside the each cloud layer box indicate the cloud layer thickness. The presence of five-layered clouds is preferentially observed during Indian summer monsoon period (June-July-August-September). There are also multi-layered cloud occurrences during winter monsoon (October and November). There are three layered clouds well separated in altitude during the months of April and May. An interesting aspect that can be noted from this figure is the distinct separation of first and second layers during all the months. This separation is relatively large during the months of April to September.

Figure 18 shows the occurrence of multi-layered clouds (up to 5) derived from radiosonde observations (black) and CloudSat observations (blue). Radiosonde derived cloud-free cases and one to five cloud layers account for 30.63%, 42.51%, 19.76%, 5.85%, 1.08%, and 0.16%, respectively. The CloudSat shows 19.78%, 47.17%, 24.74%, 6.41%, 1.81% and 0.13%, respectively. Both the ground and space based observations over Thumba show the more or less same percentage of occurrence of single-, double-, three-, four- and five-layered clouds. But in the case of percentage

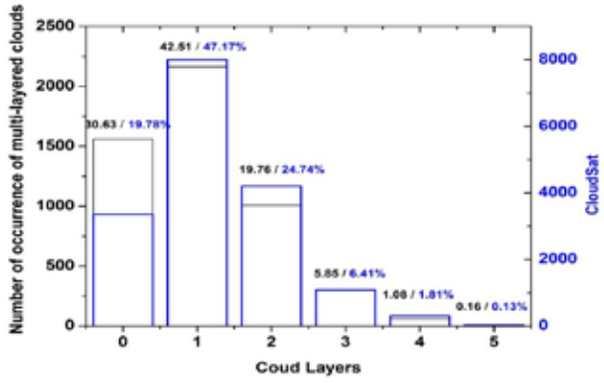

Figure 18. The frequency of occurrence of one- to five-layered clouds as observed by radiosonde measurements (balck) and CloudSat observations (blue) [Subrahmanyam and Kumar, Environment and Natural Resources Research, 2019].

of occurrence of clear days, radiosonde observations show 30.63% while CloudSat observations show 19.78%. This may be attributed to the frequency of observations as well as local time observations of radiosonde and CloudSat.

Field Experiments/New initiative

Balloon Borne observations of Buoyancy wave induced Small-scale Horizontal Structures in the Stratosphere (B3S3)

A field campaign is carried out to study the horizontal structure of atmospheric gravity waves in the stratosphere by drifting the radiosonde at a constant altitude (~31 km) using TIFR balloon facility at Hyderabad. The experiment was carried out on two days during September 2019. The balloon is released from Hyderabad and the data is received from two ground stations, Hyderabad and Solapur. The central objective is to investigate the horizontal structures induced by the atmospheric gravity waves in the stratosphere and to estimate the horizontal wave number spectrum of gravity waves in the stratosphere. On 12 September 2019 the balloon reached 31 km altitude

and drifted almost 100 km thus providing the horizontal structure of winds and temperature. Fig. 19 shows the three dimensional track of the balloon released on 12 September 2019. The observations are analysed and the horizontal wavenumber spectrum of gravity waves is estimated for the first time over a Indian region.

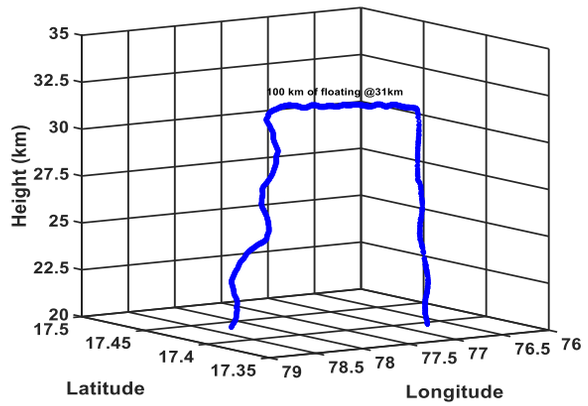

Figure 19: The track of radiosonde flown on 12 September 2019

Suryagrahan Campaign (Solar Eclipse)-2019

Solar eclipses are unique occasions to investigate how different parts of the terrestrial atmosphere respond to a well-defined, direct, quite rapid and natural cut off of the solar radiation. In this regard, a National level experimental campaign "Suryagrahan-2019" was conducted by SPL, VSSC in collaboration with other National Institutes, namely : (1) Indian Institute of Space Science and Technology (IIST, Trivandrum), (2) Cochin University of Science and Technology (CUSAT, Kochi), (3) Indian Naval Meteorological Analysis Centre (INMAC, Kochi), (4) National Atmospheric Research Laboratory (NARL, Gadanki), (5) Aryabhatta Research Institute of Observational Sciences (ARIES, Nainital), (6) Satish Dhawan Space Centre-SHAR (SDSC-SHAR, Balasore Range) and (7) Indian Institute of Tropical Meteorology (IITM, Pune) by simultaneous launching series of radiosonde and ozonesonde at 6-different locations from 25 to 27 December 2019. RH-200 sounding rockets were also launched from Thumba Equatorial Launching Station (TERLS) at 09:30 hr on 26 and 27 December 2019. Wind profilers (MST/ST/UHF) at NARL, CUSAT, ARIES and INMAC were also continuously operated along with other co-located surface observations. Analysis is in progress.

Weather Prediction at SHAR using Artificial Intelligence

As part of DTDI, ISRO-HQ initiative on Artificial Intelligence (AI), various project teams were formed to demonstrate applicability of AI models in various domains. Project 'MAUSAM' is one of them and the team members are from various ISRO centres (SPL, SHAR, NESAC and IPRC). The goal of the project is to predict the weather using AI on the day of launch at SHAR. In this regard, surface meteorological parameters over SHAR are analyzed using Python AI algorithms. The Gaussian Process Regression (GPR) model is applied to long-term rainfall data to predict heavy rainfall days over Sriharikota. Fig. 20 shows the prediction of heavy rainfall days using the GPR model. The blue colored line represents the data used for training from 1901 to 1988. The green and red color lines indicate the actual and predicted rainfall days from 1989 to 2016. Overall, the predictions are very encouraging and able to reproduce the variability of rainfall. Interestingly, it could capture the peak years of heavy rainfall days. Further, fine tuning of model parameters and exploring the other AI model to predict weather at SHAR are in progress.

Future Projections

- Heating rate profiles in the middle atmosphere using long-term composition measurements.
- Whole Atmosphere Community Climate Model (WCCAM) simulations of middle atmospheric features over Thumba.
- Ozone and Water vapour distribution over the Indian region and Indian oceanic region using GARNET observations.
- Lagrangian Models to understand the role of dynamics on the tracer distribution in the UTLS over Indian monsoon region.
- Structure and dynamics of tropical cyclone/convection using MST Radar in active aperture mode including their effects on middle atmosphere.
- Role of atmospheric circulation, ENSO and QBO in the exchange of minor constituents in the UTLS region.
- Study on the stratosphere-troposphere interactions over the Antarctica.
- Characterization of Deep Convective Cells using C-band DWR observations.
- Retrieval Polarimetric parameters using Laser Precipitation Monitor measurements.

Publications in Peer-Reviewed Journals

1. Ajayakumar R. S, Prabha R. Nair, Imran Asatar Girach, S.V. Sunilkumar, M. Muhsin, P.R. Satheesh Chandran, "Dynamical nature of tropospheric ozone over a tropical location in Peninsular India: Role of transport and water vapour", Atmospheric Environment, 218, DOI: 10.1016/j.atmosenv. 2019.117018, (2019).

2. Das, S.S., and K. V. Suneeth, "Seasonal and interannual variation of water vapour in the upper troposphere and lower stratosphere over the Asian Summer Monsoon region- In perspective of the tropopause and ocean-atmosphere interactions", 201, Journal of Solar and Terrestrial Physics, DOI: 10.1016/j.jastp.2020.105244, (2020).

3. Das, S.S., K. V. Suneeth, M. V. Ratnam, K. N. Uma, M. D. Rao, A. N. Babu, "Long-term observations of stratosphere-troposphere exchange using MST Radar and Aura MLS measurements over a tropical station Gadanki", Radio Science, DOI: 10.1029/2019RS006969, (2020).

4. Jose, L., C. Vineeth, T. K. Pant, K. K. Kumar, "Response of the Equatorial Ionosphere to the Annular Solar Eclipse of January 15, 2010", Journal of Geophysical Research: Space Physics, DOI: 10.1029/2019JA027348, (2020)

5. Koushik, N., K. K. Kumar, G. Ramkumar, K. V. Subrahmanyam, G. Kishore Kumar, W. K. Hocking, M. He, R. Latteck, "Planetary waves in the Mesosphere Lower Thermosphere during Stratospheric Sudden Warming: Observations using a network of meteor radars from high to equatorial latitudes", Climate Dynamics, 54, 4059–4074, DOI.org/10.1007/s00382-020-05214-5, (2020).

6. Koushik, N., K. K. Kumar, Tarique A. Siddiqui, "Westward Acceleration of Tropical Stratopause Zonal Winds during Major Sudden Stratospheric Warming Events", Geophysical Research Letters, 47, e2019GL086857, DOI: 10.1029/2019GL086857, (2020).

7. Kumar, A.H. and S. V. Sunilkumar, "Assessment of INSAT-3D Retrieved Temperature and Water Vapour With Collocated Radiosonde Measurements Over Indian Region", IEEE Transactions on Geoscience and Remote Sensing, 58, 6, 4000-4005, DOI: 10.1109/TGRS.2019.2960277, (2020).

8. Maurya, A. K., M. B.Cohen, K. Niranjan Kumar, D. V. Phanikumar, R. Singh, P. K. Vineeth, K. Kishore Kumar, "Observation of very short period atmospheric gravity waves in the lower ionosphere using very low frequency waves", Journal of Geophysical Research: Space Physics, 124, 9448-9461, DOI: 10.1029/2019JA027360, (2019).

9. Muhsin, M., S.V. Sunilkumar, M. Venkat Ratnam, K. Parameswaran, K. Mohankumar, S. Mahadevan, K. Murugadass, P.M. Muraleedharan, B. Suneel Kumar, N. Nagendra, Maria Emmanuel, P.R. Satheesh Chandran, N. Koushik, Geetha Ramkumar, B.V. Krishna Murthy, "Contrasting features of tropospheric turbulence over the Indian peninsula", Journal of Atmospheric and Solar-Terrestrial Physics, 197, DOI:10.1016/j.jastp.2019.105179, (2020).

10. Nair, A., S. S. Das, A. Thomas, C. Sarangi, V. P. Kanawade, "Role of Cyclone "Ockhi" in the re-distribution of aerosols and its impact on the precipitation over the Arabian Sea", Atmospheric Research, 235, DOI: 10.1016/j.atmosres.2019.104797, (2020).

11. Pramitha, M., K.K Kumar., M. V. Ratnam, S. V. B. Rao, S. V. B., G. Ramkumar, "Meteor radar estimations of gravity wave momentum fluxes: Evaluation using simulations and observations over three tropical locations", Journal of Geophysical Research: Space Physics, 124, 7184–7201. DOI: 10.1029/2019JA026510, (2019).

12. Subrahmanyam, K. V., K. K. Kumar, "Multi-Layered Cloud Distribution Over Tropical Station Using Radiosonde Humidity Observations and CloudSat Measurements", Environment and Natural Resources Research, 9, 3, DOI:10.5539/enrr.v9n3p9, (2019).

13. Subrahmanyam, K. V. and N.V.P. Kirankumar, "Characteristics of Mesoscale Convective Systems over the Indian summer monsoon using IRBRT data", Science Spectrum: Quarterly Journal of AP Akedamy of Science, ISSN no. 2455-5053, (2020) (accepted).

14. Suneeth, K.V., S.S. Das, "Zonally resolved water vapour coupling with tropical tropopause temperature: Seasonal and interannual variability, and influence of the Walker circulation", Climate Dynamics, DOI: 10/1007/s00328-020-05255-w, (2020).

Presentation in Symposium/Conferences/Workshops

National

1. Subrahmanyam K.V. and Karanam Kishore Kumar, Structure and Dynamics of precipitating clouds associated with extreme rainfall events as observed by C-band Polarimetric Doppler Weather Radar at Thumba, TROPMET-19, Andhra University, Visakhapatnam, 11-14, December 2019.

2. Subrahmanyam K.V. and Karanam Kishore Kumar, Characterization of Deep Convective Cells using C-band Polarimetric Doppler Weather Radar observations over Thumba (8.5^0 N, 77^0 E), iRAD-2020, IIT Madars, Chennai, 5-7, February 2020.

3. Das, S.S., K. V. Suneeth, K. N. Uma, C. Vineeth, and G. Ramkumar (2020), Diurnal and seasonal behavior in the stratosphere and lower mesospheric water vapour and ozone over the equatorial Indian region at URSI-Regional Conference on Radio Science 2020, held at IIT, Banaras Hindu University, Varanasi from 12-14 February 2020.
4. Suneeth, K.V., and S. S. Das (2020), Interannual variability of water vapour and tropical tropopause temperature: Zonal structure at URSI-Regional Conference on Radio Science 2020, held at IIT, Banaras Hindu University, Varanasi from 12-14 February 2020.
5. Satheesh Chandran P R, S.V. Sunilkumar, M. Muhsin and Maria Emmanuel, 'Dynamic influence of Asian summer monsoon on the variability of ozone in the upper troposphere lower stratosphere region revealed from in-situ ozonesonde observations', International Conference on the Asian Summer Monsoon Anticyclone (ASMA): Gateway of surface pollutants to the stratosphere, SRM Institute of Science and Technology (SRMIST), Chennai, India, 10-11 February 2020.
6. S.V. Sunilkumar and Maria Emmanuel, Transport of water vapour in upper troposphere and lower stratosphere and formation of cirrus clouds, International Conference on the Asian Summer Monsoon Anticyclone (ASMA): Gateway of surface pollutants to the stratosphere, SRM Institute of Science and Technology (SRMIST), Chennai, India, 10-11 February 2020.
7. Muhsin M and S.V. Sunilkumar, Heterogeneity in diurnal variation of convection over Indian Region, International Conference on the Asian Summer Monsoon Anticyclone (ASMA): Gateway of surface pollutants to the stratosphere, SRM Institute of Science and Technology (SRMIST), Chennai, India, 10-11 February 2020.

Invited Talks

Kishore Kumar K.

1. Key Note Address "Vertical distributions of the clouds and role of convection over the Asian Monsoon region", International Conference on the Asian Summer Monsoon Anticyclone 2020, SRM University, Chennai, 10-11 February 2020

Das S.S.

1. "A comprehensive study on the dynamics and chemistry of the upper troposphere and lower stratosphere using ST/MST Radars along with balloon-borne and space based measurements", URSI-Regional Conference on Radio Science 2020, held at IIT, Banaras Hindu University, Varanasi, 12-14 February 2020
2. "Upper tropospheric ozone transport from the sub-tropics to tropics over the Indian region during Asian summer monsoon", International Conference on the Asian Summer Monsoon Anticyclone 2020, SRM University, Chennai, 10-11 February 2020

Sunil Kumar S.V.

1. "Transport of the water vapour in upper troposphere and lower stratosphere and persistence of cirrus clouds in UT" International Conference on the Asian Summer Monsoon Anticyclone (ASMA): Gateway of surface pollutants to the stratosphere, SRM Institute of Science and Technology (SRMIST), Chennai, India, 11 February 2020.

Training Programme

Dr. Kandula V Subrahmanyam

1. Attended Phase-I & Phase-II of Artificial Intelligence (AI) organized by Directorate for Technology Development and Innovation (DTDI) during 4th -9th November 2019 (Phase-I) and 3rd-7th, February 2020 (Phase-II) at ISRO HQ, Bangalore.

Ionosphere Thermosphere Magnetosphere Physics

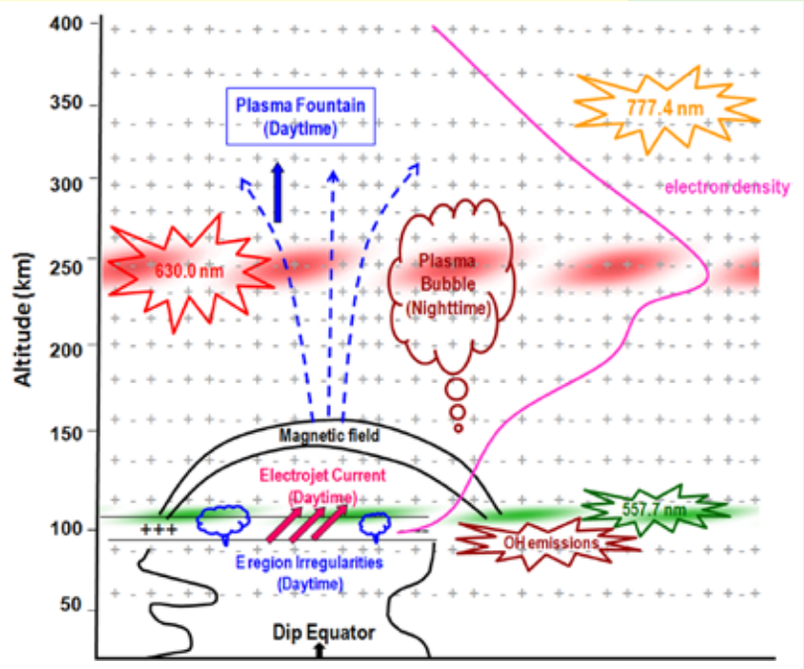

The aim of Ionosphere Thermosphere Magnetosphere Physics (ITMP) branch is to investigate the terrestrial upper atmosphere in context of its energetics and dynamics vis-à-vis the vertical and lateral coupling this region has with the magnetosphere above and lower atmosphere below it; and make use of these studies to provide better input for technological applications wherever possible. ITMP aims at extending these studies to other solar system bodies as well.

Science Team
- Tarun Kumar Pant
- Raj Kumar Choudhary
- Smitha V. Thampi
- Manju G.
- Vineeth C.
- Sandhya K. Nair
- Md. Mossarraf Hossain
- Mridula N.
- Ambili K. M.

Technical Team
- Anumod P. G.
- Manikantan Nair N.
- Mohammad Nazeer M.
- Uttam S. Purthy

Inspire Faculty
- Sneha Yadav*

Research Associates
- Ajesh A.
- Aswathy R. P.
- Deepthi Ranjan Rout
- Jayalekshmi . G. L.
- Shamayitha Ray

Research Fellows
- Keshav Ram Tripathi
- Krishnaprasad C.
- Lalitha G
- Richa Naja
- Sachin S
- Sruthy R

** Relieved in June 2020*

Equatorial Thermosphere Ionosphere Processes

Response of the Equatorial Ionosphere to the Annular Solar Eclipse of January 15, 2010

This study presents the response of the equatorial ionosphere to the noon time annular solar eclipse of January 15, 2010. This eclipse was unique in the sense that the path of totality passed through dip-equator and it occurred during noontime. The observations were made using collocated Digisonde, Meteor Wind Radar and Proton Precession Magnetometer over Trivandrum, (8.5° E; 77° N; dip lat 0.5° N), a geomagnetic dip equatorial station in India. It was found that the E, F_1 and F_2 regions of the equatorial ionosphere responded to solar eclipse with different time delays, F1 responding fast and the E and F2 regions relatively slow (Figs. 1 and 2). The delayed response of F2 region during the solar eclipses has been studied earlier and understood. The delayed response of E region, however, is quite unexpected since this region is dominated by the recombination chemistry and therefore expected to respond fast. The plausible reasons for the observed delay has been explored and it is suggested that the downward diffusion of atomic oxygen plays a major role for the observed phenomenon as the diffusion rates are known to be slower than the chemical recombination rates.

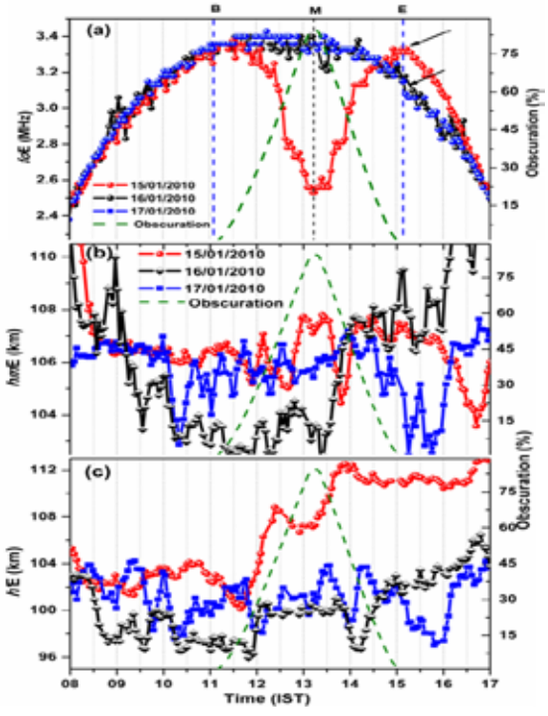

Figure 1: The time variation of (a) critical frequency of E-region(foE),(b) peak height (hmE) and (c) minimum virtual height of E region (h'E) on the day of the eclipse (15/01/2010) and the background days (16/01/2010 and 17/01/2010). The dashed green line shows the percentage of obscuration and the arrows represent the foE enhancement after the eclipse [Jose et al., J. Geophys. Res. 2020].

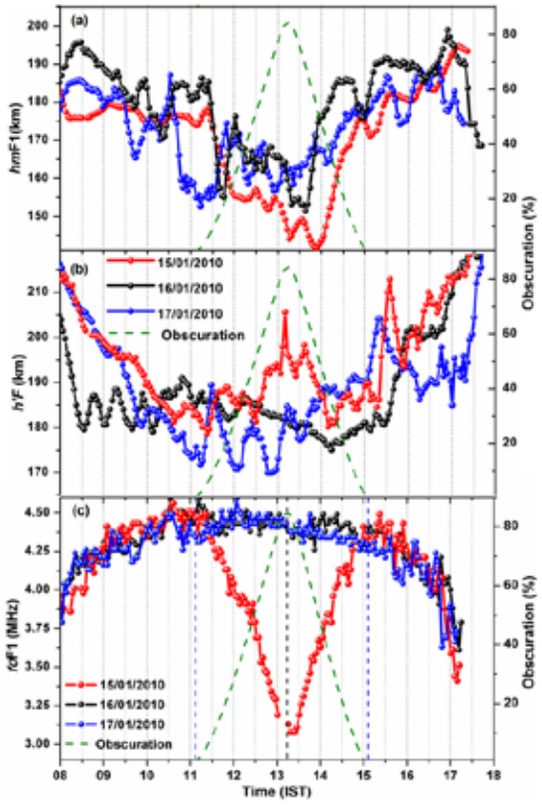

Figure 2: The time variation of (a) peak height of F1 region (hmF1), (b) minimum virtual height (h'F) and (c) critical frequency of F1 region (foF1) on the day of the eclipse (15/01/2010) and the background days (16/01/2010 and 17/01/2010) [Jose et al., JGR. 2020].

On the variability of the Equatorial Ionization Anomaly Trough over Indian region: A novel analysis using Beacon TEC measurements

In the past, studies across the globe had lot of emphasis on the location and movements of the anomaly crests, and not much attention has been given to the variability of anomaly trough. In this study, a novel method using single station beacon Relative Slant Total Electron Content (RSTEC) measurements, obtained through SPL's Coherent Radio Beacon Experiment, was proposed to estimate the location of Equatorial Ionization Anomaly Trough (EAT) and study variability therein. The feasibility of this method is established based on simulations of RSTEC using (International Reference Ionosphere) IRI model electron densities. It is seen that the trough moves 13 degree north to 3 degree north (i.e. around +/_5 on either side of the dip equator) and the trough location exhibits a systematic latitudinal change with seasons. During solsticial months when the thermospheric meridional winds are strong, the EAT location is determined by the trans hemispheric winds. During equinoctial months, when thermospheric winds are weak, the EAT location is determined by the combined effect of field aligned diffusion and the thermospheric winds (depicted in Fig. 3). The transition of EIA from winter to summer side of the dip equator, depends on the balance

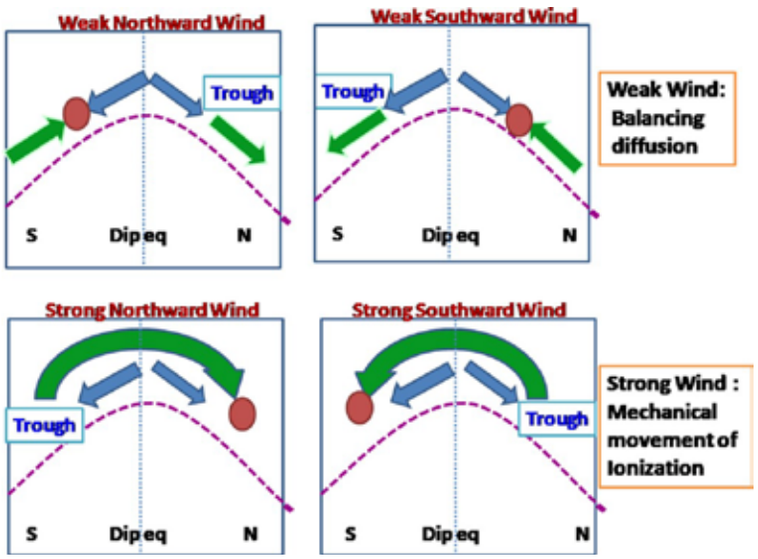

Figure 3: Gives the schematic explaining the mechanism of trough movement over the dip equatorial region [Mridula et al., ASR. 2020].

between the field aligned diffusion and thermospheric winds. Further there is a marked difference in the extent of shift between 2006 and 2007, though the mean pattern remains the same.

Reverse Fountain and the Nighttime Enhancement in the Ionospheric Electron Density Over the Equatorial Region: A Case Study.

The linkage between reverse fountain effect and anomalous enhancement in the nighttime electron density over the equatorial ionosphere, often referred as the ionospheric nighttime enhancement (INE), was explored using measurements of the total electron content (TEC) of the ionosphere from InSWIM GNSS receivers at Trivandrum, and Bangalore. The high resolution spatiotemporal two-dimensional (2D) TEC maps generated by using satellite-based augmentation system are used to visualize the reverse fountain effect. These TEC maps are found to be effective in envisaging the motion of equatorial ionization anomaly (EIA) in nighttime ionosphere and its impact on the distribution of electron density over the equatorial region. Salient features of this case study illustrate that,

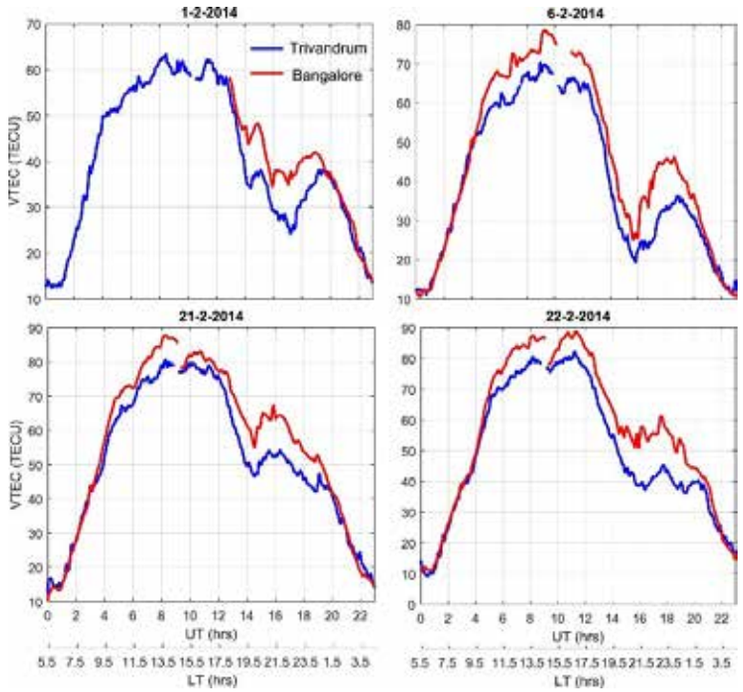

Figure 4: Temporal variation of TEC displaying the typical examples of ionospheric nighttime enhancement over Trivandrum and Bangalore. [Sneha et al, JGR, 2020]

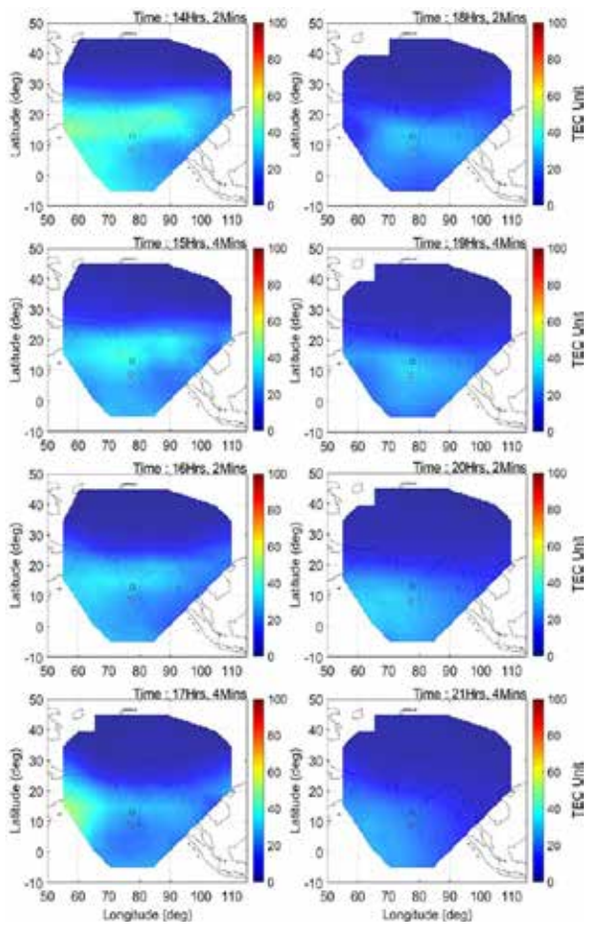

Figure 5: The 2D TEC maps generated by using SBAS (satellite-based augmentation system) for 01 February 2014. The TEC values are represented through a color code. The location of Trivandrum and Bangalore in the maps are depicted by circle and square symbol, respectively. [Sneha et al, JGR, 2020]

accompanying enhancements in the nighttime TEC, there exist a decrease in the F2 layer height, prevalence of downward vertical plasma drift, and a dramatic increase in the F2 region electron density. The 2D TEC maps reveal the persistence of well developed EIA until late evening hours and its gradual shift toward equator during the events of post-midnight INEs (Figs. 4 and 5) It is found out that the pre midnight INE is not invariably linked to the prereversal enhancement of the zonal electric field and could be associated with the redistribution of electron density caused by the reverse fountain effect. The present observations indicate that although the westward electric field serves as a prime driver, the INEs over the equatorial regions are associated with plasma motions caused by the retreating anomaly.

In-situ observations of rocket burn induced modulation of the top side ionosphere using the IDEA payload on the first ever PS4 orbiting platform

The fourth stage (PS4) of the Polar Satellite Launch Vehicle (PS4-PSLV) of the C-38 mission, was used for the first time as an orbiting platform to carry out measurements of atmospheric parameters, on June 23, 2017. The measurements were made in two phases. i) During the initial launch phase wherein the launch vehicle traversed from the launch pad to an altitude of 500 km. ii) During the 10 orbits at an altitude of 350 km (after the PS4 stage was brought down in a controlled manner). The Ionization Density and Electric-field Analyzer (IDEA) payload onboard the PS4 stage provided electron density (Ne) and electric field (EF) information in the F region altitudes. This study highlights the results from the Langmuir probe component (Ne) during the initial launch phase. The presence of a top side enhancement, is revealed in the initial phase IDEA measurements and simulations using IRI and TIE-GCM models confirm the possibility (Fig. 6).

The first of their kind in-situ observations of top side electron density enhancement concurrent with the operation of the PS4 stage of PSLV demonstrates the plausible role of rocket burn and exhaust gases in modulating the

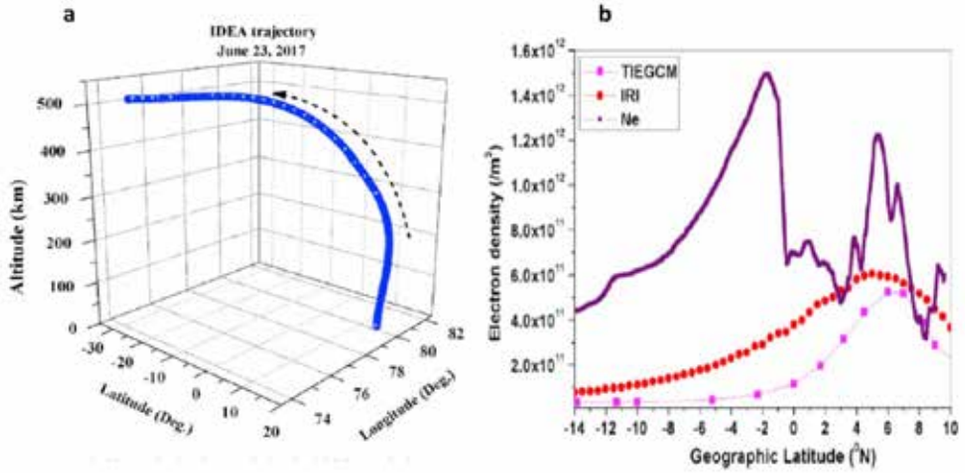

Figure 6 a)Trajectory of payload in the launch phase b) Comparison of IDEA LP electron density observations with IRI model output and TIEGCM model simulation for 23 Jun 2017[Manju et al., JASTP, 2020]

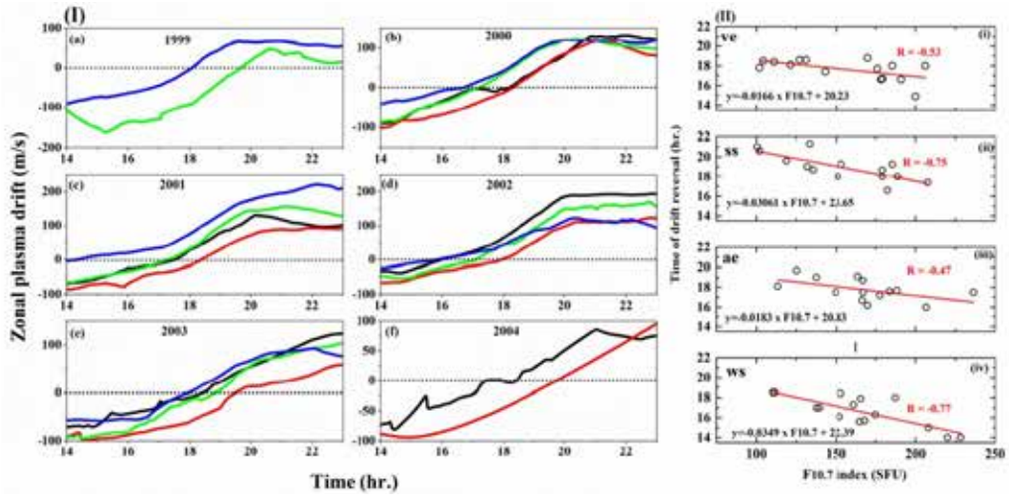

Figure 7: Seasonal pattern of the temporal variation of zonal plasma drift for the years 1999 to 2004 (ve - black curve, ss - red curve, ae - green curve and ws - blue curve) (II) The F10.7 variation of time of drift reversal for different months of all seasons. [Aswathy and Manju., JASTP. 2020].

ionosphere in the vicinity. The results indicate that the unique trajectory of the PS4 orbiting station (in the initial phase) serves as an ideal one to investigate top side electron density enhancements. Further, the mission underlines the fact that the novel orbiting platform, will be useful for carrying out measurements of multiple parameters in the near-Earth space.

On the F- region zonal plasma drift variability and its linkage with equatorial spread F(ESF)

The study analyses the delayed occurrence of the F-region ionospheric manifestations like peak vertical drift and Equatorial Spread F onset time in summer solstice of low solar activity years, using the ionosonde data at the magnetic equatorial station Trivandrum (8.5° N, 76.9 ° E) and Republic of China Satellite-1 data. The analysis reveals the unambiguous role of the time of ionospheric F- region zonal plasma drift/ wind reversal in modifying the above-mentioned phenomena. The direct control of equatorial Spread F onset by the F- region drift/ wind reversal is clearly established on a day-to-day basis in summer season. The role of the time of zonal wind/ drift reversal in modulating the ESF onset is examined quantitatively by exploring its effect on the growth rate of Rayleigh - Taylor instability. Further, the study brings out the solar activity variation of the time of F- region zonal plasma drift/ wind reversal for all seasons (Fig.7). The dependence of the F region post sunset vertical drift on the zonal plasma drift is also brought out (Fig. 8). The results highlight the need to have systematic neutral wind measurements to better address the enigmatic and multi-dimensional problem of equatorial Spread F day-to-day variability.

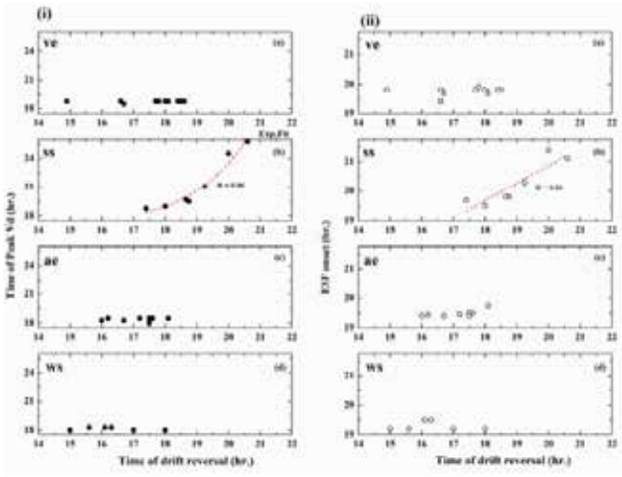

Figure 8: The correlation of monthly mean of time of drift reversal with time of peak Vd for ve (a), ss (b), ae (c) and ws (d) (ii) The correlation of monthly mean of time of drift reversal with time ESF onset for ve (a), ss (b), ae (c) and ws (d) [Aswathy and Manju., JASTP. 2020].

Space Weather and Comparative Aeronomy

Geomagnetic storm induced plasma density enhancements in the southern polar ionospheric region: a comparative study using St. Patrick's Day storms of 2013 and 2015

The occurrence of St. Patricks day (17 March) geomagnetic storms during two different years (2013 and 2015) with similar solar flux levels but varying storm intensity provided an opportunity to compare and contrast the responses of the Ionosphere -Thermosphere (IT) system to different levels of geomagnetic activity. The evolution of positive ionospheric storms at the southern polar stations Bharati (76.6°S MLAT) and Davis (76.2°S MLAT) and its causative connection to the solar wind driving mechanisms during these storms was studied using InSWIM GNSS receiver system at Bharti, Antarctica. During the main phase of both the storms, significant enhancements in

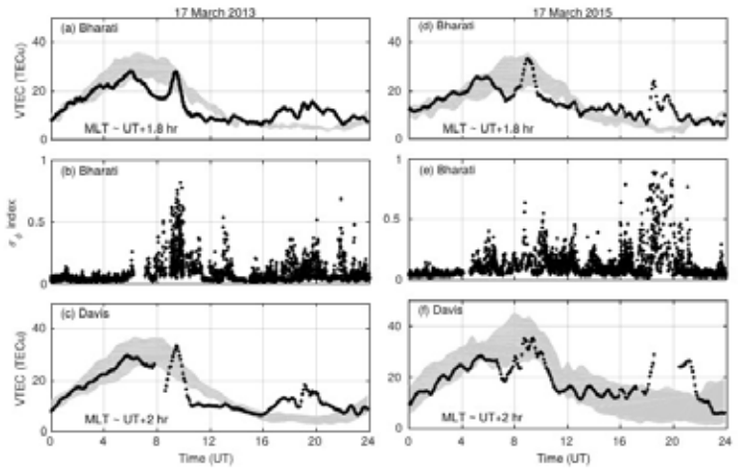

Figure 9: Panels (a) and (b) represent the diurnal variation of TEC and σ φ index, respectively, at Bharati 254 on 17 March 2013 while panel (c) represent the diurnal variation of TEC at Davis station on 17 March 2013. 255 Similarly, panels (d) and (e) represent the diurnal variation of TEC and σ φ index, respectively at Bharati on 17 256 March 2015 while panel (f) represents the diurnal variation of TEC at Davis station on 17 March 2015. The 257-black curve in panels (a), (c), (d), and (f) represent the variation in TEC respectively on the day of the storm 258 and the gray shade represents the quiet day standard deviation. [Shreedevi et.al., Space Weather, 2020].

TEC and phase scintillation were observed in the magnetic noon/midnight period at Bharati and Davis. The TEC in the midnight sector on 17 March 2015 was significantly higher compared to that on 17 March 2013, in line with the storm intensity. The TEC enhancements during both the storm events are associated with the formation of the SEDs/TOI. The strong and sustained magnetopause erosion led to the prevalence of stronger storm time electric fields (PPEF/SAPS) for long duration on 17 March 2015. This combined with the action of neutral winds at mid latitudes favored the formation of higher plasma densities in the regions of SED formation on this day. The same was weaker during the 17 March 2013 storm due to the fast fluctuating nature of IMF Bz (Fig. 9). This study shows that the duration and extent of magnetopause erosion plays an important role in the spatio temporal evolution of the plasma density distribution in the high & mid latitude ionosphere.

A comparative study of non-thermal parameters of the X-class solar flare plasma obtained from cold and warm thick-target models : error estimation by Monte Carlo simulation method

The electron transport and relaxation in the non-thermal plasma of solar flare are often described by cold thick-target model. Recently introduced warm thick-target model however is found to be more consistent for describing it and hence provide the accurate estimate of parameters of non-thermal solar flare plasma. In this study, we evaluated the consistency of cold and warm thick-target models by estimating non-thermal parameters viz., low-energy cutoff (E_c/E_{wc}), kinetic power of non-thermal electrons (P_{nth}/P_{wnth}) and non-thermal energy (E_{nth}/E_{wnth}), along with standard error (SE) and their linear statistical analysis with respect to flare duration (t_f). We evaluated the accuracy of these parameters using Monte Carlo simulation data in 2σ limits. We found that cold thick-target model gives high values

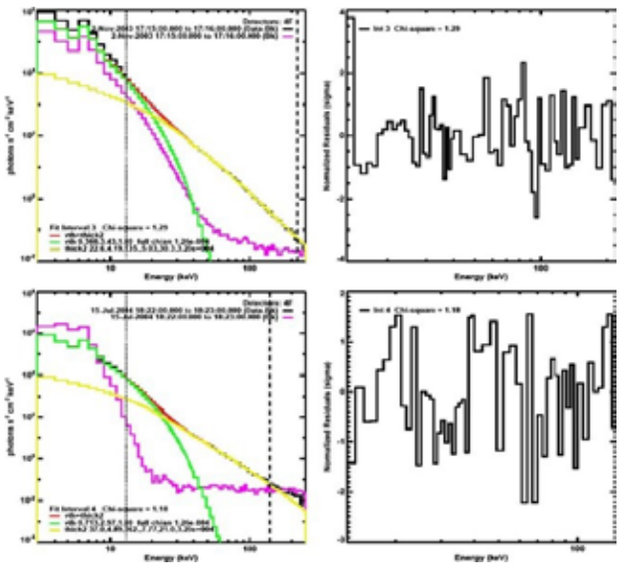

Figure 10: Figure shows two examples of the X-ray spectral fitting using the isothermal model (thermal component) and cold thick-target model (non-thermal component) in the energy domains 13–210 keV and 13–110 keV along with normalised residuals (right panels). The X-ray spectra were observed by the RHESSI spacecraft from the 2 November 2003 (X8.3) and 15 July 2004 (X1.6) solar flares respectively. In the figure, the thermal and non-thermal components of the X-ray spectra fitted with the isothermal and cold thick-target models are shown by the green and yellow line respectively. Here, the red line shows the integrated fitted line. The background flux is shown by the pink curve (Pramod et al, Astro Space Sc., 2020)

of mean and SE of the estimated parameters compare to warm thick-target model those were also found consistent with the Monte Carlo data (in both cases). We also found that the variation of E_c/E_{wc} and P_{nth}/P_{wnth} with respect to t_f give a negative / positive and positive values of correlation coefficient (r) and slope (b) respectively which account for

upper and lower limits of E_c/E_{wc} and high and slow rate of thermalization of non-thermal electrons(Fig. 10). Our results show that the warm thick-target model is a more consistent model compared to cold thick-target model that could also lead a multi-temperature component in the thermalized plasma.

Response of Martian Ionosphere to the Passage of a Co-rotating Interaction Region: MAVEN Observations

The response of Martian ionosphere to the passage of Co-rotating Interaction Region (CIR) event of June 2015 is studied using observations from several instruments aboard the Mars Atmosphere and Volatile EvolutioN (MAVEN) mission. An intense CIR arrived at Mars on 22 June 2015, during which the upstream solar wind and interplanetary magnetic field conditions were monitored by the Solar Wind Ion Analyzer (SWIA), Solar Wind Electron Analyzer (SWEA), Solar Energetic Particle (SEP), and Magnetometer (MAG) instruments aboard MAVEN (Fig. 11). The CIR event was characterized by enhancements in solar wind density, velocity, and dynamic pressure, and increased and fluctuating interplanetary magnetic field and was associated with enhanced fluxes of Solar Energetic Particles.

The Langmuir Probe and Waves (LPW) instrument onboard MAVEN provided the ionospheric observations such as electron density and electron temperature during this period. The dayside ionosphere is significantly compressed only near the peak of solar wind dynamic pressure enhancement (~14 nPa). In contrast, on the nightside, the electron density remains depleted for a longer period of time (Fig. 11). The electron temperatures are also enhanced during the period of electron depletion on the nightside. The Suprathermal and Thermal Ion Composition (STATIC) measurements

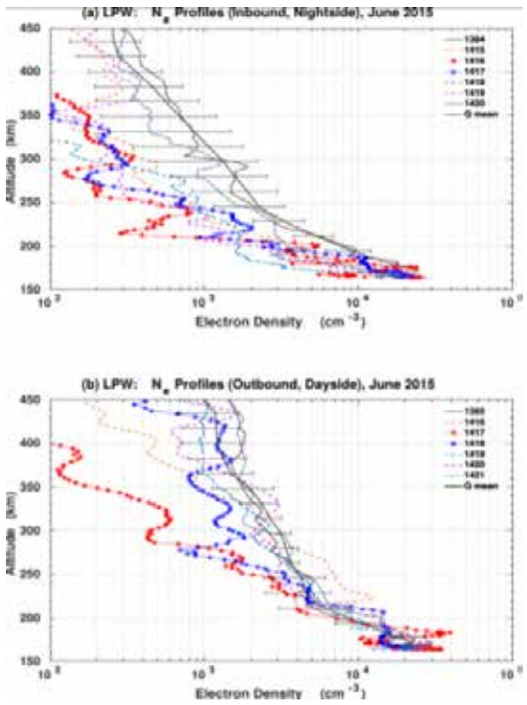

Figure 11: (a) The nightside and (b) dayside electron density profiles observed by LPW. The black thick solid line with error bar represents the mean quiet time profile and standard deviation of quiet orbits [Smitha et al., 2019, JGR]

show enhanced fluxes of suprathermal (>25eV) heavy ions in the Martian exosphere during CIR period (Fig. 12), and evidences for enhanced tailward flow of these pickup ions. The analysis suggests that the nightside ionosphere is primarily controlled by the precipitating Solar Energetic Particles and pickup ions transported across the Martian terminator and depletes significantly when the heavy ion flux in the exosphere enhances.

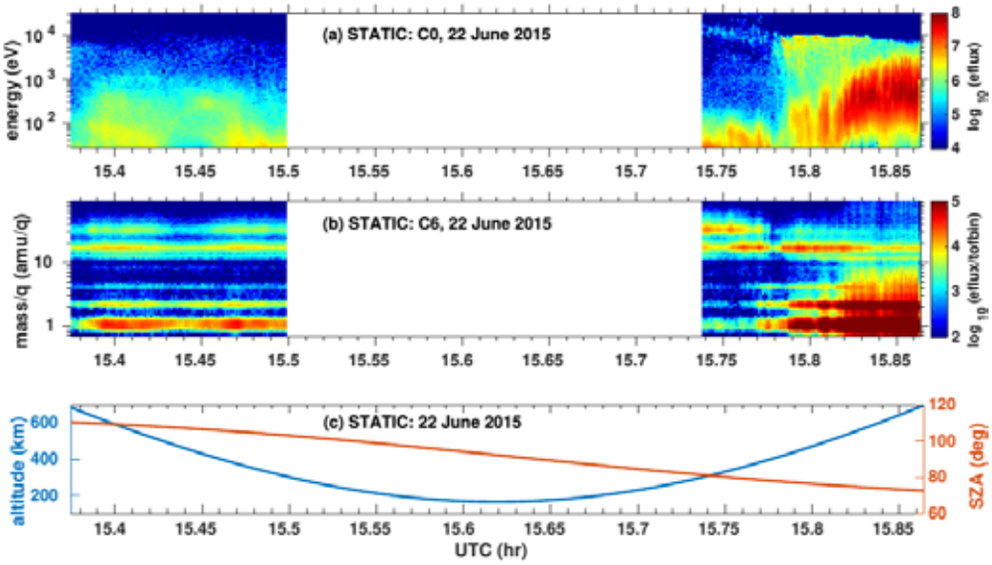

Figure 12: (a) STATIC energy-time spectrogram, (b) mass-time spectrogram of ion energy flux during disturbed orbit 1416/1417, (c) altitude and SZA during the observations. The eflux is expressed in units of differential energy flux (eV/[eV·cm²·sr·s]) [Smitha et al., JGR ,2019].

Ongoing Scientific Studies/Campaigns

Optical measurements of thermospheric Neutral winds and temperatures: First results from a dip equatorial station in India

The first ever systematic direct optical measurements have been made on the nocturnal thermospheric winds and temperatures from Trivandrum (8.5°N, 77°E, 0.5°diplat.) using a ground based high resolution Doppler imaging Fabry-Perot Interferometer (DFPI). The DFPI measures spectra and the Doppler shift of thermospheric nocturnal OI630 nm airglow emission that originates from ~ 200-300 km altitude region. The detector obtains high contrast interferometric concentric circular fringes for Doppler shifted OI630nm airglow emission. The fringe images obtained for two years have been analyzed to extract the thermospheric nighttime neutral temperatures and winds. It has been found that the observed meridional winds follow the HWM model trends while zonal wind exhibits marked differences between the two. The nocturnal temperature in general exhibits a decreasing trend with enhancements in post midnight hours on certain months. These finding are significant and results are being finalised.

Study of Equatorial Thermosphere-Ionosphere system during Solar Eclipse of December 26, 2019

The third and final solar eclipse of the year 2019 occurred on December 26, 2019, which was an annular eclipse, called as "ring of fire" eclipse. The annularity was visible in the middle east and east Asian countries. Over India, the umbra passed over the peninsular region near to the geomagnetic equator, in the south-east direction between ~8:00 and 11:00 hrs LT (Fig. 14). To study the effect of the systematic cut of solar radiation on the ionospheric currents over equatorial/low latitudes, a dedicated scientific campaign had been conducted using a chain of closely spaced fluxgate magnetometers over five locations namely Peravoor (11.89°N, 75.72 °E), Kalpetta (11.6°N, 76.08°E), Madurai (9.92°N, 78.12°E), Changanassery (9.44°N, 76.5°E) and Trivandrum (8.5°N, 76.9°E). The specific scientific objectives of the solar eclipse campaign were:

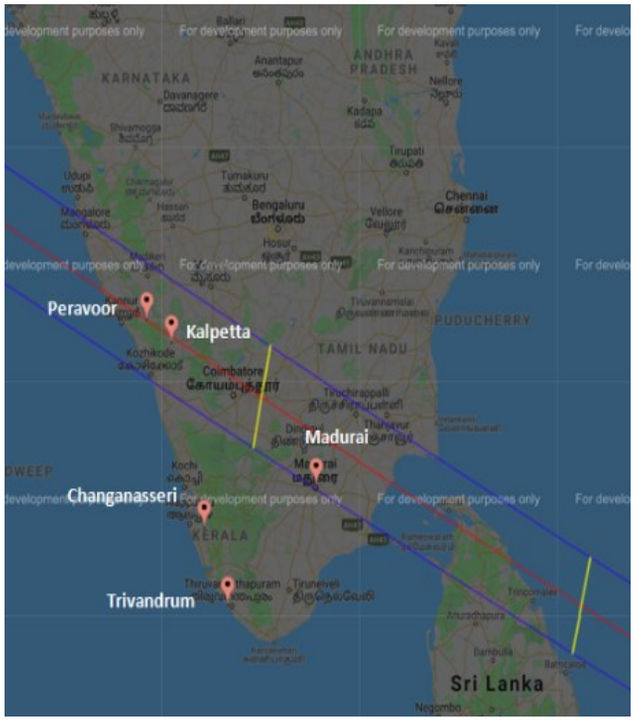

Figure 13: Path of the Solar Eclipse of December 26, 2019 over peninsular India along with the locations where magnetic field measurements have been carried out.

1. *To study the variability of ionospheric currents within and just outside the Equatorial Electrojet (EEJ) region during the solar eclipse.*
2. *To investigate the formation Counter Electrojet during/after the Solar Eclipse.*
3. *To study the longitudinal variability of ionospheric current during the passage of the eclipse shadow.*

Sounding Rocket Experiment (SOUREX-Phase-II)

The second phase of SOUREX campaign is planned by launching an intrumented RH-560 rocket flight from SHAR during February-March 2021. The main experiments onboard will be ENWi, LP and TMA, the former two payloads being operated in dual modes along with TMA for the study of ion drifts, electron density and irregularities in the upper ionospheric region. For this purpose, the required quantity of TMA for successfully imaging using ground based cameras has been worked out. Further, the locations for imaging the TMA trail have been identified as Gadanki, Kalpakkam, Kavli and SHAR. The camera and lens systems needed for the experiment have been finalized in collaboration with LEOS. The main objective of this experiment is to study the coupling of the Atmosphere - Ionosphere System (90-500km) using in situ measurements and to establish the transition from wind to drift regime in the ionosphere.

An evidence for a layer of elevated neutral density in the lunar atmosphere between 3 and 5 km altitude using DFRS measurements aboard Chandrayaan-2

Several set of ingress occultation experiments were conducted with DFRS (Dual Frequency Radio Science) payload aboard Chandrayaan-2 during October 2019 and March 2020. DFRS uses coherent radio signals at two frequencies (X, and S band), transmitted simultaneously from Orbiter and received at Ground, to study the temporal and spatial evolution of Lunar ionosphere, and atmosphere. The experiments were conducted in Open Loop mode using a Radio Science receiver at Indian Deep Station Network (IDSN), Byallalu. Theoretical estimates of the satellite Doppler were obtained and Doppler residuals were estimated after subtracting theoretical

Doppler from observed Doppler for both the frequencies. A sharp negative Doppler residual at both the frequencies were noted prior to satellite getting hidden behind the Moon. The negative Doppler residual represents bending of the radio signals due to ambient neutral medium of the probing atmosphere (which we normally assume the Moon to be bereft of). Following the standard procedure, bending angle and refractivity profiles were obtained from the Doppler residual data. An elevated layer of neutral particles of about 2 km thickness giving rise to bending of the satellite signals were noted. The base height of the layer appears to rise in altitude with increasing solar zenith angle. On assumption that the neutrals are purely of dusty origin having 0.1-micron size, the peak neutral density of the order of 10^{14} m^{-3} is obtained. The peak density decreases with decreasing solar zenith angle and no layer is seen at lower latitudes. The refractivity, bending angle, and Doppler residuals were simulated theoretically, which had a good match with the observed ones. Worth mentioning that the number density may vary depending on the dust size, and it could be of the order of 10^{11} m^{-3} if 1-micron size dust is assumed. On the other hand if the atmosphere of Moon is assumed to consist of 50% CO_2, and 50% H_2O (as reported in previous measurements), the required number density of neutral molecules may rise upto 10^{19} m^{-3} (which again is too large to be believed). We have no independent supporting evidence either to support or deny such possibilities.

Payloads and New Activities

RAMBHA-LP payload on Chandrayaan-3:

The Chandrayaan-3 RAMBHA-LP payload configuration remains similar to that flown on Chandrayaan2. The RAMBHA-LP is a Langmuir probe (LP) onboard Lander for in situ measurements of ambient electrons, ions, densities and their temperatures. The basic operational parameters and the mechanical/ electrical systems of RAMBHA-LP have therefore been kept unchanged. The RAMBHA- LP payload consists of the mechanical module i.e. probe and a boom and the control electronics module. Electronics system Proto FM of Ch-2 is to be made the FM after designer level tests. Mechanical System FM and standby are under development. The development of RAMBHA-LP boom is currently ongoing at CMSE/ VSSC.

Development of Atomic Oxygen Sensor Payload onboard PS4 Mission

In the altitude range of 100 – 500 km of the terrestrial upper atmosphere, commonly referred as 'thermosphere', the atomic oxygen (ATOX) is the most abundant atmospheric species. It plays a significant role in many of the natural reactions in terrestrial upper atmosphere, such as the formation of ozone and hydroxyl radicals in the mesosphere (50 – 100 km) and also contributes in photochemistry, ionization and energetics of the thermosphere region. At LEO altitude, it adversely influences the spacecraft materials by erosion and exerts significant aerodynamic drag resulting in the degradation of the spacecraft's orbit, especially in the high solar activity period. Hence, ATOX has received considerable attention in the space science and engineering community. In this context, Atomic Oxygen Sensor has been proposed for ISRO's PS4 orbiting lab for the in-situ measurements of the ATOX in the terrestrial thermosphere.

The proposed semiconducting material for detecting the ATOX is Zinc Oxide (ZnO) in thin film form because thin films are easier vacuum evaporate and also to package into a space-qualified unit. The thin films of ZnO will be vacuum deposited onto thin, high-purity (>99.6%) alumina substrates with evaporated gold leads to provide contacts for resistance measurement. Each ATOX sensor will consists of four films, two exposed to the ATOX environment and two covered with a layer of silicon dioxide (SiO_2). The SiO_2 overlay has been introduced to delineate the photoconductive effect due to solar UV radiation. The base sensor (ZnO alone) records the resistance change due to both ATOX and UV and the sensor with SiO_2 introduce resistance change due to photo conductance alone. Therefore, subtracting the latter from the former will give the resistance change only due to ATOX exposure. The semiconducting films need to be regenerated after ATOX exposure preferably when the sensor is at satellite perigee. For this purpose, each substrate has a thick film resistance heater made up of Ruthenium oxide in a glass frit, deposited on the opposite side of the alumina substrate to the thin films. Each heater will have a temperature sensor for controlling the temperature.

The proposed ATOX experiment will have two units, a sensor unit and an electronics unit, stacked together for ease of mounting and placement on the satellite. The sensor unit carries four zinc oxide films (two bare and two covered with SiO_2). The electronics unit contains the necessary circuitry for two-point film resistance measurement, temperature sensor and heater control. The maximum power consumption of the proposed sensor is < 5W, and the total mass is ~0.5 kg. To reduce the possibility of ATOX-induced contamination a ceramic sheet (which is resistant to ATOX attack and possess minimum out gassing property) will be used to support the sensor instead of a polymer sheet. The sensor will be mounted on the exterior face of the satellite that receives continuous ATOX exposure, whereas the electronics unit resides in the satellite interior; a harness connects the two. The rocket/satellite need to be spin stabilized. The orbit preferred is an elliptical one with perigee near 200

km and apogee above 1000 km. The ATOX measurement will be made near perigee, when the ATOX acts on the semiconductor and alters its resistance. The regeneration mode will be activated near apogee, where minimum ATOX is present, and the ZnO films can be renewed by heating.

Development of Upper-atmospheric Visible Airglow Spectral Imager (UrVASI) for DISHA-Aeronomy Satellite

DISHA is ISRO's forthcoming small Satellite Aeronomy mission to study the Disturbed and quiet time Ionosphere-thermosphere System at High Altitudes. UrVASI, a proposed payload onboard DISHA, is a diffraction grating based spectral Imager with CMOS/CCD as the detector. The spectral band of the instrument is 500-750 nm and the resolution envisaged is 0.1 nm. The primary scientific objectives of this experiment are, the investigation of *(i) Coupling between different atmosphere regions through lower atmosphere wave forcings (ii) manifestations of such processes inthe evolution of large-scale processes like the Equatorial Ionization Anomaly,Equatorial Spread-F (ESF) and Midnight Temperature Maximum (MTM) etc.* The initial Zemax design of URVASI has been carried out with the help of experts at Space Application Centre, Ahmedabad.

Development of Narrow band oxygen Airglow detection in the Venusian Atmosphere (NAVA) for Venus Mission

NAVA is a Fabry-Perot (FP) based two channel spectral Imager to detect oxygen airglow emissions in the Venusian atmosphere during both day and nighttime. Two narrow band (1 nm) interference filters of central wavelengths 557.7 nm and 630.0 nm will be used for pre-filtering the wavelengths, which will be passed through the FP etalon (nighttime without FP) then focused to the CMOS detector. The scientific objectives of NAVA are *(i) to study the interaction of the solar radiations and charged particles with Venusian Upper atmosphere, (ii) to study the transport of atmospheric species from dayside to nightside of the Venus (iii) detection of Oxygen Redline in the Venusian atmosphere etc.* The initial optical design of NAVA has been completed and reviewed in the Baseline Design Review committee.

Figure 14: The in-house developed Nighttime Photometer.

Development of an Automatic Nighttime Photometer for Airglow Network

The in-house developed Nighttime Photometer has been augmented to light weight, fully Automatic Nighttime Photometer (ANP) suitable for remote operations (Fig.14). This is capable of measuring five airglow emissions (557.7, 630.0, 777.4, 731.6 and 740.2 nm) nearly simultaneously. This photometer will enable multidirectional observations from multiple field locations and is significant capacity enhancement in the field of optical aeronomy from SPL. The details of the instrument are given later in this report.

Setting up of an Optical Instrumentation and Calibration Laboratory (OICL)

Space Physics Laboratory is involved in the development of cutting-edge optical instruments for ground-, rocket- and satellite- based platforms. In addition, four optical payloads have been accepted for the forthcoming Venus, Aeronomy Satellite (DISHA) and PS4 missions of ISRO. To design, develop, test and calibrate these instruments and also the ground based instruments an optical laboratory and calibration facility is being setting up at SPL. To begin with an optical bench with essential mounts, light sources, lasers, filters, lenses etc. have been set up. The partitioning for the passage for AC unit of InSWIm lab is in progress.

Electrostatic charging of the sunlit hemisphere of the Moon under different plasma conditions

Accounting for the continuous interaction of the solar radiation, the development of electrostatic charge on the sunlit lunar regolith under extreme plasma conditions has been investigated. The photoemission of electrons from the lunar surface corresponding to the solar radiation spectrum, electron energy-dependent secondary electron emission and simultaneous collection of the ambient non-Maxwellian plasma electrons/ions have been considered the dominant charging mechanisms. The lunar surface potential has been derived using the dynamical balance of the photoemission and plasma accretion currents over its surface-the potential dependence of the charging currents has consistently been accounted for. The outcome infers that depending on topography and location along with realistic plasma/surface parameters, the lunar surface may hold significant contrast in charging, and it may differ by the orders of magnitude.

Future Projections

The last year has been an important year for ITMP as the flight models of the proposed RAMBHA payload i.e. DFRS aboard orbiter and LP on Vikram (Lander), were flown ISRO's Chandrayaan-2 mission. The DFRS aboard orbiter has been making systematic occultation measurements since then. For the coming year, our efforts will be to bring out the first set of direct plasma measurements from Lunar polar region. Efforts are on to populating existing INSWIM chain of stations with ground based optical spectro-photometers. We are also making systematic nighttime measurements of thermospheric temperature and wind from Thumba. The first results on these will be forthcoming soon. In the recent years, ITMP has been attempting a closure on the problem of Equatorial Spread-F. We aim to achieve it soon. Our attempts to extend the scope of our studies to planetary ionospheres have been yielding very significant results, involving both measurements and models. We aim to continue the endeavour also by actively participating in ISRO's forthcoming planetary missions through developing experiments/payloads in-house.

Publications in Peer-Reviewed Journals

1. Ando, H., Takeshi Imamura, SilviaTellmann, Martin Pätzold, Bernd Häusler, Norihiko Sugimoto, Masahiro Takagi, Hideo Sagawa, Sanjay Limaye, Yoshihisa Matsuda, Raj Kumar Choudhary and Maria Antonita, 2020, Thermal structure of the Venusian atmosphere from the sub-cloud region to the mesosphere as observed by radio occultation, Sci Rep 10, 3448, DOI:10.1038/s41598-020-59278-8, (2020).

2. Aswathy, R.P., Manju, G., Time of evening zonal drift reversal in F- region and its implications for post sunset ionosphere, Journal of Atmospheric and Solar-Terrestrial Physics, DOI:10.1016/j.jastp.2020.105210, (2020).

3. Choudhary R. K., K. R. Bindu, Kumar Harshit, Rahul Karkara, K. M. Ambili, T. K. Pant, Devadas Shenoy, Chandrakanta, N. Hemanth Kumar Reddy, T. K. Rajendran, M. Nazer, and M. Shajahan, Dual Frequency Radio Science experiment onboard Chandrayaan-2: a radio occultation technique to study temporal and spatialvariations in the surface-bound ionosphere of the Moon, Current Science, Vol. 118 (2), DOI: 10.18520/cs/v118/i2/210-218, (2020).

4. Krishnaprasad C., Thampi, S. V., & Bhardwaj, A., On the response of Martian ionosphere to the passage of a corotating interaction region: MAVEN observations. Journal of Geophysical Research: Space Physics, 124, 6998–7012, DOI:10. 1029/2019JA026750, (2019).

5. Kumar, P., Choudhary, R.K., Sampathkumaran, P. and Mandal, S., 2020, A comparative study of non-thermal parameters of the X-class solar flare plasma obtained from cold and warm thick-target models; error estimation by Monte Carlo simulation method; Astrophysics and Space Science, 365(1), p.18, DOI: 10.1007/s10509-020-3731-9, (2020).

6. Kureshi, P., Keshav R. Tripathi, and S.K. Mishra, Electrostatic charging of the sunlit hemisphere of the Moon under different plasma conditions; Astrophysics and Space Science, 365:23, DOI: 10.1007/s10509-020-3740-8, (2020).

7. Jose, L., C. Vineeth, T. K. Pant and K. K. Kumar, 2020, Response of the Equatorial Ionosphere to the Annular Solar Eclipse of January 15, 2010, Journal of Geophysical Research, DOI: 10.1029/2019JA027348, (2020).

8. Manju, G., Tarun K. Pant, Mridula N., Aswathy R. P., P. Sreelatha, Rosmy John, Satheesh Thampi R., Aneesh. N. and Abhishek J. K., In-situ observations of rocket burn induced modulations of the top side ionosphere using the IDEA payload on-board the unique orbiting experimental platform (PS4) of the Indian Polar orbiting Satellite Launch Vehicle mission, Journal of Atmospheric and Solar Terrestrial Physics, DOI:10.1016/j.jastp.2020.105203, (2019).

9. Manju, G., Tarun K. Pant, P. Sreelatha, Santhosh J. Nalluveettil, P. Pradeep Kumar, Nirbhay Kumar Upadhyay, Md. Mosarraf Hossain, Neha Naik, Vipin Kumar Yadav, Rosmy John, R. Sajeev, Jothi Ramalingam, Philip George, Amarnath Nandi, N. Mridula, Aswathy R. P. Janmejay Jaiswal Rana, Snehil Srivastava and Satheesh Thampi, New outlook on lunar near surface plasma environment from Chandrayaan-2 lunar lander platform: RAMBHA_LP Lpayload perspective, Current Science, 118 (3), 383, DOI: 10.18520/cs/v118/i3/383-391, (2020).

10. Mridula, N., Tarun Kumar Pant, G. Manju, On the variability of the Equatorial Ionization Anomaly Trough over Indian region: A novel analysis using Beacon TEC measurements, Advances in Space Research, DOI:10.1016/j.asr.2020.04.040, (2020).

11. Singh, P.R., C.M. Tiwari, S.L. Agrawal, Tarun Kumar Pant, Periodicity Variation of Solar Activity and Cosmic Rays During Solar Cycles 22 – 24, Solar Physics, 294:118, DOI: 10.1007/s11207-019-1511-x, (2019).

12. Shreedevi P.R., R.K. Choudhary, Yiqun Yu, Evan G. Thomas, Morphological study on the ionospheric variability at Bharati, a polar cusp station in the southern hemisphere, Journal of Atmospheric and Solar Terrestrial Physics, Volume 193, doi: DOI:10.1016/j.jastp.2019.105058, (2019).

13. Shreedevi, P. R., Choudhary, R. K., Thampi, S. V., Yadav, S., Pant, T. K., Yu, Y., et al., Geomagnetic storm induced plasma density enhancements in the southern polar ionospheric region: a comparative study using St. Patrick's day storms of 2013 and 2015, 2020, Space Weather, 18, DOI:10.1029/2019SW002383, (2020).

14. Sivakandan, M., Mondal, S., Sarkhel, S., Chakrabarty, D., Sunil Krishna, M. V., Chaitanya, P. P., A. K. Patra, R. K. Choudhary , T. K. Pant, A. K. Upadhayaya and Takuya Sori, Midlatitude spread-F structures over the geomagnetic low-mid latitude transition region: An observational evidence. Journal of Geophysical Research: Space Physics, 124, DOI:10.1029/2019JA027531, (2020).

15. Sumod, S.G., and Tarun Kumar Pant, An investigation of solar fare effects on equatorial ionosphere and thermosphere using co-ordinated measurements, Earth, Planets and Space, 71:125, DOI:10.1186/ s40623-019-1105-8, (2019).

16. Das, T.P., Smitha V. Thampi, M.B. Dhanya, Neha Naik, P. Sreelatha, P. Pradeepkumar, G. Padma Padmanabhan B. Sundar, Dinakar Prasad Vajja, Amarnath Nandi, R. Satheesh Thampi, Vipin K. Yadav, J. K. Abhishek, , Md. Nazeer, P. T. Lali, Rosmy John, A. V. , Vijay Kumar Sen, M. Ramprabhu and A. Ajay Krishna, 2020, CHandra's Atmospheric Composition Explorer-2 onboard Chandrayaan-2 to study the lunar neutral exosphere, Current Science, vol. 118 (2), DOI: 10.18520/cs/v118/i2/202-209

17. Mukundan,V., Smitha V. Thampi, Anil Bhardwaj, C. Krishnaprasad, The dayside ionosphere of Mars: Comparing a one-dimensional photochemical model with MAVEN Deep Dip campaign observations, Icarus, 337, 2020, DOI:10.1016/j.icarus.2019.113502, (2020).

18. Mukundan,V., Smitha V. Thampi, Anil Bhardwaj, C. Krishnaprasad, Model calculation of ionization efficiency in the Martian dayside ionosphere using MAVEN observations, MNRAS, DOI:10.1093/mnras/staa2123, (2020).

19. Yadav, S., Choudhary, R. K., Kumari, J., Sunda, S., Shreedevi, P. R., & Pant, T. K., Reverse fountain and the nighttime enhancement in the ionospheric electron density over the equatorial region: A case study. Journal of Geophysical Research: Space Physics, 124, DOI:/10.1029/2019JA027286, (2020).

20. Yadav, S., Shiokawa, K., Oyama, S., & Otsuka, Y, Multievent analysis of oscillatory motion of medium scale traveling ionospheric disturbances observed by a 630 nm airglow imager over Tromsø, Journal of Geophysical Research: Space Physics, 125, DOI: 10.1029/2019JA027598, (2020).

Presentation/participation in Symposium/Conferences/Workshops

1. Manju G., Tarun Kumar Pant, Mridula N., "In-situ observations of rocket burn induced modulations of the top side ionosphere using the IDEA payload on-board the unique orbiting experimental platform (PS4) of the Indian Polar orbiting Satellite Launch Vehicle mission", URSI-Regional Conference of Radio Science, Indian Institute of Technology, BHU, UP, February 12-14, 2020.

2. Md. Mosarraf Hossain, C. Vineeth and Tarun Kumar Pant, "Optical measurements of thermospheric winds and temperatures, and investigations on the midnight temperature maximum over an equatorial station: First results", URSI-Regional Conference of Radio Science, Indian Institute of Technology, BHU, UP, February 12-14, 2020.

3. Tarun Kumar Pant, Manju, G., Zonal Wind Structures in ionosphere, URSI-Regional conference of Radio Scienc, Indian Institute of Technology, BHU, UP, February 12-14, 2020.

4. Tarun Kumar Pant, Manju, G., C. Vineeth and Md. Mosarraf Hossain, Observations of Equatorial Lower Thermosphere-ionosphere - Overview of Sounding Rocket Experiment (SOUREX), URSI-Regional Conference of Radio Science, Indian Institute of Technology, BHU, UP, February 12-14, 2020.
5. Krishnaprasad, C., Smitha V. Thampi, and Tarun K. Pant (2020), Energization of Martian Heavy Ions during Solar Energetic Particle Events: MAVEN Observations, Indian Planetary Science Conference, Physical Research Laboratory, Ahmedabad, February19-21, 2020.
6. Smitha V. Thampi, ISAMPE National Conference on Composites - INCCOM-16, Trivandrum, 2020.

Deputations

Tarun Kumar Pant

1. "Space Weather Task Team (SWTT)", CGMS working group meeting, May 25-29, 2020

Raj Kumar Choudhary

1. VeXAG 2019 meeting at LASP, Boulder, CO, USA during 06 – 11 November 2019 as an ISRO delegate.

Invited Talks

Tarun Kumar Pant

1. " Equatorial upper atmosphere and Space Weather – Results from India ", International Space Weather Workshop, International Centre for Theoretical Physics (ICTP), Trieste, Italy, May 20-24, 2019
2. "Introduction to Space Science", ISRO's Induction Training Program (IITP-32), Vikram Sarabhai Space Centre, November 5, 2019
3. "Space Science – An Emerging Perspective", National Conference on Fundamental and Applied Physics, Department of Physics, University College, November 12-13, 2019
4. "Near Earth Space - New Developments", IMPRESS 2020, Indian Institute of Geomagnetism, Navi Mumbai, February 3-6, 2020
5. "Near Earth Space: Challenges and Achievements", Department of Electronics and Communication Engineering (ECE), University College of Engineering (UCE), Osmania University (OU), Hyderabad, February 26, 2020
6. "Earth's Upper Atmosphere - emerging view ", Special Teacher's Training Program (STTP), Department of Electronics and Communication Engineering (ECE), University College of Engineering (UCE), Osmania University (OU), Hyderabad, February 27, 2020
7. "Exploration of Earth and Space - Emerging Perspective", Lead Talk in Physics, 14th Uttarakhand State Science and Technology Congress (USSTC) 2019-20, Uttarakhand State Council for Science and Technology, Dehradun, February 27-29, 2020

Raj Kumar Choudhary

1. "Exploring the ionosphere of Venus using Radio Occulation technique" at Indian Planetary Science Conference (IPSC-2020) at , PRL, 19-21 February 2020.
2. "Radio occultation for moon and other planetary ionosphere" at 4th URSI Regional Conference on Radio Science (URSI-RCRS 2020), held at IIT-BHU, Varanasi, India from 12-14 February 2020.

Krishnaprasad C.

1. Space and Planetary Science: An Introduction at "Sasthra Padham" program of Govt. of Kerala for higher secondary school students organised at Govt. Victoria College, Palakkad (31 January 2020).

Smitha V Thampi

1. Science Observations: CHACE-2/Chandrayaan-2, Indian Planetary Science Conference (IPSC-2020), PRL, Ahmedabad, India 19-21 February 2020 (Invited talk, with contributions from CHACE-2 team).
2. Webinar on "Space Weather" at B. C. M. College, Kottayam (23 May 2020).

Trainings Programme

Manju G

1. DTDI training program on Artificial Intelligence, November, 2019.

Md. Mosarraf Hossain

1. Structured training programme on “Scientific Satellite Missions”, 22-28 Jan-2020, jointly organized by SAC and PRL, Ahmedabad.
2. Visiting Faculty at Department of Physics, Indian Institute of Space Science and Technology (IIST), Trivandrum for conducting M. Tech. (Optical Engineering) course entitled “Optical Fabrication and Testing”, July-November, 2019.

Mridula N

1. Evaluator at National Childrens’ Science Congress, Trivandrum, December, 2019.
2. National conference for Women on Climate change, Mussoorie, February 2020.

Krishna Prasad C.

1. Heliophysics Summer School 2020 organized by CPAESS/UCAR, Boulder, CO, USA, July 2020.

Public Outreach

Manju G.

1. Evaluator at National Childrens’ Science Congress, Trivandrum, December, 2019.

Vineeth C.

1. Convener, Resource Material/Content Generation Committee constituted for celebrationg for World Space Week-2020 (4-10 October, 2018).

Planetary Science Branch

Planetary Science Branch (PSB) of SPL plays a major role in planetary exploration by spreading its wings on developing the state-of-the art scientific payloads for the space and planetary missions of ISRO as well as analysis and interpretation of the scientific data. The entire research and development activities of PSB is planned under the umbrellas of three major themes. These themes are (a) interaction of solar radiation with planetary atmospheres and the processes initiated through this interaction, (b) solar wind and its interaction with different planets and planetary objects, and (c) planetary neutral atmospheres through in-situ observations. Since the prestigious Chandrayaan-1 mission of ISRO, PSB was involved in the experiments like Sub-keV Atom Reflecting Analyser (SARA) onboard CH-1, Mars Exospheric Neutral Composition Analyser (MENCA) on-board Mars Orbiter Mission (MOM) and Chandra's Atmospheric Composition Explorer (CHACE-2) onboard CH-2 Mission. These experiments were very successful in terms of its scientific outcomes. The data archival and analysis of MENCA and CHACE-2 payloads are also in progress. In terms of instrumentation, presently PSB is focussing on the scientific payloads like Plasma Analyser Package for Aditya (PAPA) for Aditya-L1 Mission and Venus Ionospheric and Solar Wind Analyser (VISWAS), Venus Ionospheric Plasma wavE detectoR (VIPER) for the upcoming Venus Mission. Payloads like Plasma AnalyseR for the Environment of Mars (PREM) and the magnetometers (flux gate and search coil) for the Mars Orbiter Mission -2 (MOM-2) of ISRO are also under development. As per the developmental needs, the High Vacuum Space Simulation Facility (HVSSF) of SPL and the advanced Payload Operation Centre (POC) of SPL are being routinely augmented.

Science Team

Satheesh Thampi R
Vipin Kumar Yadav
Dhanya M. B.
Venkataraman V
Abhishek J.K

Technical Team

Dinakar Prasad Vajja
Aneesh A. N.

Research Associates

Vrinda Mukundan*

Research Fellows

Govind G. Nampoothiri

* Relieved in June 2020

Interaction of Solar Radiation with Planetary Atmospheres and the Processes Initiated through this Interaction

A Photochemical Model for the dayside ionosphere of Mars

The Martian ionosphere is mainly produced by the ionization of the atmospheric neutral gases by solar EUV-photons and EUV-produced photoelectrons. Collisions of these photons and photoelectrons with the dominant neutral molecules, such as CO_2, CO, and N_2, result in the formation of ionized species, like CO_2^+, O_2^+, and N_2^+. They initiate a chain of chemical reactions in the upper atmosphere, including dissociation, ionization, charge exchange and recombination reactions and results in an ionosphere with O_2^+as the most dominant ion. In the present study a one dimensional photochemical model for the dayside ionosphere of Mars has been developed for calculating the density profiles of ions and electrons under steady state photochemical equilibrium condition. Presently, the Mars Atmosphere and Volatile Evolution Mission (MAVEN) is providing in-situ composition measurements and unprecedented data on Martian thermosphere and ionosphere. The model simulated the conditions that prevailed on Mars during the deep dip (DD) campaigns of MAVEN. During deep dips the spacecraft went deeper into the atmosphere with periapsis at around 120-130 km, the region near the ionospheric peak, as compared to nominal orbits for which typical periapsis is at ~150 km. Two orbits each from three dayside deep dip campaigns viz. DD2, DD4, and DD8 are chosen and the MAVEN measured neutral densities, solar flux and electron temperatures for those respective orbits are used as input to the model. The modelled ion profiles are compared with the ion mode observations of Neutral Gas Ion Mass Spectrometer (NGIMS) and electron density estimates from Langmuir Probe and Waves (LPW). Such a comparison for the deep dip periods is reported for the first time, which showcases the level of the current understanding of the ion chemistry in the Martian ionosphere. Comparing the model calculations with MAVEN observations helps to validate our understanding of the physical and chemical processes occurring in the atmosphere. The differences and similarities between model and the observations give insight into whether our current understanding of the atmospheric processes are capable of forming the observed features of the Martian ionosphere.

In addition to the major ions O_2^+ and CO_2^+, the model calculated the profiles of 11 more ions viz. N_2^+, N^+, OH^+, $OCOH^+$, HNO^+, HCO^+, C^+, O^+, N_2H^+, and NO^+. The model could correctly reproduce the similar altitude variation as the observed O_2^+, CO_2^+ and the observed electron density. However, the magnitude of the modelled profiles seems to be a factor of ~1.5, 2.5, and ~1.5 larger than the NGIMS-O_2^+, NGIMS-CO_2^+, and LPW-electron densities, respectively (Fig. 1). To understand this, the model inputs were tweaked and the sensitivity analysis showed that reducing the NGIMS-measured CO_2 density or the LPW-measured electron temperature by a factor of four can bring good match between the modelled and the observed electron density profiles. Since reducing the NGIMS-measured CO_2 density could reproduce the observed O_2^+, CO_2^+ (and therefore the electron density profile), this seems to be the most viable option. This indicates an over estimation in the neutral CO_2 density measured by NGIMS. However, the model could very well reproduce the observed profiles of the ions O^+, C^+, and N^+ using the actual NGIMS-CO_2 density without applying any scaling factor. Therefore, the simulations cannot conclusively confirm that the neutral CO_2 densities are exactly off by a factor of four, but only indicate a possibility of overestimation in the NGIMS-CO_2 density.

The model overestimates the NO^+ by one order of magnitude when the NO density profile reported using the previous version of the NGIMS data is used for the calculation. Using the available modelled profiles of NO as input could reduce the difference between the modelled and the observed NO+ densities. Similar is the case with HNO^+ where model predicted densities were much lesser than the observations. The study suggests that either with the currently existing chemistry scheme, the models are not able to reproduce the observed HNO^+ density, or the NGIMS could be overestimating the HNO^+. The $OCOH^+$ density profile is found to be highly sensitive to the structure of the neutral H_2 profile used as input to the model. For the water group ion OH^+, the model calculations are consistent with the observations at higher altitudes (>150 km). This study

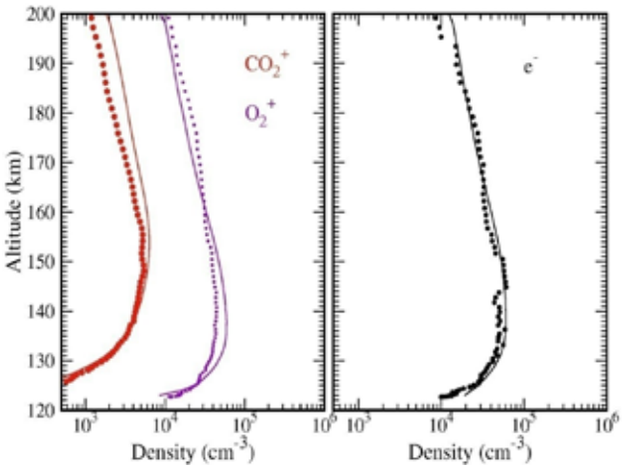

Figure 1:The left panel shows the modelled profiles of CO_2^+ (red lines) and O_2^+ (blue lines) compared with the NGIMS observations (solid symbols) for the deep dip campaign 4 (DD4) orbit 1824. The modelled CO_2^+ (O_2^+) profiles are scaled by a factor of 2.5 (1.5) to make them in agreement with the observations. The right panel shows the modelled electron density profiles (lines) compared with the LPW observations (solid symbols) for the same orbit. The modelled profiles are scaled by a factor of 1.5 to make them in agreement with the observations. (Vrinda M. et al, 2020, Icarus)

is the first attempt to compare the minor ion concentrations observed during the MAVEN DD campaigns with the outputs of a photochemical model.

Model calculation of ionization efficiency in the Martian dayside ionosphere using MAVEN observations

The ionization efficiency (η), which is defined as the ratio of the electron impact to the photon impact ionization rates, is calculated for the dayside Martian ionosphere using Mars Atmosphere Volatile EvolutioN (MAVEN) observations of neutral density and solar flux as input to the model. To calculate the secondary (electron impact) ionization rates, the photoelectron flux is computed using the Analytical Yield Spectrum (AYS) approach. Model calculations suggest that η should increase consistently as altitude decreases in the lower ionosphere. However, when the secondary ionization rates are calculated using the SWEA/MAVEN measured photoelectron flux, the ionization efficiency remains constant in the region 160–250 km. This behaviour is not in agreement with the theory of the altitude variation of ionization efficiency. The reason for this discrepancy is examined in detail. It is suggested that this disagreement is caused by the altitude-independent nature of MAVEN measured photoelectron flux. In two MAVEN deep dip orbits SWEA measured flux showed an altitudinal variation and the η curve estimated using these observations showed the variation in agreement with the theory. This suggests that the ionization efficiency calculated using SWEA/MAVEN measured photoelectron flux will show an altitude-dependent behaviour only when the instrument can resolve the altitudinal variation in the electron flux. The ionization efficiency for two MAVEN dayside deep dip campaigns were also calculated. The efficiency of CO_2 and O showed an increase of 30% and 60%, respectively, at 130 km as compared to its value at 200 km.

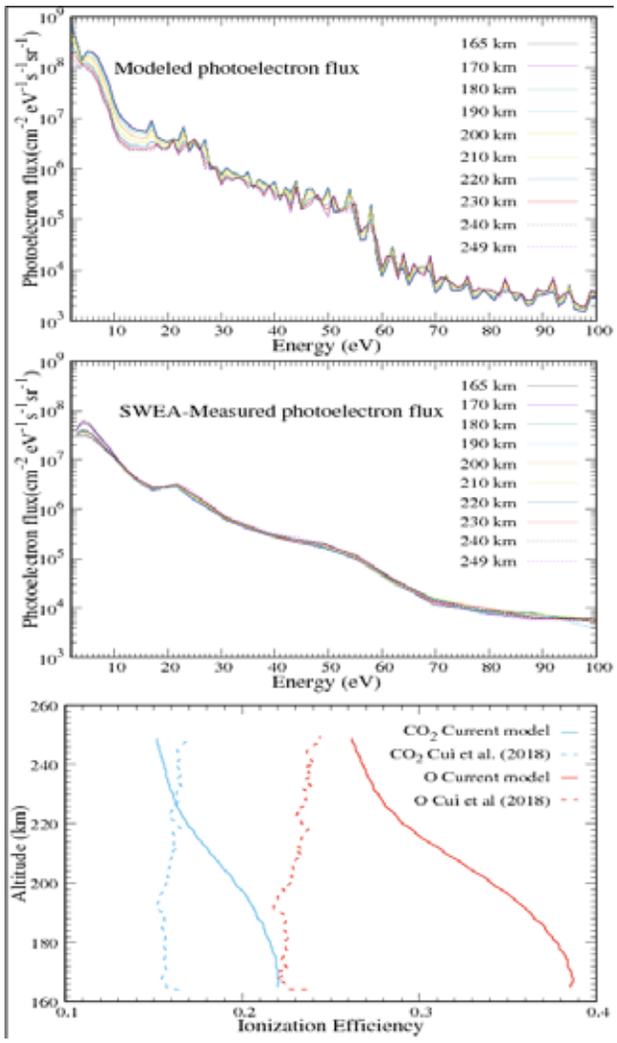

Figure 2: The top and the middle panel show the modelled photoelectron flux, and (SEA-measured photoelectron flux at different altitudes for O3043, respectively. The bottom panel is the ionisation efficiency of CO2 (blue) and O(red) calculated in the present study (solid curves) using modelled photoelectron flux compared with the calculations of Cui et al. (2018) (dashed curves).

Solar wind and its interaction with planets and planetary bodies

Plasma Analyser Package for Aditya (PAPA) onboard Aditya-L1

The development of PAPA payload is in full swing and most of the subsystems like front end electronics (FEE), high voltage programmable power supply (HVPPS) and PAPA Processing Unit (PPU) Engineering Models (EM) are realised and are independently interfaced with the EM sensor and the functionality tests were performed. The integrated test of Engineering Model (EM) is also completed and the performance is normal. The parallel development of Qualifying and Flight Models (QM&FM) are in progress. The two major parameters expected from the PAPA payload are the energy (for electron/ions) and mass information (ions) of the solar wind. The comparison of the experimental results from EM is matching with that of simulations and is satisfactory.

Angular Response study of PAPA Engineering Model

Plasma Analyser Package for Aditya (PAPA) payload has a field of view of 130°× 30° at each sensor (SWEEP & SWICAR) with an angular resolution of 4° × 30°. The field of view is necessary to cover the angular spread of the incoming solar wind particles, and the angular resolution helps to accurately map the particle alignment with the interplanetary magnetic field.

A series of laboratory tests were conducted to determine the field of view and angular resolution using the PAPA engineering model. The angle of particle incidence was varied from -90° to +90° with respect to the normal and corresponding sensor response was mapped. The particle beam used was that of helium ions (He^+) with energy of 3000 eV and at a vacuum level of 2×10^{-6} mbar. The field

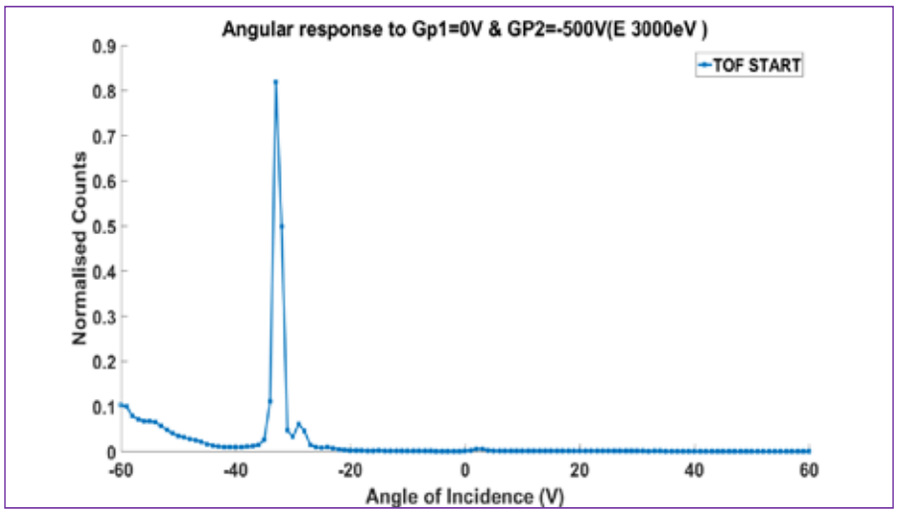

Figure 3: Angular response of SWICAR sensor @ 3000 eV particle energy when left Guiding Plate voltage was at 500 V.

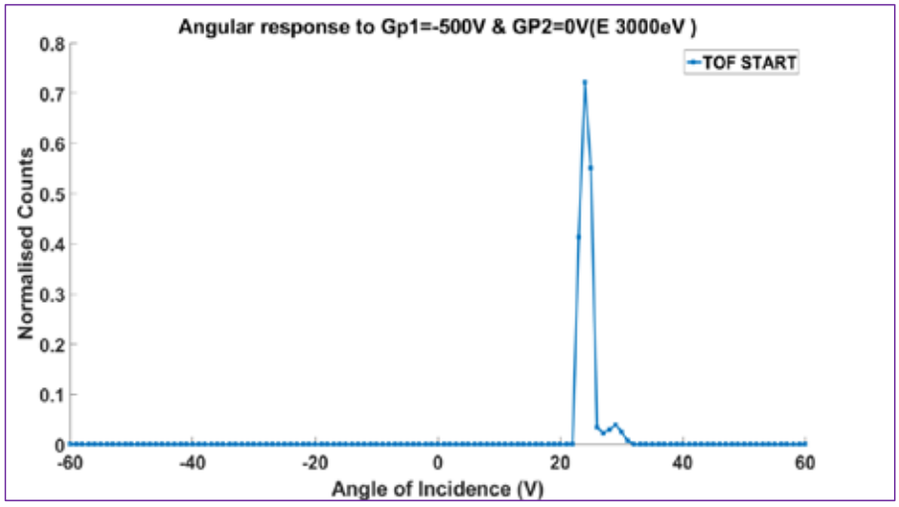

Figure 4:Angular response of SWICAR sensor @ 3000 eV particle energy when right Guiding Plate voltage was at 500 V.

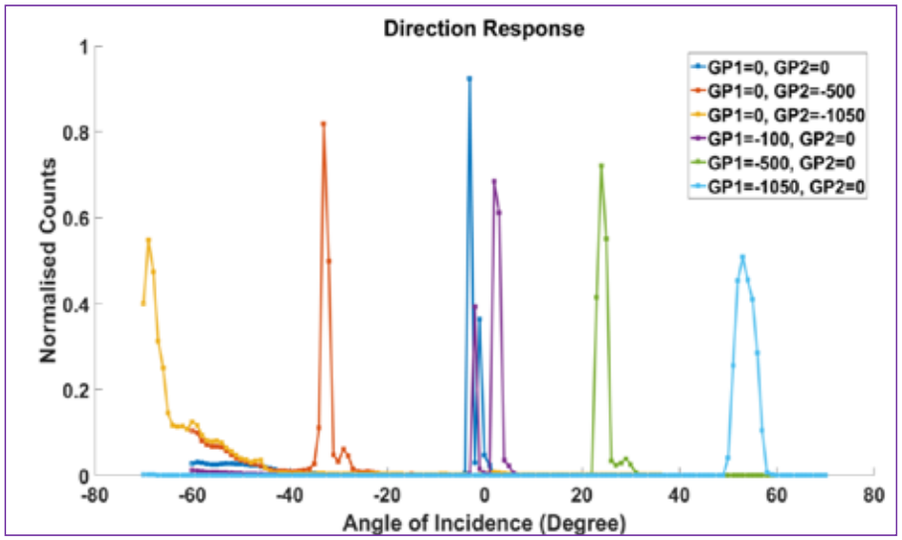

Figure 5: Angular response of SWICAR sensor at six different angles

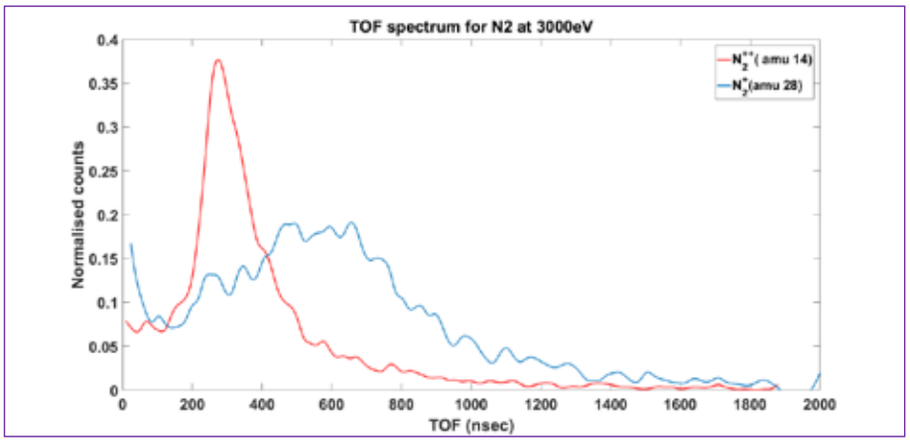

Figure 6: TOF spectra for two charge states of nitrogen (N_2^{++}, N_2^{+}). Blue curves represent the ions with single charge state and the red curves represent those withdouble charge state.

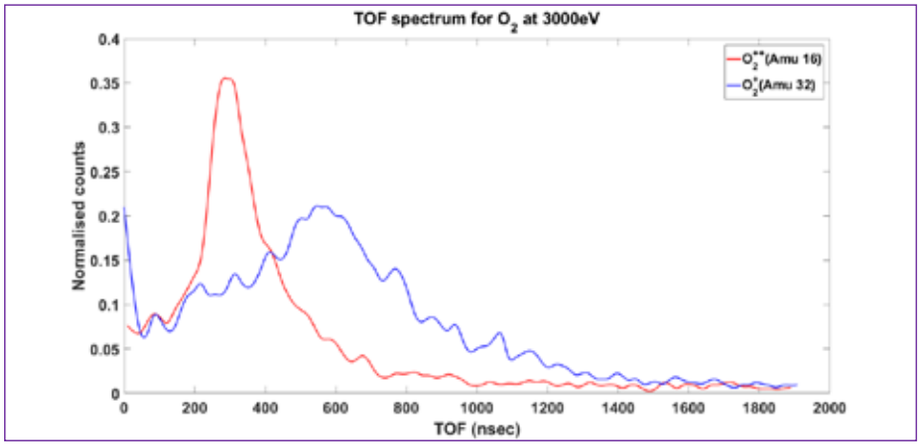

Figure 7: TOF spectra for single (blue) and double (red) charge states of O_2.

of view was determined to be 130° in the azimuth. The resolution was found 4° at all angles. The angular response of SWICAR sensor at 3000 eV is shown in Fig. 3.

Fig. 2 shows that corresponding to a Guiding plate voltage of 500V, SWICAR allows only particles within a narrow angular range of 4° centred around 33°. Fig. 4 shows the response for the right guiding plate, and it is found that that a voltage of 500 V on the other guiding plate gives a pass band centred around 24°. The asymmetry in the angle is due to the uncertainty in the 0° position between PAPA Payload and ion gun. Fig. 5 shows the angular response at six different angles within the field of view of PAPA.

Table 1. Summary of tests conducted on CEM detectors

Sl. No	Test	Test Condition	Test method
1	Visual Inspection	X 10 Magnification	MIL-STD-883, Method 2009
2	Go/no go Check	functional	-
3	Vibration	8.5 (Thrust) /7.9 grams (Lateral) random, 2 minutes.	-
4	Visual Inspection	X 10 Magnification	MIL-STD-883, Method 2009
5	Serialization	Segregate the components based on date code and mfr.	Each component is marked with a serial number.
6	Pre Burn-in	SRC	As per the test plan document.
7	Burn-in	168 Hrs , 65°C	MIL-STD-883, Method 1015, Method C
8	Post burn-in	SRC	-
9	Final visual Inspection	X 10 magnification	MIL-STD-883, Method 2009
10	Dehydration baking	24 hrs at 65°C	

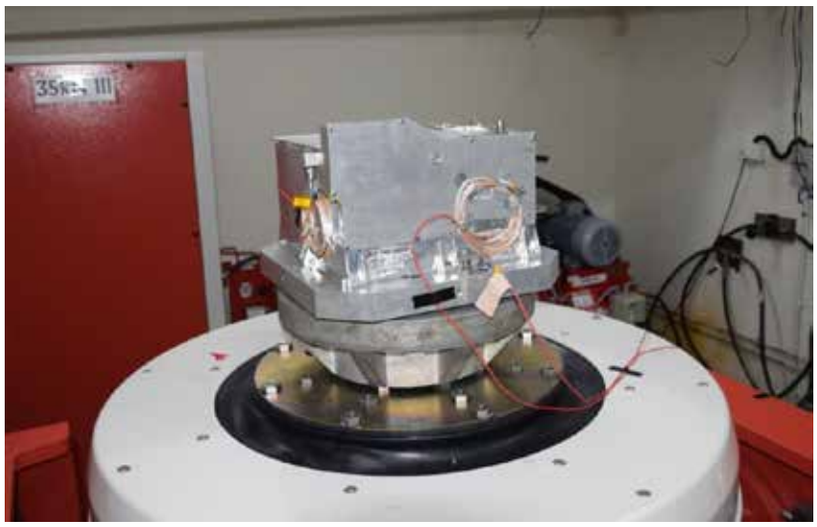

Figure 8:CEM detector vibration test setup for PAPA using engineering model.

Test Article	CEM Detector EM (PAPA)	Date/Time	Tue Aug 20 2019 14:30:59
Frequency Resolution	4Hz	Run Name	XX Axis Random DQT 10sec_1
Location ID	Near SWICAR STOP detector	Full Level Time	0:02:00.06

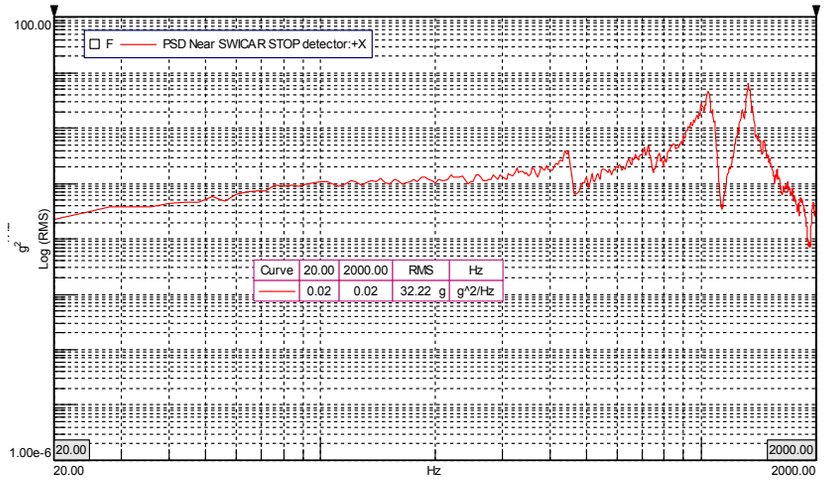

Figure 9: X-axis random vibration results for SWICAR STOP detector.

Charge state identification of ions using PAPA

The Time of Flight (TOF) section of PAPA payload was tested using ionic species with different charge states using the ECR ion source at the high vacuum space simulation facility (HVSSF). Doubly and singly ionised Nitrogen and Oxygen ions at different energies were tested as input to the payload. It was found that the measured time of flight values were in agreement with the theoretical estimates and the difference in the values is also consistent with the estimated ones.

Table 2: Expected radiation dose in different phases of the Aditya-L1 mission

	Radiation Dose in Silicon		
Al absorber thickness (mm)	Transfer orbit (11 Days)	Transit (101Days) + 5 Year Halo orbit(rad(Si))	Mission Total Dose
2.00	1.61×10^4	1.19×10^4	2.80×10^4

Table 3: Comparison of observed and theoretical time of flight values obtained using PAPA -EM

Species and Energy	Observed TOF (nS)	Theoretical TOF (Without Energy loss at Carbon foil) (nS)	Difference (nS)
He (3000 eV)	278	237	41
He (5000 eV)	211	183	28

Figure 10: Proton beam displacement damage test setup at TIFR, Mumbai

The tests were carried out for particle beams of N_2^{++}, N_2^{+}, O_2^{+}, O_2^{++} ions at anenergy of 3000eV and at a vacuum level of 5×10^{-6} mbar. Figs. 6 and 7 shows the time of flight spectrum for both singly and doubly ionised Nitrogen and Oxygen molecules respectively. The broadening of spectrum is due to the energy distribution and angular spread of ions when passing through the ultra-thin carbon foil.

CEM detector and Carbon foil vibration Tests

PAPA payload uses four Channel Electron Multiplier (CEM) detectors and one carbon foil for the electron and ion measurements. These detectors are to be tested and qualified for the space usage at different vibration and temperature levels as given in the Environmental test level specifications document. The detectors were mounted in the PAPA engineering model and corresponding vibration tests were performed. Table-1 summarises the list of tests carried out on CEM detectors in sequence. Fig.8 shows the PAPA engineering model with the detectors and dummy electronics card (to simulate the mass) mounted on the X-Y plane of the vibration table and Fig. 9 shows the test result.

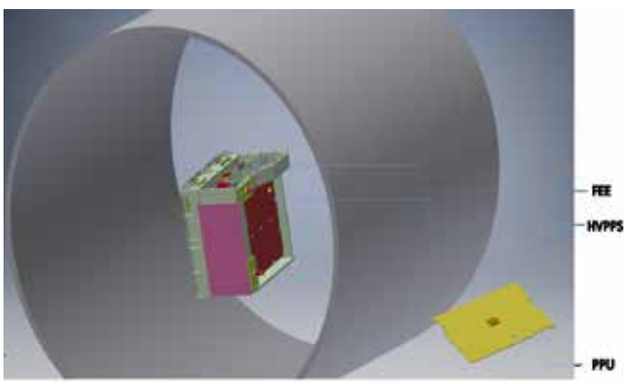

Figure 11:Schematics of PAPA-EM Test configuration

Total ionisation Dose (TID) and proton beam displacement (DD) damage test for PAPA payload electronic components

PAPA payload is expected to be exposed to radiation environment during its transfer orbits, 101 days transit period from earth to L1 insertion and 5 years in halo orbit (Table 2). So, all the detectors used in the payload are expected to meet the Displacement Damage Dose of 2.17×10^8 MeV/g or Displacement Damage Equivalent Fluence (DDEF) of 3.14×10^{10} (10 MeV proton).The Total Ionisation dose was tested using ^{60}Co Gamma-rays at the ISITE facility, Bangalore, and the Displacement damage test was conducted at Pelletron Linear Acceleration facility at TIFR Mumbai (Fig. 10). The CEM detectors successfully cleared both the TID and DD tests.

PAPA EM test results with integrated PPU

Pre integration tests of PAPA payload Engineering Model were carried out at HVSSF, SPL. The PAPA processing unit (PPU) card was kept outside the vacuum chamber whereas the front end electronics (FEE) and the high voltage programmable power supply (HVPPS) cards were integrated with the chassis,and were kept inside vacuum. The complete biasing and data acquisition commands are carried out using the PPU card. Fig. 11 shows the schematics of the test setup. Testing for two of the particle energy settings were performed two times (for consistency check) and the corresponding time of flight results are described below for a Vacuum level of 9×10^{-7} mbar, for He^+ ions, with flow rate of 10 sccm, RF of 10 W, horizontal deflection of +100V, and for energies of 3000 eV and 5000 eV.

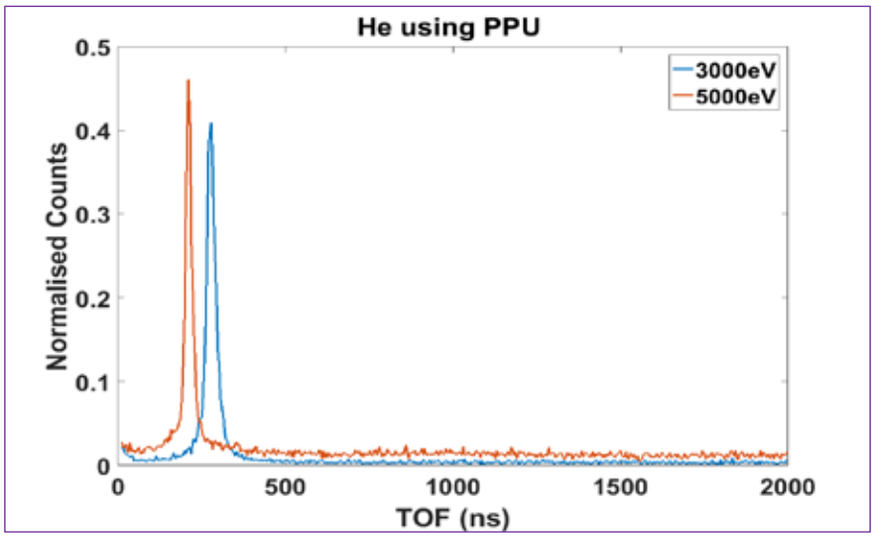

Figure 12:TOF spectra for helium ions (He^+)of energies 3000 eV and 5000eV

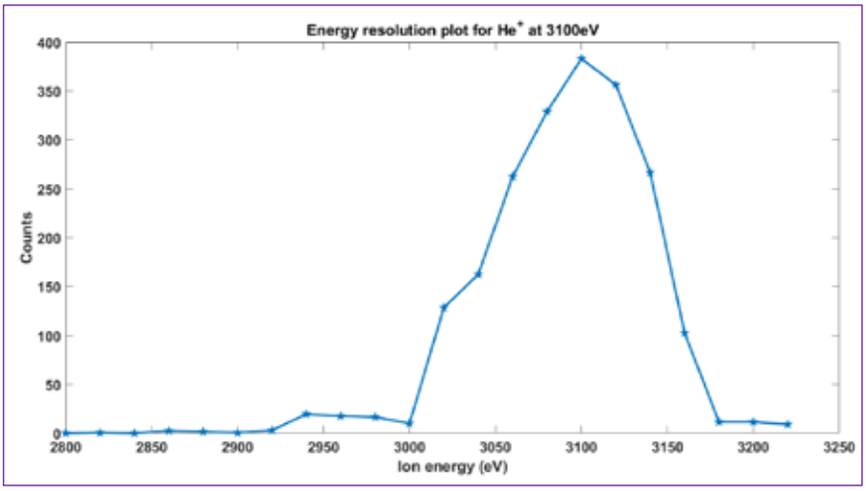

Figure 13: Energy responsefor He^+ at 3100 eV for PAPA EM

Fig. 12 shows the time of flight spectrum of helium ions for energies of 3000 eV and 5000 eV. From the spectrum the observed time of flight values are taken and are compared with the theoretically expected values and are shown in Table.3. Fig. 13 shows the energy resolution plot for helium ions at 3100 eV and is less than 8%..

Surface stoichiometric studies of cupric oxide coating for PAPA

Both the SWICAR and SWEEP sensors of PAPA have Electrostatic Analysers (ESA) to measure the energy of charged particles. Solar UV photons that undergo multiple reflections within the analyser structure can generate photoelectrons or stimulate channel electron multiplier (CEM) detector. The most significant UV contribution from the sun is through the Lyman alpha line at 121 nm with an intensity of 2.4 x 10^{11} photons cm^{-2} s^{-1} at 1 A.U. These photons are enhanced typically by a factor of 3 during the solar maximum. Hence it is essential to reduce the intensity of this potential background source. Previous missions have employed a low reflectivity coating based on copper oxide in the internal surface of the analyser plates to suppress the UV contribution. Cupric oxide (CuO), is a p-type semiconductor with excellent UV absorption characteristics. band gap energies in the range of 1.56 and 1.85 eV for its thin films. The CuO coating was established by chemically oxidising the Aluminium surface with sodium chlorite. The stoichiometry of the coating was studied using Raman spectroscopy. Fig. 14 represents the Raman spectra of the CuO coating. The peaks at 282, 330 and 616 and 1094 cm^{-1} show the presence of nanocrystalline CuO particles that are used for UV suppression in ion-optical instruments.

UV response studies of the CuO coating

The efficiency for suppressing the UV photons by the CuO coating was studied by illuminating it with a high brightness Hamamatsu make, vacuum UV lamp (L10366 series).

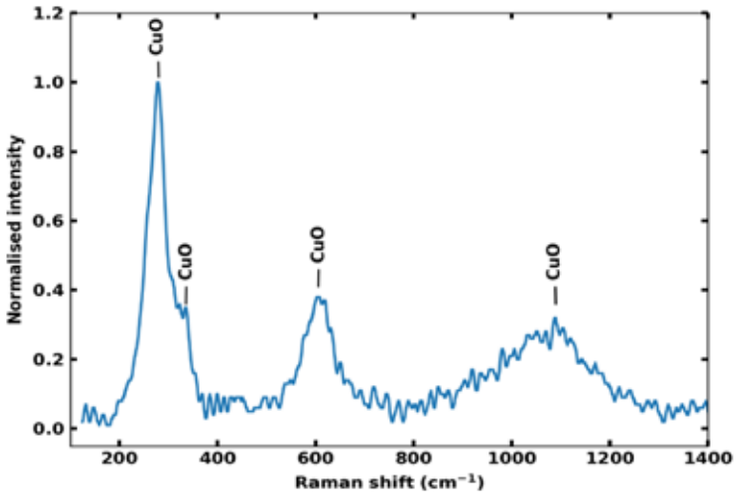

Figure 14. Raman spectra of CuO coating

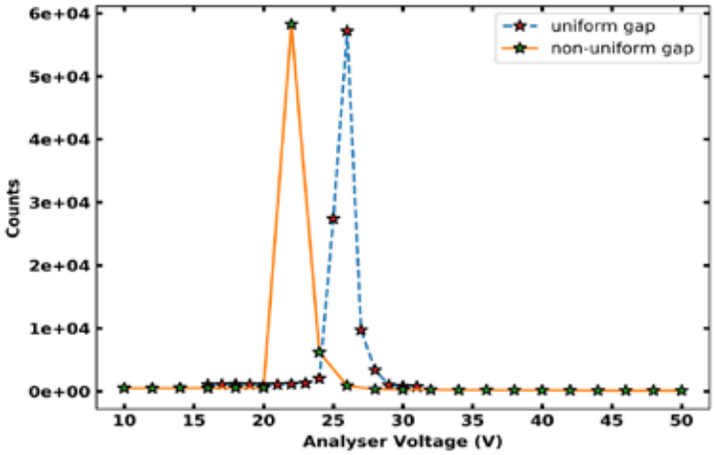

Figure 15: Change in the applied voltage due to a non -uniform gap s

Calibration of the UV lamp

The power density of the UV lamp was measured at ISRO Inertial Systems Unit (IISU) using a UV radiometer RM 22, with a UVC sensor manufactured by OpsytecDr. Grobel, which is sensitive to the wavelength range 200 to 280 nm. The UV power meter directly gives the integrated power density of the UV lamp. The power density was measured at various working distance from the source. This calibration was used to deduce the number of photons entering the aperture of PAPA.

Comparison of UV induced photoelectron counts between bare and coated ESA

The UV induced photoelectron counts as measured by the Channel Electron Multiplier (CEM) on the bare (uncoated) and the coated prototype of the Electrostatic Analyser (ESA) were compared. A comparison between the bare and coated ESA showed an UV induced photoelectron suppression by a factor of 10^3. Also the reflectivity of the coating was not observed to change significantly even after repeated usage.

Effect of the non-uniformity of the electrostatic analyser

The spacing of 3mm was designed between the curved analyser plates in PAPA for its optimal performance. Deviations in the gap setting during the mechanical fabrication can arise owing to its curved geometry. The effect on the deviation in the applied voltage to the analyser plates for each of the desired energies from those of the uniform gap setting was studied. The sweeping of analyser plate voltages while keeping the energy constant at electron/ion source showed the desired voltage for a given energy to slightly shift towards a lower voltage than those envisaged earlier with a uniform gap setting (see Fig 15).

Similarly, the width of the energy peak was found to increase during a non-uniform gap setting while sweeping the energy after maintaining a constant voltage corresponding to that energy at the analyser plates (see Fig 16). These studies gain significance during the final calibration of the instrument.Fig. 17 shows PAPA ESA Proto-model with CuO coating.

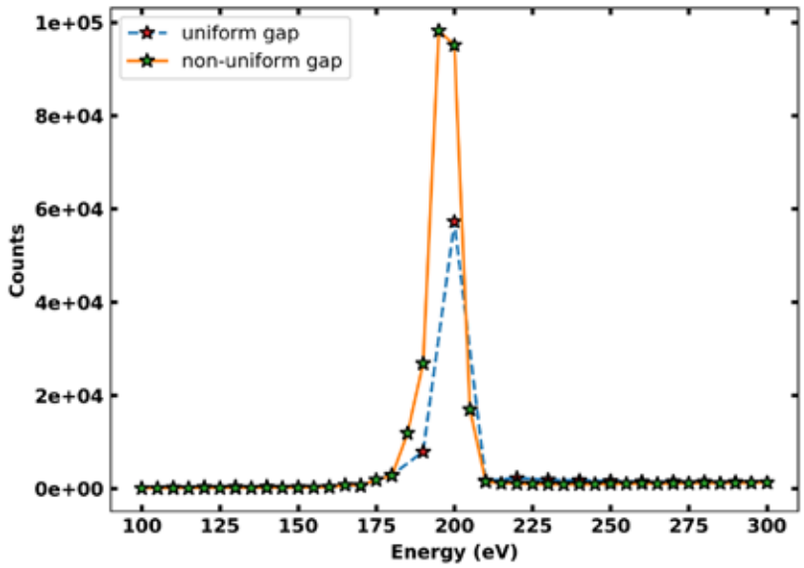

Figure 16: Change in the width of the energy peak due to non-uniform gap setting

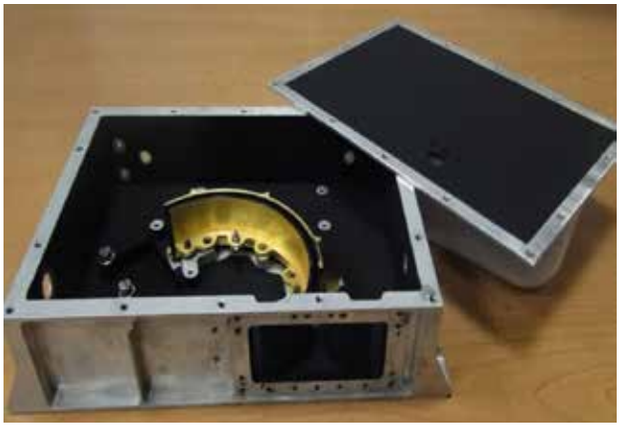

Figure 17: PAPA ESA Proto-model with CuO coating

High Vacuum Space Simulation Facility

In recent times, High Vacuum Space Simulation Facility (HVSSF) (Fig. 18) was augmented with new spectrophotometerand installation of mu metal shielding.

Installation of Cary 5000 UV-VIS-NIR Spectrophotometer

A Cary 5000 UV-VIS-NIR Spectrophotometer (Fig.19) for measuring the reflection and transmission properties of coating as a function of wavelength (175 nm to 3300 nm) was augmented with HVSSF. The instrument uses photomultiplier tubes for detecting photons in the UV and Visible wavelengths and PbS detector in the NIR. It has an external diffuse reflectance accessory (DRA) for measuring the reflectance. The instrument is capable of measuring both the total reflectance (that includes both the specular and diffuse components) and the diffuse components separately. It provides variable slit widths ranging from 0.01 to 5 nm for providing the required wavelength resolution. This instrument will have potential usage in characterizing the coating that is used for suppressing the UV induced photoelectrons in space borne plasma analysers. The study of the copper oxide coatings made for PAPA and those for the upcoming mission for Mars and Venus will completely rely on this instrument. Also the quality and light leakage at NIR wavelengths for the interference filters used by other groups at SPL can be studied by measuring its transmission properties at these operating wavelengths.

Figure 18:High Vacuum Space Simulation Facilityof SPL

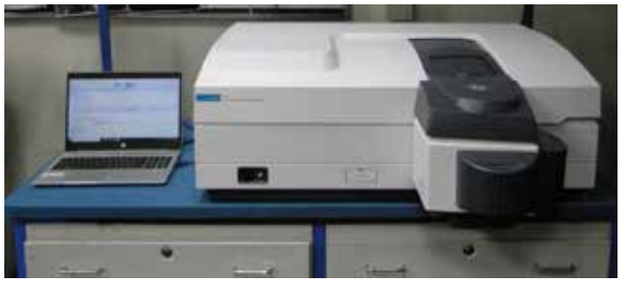

Figure 19:Photograph of the UV-VIS-NIR Spectrophotometer

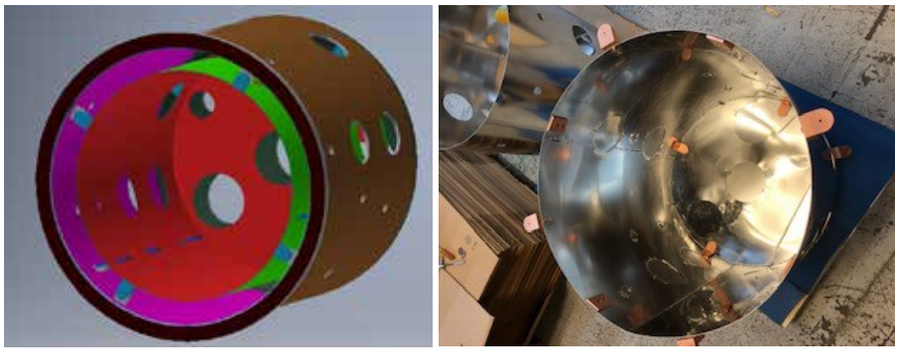

Figure 20: Mu Metal shielding in HV Chamber

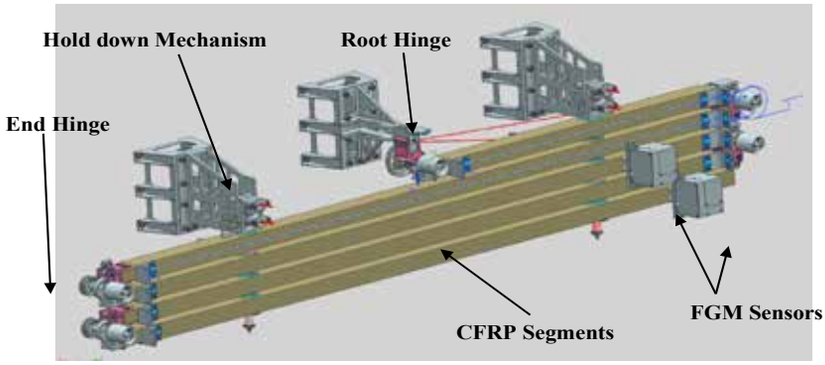

Figure 21: Front view of the deployable boom in stowed condition. The two FGM sensors can be seen on the right side.

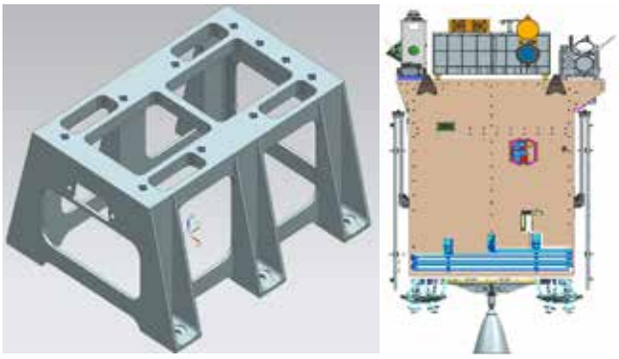

Figure 22: (Left) the hold-down interface bracket, (Right) The deployable boom for FG Magnetometer interfaced with spacecraft.

Installation of mu-metal shielding

Mu metal is a soft ferromagnetic material that does not retain a macroscopic internal field after the removal of an external magnetizing field. The high permeability of Mu-metal provides a low reluctance path for magnetic flux, leading to its use in magnetic shields against static or slowly varying magnetic fields. Magnetic shielding made with high-permeability alloys like mu-metal works not by blocking magnetic fields but by providing a path for the magnetic field lines around the shielded area. Thus, the best shape for shields is a closed container surrounding the shielded space. In light of this, a double layered mu-metal shield with a layer thickness of 2mm each was designed to exactly fit inside the 1m cylindrical chamber in HVSSF (Fig. 20).

CHACE-2 QM output verification and Proto Model Telecommand tests using Checkout System

For ensuring the accurate decoding of data from CHACE-2 payload onboard CHANDRAYAN-2, independent output measurements are being carried out at HVSSF.

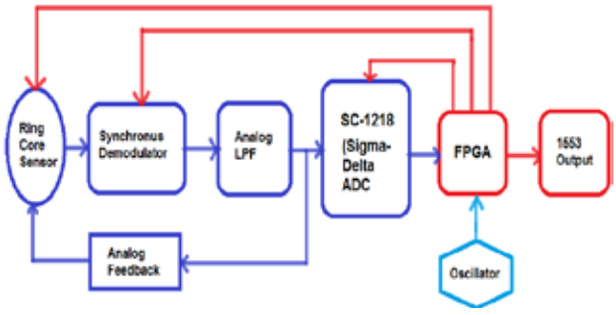

Figure 23: FGM sensor block diagram.

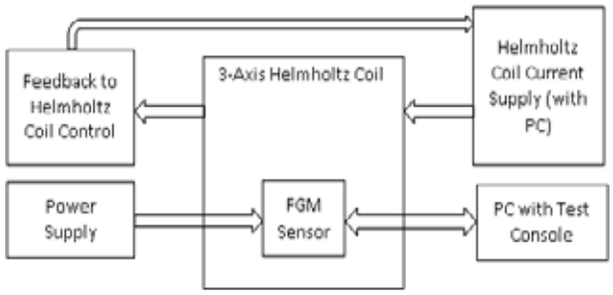

Figure 24: Blockdiagram of the calibration setup

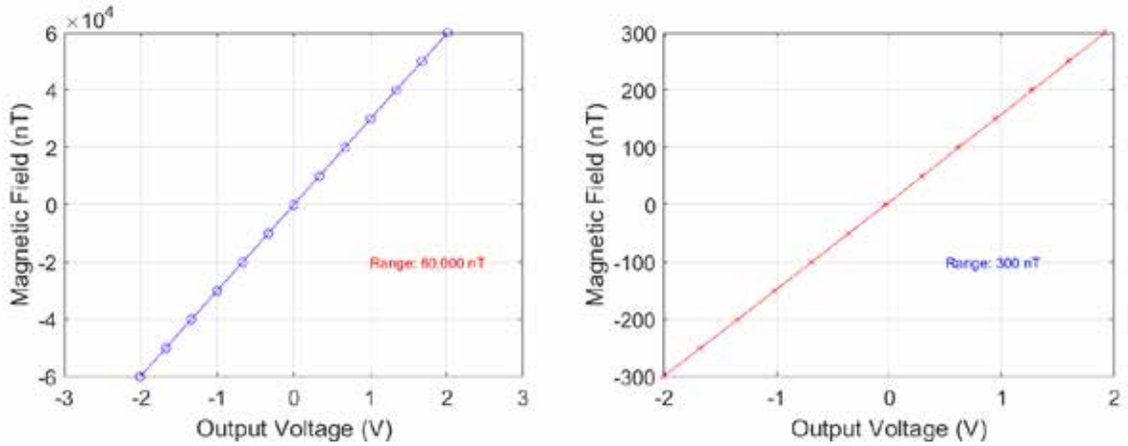

Figure 25:FGM sensor calibration (left) for the highest range of ± 60,000 nT, (right) for the lowest range of ± 300 nT.

Various parameters are tuned to match the flight settings and response of the instrument is verified. CHACE-2 telecommand response was also verified using the proto model at HVSSF.

Electron current measurement by VIT Students

VIT University students pursuing the development of a rocket borne payload to measure the concentration of Meteor Smoke Particles (MSP) in the altitude range 60–100 km visited HVSSF in order to test the I-V converter signal conditioning electronic sub system. The system is designed to measure the electron current generated from the Faraday cup detector on the MSP sensor. The tests were carried out using a Pico-source meter, which provided 1 nA current to the signal conditioning unit.

Fluxgate Magnetometer onboard Aditya-L1 Spacecraft

The deployment mechanism for the fluxgate magnetometer onboard Aditya-L1 is modified so that the boom, which is holding a dual set of triaxial fluxgate magnetic sensors, can be deployed on ground for testing. A half-segment of 67.5 cm is added to the existing four CFRP segments of 140 cm each resulting in an increase in the overall length of the boom to 627.5 cm as shown in Figs. 21-22.

The FGM layout has been modified and the updated magnetometer schematic is shown in Fig. 23. The FGM sensors are calibrated in the extreme measurement ranges with the calibration set-up as shown by a block diagram in Fig.24 and the results in Fig. 25.

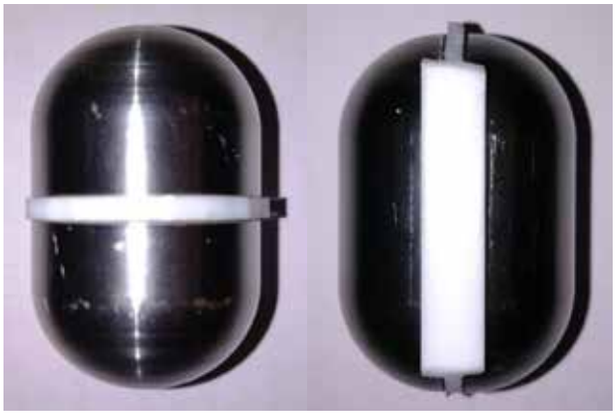

Figure 26:LP prototypes of same dimensions (50 mm long × 30 mm wide) partitioned horizontally and vertically. The two partitions are mechanically integrated but electrically insulated (white colour, Teflon) with each other.

Prototypes of VIPER realized at SPL/VSSC

VIPER (Venus Ionospheric Plasma wavE detectoR) is a suit of four instruments onboard first Venus mission having a customized Langmuir probe (LP) and a triaxial electric field sensor (EFS) andto be developed in-house at SPL/VSSC, and triaxial fluxgate magnetometer (FGM) and triaxial search-coil magnetometer (SCM) to be developed at LEOS, Bengaluru. The prototypes of LP are designed and developed at SPL/VSSC. Preliminary tests are carried out on these LP prototypes for performance evaluation which have dimensions 50 mm × 30 mm. These LPs are cut into two halves (as shown in Fig. 26), horizontally in one configuration and vertically in another so that one half can be swept from a negative to positive voltage so as to obtain the I-V characteristics whereas the other half can be kept on a fixed positive bias voltage to acquire the plasma electron saturation current.

The preliminary performance evaluation tests of these LP prototypes are carried out in a 50 cm long and 40 cm diameter cylindrical vacuum chamber at the HVSSF, SPL with a low energy electron source. For SS304 work function of ~4.5 eV and accounting for the approximate loss in this path 50 cm path, the incident electron energy was fixed at 6 eV to negate the possibility of generation of secondary electrons from the LP prototypes by the striking electrons.

In the vacuum chamber, the LP prototypes were placed on a non-conducting, insulating holder which was installed at a distance of 50 cm from the electron gun mouth at the vacuum chamber pressure of 1.7×10^{-6} mbar which is a pre-

Figure 27: LP prototypesmounted in the vacuum chamber horizontally (left) andvertically (right).

requisite for operating the electron source also as shown in Fig.27.Four different set of performance evaluation tests were carried out as given in table 4.

Table 4. Different configurations used for performance evaluation

Set No.	LP Partition	LP Orientation
1.	Horizontal	Horizontal
2.	Horizontal	Vertical
3.	Vertical	Horizontal
4.	Vertical	Vertical

In all four cases, two sets of experiments were carried out, in first case the probe current is measured at one partition with sweep voltage with the other partition at 0 V bias and in the second case the probe current is measured at one partition with sweep voltage with the other partition at +0.5 V bias. The observations are shown in Figs. 28-29.

From preliminary analysis, it is observed that the vertical portioned LP performed better than the horizontally partitioned LP. However, for conclusive observation the LP prototypes are to be tested in a vacuum chamber filled with plasma so that the prototypes are immersed in the plasma from all sides. Efforts are ON to perform these evaluation tests in a vacuum chamber at Institute for Plasma Research (IPR), Gandhinagar where low density and low temperature plasma can be produced for sufficiently long duration.

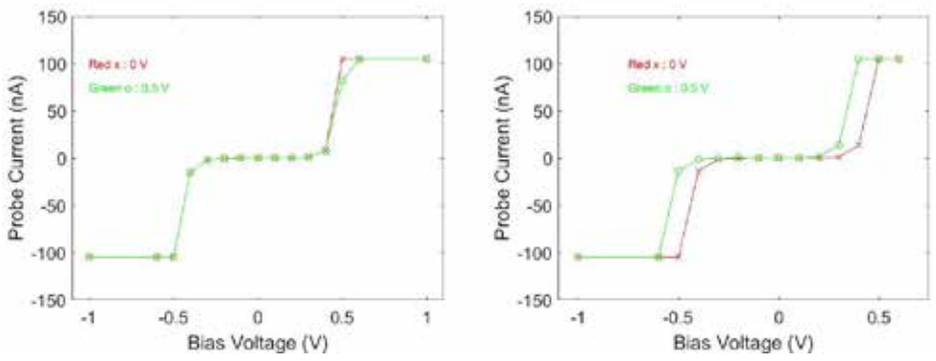

Figure 28:Performance evaluation with LP configuration as perset 1 (left) and set 2 (right).

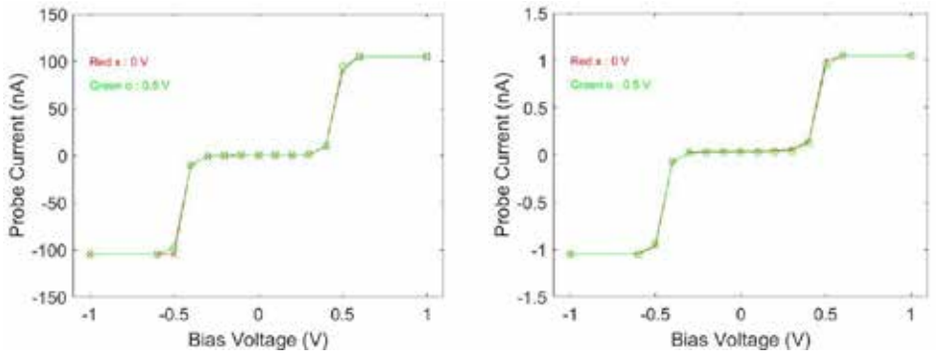

Figure 29:Performance evaluation with LP configuration as per set 3 (left) andset 4 (right).

Investigation of the response of Martian atmosphere to interplanetary coronal mass ejection

The dynamics of the upper atmosphere and its interaction with the solar radiation and the particles in the solar wind determine the stability and long term evolution of planetary atmospheres. Escape of atmospheric gas in to space is considered as an important mechanism for the observed climate change in Mars. The study of the effects that interplanetary coronal mass ejection (ICME) result on the upper atmosphere, ionosphere, magnetosphere and on the atmospheric loss rate gains significance owing to the increased occurrence of such events in the early Martian history and their potential contribution to the escape rate of atmosphere. The Mars Atmosphere and Volatile Evolution (MAVEN) mission to Mars was used to study the response of a recent ICME events on the escape rate of atmospheric molecules and atoms. The Solar Wind Ion Analyser (SWIA) showed density and velocity enhancement associated with the ICMEs. The Extreme Ultraviolet Monitor (EUVM) onboard MAVEN showed the enhancement in the flare irradiance associated with the ICMEs. The magnetic topology associated with the ICMEs from the Solar Wind Electron Analyser (SWEA) showed electron pitch angle distribution of supra thermal electrons in the upstream of Mars bow shock. The Solar Energetic Particle (SEP) events were noticed to be in consistent with the passage of ICMEs. The Suprathermal and Thermal Ion Composition (STATIC) showed the presence of high energetic heavy ions in the flux ropes. The auroral emissions measured using Imaging Ultraviolet Spectrograph (IUVS) from the limb scan across the upper atmosphere showed emissions from the UV CO_2^+ doublet at 289 nm and CO Cameron bands that are excited due to particle impact on CO_2. These MAVEN observations will be modelled to estimate the ion loss rates from the Martian atmosphere.

Investigation of vibrationally excited Polycyclic Aromatic Hydrocarbons at mid-infrared wavelengths in Comets

The evolution of organic molecules on their journey from molecular clouds to the early solar system is not well understood. The regions in the interstellar medium (ISM) with high density host molecular clouds consisting of gas and dust that form the raw materials for forming stars and planetary systems in the future. Comets are considered to be primitive bodies formed during the formation of solar system that contain agglomerate of frozen gases, ices and rocky debris. Comets are formed in the outer solar system and stored either in the Oort cloud or in the Kuiper belt region. It is believed that comets are made of unaltered interstellar materials and preserve the early stages of solar nebula. Polycyclic Aromatic Hydrocarbons (PAH) molecules consisting of fused benzene rings with a wide spread presence in the ISM of our own and external galaxies are believed to be frozen in comets. The solar radiations heat up the icy material of the comet to form coma during their entry into the solar system. During their sublimation process the exposed cometary nucleusexhibit signatures that are characteristics of its composition. The infrared emission bands at 3.3, 6.2, 7.7, 8.6 and 11.2 um are attributed to the C-H stretching and bending vibrations and C=C stretching modes of PAH molecules. Detection of these vibrational transitions in comets will establish the link between the ISM and comets. The public archival data from the Infrared Spectrometer (IRS) on board Spitzer Space Telescope in the wavelength between 5.3 to 38 um was used for the present study. The continuum was subtracted from the observed spectra to bring out the weak PAH emissions. Our analysis showed the presence of PAH on four comets that approached Sun during its observation with its position well suited for the detection of PAH at mid-infrared wavelengths.

Planetary Neutral Atmospheres Through In-Situ Observations

Observations from CHACE-2 (Chandra's Altitudinal Composition Explorer-2) on Chandrayaan-2 Orbiter

Following the launch of Chandrayaan-2 (CH2) orbiter on 22 July 2019, CHACE-2 had four observations enroute and before achieving the final orbit of 100 × 100 km. The normal phase observations (NPO) started from 04 September 2019 onwards. Initially in the NPO phase, CHACE-2 was operated for 2 hours per operation and two such operations per Earth day, which was later enhanced to 4 fours with two such operations per Earth day. The spectra quality and the functionality have been found to be satisfactory, with the housekeeping parameters within limits (Fig. 30). Since the orbital plane of CH_2rotates with respect to Sun direction, there were observations in the dawn-dusk and noon-midnight planes. Currently, the distribution of Argon-40 in the lunar exosphere is being analysed.

Ground Segment Activities of Payloads in Planetary and Space Missions of ISRO

Following the launch of Chandrayaan-2 orbiter, the ground segment activities for CHACE-2include the post launch data processing and the operations planning. For PAPA on Aditya-L1, the activities are progressing.

CHACE-2 Data Processing Pipelines Operational at ISSDC

CHADViS (CHACE-2 Data Visualization Software) for the quick look display of science and housekeeping parameters and CHACE-2 Data Archival Software

(CHADAS) for long term archival of science data are continuously Space operational at Indian Science Data Center (ISSDC), Byalalu, Bangalore.

Long Term Archival (LTA) of CHACE-2 Data for Public Release

The CHACE-2 data products along with the label files generated as per Planetary Data System version 4 (PDS4), have been verified for PDS4 compliance by the ISDA working group. The work towards the complete PDS4 structure, which includes all documents, calibration information, mission information etc. in addition the data products, which will be eventually used for the public release of data after the lock-in period, is progressing. The Software Interface Specification (SIS) document has been generated. A peer review committee has been formed for the scientific review of the data products.

Ground Segment Activities for PAPA payload on Aditya-L1

The data products and the requirements for the quick look display have been arrived at. The development of software pipelines for the quick look display and archival of science data are in progress.

Payload Operation Centre at SPL

The payload operation centre in SPL has been receiving data from CHACE-2 payload on Chandrayaan-2 orbiter and MENCA on Mars Orbiter Mission.

Level-0 data sets for CHACE-2 operationsin different phases such as Earth-bound phase, cruise phase and normal phase observations have been regularly received from ISSDC via NKN-VRF link. These data sets are processed using automated software pipelines in POC; quick look plots are generated to verify the payload functionality. Also, a chain to generate the data products for archival also runs in POC.

MENCA had limited observations in 2019 with higher periapsis altitude (>4000 km) and a few observations when MOM had periapsis at lower altitudes (<250 km) in the Martian atmosphere in the year 2020. The data sets is being received in POC and processed through automated pipelines. The detailed analysis is in progress.

Development of dual mode Quadrupole Mass spectrometer

Following the demonstration of dual mode (ion and neutral) operation of mass spectrometer in the laboratory, the same has been accepted for the Venus Orbiter Mission of ISRO. The Baseline Design Review (BDR) has been completed. It has been suggested to use a boom to mount the payload away from spacecraft to reduce the effect of degassing of spacecraft on the payload observations. The work towards this is under progress in coordination with IISU.

Future Projections

Immediate Goals

The following studies will be carried out in near future.

- Continuation of Mars exospheric and Lunar plasma environment studies using the available data from MENCA onboard MOM and SARA onboard CH-1 missions respectively.
- Lunar exospheric studies using data from CHACE-2 onboard CH-2 mission.
- Solar wind electron and proton temperature anisotropy studies using data from solar missions.
- Plasma wave studies using data from the earlier missions
- Development of algorithms for processing of PAPA data and the software pipelines for various ground segment activities.
- Realisation of PAPA qualifying and flight models-QM&FM
- Realisation of QM&FM of fluxgate magnetometers of Aditya-L1 mission.
- Martian plasma environment and escape mechanisms using MAVEN data.

Long Term Goals

Solar wind and plasma wave studies using the data from PAPA and Magnetometer payloads of Aditya-L1 mission. Design and development of plasma analysers and dual mode neutral mass spectrometer and Energetic Neutral Atom (ENA) sensor for the upcoming MOM-2 and VENUS missions. Development of plasma wave sensor package and magnetometers for future missions. Studies on planetary plasma environment of the unmagnetized planets such as Mars and Venus using the data available from the past and contemporary missions.

Publications in Peer Reviewed Journals

1. Mukundan, V., S. V. Thampi, A. Bhardwaj, C. Krishnaprasad (2020), The dayside ionosphere of Mars: Comparing a one-dimensional photochemical model with MAVEN Deep Dip campaign observations, Icarus, 337, 113502, DOI:10.1016/j.icarus.2019.113502.
2. Mukundan, V., S. V. Thampi, A. Bhardwaj, and C. Krishnaprasad (2020), Model calculation of ionization efficiency in the Martian dayside ionosphere using MAVEN observations, MNRAS 497, 2239–2249, DOI: 10.1093/mnras/staa2123.
3. Das, T. P., S. V. Thampi, M. B. Dhanya, N. Naik, P. Sreelatha, P. Pradeepkumar, G. P. Padmanabhan., B. Sundar, D. P. Vajja, A. Nandi, R. S. Thampi, V. K. Yadav, J. K. Abhishek, Md. Nazeer, P. T. Lali, R. John, A. V. Aliyas, V. K. Sen, M. Ramprabhu, A. A. Krishna (2020); "Chandra's Atmospheric Composition Explorer-2 (CHACE-2) aboard Chandrayaan-2 to study the lunar neutral exosphere", Current Science, 118 (2), 202-209, DOI:10.18520/cs/v118/i2/202-209.
4. Manju, G., T. K. Pant, P. Sreelatha, S. J. Nalluveettil, P. P. Kumar, N. K. Upadhyay, Md. M. Hossain, N. Naik, V. K. Yadav, R. John, R. Sajeev, J. Ramalingam, P. George, A. Nandi, N. Mridula, R. P. Aswathy., J. J. Rana, S. Srivastava and S. Thampi (2020), "Lunar near surface plasma environment from Chandrayaan-2 Lander platform: RAMBHA-LP payload", Current Science, 118 (3), 383-391; DOI:10.18520/cs/v118/i3/383-391.
5. Manju, G., T. K. Pant, N. Mridula, R. P. Aswathy, P. Sreelatha, R. John, R. S. Thampi, A. N. Aneesh, J. K. Abhishek (2020), In-situ observations of rocket burn induced modulations of the top side ionosphere using the IDEA payload on-board the unique orbiting experimental platform (PS4) of the Indian Polar Orbiting Satellite Launch Vehicle mission,Journal of Atmospheric and Solar–Terrestrial Physics, 199, 105203, DOI:10.1016/j.Jastp.2020.105203.

Publications in Conference Proceedings

1. Vipin K. Yadav, "Plasma Waves inand around the Moon"; Proceedings of the URSI Regional Conference on Radio Science (URSI-RCRS 2020); February 12-14, 2020; Indian Institute of Technology (IIT-BHU), Varanasi, Uttar Pradesh;Page:1-4;doi:10.23919/URSIRCRS49211.2020.9113523

Scientific / Technical Reports

1. UV induced electron emission measurement from CuO coated samples; V Venkataraman and Abhishek J.K.; SPL/PAPA/Ebanol/062019; June, 2019.
2. ChaDViS User Manual; Ajay Krishna A, and M. B. Dhanya; Version 1.0; July 2019.
3. ChaDAS User Manual; Ajay Krishna A, And M. B. Dhanya; Version 1.0; July 2019.
4. PAPA onboard Aditya-L1 Mission Requirements (Version 2.0); PAPA Team;AdityaL1-PAPA-MR; August, 2019.
5. Channel Electron Multiplier detector and Carbon foil for Plasma Analyser Package for Aditya (PAPA) payload of Aditya-L1 Mission; Ginju V. George and Abhishek J. K.; PAPA/DQ/SR-01/19; September, 2019.
6. UV induced photoelectron study of cupric oxide (CuO) coating for PAPA; V. Venkataraman, Abhishek J.K., R. Satheesh Thampi; PAPA-Photoelectron-CuOCoating-02; October, 2019.
7. Engineering Model Test Plan of PAPA on Aditya-L1; Abhishek J.K. and R. Satheesh Thampi; AdityaL1-PAPA-EM-TP, December, 2019.
8. Baseline Design Review (BDR) Document of Venus Ionospheric Plasma wavE detectoR (VIPER) Payload onboard Venus Orbiter; VIPER Team*, SPL (VSSC)/LEOS *Vipin K. Yadav (Principal Investigator), VIPER-BDR-2020, January, 2020
9. Engineering Model test results for Plasma Analyser Package for Aditya (PAPA) payload of Aditya-L1 Mission; Abhishek J.K; SPL/PAPA/EM/012020; January, 2020
10. Estimate of UV induced photoelectron background at the Lagrangian (L1) point for PAPA; V. Venkataraman, Abhishek J.K., R. Satheesh Thampi; PAPA-Photoelectron-CuOCoating-03; 11 February, 2020

11. AdityaL1-PAPA-HVPPS-FEE-PPU-Requirements; Dhanya M.B., Abhishek J.K.;PAPA/SWReq./Issue-2; March, 2020
12. Functional Requirement Document (FRD) of Fluxgate Magnetometer; Magnetometer Team*, SPL/LEOS/URSC/PRL/IIG *Vipin K. Yadav (Principal Investigator), FGM-FRD-2020, May, 2020
13. Magnetometer Payload Instrument - Preliminary Design Review (PDR) Report (Revised); Magnetometer Team*, SPL/LEOS/URSC/PRL/IIG *Vipin K. Yadav (Principal Investigator), FGM-PDR-2020, June, 2020
14. Science Compliance Document for VIPER Payload onboard Venus Orbiter; Vipin K. Yadav (Principal Investigator), SPL/VSSC;VIPER-SCD-2020, June, 2020

Presentations in Symposia/Workshops/Conferences

1. Vipin K. Yadav; "Plasma Waves in Space: What we (don't) know", Brainstorming session on "Planetary Sciences: Current Trends & Future Perspectives"; Space Physics Laboratory (SPL), Vikram Sarabhai Space Centre (VSSC), Thiruvananthapuram; August 19, 2019.
2. R. Satheesh Thampi; "Plasma Analyser package for Aditya (PAPA): Status and Schedule"; Payload Progress Monitoring Committee (PPMC) Second Meeting; ISRO HQ, Bengaluru; December 9, 2019.
3. Vipin K. Yadav; "Fluxgate Magnetometer: Status and Schedule"; Payload Progress Monitoring Committee (PPMC) Second Meeting; ISRO HQ, Bengaluru; December 9, 2019.
4. R. Satheesh Thampi; "PAPA payload Status and Schedule" Director's Technical Review (DTR) by Director, URSC; December 12, 2019. (Through video-conferencing)
5. Vipin K. Yadav; "Venus Ionospheric Plasma wavE detectoR (VIPER)"; Baseline Design Review (BDR) Meeting of Venus Payloads Phase 2; ISRO HQ, Bengaluru; January 20-21, 2020.
6. R. Satheesh Thampi; "Venus Ionospheric and Solar Wind particle AnalySer (VISWAS)"; Baseline Design Review (BDR) Meeting of Venus Payloads Phase 2; ISRO HQ, Bengaluru; January 20-21, 2020.
7. Vipin K. Yadav; "Plasma Waves in and around the Moon"; 4th URSI Regional Conference in Radio Science (URSI RCRS-2020); IIT (BHU), Varanasi; February 12-14, 2020.
8. Vrinda Mukundan, et al., "Calculation of ionization efficiency in the Martian dayside ionosphere: modelling using MAVEN observations, Indian Planetary Science Conference at Physical Research Laboratory, Ahmedabad; February 19-21, 2020.
9. Vipin K. Yadav; "Fluxgate Magnetometer: Instrument and Science"; 1st Aditya-L1 Science Meet; ISRO HQ, Bengaluru; March 6-7, 2020.
10. R. Satheesh Thampi; "Plasma Analyser package for Aditya (PAPA): Instrument and Science"; 1st Aditya-L1 Science Meet; ISRO HQ, Bengaluru; March 6-7, 2020.

Invited Talks

Vipin K. Yadav

1. "Plasma waves around Comets", 3rd Asia-Pacific Conference on Plasma Physics (AAPPS-DPP 2019), Hefei, China;November 4, 2019.

Dhanya M. B.

1. "Magnetic Anomalies On The Moon", Indian Planetary Science Conference (IPSC-2020), Physical Research Laboratory (PRL), Ahmedabad, 19-21 February 2020.

Public Outreach

Dhanya M. B.

1. Member, Functional Committee for Resource Material and content Generation, World Space Week 2019, VSSC.
2. Member, Functional Committee for Lecture Programme, World Space Week 2019, VSSC.

Deputations

Vipin K. Yadav

1. 3rd Asia-Pacific Conference on Plasma Physics (AAPPS-DPP 2019); Hefei, China; November 04-08, 2019.

Training Programme

R. Satheesh Thampi

1. One-day training on "Patent drafting and Patent Filing"; HRDD, VSSC, Thiruvananthapuram; September 20, 2019.

Dhanya M.B.

1. Training On Artificial Intelligence (Phase-1) for ISRO/DOS Scientists/Engineers, ISRO HQ, Bangalore, November 4-9, 2019.
2. Training On Artificial Intelligence (Phase-2) for ISRO/DOS Scientists/Engineers, ISRO HQ, Bangalore, February 3-7, 2020.

V. Venkataraman

1. Structured Training Programme (STP) on "Scientific Satellite Missions: Payload Definitions, Development and Data Utilization"; Space Application Centre (SAC), Ahmedabad; January 22-28, 2020.

Atmosphere Technology Division

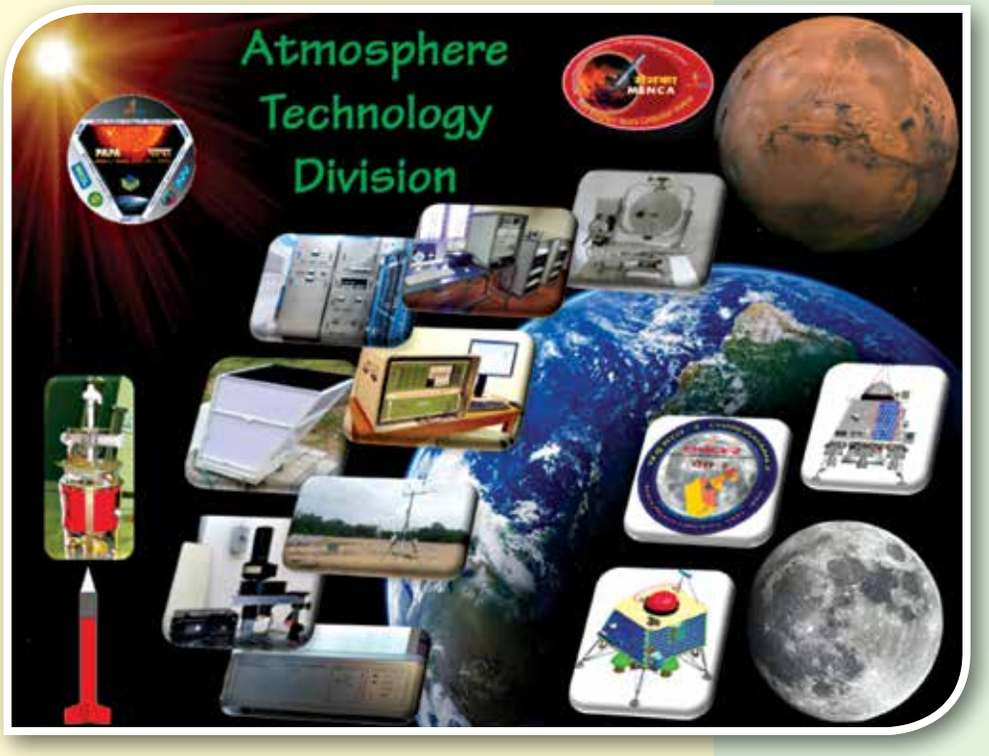

Atmosphere Technology Division (ATD) focuses on the technological aspects of experiment systems designed for atmospheric, space and planetary science areas, including the development and testing of balloon, rocket and space-borne payloads from the proof of concept and development of ground-based systems for in-situ probing and remote sensing of the atmosphere. ATD is also responsible for the augmentation and maintenance of the on-going experimental systems, providing technical support to the scientific activities of SPL and maintenance of the common technical facilities. It works in close coordination with the scientific branches of SPL and provides technical expertise for realization of scientific ideas.

Scientists/Engineers

K. Rajeev
Dinakar Prasad Vajja
N. Manikantan Nair
P. P. Pramod
M. Mohammed Nazeer
P. T. Lali
A. N. Aneesh

Technical Team

P. G. Anumod
B. Satheesh Kumar
Uttam S. Purty

Executive Summary

Atmosphere Technology Division (ATD) has made significant contributions to the scientific and technical activities of SPL during the reporting period. These include contributions to the following ongoing activities: (i) Technology development program (TDP) for the development of payload for solar occultation experiment, (ii) TDP for Atomic Oxygen sensor, (iii) Testing of the EM modules of PAPA onboard Aditya-L1, (iv) Steps for the fabrication of electronic cards for ChaSTE payload onboard Chandrayaan-3, (v) Development of a 2.5 kW power amplifier module for radar systems, (vi) Augmentation of the night time photometer, (vii) Operation and maintenance of HF Radar and Digisonde, (viii) Operation and maintenance of Clean Room, (ix) Installation and maintenance of experimental systems, and (x) Mechanical fabrication activities for scientific instruments. ATD is also responsible for the operation, maintenance and upgradation of the common electronic facilities at SPL.

Development of Payloads for Space Missions

Plasma Analyser Package (PAPA) Payload onboard Aditya-L1 Mission

PAPA is a payload scheduled to be flown onboard Aditya-L1 mission, which is the first Indian solar mission. It is being jointly developed in-house by SPL, AVN and other entities of VSSC. All the major design parameters of PAPA payload were extensively tested with its Engineering Model (EM). Its performance matched well with that of the simulated results.

Testing of Energy and Angular Resolutions of PAPA

Energy resolution of the electrostatic analyser section and time of flight of the mass analyser section of the payload were tested with ions of different energy, mass and charge state. Field of view and angular resolution of the instrument were also verified.

Thermal Study of PAPA

A thermal study was carried out on the PAPA EM for understanding heat dissipation at different internal locations of the payload. Seven thermocouple sensors were mounted at different locations (CEM detectors, different electrodes and DC-DC converter) of the payload (Fig.1). Temperature profiles of these sensors were recorded for 2 hours of operation.

Vibration and Total Ionization Dose Test (TID) for the Channel Electron Multiplier (CEM) Detector

The CEM detectors and Carbon foil to be used in the PAPA payload underwent various screening and qualification tests such as vibration and TID tests. The vibration test was carried out after mounting the CEM detector and the Carbon foil to the EM chassis. Their performance was recorded before and after the vibration tests. The TID test for the CEM detector was carried out at the ISITE, Bangalore. Cobalt-60 Gamma-ray source was used for this test.

Development of Python Application for Testing of Energy and Angular Resolutions

A python application has been designed and developed for evaluating the energy and angular resolutions of the PAPA EM in the absence of the PPU (PAPA Processing Unit). Its test set up is shown in Fig.2. The CEM sensors and the Front-End Electronics (FEE) cards were mounted inside the EM chassis and a high voltage bias for the detectors and various electrodes were fed from the laboratory high voltage power supply. The CEM pulse output was recorded using dual counter/timer equipment. The python application controlled the electron source, high voltage power supply and vacuum compatible stepper motor

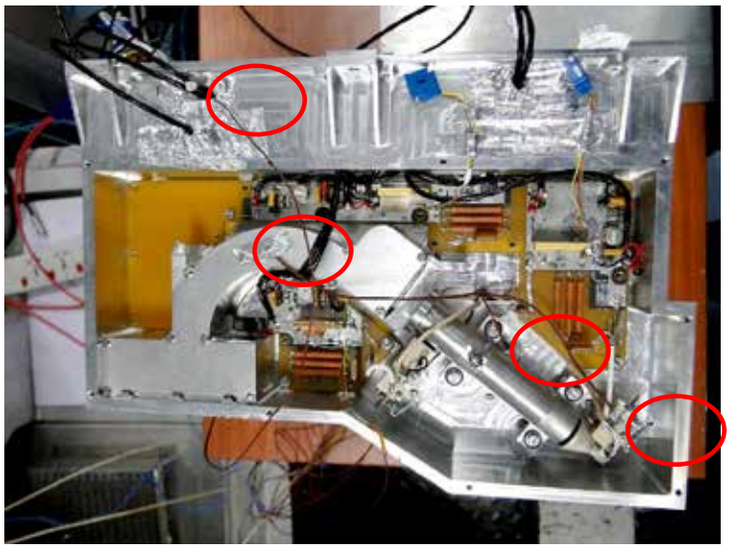

Figure 1: SWICAR Section of the PAPA EM. Thermocouple locations are highlighted in red.

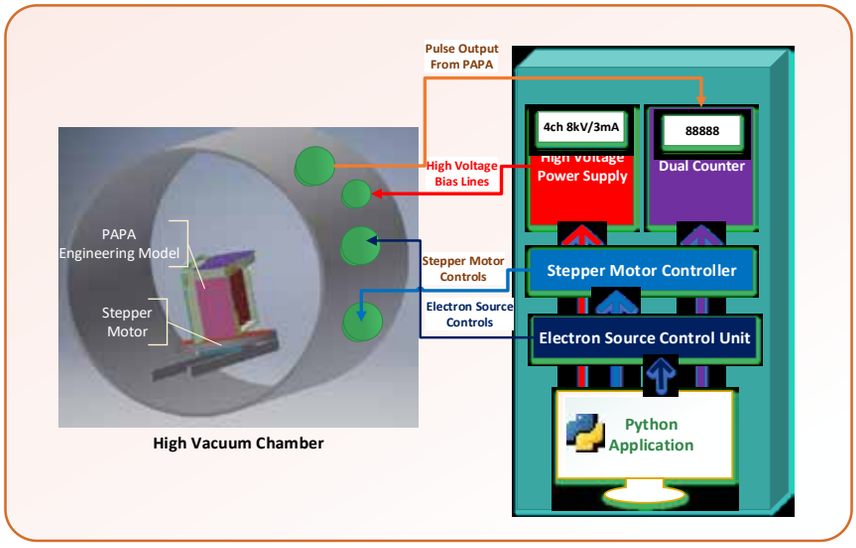

Figure 2: Schematic of Test Setup of the PAPA EM

remotely via RS-232 serial communication link. The application can set parameters such as high voltage bias, electron source output flux, rotation angle of stepper motor. It can also record counts for each setting in computer.

Development of Python application for Testing the High Voltage Programmable Power Supply (HVPPS)

A python application was developed for controlling the HVPSS cards of the PAPA payload. It was used for evaluating performance of the payload such as energy resolution and time of flight. It interfaces to the HVPPS unit through a checkout card using RS-232 serial link. It handles complete operation of the HVPPS such as enabling/disabling of high voltage generator for SWICAR and SWEEP sections, ramping up/down the individual voltages tied to different electrodes and detector bias lines. It also records voltages of each individual high voltage lines.

Development of Test Platform for Radiation Testing of Electronic Components

A few electronic components of the PAPA payload (charge sensitive preamplifier/discriminator, FIFO memory and time to digital converter) are industrial grade ICs. These components have to be qualified for space use. Single event radiation tests, Single Event Latch up (SEL) and Single Event Upset (SEU), have to be performed on these components at IUAC, New Delhi. A test platform was developed based on PIC18F6520 microcontroller for testing these ICs for 20 minutes effective exposure to radiation.

ChaSTE (Chandra's Surface Thermo-Physical Experiment) Payload onboard Chandrayaan-3 Lander

ChaSTE is one of the payloads planned onboard Chandrayaan-3 Lander. It is similar to the ChaSTE payload flown onboard Chandrayaan-2 mission. ChaSTE onboard Chandrayaan-3 is being fabricated at SPL in collaboration with various entities of VSSC and PRL. Primary objective of this payload is to make in-situ observations of temperature at multiple levels in the top 100 mm layer of the lunar regolith by deploying a thermal probe consisting of 10 RTD sensors. This will provide temperature profile of the poorly conducting lunar regolith and its time evolution during the lunar day. A heater is also attached to the probe for thermal conductivity measurements.

On-board Electronics of the ChaSTE Payload

The electronics module consists of processing electronics card and front-end electronics card. The processing electronics was designed at SPL. It drives BLDC motors for the probe deployment and penetration operations of the probe, acquires digitized sensors data from the front-end card and interfaces to Lander for data transfer, telecommand reception and telemetry generation. The front-end electronics was designed and fabricated at PRL and does the signal conditioning of RTD sensors and digitization of the signals. All electronic components have been provided from the Chandrayaan project. SMD components have been soldered by using re-flow process. Soldering of leaded components is in progress. Chassis fabrication is also in progress.

Technology Development Programme (TDP)

Development of the Payload for Solar Occultation Experiment

Development of payload for solar occultation experiment is a Technology Development Programme (TDP) of SPL/VSSC. The main objective of this payload is to measure the altitude profiles of aerosols and thin clouds above the thick cloud layers in any planetary atmosphere, including the Earth. The payload consists of three units, optics unit, gimbal unit and electronics unit.

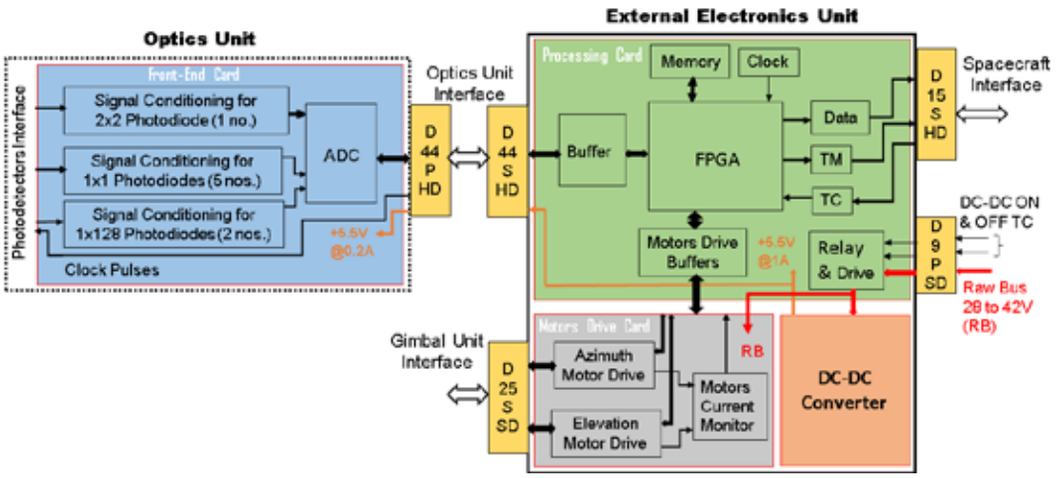

Figure 3: Block Diagram of the Payload Electronics

The electronics unit (Fig.3) is divided into three cards: front-end card, motors drive card and processing card. The front-end card is for signal conditioning of photodetectors and digitization of the analog signals. The motor drive card drives the azimuth and elevation motors of the gimbal unit and uses the information of Sun angles. The processing card acquires digitized data at a fixed rate and packetizes the data with necessary information (such as header, measurement time, packet number, gimbal rotation angles, checksum). It also interfaces to the spacecraft for payload data transfer, telecommand reception and telemetry generation. Power supply for the electronics is regulated +5.5 V at 1.2 A and raw bus.

Design of the front-end card (Fig.4) has been completed. The card has multiple signal conditioning channels for one 2x2 element photodiode, five numbers of 1x1 element photodiodes and two numbers of 1x128 element linear photodiode arrays. Each signal conditioning channel includes trans-impedance amplification, multiple-gain selection, noise filtering, single-ended to differential converters and charge reserving for ADC. These are detailed here.

Trans-Impedance Amplifiers

Trans-impedance amplifiers have been designed for 2x2 element and 1x1 element photodiodes for converting their output currents to voltages. The 1x128 element photodiode arrays have in-built current-to voltage conversion. photo voltaic mode was chosen for operating the photodiodes to minimize dark current noise. Gain of each amplifier was set based on the maximum output current of photodiode and its integration time was chosen as equal to signal measurement rate. The amplifiers have been implemented by using operational amplifiers of low input bias current and less noise density for measuring low currents precisely.

Bias Voltages for the Trans-Impedance Amplifiers

Since the trans-impedance amplifiers operate with single supply, bias voltage has to be applied to each amplifier to measure photodiode current in low light conditions.

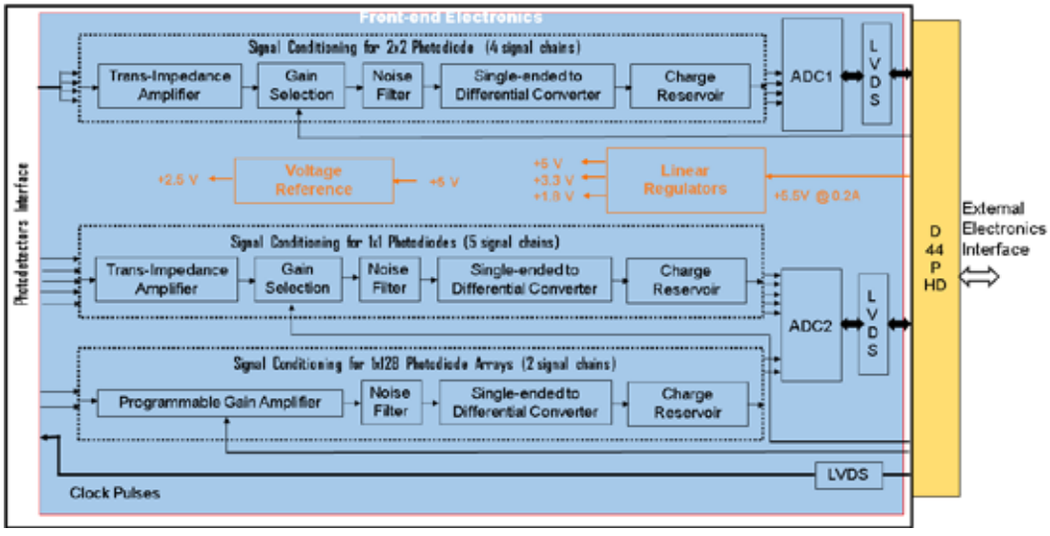

Figure 4: Block Diagram of the Front-end Electronics

This eliminates errors due to non-linear output swing of the amplifier at supply voltages. Suitable bias voltages are derived from the supply voltage by considering the amplifier's input common mode voltage range and output swing.

Programmable Gains

In the real-time operation, outputs of the photodetectors may slightly differ from the expected or simulated values. In such a scenario, multiple gains are required to fully utilize dynamic range of the ADC for better SNR. To meet this requirement, selectable four gain options have been provided for each photodiode signal as (i) expected gain, (ii) 20% more than the expected gain, (iii) 20% less than the expected gain and (iv) 50% less than the expected gain (safe mode). Two analog switches have been used for gain selection to avoid errors due to on-resistance and leakage current of the switches. Bandwidth effect due to parasitic capacitance across the switches in off state was also considered in the implementation.

Noise Filters

Noise or anti-alias filter is required to pass signal of interest and attenuate any high frequency signals in order to avoid aliasing with sampled signals. Measurement resolution required to meet the payload's dynamic range is 14-bit. The filters have been designed to pass the signals and attenuate noise components to a level equal to 14-bit resolution at the Nyquist frequency.

Analog to Digital Conversions

The analog voltage signals of the photodetectors have to be digitized for further analysis. A high resolution delta-sigma Analog to Digital Converter (ADC) with 8 differential inputs will be used for digitization. Two of such ADCs will be used for all the photodetector signals. The ADC can meet the payload's dynamic range and measurement rate requirements.

Single-ended to Differential Converters

Single-ended to differential converters have been implemented for driving differential inputs of the ADC for better static and dynamic performance. The drivers have good DC characteristics such as offset, bias current, temperature drift, rail-to rail swing and AC characteristics such as distortion and group delay between inverting and non-inverting paths.

Charge Reservoirs

Charge reservoir is used to store energy to charge ADC internal sampling capacitor. It also provides a place for the capacitor's charge to go. These have been designed for charging the ADC sampling capacitors within its acquisition time without settling error for 14-bit accuracy.

Low Voltage Differential Signaling (LVDS)

LVDS has been used for clocking the ADCs and the 1x128 element photodiode arrays and reading digitized data from the ADCs. These can transmit the signals with low jitter and can eliminate common-mode noise effectively.

Voltage Regulations

Operating voltages for the front-end card are derived by regulating the supply voltage. The derived voltages are +5 V, +3.3 V and +1.8 V. Linear regulators have been used for deriving the voltages and reducing low frequency ripple noise. Ferrite beads along with proper decoupling capacitors have been implemented to attenuate high frequency noise.

Voltage Reference

An external high precision +2.5 V voltage reference has been used as voltage reference for the ADCs. It is suitable for measurements with14-bit resolution and dynamic load of the ADCs.

Development of ATomic Oxygen Sensor (ATOXS)

Development of the ATOXS is one of the Technology Development Programmes of SPL. Scientific objective of the sensor is to measure the atomic oxygen density in the upper atmosphere of the Earth and there by understand the role of atomic oxygen in various processes in the upper atmosphere-ionosphere region. Zinc Oxide (ZnO) film will be used as the sensing element. Resistance of the film changes when reacts with the atomic oxygen.

The ATOXS system consists of a sensor unit and an electronics unit. The sensor unit will be mounted on exterior face of the satellite that receives continuous exposure to the atomic oxygen, whereas the electronics unit resides in the satellite interior. The sensor unit contains two ZnO films (one bare and one coated with SiO_2). The film coated with SiO_2 will be used as a reference to nullify effect of UV radiation. Thin films of ZnO will be vacuum deposited onto high-purity (>99.6%) alumina substrates with evaporated gold leads. The leads act as contacts for resistance measurement. The sensor unit has also a heater for reusing the film and a temperature sensor. The electronics unit contains the necessary circuitry for the resistance measurements, temperature sensor and heater control. The conceptual model of the electronics for atomic oxygen sensor has been worked out and will be used for the preliminary sensor development and characterization.

Ground based Systems for Scientific Studies

Augmentation of Night-Time Photometer

The night-time photometer is an in-house developed optical instrument capable of measuring five different airglow emissions from Earth's near space nearly simultaneously.

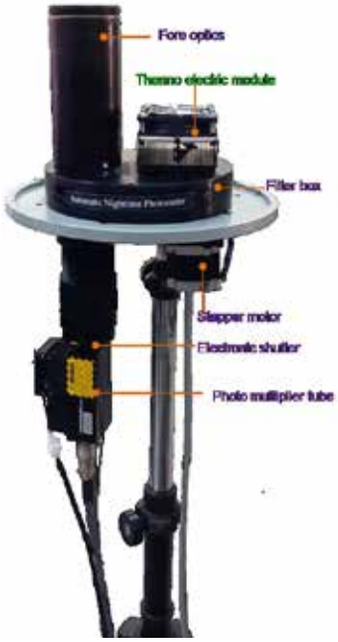

Figure 5: The automatic Night-time Photometer

Interference filters are the wavelength selectors used in the instrument. The ambient temperature has a profound effect in changing the central wavelength of the interference filters. With the increase/decrease of temperature, the peak transmission gets shifted to higher/lower wavelength side. This necessitates the need for controlling the temperature of the filter box to the optimum operating temperature of the filters. The optimum temperature of the filters used at present is 28 ± 0.1°C. For this purpose, a thermos-electric module (Make: Laird), which can maintain the required temperature in the operating temperature is used in the instrument to control the filter box temperature at 28 ± 0.1°C (Fig.5). The module requires 30W power at 12V. RS-232 based interface at 115200 baud rate has been added to the existing data acquisition software of the photometer for commanding the module and monitoring temperature.

Data Acquisition Software for Automatic Weather Station (AWS)

AWS system installed by SPL at Dehradun (Graphic Era University, for metrological monitoring as part of trace gas studies) stores data in its internal memory. In this instrument, the data can be accessed only manually and have to be copied frequently to avoid data loss due to memory overflow. To overcome this, an automatic logging software has been developed to interface with the system through RS-232 interface. The software acquires data through commands at 9600 baud rate and stores it in PC with proper format. It also displays necessary information in graphical and tabular format.

HF Radar System

The HF radar is a phase coherent, mono-static, pulsed radar operating at 18.1 MHz. It is a powerful tool to study the plasma instability processes responsible for the generation of Equatorial Electrojet (EEJ) and Equatorial Spread-F (ESF) irregularities. The antenna system of the HF radar comprises of a 12 x 6 antenna array spread over a physical area of 10,000 m² with elements mounted on antenna mast with a height of 6 m. Feeder network has been developed for 18.1 MHz operation and three beam orientations. The feeder lines were made using RG-218, RG-213 and RG-63 coaxial cables. In addition to its regular operations, the radar was also operated during observation programs in connection with the solar eclipse campaign and equatorial Spread-F studies. Figure 6 shows the Doppler spectra of E region irregularities observed by HF radar in the West beam at range gates from 91 km to 112 km on 12 June 2020 at 15:08 LT.

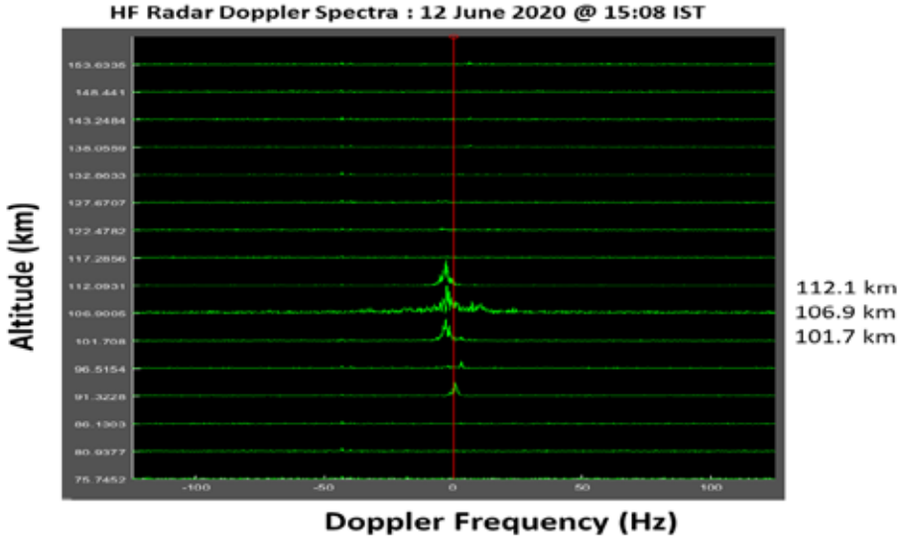

Figure 6: Doppler spectra of E region irregularities observed by HF radar in the west beam at range gates from 91 km to 112 km on 12 June 2020 at 15:08 LT.

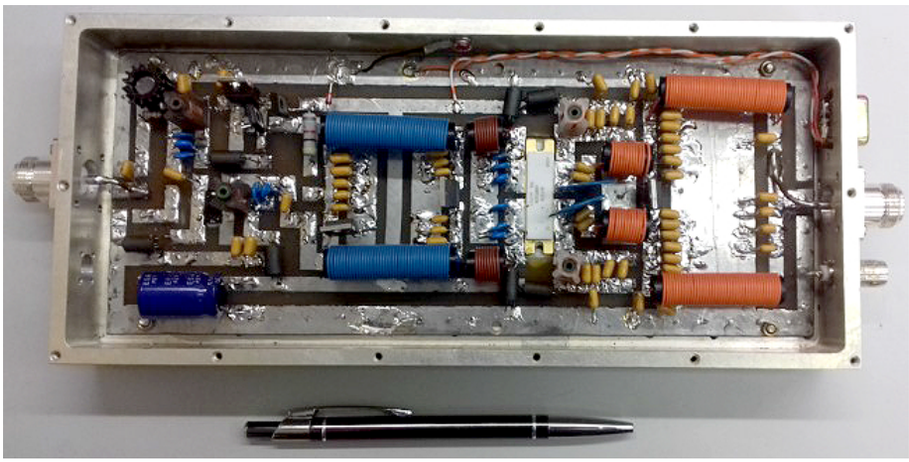

Figure 7: Three Stage Driver

2.5 kW RF Power Amplifier Module for Radar systems

A 2.5 kW high power amplifier has been designed, which will be a building block for the development of a 50 kW amplifier for the radar systems being operated at SPL. This amplifier is based on a balanced combination of two single-ended 1.25 kW amplifiers and combined using lumped element based Wilkinson type 2-way power combiners/dividers. This design has several advantages such as better stability, good input/output impedance matching and narrow bandwidth in a compact structure, at less cost. The input power required for the 2.5 kW power amplifier is more than 35 W, while the signal generated by the radar controller is 2.5 mW. Hence, a three stage driver circuit (Fig.7) with necessary stages of impedance matching and tuning circuits have been designed and developed for pre-amplifying the signal from the radar controller to the required input level of the 2.5 kW power amplifier (Fig.8). The circuit design and simulations were carried out using ADS software. Their prototype models have been in-house fabricated. The module was tested with the radar system.

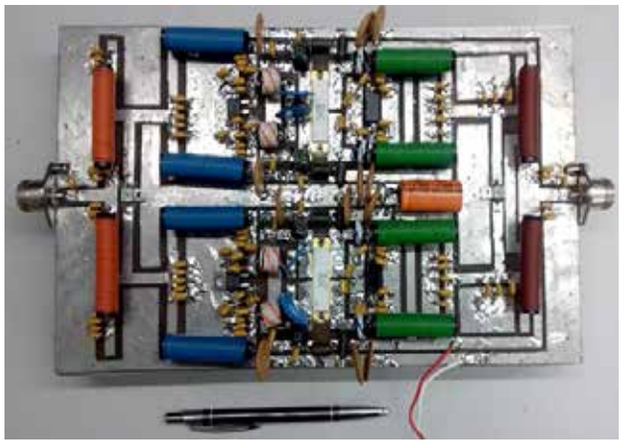

Figure 8: The 2.5 kW Power Amplifier

Installation, Operation and Maintenance of Scientific Instruments

Operation and periodic maintenance of the scientific instruments such as micro-rain radar, disdrometer, and meteorological sensors have been carried out. Preventive breakdown maintenance was done for the 32-m meteorological tower. This involves i) checking verticality of the tower by using theodolite instrument, ii) tightening of all the screws, removing the rust and re-painting the joints, iii) adjusting the guy wires and, iv) verifying the sensors. This meteorological tower also provides wind data to meteorology facility, TERLS during every RH 200 launch.

As part of ISRO's weather network for providing the surface meteorological data, a new 10-m AWS (ISRO-0026) was installed at TERLS (Fig.9). It has sensors for measurement of wind speed, wind direction, temperature, humidity,

Figure 9: ISRO's Automatic Weather Station installed at TERLS

rain gauge, pressure, solar radiation, soil temperature and moisture.

Experiment and Common Facilities

Operation and Maintenance of the HVSSF

The HVSSF of SPL is being operated and maintained routinely for development, testing and calibration of scientific payloads. The high vacuum chamber has also been augmented with a Cary 5000 UV-VIS-NIR Spectrophotometer and a Mu Metal shielding. The HVSSF is being used extensively for experimental, calibration and sensitivity studies, characterization of sensors and testing of spaceborne scientific payloads. Accuracy of the CHACE-2 payload onboard Chandrayaan-2 mission has been re-verified by performing measurements with an equivalent proto model of the instrument loaded with the flight tuned parameters. Its telecommand response was also verified using the model. Development, testing and calibration of the PAPA payload is being carried out at present.

Automation of Electronic Sub-Systems in the High-Vacuum Space Simulation Facility (HVSSF)

A flexible and configurable software system has been designed and developed in Python platform for automation and remote operation of all sub-systems in the HVSSF. The sub-systems were connected and controlled over RS-232 serial link. Setting up of all operational parameters and monitoring the parameters in real-time are the major responsibilities of the software. As part of this development, the required driver programs have been developed for laboratory DC power supplies (single channel 60V/1.5A and 3-channel 30V/3A), 4-channel 8 kV DC power supply, 20 kV DC power supply, vacuum compatible stepper motor, dual counter/timer and 2 keV electron gun power supply.

Operation and Maintenance of Clean Room

The Clean Room facility at SPL (with Class 10000 and Class 100000 Clean Rooms equipped with work benches of Class 100 and Class 1000 Laminar Flow Tables) has been utilized for the testing and development activities for scientific payloads of SPL and for the requirements from other entities of VSSC. Regular up-keep and maintenance of the Clean Room have been carried out.

Mechanical Engineering Activities

The following mechanical engineering activities were carried out at SPL workshop and CAD design unit: (1) design and generation of fabrication drawings for the Automatic Nighttime Photometer, (2) design and generation of fabrication drawings for Langmuir Probe (LP) assembly, (3) design and generation of fabrication drawings for ENWi probe assembly, (4) mechanical support for fabrication of LP and ENWi probes, (5) modification of MWR control unit chassis by providing additional fixture, (6) mechanical support for installation of new drilling machine and Lathe at SPL mechanical work shop, (7) mechanical support for establishing Hydrogen/Helium shed at ASL building, TERLS.

Technical Reports

1. Dinakar Prasad Vajja, Hardware Requirement Specifications of Front-end Electronics of Payload for Solar Occultation Experiment, SPL-TR-04-2020, June 2020
2. Dinakar Prasad Vajja and Sunil Kumar SV, Conceptual Design and Specifications of Payload for Solar Occultation Experiment, SPL-TR-03-2020, June 2020
3. Anumod P.G., C. Vineeth and Satheesh Kumar B., Automatic Nighttime Photometer (ANP) for Measuring Faint Airglow emissions from Earth's Near Space, May, 2020
4. Sunil Kumar SV and Dinakar Prasad Vajja, Baseline Design Review Document: Solar occultation Photometry for vertical profiling of Aerosol and thin clouds in Venusian atmosphere (SPAV), SPL: VSSC/BDR/SPAV/01, 2019
5. Tanmay Singhal, Aasik V and Dinakar Prasad Vajja, Mission Operational Plan for ChaSTE Payload of Chandrayaan-2, VSSC-MVIT-ASMG-SSMD-TR-1275-2019

Training Programme

Dinakar Prasad Vajja

1. Patent Drafting and Patent Filing, HRDD, VSSC, 20 September, 2019.
2. Dinakar Prasad Vajja, Training on E-procurement, HRDD, VSSC, 27 January, 2020

Anumod PG

1. Introduction to Optimization in Engineering Design, HRDD, VSSC, 31 October, 2019.

Office and Administrative Support

Team

Geetha C.

Shajahan J.

Salini M. S.

Shiji N. D.

Simi Ismail

Yoosaf N.

SPL administration facilitates the administrative and secretariate requirements for a smooth and effective functioning of SPL by providing co-ordination, communication and logistics. Besides the general administration, office management and housekeeping of SPL, it caters to the necessary official assistance to different ISRO projects such as ARFI, ICARB, RAWEX and NOBLE. It co-ordinates and provides logistic support for different national observation campigns of SPL. Also SPL administration is responsible for coordinating activities within SPL, involving other Divisions, Facilities of VSSC and/or other ISRO centers and different Institutions/Universities. It meets the administrative requirements of different payload such as ChaSTE, RAMBHA and PAPA development for different ISRO's space missions.

Research programme facilitated by ISRO fellowship program including research fellowship program and research associate program is a major activity of SPL. SPL administration provides the required assistance in terms of documentation, intervening between universities and organizing PhD Synopsis/Defence, Doctoral Committee meetings, student reviews, regular student/faculty seminars and Central Level Monitoring Committee meeting of VSSC. It also supports for arranging Seminar Talks/Invited Talks in SPL by leading scientists from India and abroad and arranges necessary logistics required during their visit and stay.

ACADEMIC PROJECTS

Well aware of societal commitments, SPL boasts a strong capacity building programme by imparting in-house training through M.Sc. & B.Tech. project work, and M.Phil. & M.Tech. dessertation supervision to young students of different colleges, institutes and universities. SPL also hosts Summer Research Fellows of Indian Academies and INSPIRE fellowship awardees for two months project works. During the academic year 2019-2020, a total of 16 students underwent the training under different disciplines of SPL.

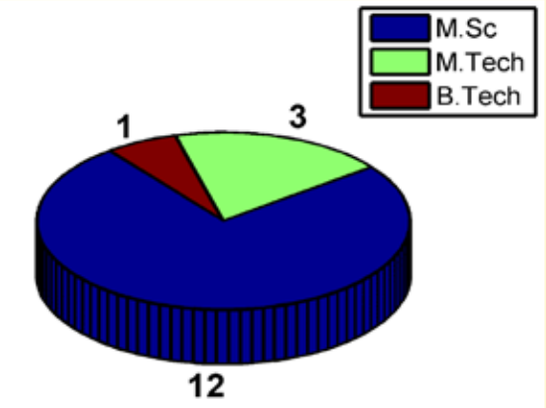

M.Tech. Projects

- **Anie K. Lal,** Cochin University of Science and Technology, "Investigations on the aerosol boundary layer interactions over the Indo-Gangetic Plain", July 2019-June 2020, [Supervisor: Vijayakumar S. Nair]
- **Shilpa K.,** Dept. of Water Resources & Ocean Engineering, NIT, Karnataka, "Soil Moisture Retrieval from Multi-frequency PolSAR Data" [Supervisor: Dr. Suresh Raju C]
- **Lubnas S.,** TKM College of Engineering, Kollam, Kerala, Design, "Develop and Test a customized Langmuir Probe for Future Space Missions", Aug 2018 – July 2020, [Supervisor Dr. Vipin Kumar Yadav]

M.Sc. Projects

- **Reshma Rajan**. M.Sc Physics, Sree Narayana College, Cherthala, "Investigations on the cloud condensation nuclei properties of South Asian outflow", January -March 2020, [Supervisor: Vijayakumar S. Nair]
- **Neema T. S.,** Karpagam Academy of Higher Education, Coimbatore, "Microwave dielectric properties of natural earth materials and emissivity studies", November 2019-January 2020, [Supervisor: Dr. Renju R]
- **Rohith K.,** Karpagam Academy of Higher Education, Coimbatore, "Microwave interaction with atmospheric constituents and dielectric properties of hydrometeors", November 2019-January 2020,[Supervisor: Dr. Renju R]
- **Malavika Manoj**, Amrita Vishwa Vidyapeetham, "Retrieval of Soil Moisture from Passive Microwave Satellite Data", April 2020- June 2020. [Supervisor: Dr. Nizy Mathew]
- **Sree Lekshmy M. R**., Dr Palpu College for Arts and Science, Pangode, Trivandrum, "Study of the total electron content of the ionosphere over Kavaratti, and Trivandrum and their intercomparison for different constellations of Global navigation satellite systems", July 2019 – January 2020. [Supervisor : Dr R. K. Choudhary]

- **Jyothy M.,** Dr Palpu College for Arts and Science, Pangode, Trivandrum, "A comparitive study on the total electron content of the ionosphere over Trivandrum, and Port-Blair using multi-frequency, multi-constellation GNSS receiver systems", July 2019 – January 2020. [Supervisor: Dr R. K. Choudhary]
- **Priyalekshmi** ., University of Kerala, Karyavattom, Trivandrum, "On the climatology of geo-effective solar flares during the 24th solar cycle and the parameters controlling the intensity of flare time emissions", January2020- July 2020. [Supervisor: Dr Manju G].
- **Vaisakh G.**, Govt. Victoria College, Palakkad, "The influence of gravity waves on the ionospheric F region over the location of Thiruvananthapuram during solar minimum conditions: A case study",July 2020-August 2020, [Supervisor: Dr Mridula N].
- **Chandni**, Govt. Victoria College, Palakkad, "A statistical study on the features of major geomagnetic storms during 1980 to 2010, spanning three solar cycles", July 2020-August 2020. [Supervisor: Dr Mridula N].
- **Sanoj S. S.**, University of Kerala, Karyavattom, Trivandrum, "Study of SEP events and their interaction with Martian ionosphere", January 2020 to June 2020.[Supervisor: Smitha V. Thampi]
- **Ms Anjana V. S**., Cochin University of Science and Technology, Kochi," Changing Precipitation Patterns over the Southern Indian Peninsula: A Study using Global Precipitation Climatology Project", January-March, 2020, [Supervisor: Dr. K. Kishore Kumar]
- **Lis Mary Antony**, Department of Physics, Saint Joseph's College (Autonomous), Devagiri, Calicut, Kerala, "Magnetism and its existence in Various Planets in our Solar System", May-June 2020, [Supervisor: Dr. Dhanya M.B.]

B.Tech. Projects

- **V J Anand, Reshma S R, Salu M R**, Department of Electrical and Electronics Engineering, Trinity College of Engineering, Thiruvananthapuram, APJ Abdul Kalam Technological University. "2 Axis Gimbal Mechanism for Solar occultation project", January-February 2020 [Supervisor: Mr. Dinakar Prasad Vajja]

हिन्दी गतिविधियां

वीएसएससी की हिन्दी समितियों की सदस्यता

1. विपिन कुमार यादव, सदस्य, वीएसएससी अंतर्जाल वेबसाइट पर हिन्दी अंतर्वस्तु की विवीक्षा समिति; मई, 2016 से।

2. विपिन कुमार यादव, सदस्य, वीएसएससी आंतरजाल वेबसाइट पर हिन्दी अंतर्वस्तु की विवीक्षा समिति; सितंबर,2018 से।

हिन्दी में मौखिक प्रस्तुतियाँ

1. विपिन कुमार यादव,"मानव-सहित अन्तरिक्ष यान की तकनीकी चुनौतियाँ";तकनीकी हिन्दी संगोष्ठी: "मानवोचित प्रमोचन यान: तकनीकी चुनौतियाँ"; अक्तूबर 22-23, 2019;इसरो जड़त्व प्रणाली यूनिट (IISU), तिरुवनन्तपुरम, केरल।

हिन्दी में तकनीकी लेख

1. विपिन कुमार यादव; "गगनयान के सम्मुख जैविक चुनौतियाँ";तकनीकी सत्र;अंतर-केंद्र हिन्दी तकनीकी संगोष्ठी: "गगनयान-चुनौतियाँ"; सितंबर 25-26, 2019;सतीश धवन अन्तरिक्ष केंद्र (SHAR), श्रीहरीकोटा, आंध्र प्रदेश. पृष्ठ: 38-43

2. .विपिन कुमार यादव; "मानव-सहित अन्तरिक्ष यान की तकनीकी चुनौतियाँ";तकनीकी सत्र;तकनीकी हिन्दी संगोष्ठी: "मानवोचित प्रमोचन यान: तकनीकी चुनौतियाँ"; अक्तूबर 22-23, 2019;इसरो जड़त्व प्रणाली यूनिट (IISU), तिरुवनन्तपुरम, केरल। पृष्ठ: 254-262

हिन्दी में राजभाषा लेख

1. लक्ष्मी जी. एवंविपिन कुमार यादव; "राजभाषा हिन्दी एवं सर्वाधारी समाधान"; राजभाषा सत्र; तकनीकी हिन्दी संगोष्ठी संगोष्ठी: "हिन्दी को सर्वग्राह्य बनाने के उपाय"; अक्तूबर 22-23, 2019; इसरो जड़त्व प्रणाली यूनिट (IISU), तिरुवनन्तपुरम, केरल। पृष्ठ: 279-285

पत्रिका "गगन" में हिन्दी लेख

1. विपिन कुमार यादव; "मेरी प्रथम जापान यात्रा-2"गगन-49; अप्रैल – सितंबर2019, पृष्ठ: 12-14

2. विपिन कुमार यादव; "क्या बात है..." गगन-49; अप्रैल – सितंबर 2019, पृष्ठ: 26

3. विपिन कुमार यादव; "मेरी प्रथम चीन यात्रा" गगन-50; अक्तूबर 2019 – मार्च 2020, पृष्ठ:08-12

हिन्दी में निर्णायक / मंच संचालन

1. विपिन कुमार यादव;निर्णायक,"वीएसएससी के वाहन-चालकों के लिए हिन्दी समाचार-पत्र वाचन प्रतियोगिता"; हिन्दी माह समारोह; अगस्त 19 –सितंबर 18, 2019; विक्रम साराभाई अन्तरिक्ष केंद्र, तिरुवनन्तपुरम, केरल।

2. विपिन कुमार यादव;संचालन,वीएसएससी अहिंदी-भाषी कर्मचारियों के लिए हिन्दी प्रश्नोत्तरी; हिन्दी माह समारोह; अगस्त 28, 2019; वीएसएससी, तिरुवनंतपुरम, केरल।

हिन्दी प्रशिक्षण में भागीदारी

1. विपिन कुमार यादव; आधिकारिक भाषा के कार्यान्वन हेतु वीएसएससी के विभागीय हिन्दी समायोजकों व वेबसाइट केंद्र-बिन्दुओं के लिए आधिकारिक भाषा का अभिविन्यासी कार्यक्रम; जनवरी 13, 2020; हिन्दी अनुभाग, वीएसएससी, तिरुवनंतपुरम, केरल।

2. विपिन कुमार यादव; वीएसएससी की हिन्दी गृह-पत्रिका '**गगन**' के नियमित लेखकों हेतु एक अभिविन्यासी कार्यक्रम; जनवरी 13, 2020; हिन्दी अनुभाग, वीएसएससी, तिरुवनंतपुरम, केरल।

3. उमा के एन, सितंबर -2019 में वीएसएससी में आयोजित हिंदी सप्ताह समारोह के दौरान हिंदी एलोक्यूशन प्रतियोगिता में प्रथम पुरस्कार।

VISITORS

- **Prof. Devdutta S. Niyogi,** Purdue University, USA, "Improving Urban Severe Weather Prediction and Resilency", 26 July 2019.
- **Dr. V. K. Anandan, ISTRAC**, "A new approach to wind profiling with radars",20 September 2019.
- **Prof. V Chandrasekar**, Distinguished Professor, Colorado State University, Colorado, USA. "Microphysics and dynamics with dual-polarisation radar: Journey from invention to recent advances", 07 January 2020.
- **Prof. Saji Hameed**, Professor, University of Aizu, Japan, "The Indian Ocean Dipole - what we know and what we don't know", 06 March 2020.
- **Prasanth A Pillai**, IITM Pune, 06 March 2020.
- **Sridhar Balasubramanian**, IIT Bombay, 06 March 2020.

BRAINSTORMING MEETING

Space Physics Laboratory held a two-day brainstorming meeting during August 13-14, 2019 on important scientific themes having global implications that have prominently emerged from the research in different divisions in SPL. These themes were related to atmospheric aerosols, radiation & chemistry, atmospheric dynamics, and the plasma environments of Earth and other planetary bodies. The prime objective of this meeting was to brainstorm and (i) possibly identify potential science questions in view of the current global research trends, (ii) evolve a program/mechanism to steer the research in India in these broad areas, and (iii) discuss the future directions. The meeting was scientifically quite invigorating. A few key science questions/gap areas were discussed and deliberated upon. A few established and active researchers/scientists from institutions across the country, as listed below, participated in this brainstorming meeting.

- **Prof. S. Gurubaran**, IIG, Mumbai
- **Dr. S. Tulasi Ram**, IIG, Mumbai
- **Dr. Nirvikar Dashora**, NARL, Gadanki
- **Prof. Ashik Paul**, University of Calcutta, Kolkata
- **Dr. Arun Kumar Upadhyaya**, NPL, New Delhi
- **Dr. S. Abhilash**, CUSAT, Cochin
- **Dr. Govindan Kutty**, IIST, Valiamala
- **Prof. Prasad Kumar Bhaskaran**, IIT, Kharagpur
- **Dr. Geeta Vichare**, IIG, Mumbai
- **Dr. Chandan Joshi**, JECRC University, Jaipur
- **Dr. Bhalamurugan Sivaraman**, PRL, Ahmedabad
- **Dr. N. Venkateswara Rao**, NARL, Gadanki
- **Dr. Umesh Kadhane**, IIST, Trivandrum
- **Dr. Vinu Valsala**, IITM, Pune

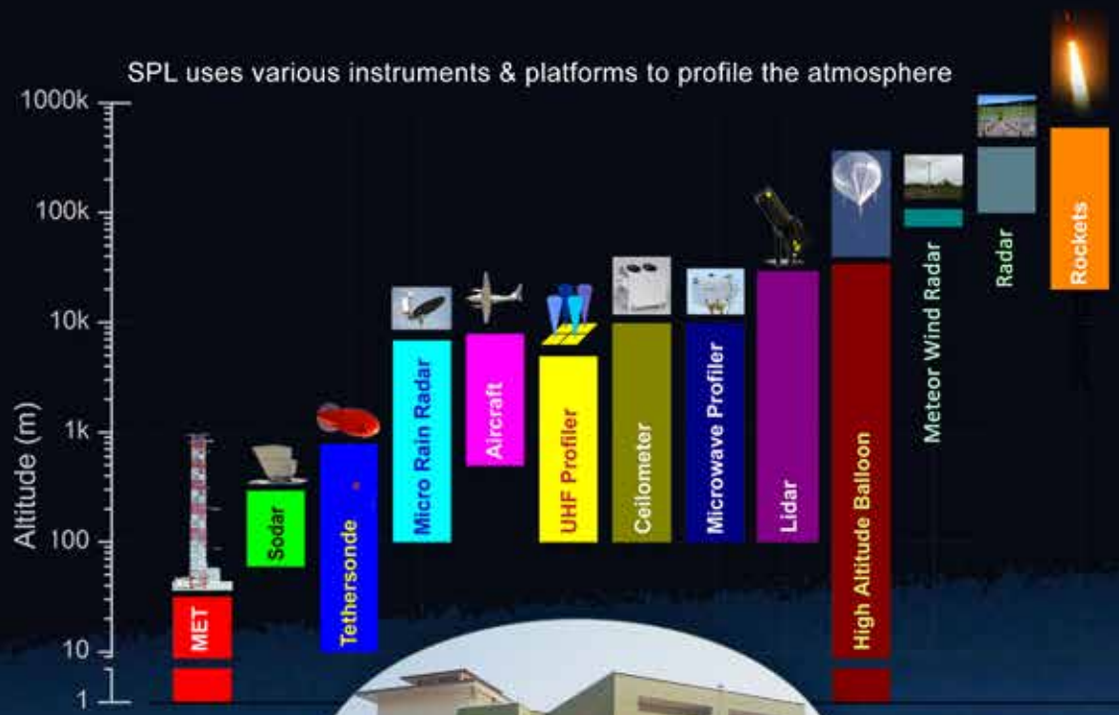

SPACE PHYSICS LABORATORY

Vikram Sarabhai Space Centre, Thiruvananthapuram - 695 022, INDIA

Email: directorspl@vssc.gov.in, Ph: +91 471 256 3663, Fax: +91 471 270 6535

https://spl.gov.in